Università degli Studi di Napoli "Federico II"

FACOLTÀ DI INGEGNERIA
Corso di Dottorato in Ingegneria dei Materiali e delle Strutture

Tesi di Dottorato di Ricerca
XXVIII Ciclo

Digital Holography Microscopy at Lab-on-a-Chip scale: novel algorithms and recording strategies

Coordinatore:
Ch.mo Prof. Giuseppe Mensitieri

Tutor:
Ch.mo Prof. Paolo Antonio Netti
Dott.ssa Melania Paturzo

Candidato:
Vittorio Bianco

Anno Accademico 2015–2016

To Lorenzo:

If you can keep your head when all about you
Are losing theirs and blaming it on you,
If you can trust yourself when all men doubt you,
But make allowance for their doubting too;
If you can wait and not be tired by waiting,
Or being lied about, don't deal in lies,
Or being hated, don't give way to hating,
And yet don't look too good, nor talk too wise:

If you can dreamand not make dreams your master;
If you can think-and not make thoughts your aim;
If you can meet with Triumph and Disaster
And treat those two impostors just the same;
If you can bear to hear the truth you've spoken
Twisted by knaves to make a trap for fools,
Or watch the things you gave your life to, broken,
And stoop and build'em up with worn-out tools:

If you can make one heap of all your winnings
And risk it on one turn of pitch-and-toss,
And lose, and start again at your beginnings
And never breathe a word about your loss;
If you can force your heart and nerve and sinew
To serve your turn long after they are gone,
And so hold on when there is nothing in you
Except the Will which says to them: 'Hold on!'

If you can talk with crowds and keep your virtue,
Or walk with Kings-nor lose the common touch,
If neither foes nor loving friends can hurt you,
If all men count with you, but none too much;
If you can fill the unforgiving minute
With sixty seconds' worth of distance run,
Yours is the Earth and everything that's in it,
And-which is more-you'll be a Man, my son!

Rudyard Kipling

CONTENTS

LIST OF FIGURES VII

LIST OF ACRONYMS XI

INTRODUCTION 1

1 TOWARD LABORATORIES ON A CHIP 7
- 1.1 The Optofluidic concept . . . 9
- 1.2 LoC analysis of biological samples . . . 12
- 1.3 Optofluidic microscopy: LoC imaging of biomaterials . . . 15
  - 1.3.1 Flow cytofluorimetry . . . 16
  - 1.3.2 Scanning based approaches: the optofluidic microscope . 17
  - 1.3.3 Non interferometric phase retrieval . . . 20
  - 1.3.4 Interferometric phase retrieval . . . 27
  - 1.3.5 Proposed approach . . . 33

2 DIGITAL HOLOGRAPHY 39
- 2.1 Hologram formation . . . 42
  - 2.1.1 Noise components . . . 46
  - 2.1.2 Recording on digital supports . . . 46
- 2.2 Numerical reconstruction . . . 49
  - 2.2.1 Convolution method . . . 51
  - 2.2.2 Angular Spectrum method . . . 52
- 2.3 Digital Holography microscopy . . . 54

3 DH MICROSCOPY THROUGH COMPLEX MEDIA 69
- 3.1 Imaging through static scattering layers . . . 71
  - 3.1.1 Turbid Lens Imaging (TLI) . . . 72
  - 3.1.2 An approach based on the speckle memory effect . . . 73
  - 3.1.3 Coherent imaging through scattering microfluidic channels 74
- 3.2 DH microscopy through turbid flowing fluids . . . 83
  - 3.2.1 Theoretical background . . . 84
  - 3.2.2 Microfluidic application of the Doppler theory . . . 88
- 3.3 Clear coherent imaging through quasi-static turbid media . . . 91
  - 3.3.1 Working principle of Multi-Look Digital Holography . . . 92

- 3.3.2 Exploiting the Brownian motion of small colloidal particles 94
- 3.3.3 Imaging through a live bacteria suspension 99
- 3.4 Clear coherent microscopy through blood 106
  - 3.4.1 Blood flow producing a speckle-like pattern 108
  - 3.4.2 Imaging adherent cells through a turbid flow of RBCs . . 115

4 EMBEDDING DH IMAGING FUNCTIONS ONBOARD CHIP 125
- 4.1 Phase Shifting Space-Time Scanning Interferometry (PS-STSI) . . 126
  - 4.1.1 Theoretical formulation of PS-STSI 128
  - 4.1.2 Phase retrieval adopting PS-STSI 130
- 4.2 Optofluidic DH microscopy with custom FoV using a LSA 137
  - 4.2.1 Phase Shifting Microfluidics STSI (PS-µSTSI) 138
  - 4.2.2 Microfluidics Space-Time Digital Holography (µSTDH) . 143
- 4.3 DH microscopy using polymer lenses printed on-chip 149
  - 4.3.1 Interferometric characterization 151
  - 4.3.2 Imaging test 155
- 4.4 Common path off-axis DH microscopy on-chip 158

CONCLUSIONS 169

REFERENCES 181

LIST OF PUBLICATIONS 201

ACKNOWLEDGEMENTS 207

LIST OF FIGURES

Figure 1.1 Iterative solutions to the phase retrieval problem. (a) Gerchberg-Saxton (GS) algorithm. (b) Input-Output (IO) algorithm. 22

Figure 1.2 Sketch of the typical DILH setup for microfluidic imaging. Light scattered from the samples interferes with undisturbed light on the recording device. 30

Figure 2.1 (a) Hologram recording: the interference pattern produced by the reference wave and the object wave is recorded; (b) Image reconstruction: light diffracted by the hologram reconstructs the object wave. 40

Figure 2.2 Schematic view of the angular extent of the object: θ_{max} is the angular extent of the object and the maximum angle between object and reference wave; d_0 is the distance along the optical axis between the CCD chip and the object; D is the transversal size of the object, normal to the optical axis. 47

Figure 2.3 Geometry for recording and numerical reconstruction of digital holograms. The object (a star in this sketch) is in the plane $(x, y, z = 0)$. The hologram is recorded in the acquisition plane $(x', y', z = d_0)$, capturing an out-of-focus object information. Numerical propagation of the hologram from the acquisition plane to the reconstruction plane, $(x_R, y_R, z = d_0 + d)$, allows to scan all the planes along the optical axis, z, till providing the refocused image of the object. 48

Figure 2.4 DH microscopy setup in transmission configuration. FS: Fiber Splitter. MO: Microscope Objective. BS: Beam Splitter/Combiner. IP: Image Plane. HP: Hologram Plane. The inset on the right shows a sketch of the sample plane, where the LoC is positioned, and a phase-contrast map of fibroblast cells in suspension. 55

Figure 2.5 Fibroblast cells are let adhere on the inner substrate of a microfluidic channel, where RBCs are then inserted. Figures (a-d) shows the holograms, H_S, of the samples corresponding to four different portions of the channel, recorded using the setup sketched in Fig. 2.4. 56

Figure 2.6 Amplitude Fourier spectra, $|\mathcal{FFT}\{H_S\}|$, of the holograms shown in Fig. 2.5. The three main orders of diffraction are clearly recognizable and, due to the off-axis geometry introducing a spatial carrier, these are just slightly overlapped and can be spatially filtered out to extract the +1 term. 58

Figure 2.7 An example of amplitude reconstructions, at distance z=+20 cm from the recording plane, of the holograms shown in Fig. 2.5. The reconstruction is performed by means of the Fresnel method, i.e. the signals, $|C(x_R, y_R, d)| = |\mathcal{F}r\{H_S\}|$, are shown. The three main orders of diffraction are clearly recognizable. In this case, despite the introduction of a spatial carrier due to the off-axis geometry, its frequency is not enough large to avoid overlapping between the diffraction orders, so that a non optimal extraction of the +1 order can be obtained. . . . 59

Figure 2.8 Amplitude DH reconstructions, $\left|C^{+1}(x_R, y_R, d)\right|$, of the holograms shown in Fig. 2.5. 60

Figure 2.9 Wrapped phase reconstructions, $\Psi(x_R, y_R, d)$, of the holograms shown in Fig. 2.5. 60

Figure 2.10 Unwrapped phase-contrast maps, $\hat{\varphi}(x_R, y_R, d)$, of the holograms shown in Fig. 2.5. 62

Figure 2.11 Pseudo-3D views of the unwrapped phase-contrast maps, $\hat{\varphi}(x_R, y_R, d)$, shown in Fig. 2.10. The phase values are expressed in radians. 62

Figure 2.12 An overview of all the DH reconstruction steps in the case of a C-elegans embryo. (a) Hologram, H_S. (b) Amplitude Fourier spectrum, $|\mathcal{FFT}\{H_S\}|$. (c) Amplitude reconstruction, $\left|C^{+1}(x_R, y_R, d)\right|$. (d) Wrapped phase reconstruction, $\Psi(x_R, y_R, d)$. (e) Unwrapped phase-contrast map (inverted colors), $-\hat{\varphi}(x_R, y_R, d)$. 63

Figure 2.13 An overview of all the DH reconstruction steps in the case of two C-elegans embryos. (a) Hologram, H_S. (b) Amplitude Fourier spectrum, $|\mathcal{FFT}\{H_S\}|$. (c) Amplitude reconstruction, $\left|C^{+1}(x_R, y_R, d)\right|$. (d) Wrapped phase reconstruction, $\Psi(x_R, y_R, d)$. (e) Unwrapped phase-contrast map (inverted colors), $-\hat{\varphi}(x_R, y_R, d)$. 64

Figure 2.14 An overview of all the DH reconstruction steps in the case of a live C-elegans specimen (L1 adult stage), recorded at three different time instants. (a) Holograms, H_S. (b) Amplitude reconstructions, $\left|C^{+1}(x_R, y_R, d)\right|$. (c) Wrapped phase reconstructions, $\Psi(x_R, y_R, d)$. (d) Unwrapped phase-contrast map, $\hat{\varphi}(x_R, y_R, d)$. 65

Figure 2.15 Post-processed phase-contrast maps of live C-elegans embryos (a-d) and L1 stage adult samples (e-h). 66

Figure 3.1 Imaging through scattering microfluidics [158]. (a) White-light image of a microfluidic chip with four channels. A salt deposit is settled only in the second channel (red dashed box), with opacity increasing from left to right. (b) White-light view of a different portion of the chip, with the maximum layer thickness. (c-d) Only the left part of a test target is placed behind a scattering channel imaged respectively by (c) white-light microscopy and (d) coherent laser microscopy at $\lambda = 632,8\mu m$. (e) Coherent laser microscopy of the target in absence of the scattering layer. (f-g) White-light images of the salt deposit inside the chip obtained with (f) 20x and (g) 50x magnification. 75

Figure 3.2 Sketch of the experimental set-up [158]. On the right side of the image a phase contrast map is shown of the cell flowing through the scattering channel along the x nominal direction. 78

Figure 3.3 Phase-contrast mapping of a sample cell flowing into a clear microfluidic channel. In the inset the top view is shown [158]. 81

Figure 3.4 Derivative of the average phase-contrast vs. time. An example of mean velocity estimation employing four gates is shown. On the right the scattering channel is sketched showing in green, for each plot, the window where the average is performed [158]. 81

Figure 3.5 Holographic reconstructions of a sample cell flowing into a scattering channel [158]. (a) SL phase-contrast map. (b) ML phase-contrast map. 83

Figure 3.6 Phase-contrast mapping of a sample cell flowing into a scattering microfluidic channel [158]. A side-view is shown along the columns of the image at fixed row. (a) SL. (b) ML. (c) SL post-filtered. (d) ML post-filtered. 84

Figure 3.7 DH microscopy through flowing colloidal solutions [115]. The Doppler frequency shift experienced by scattered photons is used to discard the contribution of the turbid medium. 89

Figure 3.8 Imaging bovine spermatozoa layered on a microfluidic channel respectively filled with (a,b) water and (c-f) milk. (a,c,e) Amplitude reconstructions. (b,d,f) Phase-contrast mapping. (c,d) Severe image degradation in the case of quasi-static liquid. (e,f) Clear imaging and phase mapping in the case of liquid flowing at $v = 330\mu m/s$ [115]. 90

Figure 3.9 Amplitude images of spermatozoa in turbid medium [166]. (a) N=1, $v = 0\ \mu m/s$; (b) N=250, $v = 0\ \mu m/s$; (c) N=25 (decimated), $v = 0\ \mu m/s$; (d) N=1, $v = 330\ \mu m/s$. 96

Figure 3.10 Normalized speckle contrast versus N [166]. 97

Figure 3.11 ML improvement versus v [166]. 98

Figure 3.12 Amplitude images ofa test target seen through a colloidal solution [166]. (a) $\nu = 0$ $\mu m/s$, N=1; (b) $\nu = 0$ $\mu m/s$, N=25; (c) $\nu = 30$ $\mu m/s$, N=1; and (d) $\nu = 30$ $\mu m/s$, N=25. (e) Image amplitude signals in the box under test. 98

Figure 3.13 Phase contrast mapping through quasi-static milk [166]. (a) $\nu = 0$ $\mu m/s$, N=1; (b) $\nu = 0$ $\mu m/s$, N=50; (c) $\nu = 30$ $\mu m/s$, N=1; and (d) $\nu = 30$ $\mu m/s$, N=25. (e) Enhanced pseudo-3D view of the map in (b). 100

Figure 3.14 A sketch of the experiment aimed at imaging a test target through a severely scattering bacteria volume [169]. On the right a 20x microscope image of the bacteria suspension is shown. 101

Figure 3.15 Average correlation coefficient [%] between holograms couples acquired at time lags τ [169]. 102

Figure 3.16 Imaging a test target through a thin scattering bacteria layer [169]. (a) Hologram of the target shown in the inset. (b) Hologram spectrum (+ 1 order). (c) ML reconstruction. 103

Figure 3.17 Amplitude reconstructions of a test target (200 lines/mm) through bacteria volumes at different concentrations [169]. (a,d,g) SL images. (b,e,h) ML images. (c,f,i) Image contrast over the lines indicated with the horizontal bars. Blue: SL image. Red: ML image. 105

Figure 3.18 (a) Dispersion index [%] vs. the number of looks, N. In the insets some of the corresponding n-looks amplitude reconstructions are shown. (b-d) To show MLDH flexible focusing a hair is inserted along the object beam path. (b) SL, target on focus. (c) ML, target on focus. (d) ML, hair on focus [169]. 106

Figure 3.19 Tamura coefficient vs. z[cm]. The inset on the bottom-left corner shows the SL reconstruction. The insets indicated by the vertical arrows show ML reconstruction after propagation at various distances [169]. 107

Figure 3.20 Imaging a test target through stationary blood [167]. (a) White-light image. Only the left side of the target is placed behind a microfluidic channel filled with blood. (b) White-light image of the channel filled with blood. (c) SLDH amplitude reconstruction. (d) MLDH amplitude reconstruction. (e) Sketch of the set-up used to obtain the images in (a) and (b). MO: Microscope Objective. 109

Figure 3.21 (a) Correlation coefficient with respect to the first acquisition, as a function of v and the frame index, n. (b) Global correlation coefficient as a function of the fluid speed, v [167]. 111

Figure 3.22 Amplitude SL reconstructions of the test chart through blood flowing at different velocities [167]. 113

Figure 3.23 Comparison between SL (left) and ML (right) amplitude reconstructions of the test chart seen through blood moving at different velocities. Thanks to the ML gain the target gets visible at lower speed [167]. . . 114

Figure 3.24 Normalized dispersion index, D [%] versus v. The plot is obtained for N=50 holograms being processed [167]. 115

Figure 3.25 An overview of the experiments so far carried out to investigate the problem of revealing targets hidden behind turbid/scattering layers. For each case, the ratio R between the characteristic length of the occluding objects and target size is reported. Depending on R, different strategies have to be adopted to solve the imaging problem [168]. . . . 116

Figure 3.26 The experimental conditions: a cell adheres on the inner wall of a microfluidic channel with the RBC flow occupying different positions on the optical axis [168]. An out-of-focus recording in the plane (x', y') collects information from the whole volume and numerical reconstruction is performed in the cell best-focus plane, $(x_{R,M}, y_{R,M}; z = z_{R,M})$. 118

Figure 3.27 Imaging a fibroblast cell adhering on the channel wall [168]. (a) Amplitude reconstruction in the case of transparent medium. (b) Hologram acquired after injecting RBCs inside the channel. (c) SL amplitude reconstruction of the hologram in (b). (d) ML amplitude reconstruction, where the image of the adhering cell is recovered from turbidity. . . . 120

Figure 3.28 Noise contrast vs. the number of looks [168]. 122

Figure 3.29 Phase-contrast mapping [115,168]. (a) Phase reconstruction in the case of the channel filled with transparent medium. (b) The SL phase reconstruction in the case of the channel filled with RBCs. (c) The ML phase reconstruction. (d) The pseudo-3D view of the phase map in (a). (e) The pseudo-3D view of the phase map in (c). 124

Figure 4.1 Set-up employed to build-up synthetic interferograms [215]. BS: Beam Splitter. M: Mirror. MO: Microscope Objective. BC: Beam Combiner. MS: Moving Stage. S: Sample. D: Detector. On the bottom the process of synthesis of an extended FoV space-time interferogram is sketched. The red line indicates the active sensor elements at each acquisition in case a linear detector is employed. The interferometric fringes are reported with the blue solid lines. 127

Figure 4.2 Interferometric imaging of a test resolution target [215]. (a) Acquired limited FoV interferogram. (b) Extended FoV synthetic interferogram built from the red column in Fig. 4.2(a) while scanning the target along the x' direction. 130

Figure 4.3 Interferogram synthesis from one single detector row (red line)[215]. Extended FoV is achievable exploiting the object shift. Improved visualization is also obtained, as the noise is constant along the t axis. . . 131

Figure 4.4 Synthetic interferogram of a PDMS drop. The red circled zones show the areas where the fringe spacing is too small to properly sample the high slope object parts [215]. 132

Figure 4.5 Flow chart illustrating the processing blocks of the PS-STSI technique [215]. 133

Figure 4.6 PS technique applied to a synthetic interferogram [215]. (a) Microscope image of a complex shape PDMS drop deposited on a plane substrate. (b-c) Synthetic amplitude (b) and wrapped phase (c) of the drop, obtained applying the three step PS algorithm. (d) Unwrapped phase-contrast map of the drop. 134

Figure 4.7 Pseudo 3D phase-contrast map of the PDMS drop obtained after unwrapping the signal reported in Fig. 4.6(c) [215]. 135

Figure 4.8 A PDMS micro-axicon and a PDMS drop are deposited on a plane substrate [215]. (a-b) Space-time amplitude (a) and wrapped phase (b) of the objects obtained applying the 3-step PS algorithm. (c) Microscope image of the micro-axicon. 135

Figure 4.9 (a) Syntetic interferogram of a PDMS circular drop. (b) Unwrapped phase-contrast map of the object obtained after applying the 4-step PS formula of Eq. (1.10) [215]. 136

Figure 4.10 Pseudo 3D unwrapped phase-contrast map of the PDMS circular drop of Fig. 4.9 [215]. 136

Figure 4.11 Experimental set-up for microfluidic SpaceTime Scanning Interferometry (μSTSI) [232]. Because of intrinsic scanning due to the sample flow, it is possible to build, with a compact Linear Sensor Array (LSA), a SpaceTime Digital Hologram (STDH) providing phase-contrast mapping with unlimited FoV in the flow direction. LS: laser source. BS: beam splitter. BC: beam combiner. S: sample. MO: microscope objective. M: mirror. 139

Figure 4.12 μSTSI synthesis [232]. Fibroblasts placed inside the channel are accelerated by an air bubble. The figure shows the process of generating a space-time interferogram with enlarged FoV (b), starting from limited FoV recordings (a). The red solid lines in (a) show the detection gate, i.e. the line used to build up the interferogram in Fig. 4.12(b). 141

Figure 4.13 Full-field recovery by PS-μSTSI. Experiments carried out using different test samples show the retrieval of the whole complex object field after applying a PS-μSTSI technique [232]. (a) Amplitude reconstruction and (b) phase-contrast map of polystyrene beads. (c) High throughput phase contrast imaging of fibroblast cells flowing at constant velocity is shown, along with the corresponding extended FoV synthetic interferogram (in the inset). 141

Figure 4.14 The phase-contrast map of C. elegans is estimated by PS-μSTSI [232]. (a) A sketch of the experiment. (b) Synthetic interferogram. (cd) Phase maps obtained before (c) and after (d) compensating the curvature due to the channel shape. 144

Figure 4.15 Synthesis of STDH. C. elegans is imaged with high magnification (M = 50) while flowing along the channel [232]. (a) Time sequence of limited FoV optical images showing small portions of the sample, recorded in-focus with a 2048x2048 CCD sensor for comparison. (b) STDH: a large FoV synthetic hologram is built up from out-of-focus recordings by using a single line detector, carrying 3D information from the whole sample at a glance. (c) The inset shows the interference fringes along a line orthogonal to the flow direction. 147

Figure 4.16 STDH z-scanning and phase-contrast mapping after propagation at the best-focus distance of the sample, z=21.7 cm. (a) Amplitude images extracted from the z-scanning stack are reported, showing the STDH automatic refocusing to estimate the best-focus distance of the sample. (b) Wrapped phase corresponding to the amplitude map in the red box in Fig. 4.16(a). (c) Unwrapped phase [rad]. (d) The inset shows details of the object, where the areas with different optical thicknesses are recognizable and reveal the inner structure of the worm [232]. The bottom part of Fig. 4.16(d) is reproduced from ref. [237]. 148

Figure 4.17 (a) Schematic view of the experimental set-up of the pyro-EHD printing system and side view images of a typical sequence of dispensed droplets. (b) Cross section view of a polymer lens on a surface treated using Fluorolink S10 providing a hydrophobic condition. (c) The representative image of the thin fluorinated layer onto microfluidic chip with printed and cured lenses formed with different diameters of 150-1500μm [249]. 150

Figure 4.18 Interferometric set-up adopted to characterize the lens optical properties [249]. (a) Mach-Zehnder interferometer. M: Mirror. BS: Beam Splitter. BC: Beam Combiner. MO: Microscope Objective. S: Sample plane. (b) Recorded Digital Hologram. 152

Figure 4.19 Normalized Zernike coefficients derived from the lens phase-contrast map. For each order P, the corresponding Zernike polynomial is shown [249,250]. 153

Figure 4.20 Spatial distribution of the main Zernike polynomials [249]. (a) Spherical factor. (b) Tilt along the y' axis. (c) Astigmatism. (d) Trefoil aberration. (e) Coma aberration, x' axis. 154

Figure 4.21 PDMS lenses were directly deposited onboard chip [249]. (a,b) Fibroblast cells flowing inside a microfluidic channel are imaged in focus through the lens, while out-of-focus images of the cells are obtainable outside the lens area. (c-d) A test resolution target was put behind the chip for test purposes. Two DH reconstructions show the magnification action operated by the lens. The microfluidic channel is clearly magnified as well as the target section indicated by the red box. The smallest target elements are not visible at all outside the lens (c), but these get resolved inside the lens area (d). 156

Figure 4.22 Imaging a test target and diatoms injected inside the channel. PDMS lenses are directly deposited onto the top of the chip, providing magnified imaging of the objects. (a) Optical microscope image of a test target, imaged (left) without and (right) through the lens. (b-c) Diatoms are let flow inside the channel. (Left) Imaging without the PDMS lenses. (Right) Magnified imaging of the diatoms through the lenses clearly show the formation of diatoms chains. In (b-c) the magnification operated by the PDMS lenses is $\mathcal{M}$=7. 157

Figure 4.23 LoC platform with embedded DH microscopy functionalities. (a) Top-view scheme of the chip. (b) A side-view scheme of the chip shows the diffraction grating allowing to extract the reference beam from one single impinging wavefront. The inset shows an optical microscope image of the test samples used herein, namely *Thalassiosira rotula* diatoms. (c) Optical microscope image of the grating parallel to the x axis ($\mathcal{M} = 20$). (d) Optical microscope image of the grating parallel to the y axis ($\mathcal{M} = 40$). 160

Figure 4.24 *Rotula* diatoms are let flow along the chip, and imaged as sketched in Fig. 4.23. The recordings correspond to the case of grating parallel to the y axis, shown in Fig. 4.23 (d). (a) Recorded holograms. The orthogonal interference fringes are apparent in the insets corresponding to the green boxes in figure, and these are modulated by the object distribution. (b) Amplitude Fourier spectra of the holograms in (a). (c) Amplitude reconstructions at z=0 (no propagation is performed), each one obtained after filtering out the order of interest and demodulating the hologram. (d) Recorded hologram showing a diatom chain in focus in the middle. (e) Amplitude reconstruction (at $z = 0$) of the hologram in (d) shows the objects in the blue circle in focus, while the objects in the red circle are out-of-focus. (f) Amplitude reconstruction at $z = -5cm$ shows both the chains largely defocused. (g) Amplitude reconstruction at $z = 3,56cm$ shows the refocusing of the objects marked with a blue circle. 163

Figure 4.25 Refocusing the hologram of diatoms flowing inside a chip and recorded using the common path off-axis DH microscopy scheme of Fig. 4.23. In (a-c) DH propagation at different distances is reported. Left: amplitude reconstruction. Right: Wrapped phase-contrast reconstruction. Blue circles: objects in focus. Red circle: objects out-of-focus. (a) No propagation, $z = 0$. (b) Propagation at $z = -1,53cm$ provides refocusing of the diatom chain in the middle of the FoV. (c) Propagation at $z = -3,57cm$ provides refocusing of the diatom chain on the bottom-left corner. (d-e) Unwrapped phase contrast maps shows refocusing of the chain (d) on the bottom-left corner, and (e) the top-right corner. 165

Figure 4.26 Time sequences acquired while letting diatoms flow along the channel. Diatoms form agglomerates, indicated with **A** and **B**. In particular, the unwrapped phase-contrast maps are reported, clearly showing the formation of diatom chains. Bottom: Pseudo-3D view of the unwrapped phase-contrast map corresponding to the agglomerate **B** at time $t = 0,37s$ from the reference time instant. 166

LIST OF ACRONYMS

AS: Angular Spectrum

BC: Beam Combiner

BS: Beam Splitter

CMOS: Complementary Metal-Oxide Semiconductor

CCD: Charge-Coupled Device

DEM: Dye Exclusion Microscopy

DFT: Discrete Fourier Transform

DH: Digital Holography

DIC: Differential Interference Contrast

DILH: Digital In-Line Holography

DMEM: Dulbecco's Modified Eagle Medium

ECM: Extracellular Matrix

EHD: Electrohydrodynamic

ELS: Elastic Light Scattering

ER: Error Reduction (algorithm)

FFT: Fast Fourier Transform

FoV: Field-of-View

FPM: Fourier Ptychographic Microscopy

FS: Fiber Splitter

FSC: Forward Scatter

GS: Gerchberg-Saxton (algorithm)

HIO: Hybrid Input-Output (algorithm)

HOM: Holographic Optofluidic Microscopy

HP: Hologram Plane

ILS: Inverse Light Scattering

IO: Input-Output (algorithm)

IP: Image Plane

LED: Light Emitting Diode

LoC: Lab-on-a-Chip

LOSH: Lensless Object Scanning Holography

LSA: Linear Sensor Array

LSI: Linear Space-Invariant

LTI: Linear Time-Invariant

MEMS: MicroElectroMechanical System

ML: Multi-Look

MLDH: Multi-Look Digital Holography

MO: Microscope Objective

MS: Moving Stage

MSE: Mean Square Error

NSOM: Near-field Scanning Optical Microscopy

OFM: Optofluidic Microscope

OT: Optical Tweezer

OSH: Optical Scanning Holography

PFPE: Perfluoropolyether

PSI: Phase Shifting Interferometry

PI: Propidium Iodide

PDMS: Polydimethylsiloxane

PMMA: Poly(methyl methacrylate)

PSF: Point Spread Function

PIV: Particle Image Velocimetry

QPM: Quantitative Phase Map

RBC: Red Blood Cell

ROI: Region-Of-Interest

SL: Single-Look

SLDH: Single-Look Digital Holography

STSI: Space-Time Scanning Interferometry

STDH: Space-Time Digital Holography

SNR: Signal-to-Noise Ratio

SSC: Side Scatter

SROFM: Super-Resolution Optofluidic Microscopy

SFS: Shape-From-Silhouettes

TM: Transmission Matrix

TIR: Total Internal Reflection

TIE: Transport of Intensity Equation

TLI: Turbid Lens Imaging

USAF: United States Air Force

WBC: White Blood Cell

INTRODUCTION

Microfluidics is the growing field embracing all the techniques and instruments aimed to confine liquids in small regions of space, providing accurate control of fluid streams. The physical laws governing the behavior of fluids change when scaling down to microscale. A good example in this sense is the absence of turbulence, as only laminar flows are typically allowed to establish inside a microfluidic channel. Thus, flow engineering is practicable with high accuracy to accomplish specific tasks. Optofluidics combines Optics and flow engineering to obtain new tunable and reconfigurable devices, like e.g. liquid waveguides, tunable lasers and optical switches. Along with the development of microfluidic technology, a fascinating idea has dawned upon over the last decade, which is the Lab-on-a-Chip (LoC) concept. A LoC device is a pocket platform consisting in microfluidic channels designed in order to form more or less complex circuits. Fluids can be delivered inside the LoC in controlled way and chemical/physical reactions can be induced and observed.

The LoC paradigm can be resumed in the will to emulate all the functionalities of a modern analysis lab onboard a portable device, realizable at contained costs. In particular, it has become more and more apparent as the study of biological samples can benefit from the use of a LoC environment. A cell bases its activities on external stimuli coming from mechanical interactions with other neighboring cells or the Extracellular Matrix (ECM), biochemical signals, soluble factors due to drug administration, or electrical cues. Thus, the typical behavior of a cell, e.g. the growth rate, duplication, migration, adhesion to substrates, mechanical interactions with the ECM and other cells, reaction to drugs, and death, strongly depends on the 3D shape and composition of its surrounding environment. A LoC is nowadays the most appropriate site to recreate the cellular environment and mimic all the external cues and forces affecting the cell behavior, taking advantage from the microfluidic flow control, as well as the miniaturization of components like valves, pumps, mixers and sorters.

These features make a LoC extremely promising as a novel device to embed diagnostics tools to be used at the point-of-care, allowing first screenings or accurate analysis in absence of adequate facilities and with untrained personal, e.g. in developing Countries and low-resource settings. Environmental monitoring and the emerging field of telemedicine can also benefit from the spread of LoC technology.

In this framework, imaging functionalities play a crucial role for a deep understanding of the processes occurring inside chip, and the study of biological samples in microfluidic channels requires some issues to be addressed. In the first place, label-free techniques are highly demanded, in order to avoid sample pretreatment and preventing the risk of altering its natural behavior due to markers. In the second place, quantitative information are required from the samples under analysis, e.g. thickness spatial distribution, morphologically relevant parameters, biovolume, refractive index spatial composition, or dry mass. In third place, the integration of the imaging functionalities onboard LoC devices is a highly pursued goal for point-of-care diagnostics, as the chip portability imposes to avoid the use of bulky diagnostics instruments. As it will be discussed in the following, matching these requirements needs the phase-retrieval problem to be properly solved.

Besides, in order to collect statistically relevant data, high-throughput imaging systems are demanded, able to analyze a huge number of samples in small periods of time, rapidly extracting information. This in turn results in two major needs, namely the enhancement of the performance of the imaging system, with the increase of the maximum number of samples that can be analyzed at the same time, and the improvement of the imaging robustness. With this term we indicate the capability of an imaging system to operate in non-ideal conditions, still providing reliable information.

In microfluidics, an annoying problem is the presence of scattering events that can severely degrade the imaging results and, in many cases, completely impair any imaging option. Scattering in a LoC device can be due to the presence of occluding objects forming a diffusive layer, e.g. in the case of biofilm formation, deposition of particles onto the inner channel surface, or due to the chip fabrication process resulting in roughness of the channel walls. More frequently, scattering can be due to turbidity of the liquid medium flowing inside the channels. A liquid is considered turbid when dispersed particles provoke strong light scattering, thus scrambling the object information and preventing image formation by any standard optical system. For example, the presence of a colloidal solution introduces diffusion of light, and prevents clear imaging. On the other hand, media that start off clear, often get turbid because of the chemical reactions that occur during the observed processes, thus limiting the variety of experiments that can be performed and clearly observed inside the chip. Achieving clear microscopy imaging through turbid media (in quantitative fashion) is a highly pursued goal to augment the variety of different uses of a LoC device, including experiments that, at the current technology stage, cannot be observed at all. In a wider sense, restoring clear imaging through complex media is a fascinating topic, with potential applications in many fields, from medicine (where imaging through tissues and turbid biological fluids is widely investigated) to Telecommunications, as well as Homeland Security, where natural or man-provoked impairments like smoke, dust, fog or flames have to be tackled.

These topics have recently attracted growing interest of many research groups working in heterogeneous disciplines, going from Biology and Medicine to Optics, Material and Biomedical Engineering, Physics, Signal processing and Information Engineering, and the emerging field of Bioinformatics. It has become more and more apparent that only a transdisciplinary approach can be successful to match the above mentioned requirements and make LoC diagnostics a widespread tool, worldwide used by the general public.

The proposed work is intended to provide new solutions to these problems, with the design and implementation of novel recording and image reconstruction methods. This Thesis is structured as follows:

CHAPTER 1 will be devoted to introduce the LoC paradigm, highlighting its most promising applications and the related issues to be coped with. In particular, in Section 1.1 and 1.2 we will provide an overview of the most remarkable advances in the fields of Microfluidics, LoC analysis of biological samples, and Optofluidics. Then, we will move our focus to the topic of LoC imaging, analyzing the most popular strategies to acquire information from samples inside a microfluidic environment. These will be discussed in detail and compared throughout Chapter 1, with particular reference to the phase retrieval problem and the other LoC requirements discussed above. Among the existing imaging techniques, we chose to rely on Digital Holography microscopy, as it provides label-free full field capabilities and it has shown potential to be fruitfully applied in microfluidics. However, Digital Holography microscopy needs to be properly modified in order to match the LoC demands for high-throughput, compactness and robust imaging. The approach followed throughout this Thesis work is to design, implement, and test novel recording strategies and image reconstruction algorithms specifically suitable to fulfill these requirements.

CHAPTER 2 will provide a detailed description of the holographic principle and Digital Holography microscopy.

CHAPTER 3 will afford the problem of restoring clear imaging through complex media, with reference to the specific problems arising when biological samples have to be studied in a LoC environment. Our analysis starts from the earliest works addressing this kind of problem in the framework of classical holography. Indeed, some efforts were made in the late 60s to achieve clear holographic imaging through convective fog, providing a theoretical formulation of the problem and first experimental proofs. In classical holography, the recording medium was a photographic plate and the sole amplitude image of the object was provided by optical reconstruction of the hologram. Thus, the phase of the object wavefront could not be registered and numerical processing of the hologram was not allowed neither. We address these issues in the framework of Digital Holography microscopy, taking advantage of the possibility to manipulate the hologram numerically, and paying particular attention to the problem of phase recovery from turbidity. In Section 3.1 we focus on imaging samples flowing inside scattering microfluidic channels, providing sample detection, velocity measures and phase-contrast mapping. Then we move to the more challenging situation in which scattering is due to a turbid medium, whose behavior cannot be characterized as this produces a time variable scrambling of the object information. Section 3.2 will afford the case of dynamic turbid media, with particular reference to colloidal solutions. Then, in Section 3.3 the case of quasi-static turbid media will be tackled. In particular, a novel recording and reconstruction strategy to achieve quantitative, label-free imaging through quasi-static turbid media will be presented. We will hereafter refer to this method as Multi-Look Digital Holography. In Section 3.4 this approach is applied to a colloidal solution of high interest in the field of biomedical imaging, namely blood made of Red Blood Cells (RBCs). We demonstrate that clear coherent imaging of biological samples through a turbid blood flow can be achieved thanks to a proper synthesis formula. We believe the results shown in this work can pave the way to endoscopic inspection of capillaries and blood vessels by Digital Holography microscopy, looking for cholesterol plaques settling down the vessel walls or red blood clots. On the other hand, from the imaging point of view, an interesting result is the demonstration that the presence of a turbid medium can also be fruitfully exploited to enhance the quality of a coherent imaging system. In particular, in Section 3.4.2 we show that biological samples like RBCs can act on the hologram as denoising elements helping to recover the image quality lost due to speckle noise inherently caused by the source coherence.

Chapter 4 will be devoted to afford the issues of enhancing the throughput of the imaging system and to promote the LoC compactness, with the integration of imaging functions onboard chip. In particular, a novel imaging technique, specifically conceived for optofluidic imaging and hereafter referred to as Space-Time Digital Holography, has been developed. This will be introduced in Sections 4.1 and 4.2, and its capability to dramatically augment the throughput of a coherent imaging system will be demonstrated and discussed. Sections 4.3 and 4.4 show new possibilities for miniaturizing optical components useful for Digital Holography microscopy, making them part of a LoC device in order to promote the spread of compact and portable chips for point-of-care diagnostic purposes. Noteworthy, a common path off-axis Digital Holography microscopy system all embedded on chip has been designed, implemented and tested. This will be object of discussion in Section 4.4.

1

TOWARD LABORATORIES ON A CHIP

Microfluidics is a rapidly growing field involving methods and technologies to manipulate fluids in channels with typical dimensions ranging from tens to hundreds of microns. The possibility to work with small amounts of fluid (from nanoliters to picoliters) represents a great opportunity in chemical analysis, as small quantities of samples and reagents can be treated and the typical time for analysis reduces [1-2]. Microfluidics offers new capabilities in the control of concentration of molecules in space and time, thanks to high resolution in sample separation and sorting, as well as high sensitivity in detection. A liquid confined in small regions of space (e.g. in channels with micrometer size dimensions), possesses some unique features that would not be observable if the same liquid was present in a bigger volume, because the physical laws governing the behavior of fluids change when scaling down from macroscale to microscale [3-5]. For example, at micro-scale the viscous forces prevail over inertial forces, so that low Reynolds numbers characterize any microfluidic stream and only laminar flows are allowed to establish inside the microfluidic channel [4]. The absence of turbulence assures a more accurate control and engineering of fluid streams to accomplish specific tasks [5,6].

One of the cornerstones of the microfluidic science is the Lab-on-a-Chip (LoC) paradigm. This is the principle of emulating the functionalities of a modern analysis laboratory onboard a small pocket platform, namely the LoC. A LoC is a low-cost device consisting in microfluidic channels forming more or less complex circuits where fluids can be delivered and chemical/physical reactions can be induced and observed. Along with channels imposing a fixed path to the employed fluids, a number of LoC components have been developed, to permit accurate control of the fluid streams and the processes happening inside LoCs. A LoC is thus equipped with mixers, pumps, valves, and sorters allowing to bring the desired volume of fluid in the desired position, at the required time.

As it will be discussed in the following sections, microfluidics finds a wide field of application in cell biology, in particular in the observation of cell growth, death, and adhesion properties, cell mechanics, sorting etc[7-15]. Moreover, the LoC principle has an enormous applicative potential in point-of-care diagnostics and it could have a deep impact on the way people will think to global healthcare. Indeed, the possibility to have a low-cost portable device allowing rapid analysis of biological samples for first screening purposes, achieving high throughput with no need for big amounts of samples and in the lack of adequate facilities, perfectly matches the target of the recently developing field of telemedicine [16,17]. Thus, LoC microfluidics promises to find applications in healthcare delivery and monitoring in developing countries, where the detection of diseases could be helped in absence of trained personnel or suitable structures, as well as home diagnostics in developed countries. In parallel, LoC systems could find breeding ground in public health and environmental monitoring [18,19]. Biodefence is another potential field of application of microfluidics and LoC platforms, as portable systems to detect chemical or biological threats could constitute added-value tools to be employed on the field by first responders for homeland security purposes and for military operations. The high-throughput of LoC platforms is already fruitfully exploited in the field of drug discovery, development and delivery, because these systems help to avoid expensive processes, and large volumes of reagents are not required anymore [20]. Currently developed applications of microfluidics are in the field of protein crystallization [21], control and management of multiphase flows (with production of droplets and bubbles for the creation of emulsions and foams) [22-24], bioanalysis [20], single cell and single molecule manipulation [25-27].

The real strength of microfluidics stays in the development of microfabrication techniques to build compact and low-cost devices for the manipulation of fluids at micron and sub-micron scale, like e.g., fluidic sorters, pipes, pumps, mixers or valves [28]. From this standpoint, soft lithography can be considered as the mother of microfluidics and LoCs [28,29]. At its early stage, photolithography was chosen as the preferred technique to fabricate complex microfluidic structures in glass or silicon. This is due to its successful application in the fabrication of microelectromechanical (MEMS) components and in silicon microelectronics. However, such materials were in a short while replaced by plastics. The fabrication of components for fluid manipulation is harder with rigid materials, like glass and silicon, than with elastomers. Moreover, silicon is opaque to visible light, so that a device fabricated in silicon could not be successfully adopted to analyze biological material, thus closing the door to an extremely wide field of application of microfluidics. For these reasons, today the preferred material to create microfluidic LoC devices is a polymer, namely the *Polydimethylsiloxane* (PDMS). This is a soft elastomer optically transparent to visible wavelengths. Its high biocompatibility is one of the main reasons for the rapid success of PDMS that is widely exploited for biomedical investigations and single-cell analysis onboard LoCs. However, other possibilities were explored with good results.

Examples are elastomers [30], photocurable solvent-resistant elastomers like e.g. *Perfluoropolyethers* (PFPE) [31], photocurable hydrogels [32]. In this framework, the soft-lithographic process represented a key enabling technique which promoted the spread of polymer based chips, because it allowed the low-cost fabrication of complex microfluidic assemblies with optimal reproducibility and short production time.

Integration of multiple functionalities onboard the same platform, along with portability, are key factors that justify the rapid spread of LoC devices in many research areas over the last decade, from biomedical studies to biochemical analysis [33-35], although the LoC technology is still at its embryonic stage and the promise of field portability has not been satisfied yet. The reasons for this unexpected delay are addressable to a number of factors. First, a microfluidic platform still requires additional instrumentation and methods to introduce samples and/or reagents inside the channels, and to provide flow control. Furthermore, instruments for detection (e.g. optical microscopes) are required, which can be bulky and anything but microscopic. On the other hand, sample preparation still requires procedures aimed at converting the specimen at its raw state to a form compatible with the analysis to be carried out (e.g. a blood drop needs to be first treated to separate its components from plasma in order to perform any analysis of the white or red blood cells) [1]. All these steps are still performed out of the chip, and severely hinder the application of LoCs outside laboratories for point of care diagnostics. Hence, necessary efforts are required to promote the integration of these functionalities onboard LoC platforms, as well as detection methods to afford the analysis in different unideal conditions, e.g. when samples are immersed in turbid media, the chip or the specimen cannot be pre-treated, or light scattering events occur inside the channel. The promised deep impact of LoCs in the future society needs these challenges to be won, so that the microfluidic technology can become usable by non experts in the form of widespread killer applications. These issues are currently object of study from many research groups and first-cut solutions start to be successfully proposed. Some advances in this direction will be discussed in the following sections of this work.

THE OPTOFLUIDIC CONCEPT

The impressive growth of microfluidics over the last decade is mainly due to the capability to fabricate chips equipped with devices for the accurate control and manipulation of fluids. On the other hand, microphotonics introduces the paradigm of light confinement, i.e. it squeezes the light down, to limit its propagation to small regions of space. Optofluidics is a science arising from the merge of Optics and Microfluidics with the aim to produce new tunable and reconfigurable optical elements, and to combine them to provide novel systems and functionalities. The basic principle is to exploit some unique properties of fluids to control light propagation at microscale. Each optical system exploits the laws governing the propagation of light through the interfaces between two media of different refractive index, that describe phenomena of reflection, diffusion, absorption and refraction, to manipulate the wavefront behavior in order to accomplish a specific task. The power of optofluidics is simply the possibility to vary the optical features of these interfaces in order to force changes in the optical properties of the whole system and, in turn, to obtain light with the desired properties in the desired space-time position. In the simplest cases, this can be accomplished by replacing a fluid with another having different refractive index, or introducing dyes to induce absorption phenomena inside the optofluidic system. The features of fluids offer a wide set of possibilities to act on the way light propagates. Thus, it is possible to exploit the smooth interface between immiscible fluids, avoiding unwanted diffusion problems, as well as fluid mixing that create gradients of optical properties in well localized regions of space. Thanks to the advanced control of fluids it is possible to design adaptive, tunable and reconfigurable optical systems [36]. This is with no doubt the main contribution supplied by microfluidics to face the optical challenges. Besides, the current trend in optofluidics is to make efforts toward the integration of optical components onboard LoC platforms, offering a completely new chance to solve the problem to build standalone chips with fully embedded functionalities to be employed by the general public on the field. So far, embedded optofluidic light sources, tunable lenses, sensing elements, filters, optical switches, and waveguides, were demonstrated [36-40].

According to the classification given by *Psaltis et al.* [36], three kinds of optofluidic apparatus can be recognized, respectively exploiting changeable interfaces between solids and liquids, liquid-liquid boundaries, or even the insertion of colloidal particles inside a fluid medium. As regards the first class, the guiding principle is the fabrication of solid structures with voids in some specific positions that can be filled with liquids to accomplish a specific task. Adaptive lenses were created based on this principle [41]. Optical switches can be also realized exploiting Total Internal Reflection (TIR) phenomena induced inside the channel [38]. When a light beam impinges on a boundary surface between two media of different refractive indices with an incidence angle satisfying the TIR condition, this is totally reflected in the first medium (namely the medium with higher refractive index), while only evanescent waves are allowed to establish in the second medium. The TIR phenomenon is the basis of the information transmission through optical fibers, achievable with very low energy losses. The TIR condition is satisfied when light coming from the higher refractive index medium propagates toward the discontinuity and approaches it with incidence angle larger than the critical angle. From the Snell's law, an expression for the critical angle can be derived, that links this to the ratio between the refractive indices of the two media. Hence, the capability to control one of them, filling the voids with fluids of the desired refractive index, gives the possibility to enable or deny the light propagation through the optofluidic system, i.e. to obtain an on/off switch. Acting on evanescent modes in the region with lower refractive index (namely, the cladding) has the effect of manipulating light propagation in the other medium (i.e., the core), e.g. the phase-delay of modes travelling a dielectric waveguide. Similarly, introducing liquids with absorbing dies can produce a desired effect of attenuation. Exploiting these principles, tunable optical filters based on a optofluidic micro-ring resonators were demonstrated [42,43]. Thanks to coupling effects between a waveguide and a micro-ring resonator, light that propagates through the waveguide at resonance wavelength experiences a remarkable attenuation. A change of the liquid inside the waveguide claddings results in varying the resonance condition, so that the attenuated wavelength can be accurately tuned.

In the previous section it has been underlined the major role played by soft-photolitography processes in promoting the development of microfluidic technology, as this introduced the possibility to write patterns with thinner and thinner resolution. When the size of these patterns approaches the visible wavelengths, more interaction possibilities arise, in turn resulting in higher fluidic control. The most famous proof of this paradigm, is the optofluidic tunable laser introduced in [44]. A periodic structure (precisely, a Bragg diffraction grating) is designed on the walls of a waveguide filled with a fluid of refractive index n. If light is pumped to this structure, a discrete set of wavelengths is allowed to propagate throughout the laser micro-cavity, depending on n and the grating period. Experimental proofs demonstrated the possibility to select the laser emission tones by choosing the proper liquid, or dynamically modifying the grating period acting on the soft elastomer material by fluidic pressure.

As well as the creation of solid micro-structures to confine liquids leads to the production of new embedded optical systems, it is similarly possible to take advantage from liquid-liquid discontinuities to provide a wide set of functionalities. In this sense, the L2 waveguides introduced by Whitesidess group are a groundbreaking novelty [37]. Two immiscible fluids are inserted inside a microchannel to constitute the core and the cladding of a totally liquid waveguide. High flexibility is achievable because the propagating modes depend on the liquids choice. Moreover, changing the shape of the boundaries (this is possible varying the relative flow rate between the core and the cladding streams), light steering was demonstrated [37]. Following such principle, an array of L2 waveguides filled with differently dyed liquids serves as embedded broadband light source [45]. Whenever miscible fluids are considered, well localized refractive index gradients can be obtained. Hence, light diffusion phenomena are exploitable to create optofluidic beam splitters with tunable split ratio. Manipulation of small colloidal particles by optical trapping is also used in the optofluidic framework for beam shaping purposes in order to create all optical switches or storage devices. More recent works have been proposed where colloids are thought as spherical lenses [46, 47]. Another deeply investigated field of optofluidics is aimed to exploit couplings between light and liquids to provide biochemical sensing capabilities. Optofluidic sensors can directly measure refractive index variations up to $\Delta n \div 10^{-8}$ by direct coupling, i.e. the probed fluid and propagating waves share the same region of space. In alternative, indirect coupling is established between evanescent waves and the cladding fluid. Noteworthy, a trade-off exists between the efficiency of coupling, that depends on the overall optical path experienced by light inside the fluid medium, and determines the resulting detection sensitivity, and the degree of compactness of the optofluidic sensor. High detection sensitivity requires long optical paths, which are difficult to obtain in a microfluidic environment. A solution to this issue is the introduction of resonance phenomena, able to greatly extend the light path beyond the effective size of the microfluidic channel (photonics microresonators serve at this scope) [48]. Thus, optofluidic devices can be used to excite and collect particle fluorescence in small liquid volumes, to perform surface-plasmon resonance measurements [37,49], to detect the chemical composition of probed solutions, or to create refractometers when Fibre Bragg gratings are coupled to microfluidic channels [42]. Similarly, changes in liquid absorbance can be exploited for microscope imaging purposes. A good example is the recently introduced Dye Exclusion Microscopy (DEM) technique [50]. More in general, the movement of samples dipped inside a fluid medium, where laminar flow is established, is exploitable to implement various kinds of scanning microscopy strategies with improved performance and high throughput [51].

LOC ANALYSIS OF BIOLOGICAL SAMPLES

A live cell is a fascinating biological unit that can be thought as both passive and active element of any live organism. Indeed, live cells in their natural environment undergo various kinds of external stimuli, and react to them in distinctive manners. Such stimuli can derive from mechanical interactions with other neighboring cells (cell-cell communication) as well as the extracellular matrix (ECM), biochemical signals through soluble molecules produced from other neighboring or distant cells, soluble factors due to drug administration, or electrical cues. In other words, a cell is a sensitive element basing its activities on external signals perceived by proper receptors. The ways a cell reacts to cues play a major role in characterizing its phenotype. The behaviors of a cell, e.g. the growth rate, duplication, migration, adhesion to substrates, mechanical interactions with the ECM and other cells, reaction to drugs, and death, are strictly dependent on the 3D shape and composition of its surrounding environment. It was observed that cells belonging to the same homogeneous population express diverse behaviors if these are exposed to different environmental conditions in terms of chemical stimuli, stresses by mechanical forces, electrical signals, or the simple confinement in geometrically different portions of space. Hence, the study of biological samples requires, in order to be reliable, the accurate emulation of their environmental conditions. Till the last decade, pretreated plastic planar surfaces were used to plate cell cultures, to induce their proliferation and creation of an ECM (e.g. a Petri dish was used for the scope). However, such a 2D reproduction is not sufficient to recreate the cellular environment and mimic all the external cues and forces affecting the cell behavior. In fact, cells grow in a volume so that stimuli and corresponding interactions are expected to come from a 3D stack rather than a 2D culture matrix. Moreover, the cell culture medium is often present in too high quantities and concentrations, as it is difficult to deliver the precise amount of the required soluble factor. It was clear that the study of biological matter needed for systems able to precisely emulate and control the cellular environment, offering completely new solutions to keep stable and highly reproducible experimental conditions, to allow the manipulation of very small amounts of fluid, and to induce the required cues well localized in time and space, working with small sample volumes. These reasons justify the recent adoption of LoC devices as the preferred platforms for research activities involving biological specimens, biocompatible materials, drug delivery and toxicity studies. Inside a LoC platform it is possible to:

- Study cell ensembles emulating with extreme accuracy their 3D shell in terms of geometry and volumetric cell concentration. A 3D reproduction of the ECM can be provided too. In this sense the emulation possibilities mainly depend on the capacity to fabricate chips with the required geometrical features.

- Force stress conditions by confinement in small regions of space to induce wanted behaviors.

- Exploit the capability of microfluidic circuits to supply nutrients and other soluble factors in well-defined spatial and temporal patterns.

- Provide mechanical stresses through flow shear.

- Sort homogeneous samples from heterogeneous populations on the basis of specific physical/chemical features (e.g. electrical properties or pre-added fluorescent labels/markers), till permitting single-cell analysis.

For example, it was demonstrated that endothelial cell confinement in small regions of space induces cell death by apoptosis, while the same cell population keeps on growing if let free to spread [52]. Moreover, it is possible to engineer proper substrates to let cells adhere and to control how these proliferate, i.e. to force them to duplicate along the desired division axis. Such controlled developmental process is expected to find a wide set of applications in tissue morphogenesis [53]. Similarly, the proliferation and differentiation of stem cells was controlled by acting on the chemical and geometrical environmental conditions [54]. The cell-cell mechanical interactions as well as the forces exercised by cells on the ECM can be also measured onboard chip [55]. When higher degrees of accuracy are obtainable in chip engineering, more complex biological systems can be emulated for drug screening and other toxicological testing purposes. In this sense, drug testing on tissues seen as standalone entities can fail in revealing drug toxicity, which instead would be detectable if more interconnected tissues were studied together [56]. First successful attempts to address the problem were aimed to create separate chambers with cells typical of each tissue and to exploit the channel network of a LoC device to emulate the connections between the two cell cultures [57]. Cell stimulation is an important capability for biological studies onboard chip. In particular, mechanical flow shear and transport of soluble factors can be used to investigate cellular reactions to controlled environmental distresses acting on adherent cells [58].

In the case of suspended cells, specific paths can be designed in order to expose samples to the wanted solutions and pressures, i.e. to monitor the cell response to various cascades of treatments [59]. Finally, cell sorting based on distinctive features of some populations can be provided. An example is the use of dielectrophoresis to move and separate cells with specific electrical features (e.g. membrane conductance), which was successfully proved through the selective capture of cancer cells inside a blood smear [60].

OPTOFLUIDIC MICROSCOPY: LOC IMAGING OF BIOMATERIALS

All the mentioned capabilities of LoC platforms promote their use for accurate biomedical research studies in the developed world, and point-of-care diagnostics in low-resource settings, where adequate instruments, costly facilities, and clinical laboratories for accurate analysis are still missing. It is clear that the possibility to observe the samples inside LoCs is crucial for a deep understanding of the processes occurring onboard such platforms. Hence, great effort has been spent to efficiently apply well-known diagnostic techniques to the LoC investigation of biological specimens, to design new diagnostic tools, adding them to the existing chips for information recovery, and to find novel strategies to promote the integration of the imaging and diagnostic functionalities on chip. At the early development stage of LoC analysis of biological samples, the most used diagnostic tools were still based on bulky bench-top instruments [61]. In other words, a LoC containing the sample cells was placed in the analysis plane of conventional microscopes and their functionalities were exploited. Thus, cell studies in LoCs were performed using bright field and fluorescence microscopy [62], confocal microscopy [63], phase-contrast microscopy [64] and Differential Interference Contrast microscopy (DIC) [65]. The advantage of such approach stays in the high-quality imaging achievable by consolidated and optimized methods, in terms of image contrast, resolution and Signal-to-Noise Ratio (SNR). Moreover, such systems are commercially available in the form of black boxes with user-friendly interfaces easy to use. The obvious drawback is the lack of portability, and the high costs that impair to keep the promise of microfluidics to become a groundbreaking technology usable by everyone at the point-of-care.

Nevertheless, many methods have been developed that intrinsically exploit the features of microfluidics for information recovery purposes and make efforts to embed the imaging functionalities onboard chip to result in compact devices. Different classifications are possible based on different features these methods share. First of all, label-free techniques have to be distinguished from marker-based methods, e.g. the ones based on fluorescence. Then, diagnostic strategies can be divided in two classes depending on the output they yield, so that we distinguish between qualitative and quantitative techniques. Finally, a parameter particularly relevant in optofluidics is the compactness, as it results in portability. On this basis, we will distinguish between lens-based and lensless approaches.

What would be highly desirable is a label-free full-field imaging method providing good image quality in both qualitative and quantitative fashion, and fully integrated onboard chip to promote portability. Many of the methods so far proposed follow hybrid approaches trying to match all requirements simultaneously, trying to overcome the tradeoff these impose. The most remarkable diagnostic strategies to study cells on chip will be discussed in the following sections.

Flow cytofluorimetry

Flow cytofluorimetry is one of the earliest techniques specifically designed to study biological samples in a microfluidic channel. It exploits fluidic controls to align multiple cells in order and to carry out single-cell analysis. A flow cytofluorimeter, first developed in the late 70s is a high-throughput instrument able to analyze a great number of cells (hundreds of cells in a second) suspended in a flow, so that the results can be provided in the form of reliable statistics. The technique is quantitative and it is able to yield multiparametric measures of different cell populations at a time. Cells parameters can be monitored, which are both related to their shape and physical dimensions (e.g. the cell volume, internal composition, granularity) and to their fluorescence properties. On these bases it is possible to distinguish different cell types in a heterogeneous fluid sample, and accurate cell sorting capabilities are offered too. In its simplest version, a flow cytofluorimeter consists of four main constituents, namely a fluidic system, excitation sources, optical/electronic components and a computer to collect data and put them together in the form of statistics and scatterplots. At the beginning, the cellular population under test is driven by pressure toward a flow chamber where these are aligned to analyze one cell at a time. The cell under test flows toward the detection area of the channel. There, a light beam impinges on it and a number of signals resulting from the light/cell interaction are captured making use of both optical and electronic components. The light beam can be emitted by a laser source or an arc lamp, which is cheaper but allows less sensitive fluorescence measures. The set of electronic components are mainly wavelength filters, lenses, and photomultipliers. Their function is to separate, amplify and collect three kinds of signals corresponding to specific information about the sample, to be grouped and compared as statistics and 2D plots. The first information comes from the Forward Scatter signal (FSC) which is due to the passage of the monochromatic light through the sample and is received by a photodiode at the same wavelength emitted by the laser. Its intensity is proportional to the cell size and gives a quantitative insight about its volume. Besides, a Side Scatter signal (SSC) is captured and amplified by a photomultiplier displaced at an angle of 90 degrees with respect to the FSC. This gives information about the cell morphological parameters, like e.g. cell surface roughness, presence of organelles, granularity of the cytoplasm, its density and the nucleus-cytoplasm ratio. For each cell, the couple (FSC, SSC) is represented as a point in the *cytogram*, a 2D plot whose analysis allows to discriminate between different cell populations on the sole basis of their physical features [66]. Beside the scattering measures, one or more fluorescence signals can be collected using proper bandpass optical filters. These need to be chosen according to the excitation wavelength, the adopted fluorophores/markers, and the features to measure. Multiple measures are collected to form statistics, and the results are presented in the form of histograms showing the number of cells that have presented a given fluorescence intensity (which is proportional to the binding sites) and the number of cells having expressed the emission of a specific fluorophore. In particular, this is particularly suited to study the cell life cycle. If a fluorophore is chosen that binds to the DNA, cells in different phases of their own life cycle will express different fluorescence intensities, so that these can be discriminated and counted by inspection of the histogram. Similarly, Annexin V-FITC and Propidium Iodide (PI) are employed to discriminate between live and death cells, and to study the type of cell death (i.e. Apoptosis or Necrosis) [67]. As previously discussed, flow cytofluorimetry is a widely used technique. It has many advantages related to its multiparametric feature, the high-throughput allowing reliable statistical analysis of a huge number of suspended cells, and reproducibility. It fully exploits the fluidic control to align the cells and can be arranged to sort them automatically on the basis of a given parameter. However, flow cytofluorimetry envisages the presence of a number of optics and bulky related electronic components. Above all, only ensemble information is obtained from each cell under test; in other words, a flow cytofluorimeter does not provide imaging capabilities, and it should not be confused with the quantitative microscopy techniques that will be discussed in the following sections.

Scanning based approaches: the optofluidic microscope

Scanning based techniques present many advantageous features, as these allow to inspect small portions of the sample at a time in order to achieve added-value capabilities, such as finer resolution, or even 3D imaging. The groundbreaking novelty in this direction is represented by confocal microscopy [63], introduced in 1961 by Minsky and now commercially available in the form of user-friendly microscopes. A confocal microscope use a couple of pinholes to achieve two specific functionalities. Light emitted by a laser reaches a first pinhole filter, which is mechanically actuated to scan small sample portions in order to achieve fine resolution in the plane orthogonal to the optical axis. Besides, a second pinhole serves as emission filter to allow only the passage of light from one sample plane (i.e. the plane imaged in focus through the optical system), thus avoiding disturbing contributions from all the other planes. Thus, by mechanical scanning it is possible to capture information from all the planes to form a 3D representation of the specimen, to reject background illumination light and to greatly improve the SNR. The intrinsic drawback of such method stands in the complex mechanical actuation this requires, that severely limits the possibility to miniaturize the system. In order to create a 3D surface distribution of the specimen, a long scanning of all the planes along the optical axis is required, thus protracting the acquisition time and limiting the throughput. Moreover, the sample must be kept steady during the scanning recording process, closing the door to a number of applications in the study of cellular dynamics. Similar disadvantages are shared by Near-field Scanning Optical Microscopy (NSOM) [68], where a probe tip creating a well-localized evanescent field is placed in close proximity to the sample surface and interacts with small portions of the sample to yield imaging with resolution lower than $100nm$ at the cost of recording time, throughput, and Field-of-View (FoV). Despite the useful advantages they introduced in the study of biological samples, confocal microscopy and NSOM did not exploit the microfluidic environment for imaging purposes.

In this sense, the Optofluidic Microscope (OFM) represented a cutting-edge novelty in optofluidic imaging. This technique was conceived to fully exploit the fluidic control in a microfluidic environment. Following the sample scanning principle, the capture of the transmitted signal from a small portion of the sample gives well-localized information and, in turn, fine resolution imaging. However, a complex and bulky imaging system would be required to provide scanning by mechanical actuation. The simple but effective idea of OFM is to illuminate with a collimated beam a fixed portion of a microfluidic channel and to use the sample motion to capture the light intensity transmitted from a set of apertures produced in a metal surface. The time-varying transmitted signal from each aperture is captured by a relay element and addressed to a distinct pixel of a CCD camera. Since the velocity of the specimen inside the channel is known, as well as the frame rate of acquisition, data captured from each pixel can be properly matched to synthesize an image of the sample. A linear set of apertures displaced orthogonally to the flow direction provides imaging with resolution bounded by the pixel size of the employed sensor. This point is the key feature that differentiates the OFM from other object scanning techniques.

Indeed, in its first implementation a set of skewed holes with $600\mathrm{nm}$ diameter is realized in the metal substrate, whose distance, i.e. the spacing along the oblique direction, is equal to the sensor pixel size, while the spacing between the holes along the direction orthogonal to the flow is equal to the half of the hole diameter, in order to avoid undersampling. A schematic of the system is reported in ref. [51]. In this way the ultimate resolution of the microscope is not limited by the pixel size, but rather by the hole diameter, i.e. this only depends on fabrication issues. In particular, the aperture size determines the resolution along the direction normal to the flow, while the resolution along the flow direction is bounded by the largest value between the aperture size and the result of the acquisition time (i.e. the sampling period) times the sample velocity. Hence, in a forthcoming future, nanometric resolution at least in one direction is expected for the OFM images. The OFM is a good example of exploiting the microfluidic environment for imaging purposes, as well as the features of microfluidic flow, i.e. the typically laminar flow that helps to avoid sample rotations or other unexpected motions during the overall recording time. If high frame rate sensors are associated to accurate control of the sample speed, the OFM can be thought as a high-throughput imaging system. However, as any scanning-based method, OFM is not a suitable way to investigate cell adhesion or other processes often involving non-suspended specimens (e.g., cell division, migration or cell death), but only flowing samples can be analyzed. Moreover, when objects with a few micron size are studied by OFM, significant Brownian fluctuations of the samples impair the synthesis of undistorted OFM images. Further advances have shown the application of pixel super resolution algorithms to the OFM principle (SROFM) [69]. Using a sensor with high frame rate of acquisition, a set of pixel-limited images were obtained with the same synthesis procedure of the OFM, shifted each other by a fraction of the pixel size. The pixel super-resolution algorithm was applied to the sequence to achieve imaging with $600\ \mathrm{nm}$ resolution as in conventional OFM, but without the need for the metal substrate with skewed apertures. This approach turns out to be very effective in reducing the acquisition time. Above all, the time window inside which the sample must keep stable remarkably reduces (this corresponds to one pixel size instead of the overall length of the array of skewed holes), so that it is possible to image samples that flow at non-constant velocity or slightly rotate [69].

NON INTERFEROMETRIC PHASE RETRIEVAL

The phase of a wavefield is a fundamental component carrying added-value information of objects interacting with the light beam. In particular, in setups with transmission geometries, from the phase delay of a wavefield passing through the sample it is possible to extract measures of thickness and refractive index distributions, as well as morphological information. The most of the methods for phase retrieval rely on well-assessed interferometer based acquisition schemes, which assure high degree of flexibility, reliability, and accuracy in phase recovery without binding constraints on the object shape. This is obtained recording a single fringe pattern coding the useful signal, and adopting numerical methods that deterministically extract the phase-contrast measure. Since an interference pattern has to be acquired, coherent laser sources are required and the interference between two light beams needs to be created, at the cost of setup complexity. In absence of fringes, alternative approaches have been developed to retrieve the phase-contrast map from a set of intensity measures. In some cases, a single intensity measure and an object related constraint are sufficient for the scope. Such strategies can be divided into two main categories, namely the iterative and deterministic methods.

Iterative approach

Iterative approaches to the phase retrieval problem basically rely on a four-step algorithm introduced for the first time by Gerchberg and Saxton in 1972 [70-72]. The phase retrieval problem from intensity measures can be resumed as follows. Let

$$O(x,y) = |O(x,y)| \exp(j\varphi(x,y)) \tag{1.1}$$

be the complex object field in the plane (x,y), and let

$$F_O(u,v) = |F_O(u,v)| \exp(j\psi(u,v)) = \mathcal{F}\{O(x,y)\} \tag{1.2}$$

be its Fourier transform. In Eq. (1.1) and Eq. (1.2), $|O(x,y)|$ and $\varphi(x,y)$ are the object amplitude and phase distributions in the spatial domain, while we denoted with $|F_O(u,v)|$ and $\psi(u,v)$ the corresponding distributions in the frequency domain (u,v), and $\mathcal{F}\{\ldots\}$ is the Fourier transform operator. The phase retrieval problem from two intensity measures requires the determination of φ (or its counterpart in the Fourier domain) relying on the knowledge of both $|O|$ and $|F_O|$, representing problem constraints in the two conjugate domains. The Gerchberg-Saxton algorithm (GS) [71] is based on back and forth Fourier transformation of the object signal. At each step, the measured amplitude constraint is applied to the complex field, while the phase keeps memory of the iterative process, i.e. this is updated at each iteration, as schematically depicted in Fig.1(a). In particular, the algorithm consists of the following steps:

I. Starting from an object estimate, $\hat{O}$, this is Fourier transformed.

II. The modulus of the resulting complex field, $\left|\hat{F}_O\right|$, is replaced by the measured intensity in the Fourier domain, i.e. the first constraint is applied.

III. The synthesized constrained complex field, $\hat{F}'_O$, is back transformed to generate a new complex field in the spatial domain, $\hat{O}'$.

IV. The modulus is replaced by the measured intensity in the spatial domain, i.e. the second constraint is applied.

Thus, at the k-th iteration the algorithm proceeds as follows:

$$\begin{aligned} &\hat{F}_{O,k}\left(u,v\right) = \left|\hat{F}_{O,k}\left(u,v\right)\right| \exp\left(j\hat{\psi}_k\left(u,v\right)\right) = \mathcal{F}\left\{\hat{O}_k\left(x,y\right)\right\} \hat{F}'_{O,k}\left(u,v\right) = \\ &= \left|F_O\left(u,v\right)\right| \exp\left(j\hat{\psi}_k\left(u,v\right)\right) \hat{O}'_k\left(x,y\right) = \left|\hat{O}'_k\left(x,y\right)\right| \exp\left(j\hat{\varphi}'_k\left(x,y\right)\right) = \\ &= \mathcal{F}^{-1}\left\{\hat{F}'_{O,k}\left(u,v\right)\right\} \hat{O}_k\left(x,y\right) = \left|O\left(x,y\right)\right| \exp\left(j\hat{\varphi}'_k\left(x,y\right)\right) = \\ &= \left|O\left(x,y\right)\right| \exp\left(j\hat{\varphi}_{k+1}\left(x,y\right)\right) \end{aligned} \tag{1.3}$$

At each step, the phase is updated and a squared error estimate is computed. It can be demonstrated that error reduces at each iteration, so that the algorithm stops when this is approximately zero or overcomes a proper threshold value. The GS algorithm is today widely used, as it can be generalized to solve any problem in which prior information or measured data are known in one of the two domains, or in both. The generalized version of GS is normally referred to as the Error Reduction algorithm (ER). For example, in the case of one single intensity measure, the ER required the first three steps of the GS but, in absence of the constraint in the spatial domain, an additional one have to be imposed, requiring that the object is real and non negative [70]. The convergence of the ER is demonstrated in any case. Nevertheless, it turns out to be reasonably fast to solve problems of phase retrieval from two intensity measures, but too slow when just one intensity measure is available. For this reason, several algorithms have been developed to speed up the convergence of the ER based methods. Good examples are the gradient search approaches, that make use of the Fourier transform method as a way to compute efficiently the gradient of the error [70].

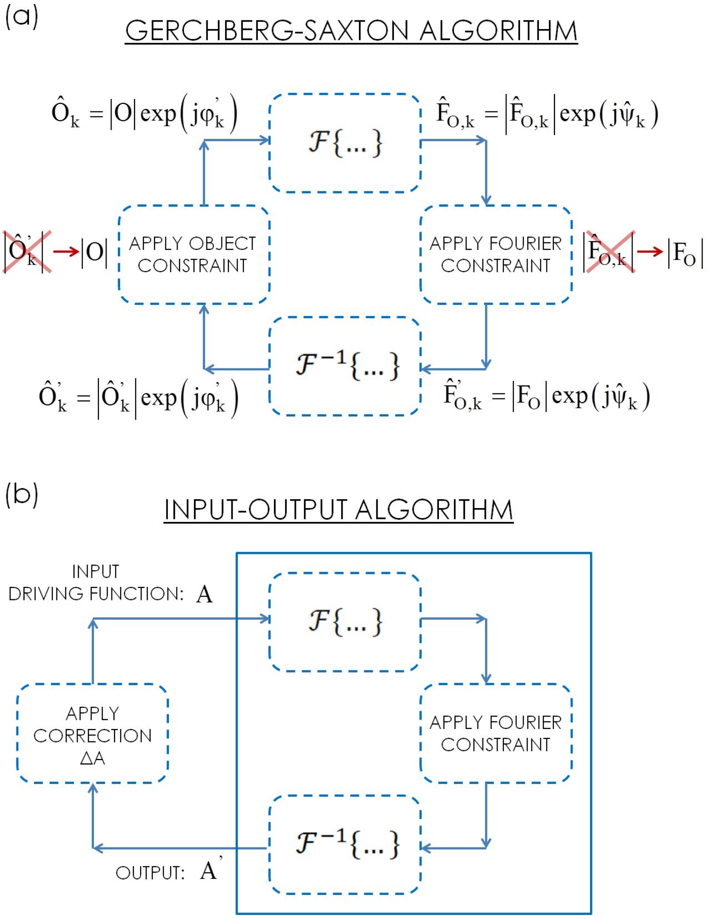

FIGURE 1.1: Iterative solutions to the phase retrieval problem. (a) Gerchberg-Saxton (GS) algorithm. (b) Input-Output (IO) algorithm.

However, the best solutions proposed so far to the problem of slow convergence of the ER are based on a different class of methods, named Input-Output (IO) algorithms. The first three steps of IO are identical to the GS but, differently from the GS, the IO is not designed as a closed loop where the output of each iteration is the input of the next one. On the contrary, a different input is chosen at each iteration, as schematically depicted in Fig. 1(b). In particular, an input function is selected in the spatial domain and this is Fourier transformed. The modulus constraint in the Fourier domain is then applied and the resulting complex function is inverse transformed to obtain an output function. These three steps can be seen as a non linear system accepting an input function A, and returning an output function A' whose Fourier transform satisfies the Fourier constraint. Hence, if A' also satisfies the object domain constraint, this turns out to be the solution. In other words, in the IO approach it is not required that the input satisfies the spatial domain constraint, but A is seen as the driving function of the next output A'. At each iteration a change in the input ΔA is applied depending on the desired change of the output, $\Delta A'$ in order to direct this to the desired point closer to the convergence. Since the relation between the input variation and the corresponding output variation is well determined for small ΔA, resulting in a proportionality law $\Delta A' = m\Delta A$, the solution to this problem can be found. For example, in the case of phase recovery from one intensity measure, where the GS is impracticable because of the too slow convergence, and the additional constraint about the object support can be applied, the basic IO algorithm after the k-th iteration results:

$$\begin{aligned} A_{k+1}(x,y) &= A_k(x,y) + m^{-1}\Delta A_k(x,y) = \\ &= \begin{cases} A_k(x,y), & (x,y) \notin D \\ A_k(x,y) - m^{-1}A'_k(x,y), & (x,y) \in D \end{cases} \end{aligned} \tag{1.4}$$

where D is the ensemble of points where the additional constraint is violated. The IO converges faster than the GS for the problem of one intensity measure. Moreover, different algorithms and convergence profiles are obtainable selecting different rules for the changes of the input function. In this sense, the best solution is demonstrated to be the Hybrid Input-Output algorithm (HIO) [70].

Noteworthy, despite the theoretical demonstration and experimental validation of the convergence of all the described strategies, any iterative approach can fail in converging to the global error minimum, or stagnation problems can occur, depending on the object shape, the SNR, the initial guess and the type of additional constraints. Moreover, the rapidity of convergence can also depend on the above factors. A different class of methods get rid of the convergence issue, relying on a deterministic approach for phase retrieval from a set of intensity measures, as described in the following section.

Deterministic phase retrieval

A non iterative approach to address the phase retrieval problem is based on acquiring a set of intensity measures of the object wavefront in different planes orthogonal to the optical axis, z, and solving a partial derivative differential equation, commonly known as the Transport of Intensity Equation (TIE). Under paraxial approximation, let $I(x, y, z) = |O(x, y, z)|^2$ be a set of intensity measures of the object in discrete positions along the z axis, and let Σ be an open and bounded domain, so that $(x, y) \in \Sigma \subseteq \mathbb{R}^2$. The derivative of the intensity signal with respect to z obeys the TIE [73-76]:

$$-k\frac{\partial I(\mathbf{r})}{\partial z} = \nabla \cdot [I(\mathbf{r})\,\Delta\varphi(\mathbf{r})] = \nabla I(\mathbf{r}) \cdot \Delta\varphi(\mathbf{r}) + I\nabla^2\varphi(\mathbf{r}), \tag{1.5}$$

where r is the position vector in the plane (x, y), ∇ is the gradient operator and k is the wavenumber. The TIE links the longitudinal derivative of the intensity distribution to the wavefront slope and its curvature. This is an elliptical partial derivative differential equation, whose solution is demonstrated to exist and to be unique under proper Boundary Conditions (BCs) [76,77]. In order to solve the TIE to obtain the phase signal, two classes of conditions can be applied, namely the Dirichlet and the Neumann BCs. If Dirichlet BCs are known from measures or prior information, the solution for the phase requires that this satisfy a condition on the domain boundary $\partial\Sigma$, i.e.

$$\varphi(\mathbf{r})|_{\partial\Sigma} = b(\mathbf{r}), \tag{1.6}$$

where $b(r)$ is a known smooth function defined on $\partial\Sigma$. In this case, it is demonstrated that the solution to the TIE always exists and this is unique [76,77]. Conversely, if Neumann BCs have to be applied to determine the phase function, it is required that

$$I(\mathbf{r})\left.\frac{\partial\varphi(\mathbf{r})}{\partial n}\right|_{\partial\Sigma} = b(\mathbf{r}), \tag{1.7}$$

where n is the direction normal to the domain boundary. However, specifying Neumann BCs does not always guarantee the existence of a solution. Noteworthy, it can be shown that, if a solution exists this is unique up to an arbitrary additive constant [77]. In order to allow the existence of a solution to the TIE under Neumann BCs, the longitudinal derivative of the intensity distribution have to satisfy the following compatibility condition, which is obtained integrating the TIE over the domain Σ, and then applying the divergence theorem:

$$\oint_{\partial\Sigma} I(\mathbf{r}) \frac{\partial \varphi(\mathbf{r})}{\partial n} ds = \iint_{\Sigma} -k \frac{\partial I(\mathbf{r})}{\partial z} d\mathbf{r}, \tag{1.8}$$

where s is the curvilinear abscissa. In practice, the second hand term in Eq. (1.8) is known from the intensity measures, while the first hand term depends on the Neumann BCs, in the sense that all of them have to satisfy Eq. (1.7). This is a necessary condition to the existence of a solution of the TIE. Under proper smoothness assumptions on $I(r)$ and $b(r)$, this is sufficient too.

A good example of the application of the TIE strategy to the optofluidic imaging framework is the method proposed by *Gorthi et al.* [74]. A microfluidic system serves as a flow cytometer aligning cells and permitting to analyze one of them at a time. When the sample reaches the illuminated area of the channel where focused light impinges, an intensity image is captured by the imaging system. The novelty of this work is the alignment of the microfluidic channel, which is tilted with respect to the optical axis. Hence, multiple intensity images can be captured while the sample flows, corresponding to different sample focal positions. In this way, a focus-stack collecting microscope is realized, and the set of intensity images can be used to retrieve the phase of the sample by solving the TIE. Resuming, the TIE approach to the phase retrieval problem is suitable whenever interferometric measurements are not available, but a set of intensities can be acquired. This requires solving the TIE equation in the cases where a solution exists, depending on the BCs. While the iterative methods need efforts to tackle the convergence issue, TIE methods have to face the problem of knowing or measuring the BCs, which is not trivial in many cases, and great effort has been spent to propose new BCs, different from the classical ones resumed above. Moreover, TIE solvers turns out to be very slow when the size of the image increases, so that various approaches have been proposed to address the computational burden problematic. Among the proposed methods, the FFT based algorithms [78] are widely used for their efficiency and simplicity, but these turns out to be sensitive to boundary artifacts, and perform better when the object is isolated inside the FoV. Such condition cannot be satisfied in many practical cases (e.g. in the case of multiple objects overlapping inside the FoV, or an object whose dimensions are larger than the FoV) and the efficient and robust solution to the TIE is still an issue.

Direct thickness measure by Dye Exclusion Microscopy (DEM)

Dye exclusion microfluidic microscopy is a recently introduced technique that exploits some of the most advantageous features of optofluidics to yield label-free quantitative imaging of multiple flowing cells [50]. Fluorescence imaging is based on marking/labeling the samples with fluorescent dyes and to illuminate them to excite the emission of photons. This is exploited to achieve high contrast and thin resolution imaging. Despite the optimal image quality of fluorescence microscopes, such a method lacks of quantitative information throughput. Moreover, sample pre-treatment is needed to observe fluorescence, which results to be invasive and sub-optimal to investigate cell dynamics without interfering with the processes under study. Instead of marking cells, the novel idea of DEM is to color the liquid buffer with an absorbing dye. The samples are let flow inside a microfluidic channel and directed toward a specific region where a light beam impinges. An optical sensor (a color camera) captures the light transmitted intensity, and the absorption difference between the sample area and the buffer is obtained. Hence, the thickness distribution of the sample can be measured [50]. Differently from interferometric techniques, where it is the optical thickness to be measured, in dye exclusion microfluidic microscopy the physical thickness of the sample is decoupled from the refractive index measure. The role played by microfluidic control in DEM is apparent, because laminar flow is exploited to sort multiple cells, address them in the measuring site of the channel, and to avoid superpositions along the optical axis. A drawback of the method is the high degree of accuracy required for calibration. Indeed, measurement errors due to scattering losses need to be compensated. These are mainly due to scattering from the sample surface, caused by refractive index discontinuities, and from internal sample structure. To compensate for internal scattering, a two color illumination scheme is implemented. One color is partially absorbed from the dyed medium and the corresponding signal is the result of both internal scattering and absorption; a second wavelength is not absorbed but only reports scattering variations and the corresponding signal can be used for system calibration. To tackle the problem of the scattering due to the refractive index variation between the sample and the medium, the dyed buffer is chosen in order to have a refractive index that matches the average refractive index of the sample. This means that the method is intrinsically not optimized to measure an heterogeneous distribution of cells sharing the same buffer. Moreover, it is required that the buffer does not penetrate the cell membrane, which limits the set of applications in the study of cell mechanics, life cycle, interactions and death.

INTERFEROMETRIC PHASE RETRIEVAL

In the following, we will resume some of the most effective imaging techniques for retrieving quantitative information from phase samples. Differently from the methods discussed above, these are based on interference processes and deeply exploit the high sensitivity to variation of the phase difference between two interfering wavefronts, in order to provide accurate thickness distribution of the samples. Thanks to the fringes, the performance is not dependent on the shape of the object or its support, and the interferometric techniques are free from convergence or boundary conditions issues. In particular, a lens-based method will be first discussed. Then we will focus on lensless approaches to the phase retrieval problem.

Phase Shifting Interferometry (PSI)

A well assessed lens-based strategy to provide an estimate of the wavefront phase and, in turn, of the sample optical thickness, relies on acquiring and processing a pattern of interference between two coherent light beams. In order to accomplish this task, many recording geometries and extraction methods have been proposed in literature. Among them, the preferred techniques for quantitative phase-contrast microscopy are the Digital Holography (DH) and Phase Shifting Interferometry (PSI). The former will be described and discussed in detail in the following Chapters. Here we focus on PSI as an interferometer based approach for deterministic (i.e. non iterative) retrieval of the quantitative phase-contrast information. The basic idea of PSI is to capture a proper set of L interferograms, acquired adopting a set-up in transmission configuration, shifted each other of a desired phase step. The combination of such interferograms provides a closed formula that synthesizes the whole complex wavefront transmitted by the object and, hence, the phase information. Let

$$\begin{aligned} O(x,y) &= |O(x,y)| \exp\left[j\varphi(x,y)\right] \\ R(x,y) &= R\exp\left[j\varphi_R(x,y)\right] \end{aligned} \tag{1.9}$$

be the object beam and the reference beam in the acquisition plane. Before interfering on the recording device (e.g. a CCD camera), the object beam passes through the sample, carrying information about its optical thickness. Instead, the reference beam goes directly toward the sensor. The detector records the interference pattern between the object wave and the reference wave, i.e. the signal

$$\begin{aligned} S(x,y) &= |O(x,y) + R(x,y)|^2 = \\ &= |O(x,y)|^2 + R^2 + 2R|O(x,y)|\cos(\varphi(x,y) + \varphi_R(x,y)). \end{aligned} \tag{1.10}$$

In PSI both the amplitude and the phase of the object beam can be extracted tuning L times the phase of the reference beam $\varphi_R = \varphi_{R,0} + \Delta\varphi_R$ (the spatial coordinates will be hereafter omitted for the sake of simplicity), and combining the corresponding L intensity measures according to proper algorithms [79,80]. For instance, if $L = 4$ intensity measures are carried out selecting the phase shift values as $\Delta\varphi_R = \{0, \pi/2, \pi, 3\pi/2\}$, we obtain:

$$\begin{cases} S_0 = |O|^2 + R^2 + 2R|O|\cos(\varphi) \\ S_{\pi/2} = |O|^2 + R^2 - 2R|O|\sin(\varphi) \\ S_\pi = |O|^2 + R^2 - 2R|O|\cos(\varphi) \\ S_{3\pi/2} = |O|^2 + R^2 + 2R|O|\sin(\varphi) \end{cases}, \tag{1.11}$$

where we put $\varphi_{R,0} = 0$ for the sake of simplicity. From Eq. (1.11) the complex object beam can be extracted:

$$O = \frac{1}{4R}\left[(S_0 - S_\pi) + j\left(S_{3\pi/2} - S_{\pi/2}\right)\right]. \tag{1.12}$$

Similarly, if three measures are carried out the complex object beam can be found as:

$$O = \frac{1+j}{4}\left[\left(S_0 - S_{\pi/2}\right) + j\left(S_\pi - S_{\pi/2}\right)\right], \tag{1.13}$$

from which the amplitude and the phase of the object wave are obtainable. In general, if L measures are carried out with uniformly spaced phase shifts $\Delta\varphi_{R,l} = \frac{2\pi l}{L}, l = 1, \ldots, L$, the phase of the object can be directly retrieved by means of an algorithm implementing the following formula (synchronous detection):

$$\varphi = -\tan^{-1}\left[\frac{\sum_{l=1}^{L} S_l \sin(\Delta\varphi_{R,l})}{\sum_{l=1}^{L} S_l \cos(\Delta\varphi_{R,l})}\right]. \tag{1.14}$$

In PS interferometry the phase variation is usually obtained introducing a delay line in the path of the reference beam, e.g. using piezoelectric actuators to move mirrors [81], rotating or tilting phase plates, using movable diffraction gratings, or acting on light wavelength or polarization [82,83], otherwise a shift of the object beam is exploited to provide phase shift. In order to retrieve the phase of the object with enough fidelity, phase shifts must be accurately provided, which can be a complex task in some cases. Moreover, in this configuration only static specimen can be investigated. Hence, the optical thickness of suspended cells cannot be recovered by PSI. Actually, this is a common drawback of all the phase retrieval methods requiring multiple observables for phase estimation. In Chapter 4 a different solution that intrinsically exploits the microfluidic environment will be proposed and discussed.

Quantitative lensless methods: DILH, HOM

The development of new imaging strategies to study biological samples in microfluidic channels is basically guided by four major needs. First, quantitative information is required for a deeper understanding of cell structure and behaviors. On the other hand, the demand for compactness needs to be satisfied in order to promote LoC portability for point-of-care diagnostic purposes. In order to obtain statistically relevant information, high-throughput imaging system needs to be developed that allow analyzing multiple specimens in reduced time. Besides, non-invasive techniques are preferred to avoid the decreases in throughput due to sample pre-treatment, and to prevent undesired alterations of the specimens. Quantitative lensless methods well match, totally or in part, these requirements. Here we focus on the two major advances in this field, namely Digital in Line Holography (DILH) and Holographic Optofluidic Microscopy (HOM). In line Holography was introduced for the first time by Gabor in 1948 [84], thought as a way to store and reconstruct the full complex information of a wavefront (the Greek term *holos* means whole). A detailed discussion on the holographic concept will be provided in Chapter 2. Here its basic working principle will be introduced to make clear the possibility to fruitfully adopt such technique in a LoC environment for biological investigation. At this scope, we will refer to setups in transmission configuration.

In Holography a coherent light beam is directed toward the sample under study. The transmitted wavefront is a complex signal carrying information on the absorbance of the sample and the phase delay this introduces on the light beam. A reference beam is then used to produce an interference pattern on the recording device (in classical holography a photographic plate was adopted as a sensor), namely the hologram. Once registered, the whole complex information of the transmitted wavefront can be reconstructed, illuminating again the hologram with the reference light. The need for a second illumination step (i.e. the reconstruction process) made classical holography a slow and low-throughput technique, unsuited for microscopy applications. Moreover, although image

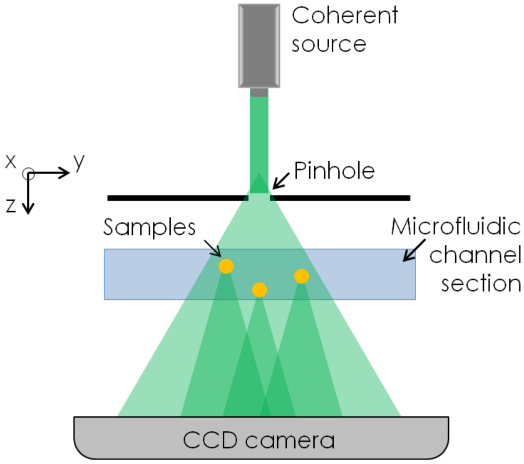

FIGURE 1.2: Sketch of the typical DILH setup for microfluidic imaging. Light scattered from the samples interferes with undisturbed light on the recording device.

formation was allowed, no quantitative phase-contrast information could be extracted. Later, with the development of electronic recording devices it became possible to store the interference pattern on a digital support that could be processed by a computer. Thus, Digital Holography was introduced, where the reconstruction process was carried out by numerical techniques, making it faster and appropriate for microscopy. Due to the simple setup, DILH has recently experienced a remarkable growth [85-87], since it is particularly suited for embedded LoC microscopy applications. A typical setup employed in DILH is sketched in Fig. 2. Light emitted by the source (typically this is a laser) first impinges on a pinhole. The field diffracted from the pinhole, namely the reference field $R(x, y, z)$, reaches the channel and encounters the specimen in the sample plane $z = z_0$. In this plane the transmitted field depends on the sample transmittance, $t(x, y)$ as follows:

$$T(x,y,z_0) = R(x,y,z_0)t(x,y) \approx R(x,y,z_0)(1 + \Delta t(x,y)) = R(x,y,z_0) + O(x,y,z_0), \tag{1.15}$$

where $O(x, y, z_0)$ is the scattered object field carrying the sample information, and Eq.(1.15) is obtained under the assumption of weakly scattering objects like, e.g. cells. In this configuration, scattered light interferes with undisturbed light coming from the pinhole aperture, and the resulting fringe pattern is recorded by a digital sensor (e.g. a CCD or a CMOS camera) located at the acquisition plane $z = z_1$. The recorded intensity signal in the plane (x', y') can be written as:

$$S\left(x', y', z_1\right) = \left|R\left(x', y', z_1\right) + O\left(x', y', z_1\right)\right|^2 = |R|^2 + |O|^2 + R^*O + RO^*, \tag{1.16}$$

where $*$ indicates the conjugate operator and the spatial dependencies have been omitted in the second half of Eq.(1.16) for the sake of clarity. The first two terms of Eq.(1.16) are generally not of interest, as these only convey intensity information, while the third and the fourth term correspond to the real and the twin image of the sample. Each of them carries the whole complex object information from which its optical thickness can be extracted. DILH reconstruction involves a proper numerical processing aimed at extracting the complex object signal O from the recorded intensity signal, S.

There are two ways to accomplish this task. The former is the numerical emulation of the holographic reconstruction process [88-89]. In other words, $S(x', y', z_1)$ has to be multiplied to the reference wave (to simulate the second illumination step typical of classical holography) and the resulting field has to be back-propagated at a distance $d = z_1 - z_0$. Sets of algorithms have been developed for the scope, that simulate the wavefront propagation along planes orthogonal to the optical axis. These will be discussed in Chapter 2. However, in DILH configurations the real and the twin image terms are spatially overlapped, so that it is not trivial to separate them [90-91]. In alternative, an iterative approach can be followed, similarly to what described in the previous section. Starting from the acquired signal $S(x', y', z_1)$, an error reduction algorithm based on one single intensity measure can be applied [70,71]. In this case, instead of alternatively switching from the Fourier domain to the spatial domain, the signal is propagated back and forth from the hologram plane, where the recorded intensity is applied as a constraint, to the sample plane, where an additional constraint on the object support is required. Obviously, this reconstruction process shares the previously discussed disadvantages of all the iterative approaches to the phase retrieval problem.

Thus, the spread of DILH as imaging technique for LoC devices resulted to be limited by both the cost and the size of coherent sources. Later, these drawbacks have been overcome by *Repetto et al.* [92] with the introduction of DILH using partially coherent laser sources, paving the way to a new set of applications of microfluidic imaging for point of care diagnostics in low resource settings. In particular, *Bishara et al.* started to develop compact devices based on microfluidics and DILH lensless imaging. The imaging strategy they introduced is commonly referred to as Holographic Optofluidic Microscopy (HOM) [93].

Differently from the previous attempts to solve the compactness issue, in HOM a Light Emitting Diode (LED) is adopted as light source. In particular, the setup is similar to DILH, involving a pinhole to increase the LED light coherence. The free-space propagation from the pinhole aperture to the sample plane allows light to increase spatial coherence (at this scope the beam needs to propagate for a distance typically ranging from $5\mathrm{cm}$ to $10\mathrm{cm}$), so that inline interference is obtainable in the sensor plane. However, in HOM the sensor has to be placed in close proximity to the microfluidic channel, e.g. a typical value for d is $\cong 1\mathrm{mm}$. Differently from DILH, a larger aperture is used, in order to increase the maximum obtainable FoV. HOM exploits microfluidic control to bring the sample in the proper position of the channel and one hologram is recorded by the sensor, that can be reconstructed by iterative algorithms, as described above. Due to the lensless setup and the recording geometry, HOM would provide a low resolution reconstruction. In particular, the resolution is limited by the sensor pixel size. However, the possibility to move the sample is advantageously exploited to acquire a set of low resolution holograms, shifted each other of a non integer multiple of the pixel size, that can be realigned to yield a set of sub-pixel shifted, low resolution holograms. These are combined by means of iterative pixel super-resolution algorithms [94-97] to synthesize a higher resolution hologram that can be reconstructed for phase-retrieval purposes. It is worth to notice that sub-pixel shifting and related algorithms do not enable to break the diffraction limit, but these are ways to circumvent the intrinsic undersampling of the hologram signal due to the pixel size. In order to break the diffraction limit and to yield real super-resolution capabilities, multiple holograms coding different spatial frequencies of the samples need to be acquired and properly combined in the Fourier domain. In other words, a larger numerical aperture has to be synthesized to obtain super resolved holograms [98].

The HOM approach has gained much attention during the last years and a great variety of applications of its basic concept have been demonstrated. A good example is the field portable holographic microscope [16-19,93,94], a compact microfluidic device developed by the Ozcan research group at the University of California-Los Angeles, UCLA (US). Making use of a LED array of different colors coupled to optical fibers, the required sub-pixel shifts are provided between multiple low resolution holograms, and the super-resolution algorithm compensate the poor magnification due to the lensless setup. The chip containing the samples is placed on top of a CMOS array, and the FoV is determined by the whole active area of the sensor, so that a wide FoV ($\cong 24\mathrm{mm}^2$) is achievable. This permits to analyze a great number of samples at a time in order to collect big amounts of data and to extract statistically relevant information. Convincing demonstrations have been given applying the device to the on chip detection of waterborne parasites [18], analysis of whole blood samples to extract the percentage of White Blood Cells (WBCs) and RBCs, to measure the hemoglobin density in a blood smear, to provide histograms of RBCs volume [17], or to differentiate various types of WBCs like in classical cytometers. Besides, other variants of field portable HOM have led to imaging systems in reflection configurations for the analysis of tissues with diagnostic purposes (e.g. the application to Pap smear test was reported). Recently, on chip tomography of a Caenorhabditis elegans (C-elegans) sample was demonstrated [99-101]. Despite the advantages these methods offer, the lensless approach constitutes an inner limitation to the available resolution. Moreover, the iterative phase retrieval algorithms perform well only under specific assumptions about the object support [61]. In particular, the samples have to be spatially sparse [70] to allow reliable phase retrieval, and the convergence to a solution is not always guaranteed, so that such methods turns out to be not quantitative in a number of practical situations where cell alignment is not feasible.

Proposed approach

In this chapter, the most effective imaging techniques adopted to study biological samples onboard microfluidic platforms have been reviewed. These can be classified on the basis of some features they share, which determine their own strengths and weaknesses, as resumed in Table 1. Generally speaking, conventional microscopes offer high resolution capabilities (often relying on fluorescence measures and sample labeling), but these are very bulky systems and they does not exploit microfluidics to achieve high throughput. On the contrary, flow cytofluorimeters are specifically designed for microfluidics, allowing alignment capabilities and single cell analysis with very high throughput of information (hundreds of cells can be analyzed in a few seconds). However, this relies on fluorescence and cell markers, and it only provides an ensemble measure of some parameters of interest (i.e. this is not an imaging technique), being useful to yield only statistical information. At this stage, flow cytofluorimeters have not been developed as compact devices.

In addition to compactness and label independence, quantitative imaging capabilities are highly sought for cell analysis. The phase retrieval problem can be afforded by lens based approaches, that can be either interferometer based or not. In PSI, multiple phase shifted interferograms are used for extracting the phase deterministically, at the cost of setup complexity and compactness. In alternative, phase can be recovered by intensity measures and computational efforts. A number of algorithms have been developed for the scope, relying on iterative methods or solving the TIE equation under proper boundary conditions. In all the cases, some issues arise about the existence of a solution, or the convergence of the algorithms in reasonable time, depending on the type of object and the recording geometry. This severely limits the throughput and the reliability of the imaging system.

A different approach is the DEM, which applies a dye to the buffer instead of marking the samples, and aims to directly obtain the sample thickness by measuring absorption differences. Since a fine calibration process is required, which is often sample dependent, the number of cases where DEM can be usefully adopted is limited and it did not undergo broad attention after its introduction. On the other hand, lensless imaging techniques try to match a number of requirements, giving high priority to compactness, in order to favorite the spread of portable devices for point of care diagnostics and imaging in low resource settings. The OFM, introduced in 2006, is a cutting-edge solution that fully exploits the sample motion in a microfluidic channel and allows lensless on chip imaging with reasonable resolution through a scanning paradigm. However, the method is not quantitative, and requires the samples to be stable during the overall scanning time. This unavoidably increases the complexity of the recording process and lowers the throughput. Other lensless approaches based on DILH place the channel containing the samples directly onto the sensor, and exploits iterative computational methods to get the phase. In particular, HOM replaced the laser source with low coherence, cheap, and compact LEDs. Multiple lensless, low-resolution observations of the samples, sub-pixel shifted each other, can be combined by means of a pixel super resolution algorithm to obtain a reconstruction with higher resolution. Although HOM does not overcome the diffraction limit, this algorithm allows to compensate the undersampling due to the sensor pixel dimension. However, the limited resolving capability remains the main drawback of HOM and the other lensless techniques. Moreover, although wide FoV is achievable, the quantitative information throughput is still limited by convergence problems shared by all the iterative approaches discussed above.

Therefore, the proposed approach to the study of biological material onboard LoC platforms cannot rely on iterative algorithms. The efforts of this work are addressed toward the development of algorithms and recording strategies to improve the imaging performance in microfluidic environments, trying to overcome the drawbacks of the existing techniques. At this scope, we chose to rely on Digital Holography (DH) microscopy. As it will be shown in the following

Chapters, this imaging modality is intrinsically suitable for label-free quantitative phase-contrast microscopy of suspended flowing cells, or samples adhering on channel substrates. In DH microscopy, the complex object wavefront can be recovered without the need for iterative approaches, getting rid of boundary condition issues, and with a single interferometric measure. This augments the versatility of DH microscopy because a unique solution to the phase retrieval problem always exists and it is straightforward to retrieve. Moreover, in DH the sample information can be acquired out-of-focus, and refocusing can be performed by numerical techniques. This possibility permits to capture data coming from a whole liquid volume in a single shot recording, followed by reconstructions at different focus planes. Indeed, the hologram contains the 3D information of objects displaced in different positions along the optical axis, i.e. the signal coming from the objects in focus and the diffraction from out-of-focus objects. If microfluidic control is exploited, these features allow high throughput imaging. At this stage, efforts are required to add compactness to DH microscopy systems. Besides, some problems have to be faced, which are related to the interaction of light with obstacles impairing clear imaging inside LoCs, e.g. fluid turbidity due to processes happening inside the chip, roughness of the chip surface, presence of multiple occluding objects inside the channel provoking unwanted light scattering, or biofilm formation. Solving such problems is crucial for a deep understanding of the processes induced and observed in LoC platforms, and to avoid pretreatment of the liquid sample or fine cell alignment (such as in flow cytofluorimetry).

In Chapter 2, DH will be discussed in detail. Chapter 3 is devoted to describe DH techniques for quantitative phase-contrast microscopy of transparent samples dipped inside turbid media, hidden behind occluding objects, or imaged through scattering layers. The problem of designing compact LoC platforms with embedded imaging functionalities, and providing high throughput, will be afforded in Chapter 4. At this scope, we will introduce a novel imaging modality, named Microfluidics Space-Time Digital Holography (μSTDH), providing label-free, unlimited FoV, quantitative, 3D imaging using a linear array detector embedded onboard chip. Possible advances of μSTDH, aimed to increase the imaging system miniaturization, will be discussed.

	Output	Resolution	Compactness	Throughput	Label free	Thickness distribution measurement			Refocusing
						Availability	Number of measures	Computation time	
Conventional Microscopy	Image	High/Very High	Very low, bulky	Variable	Yes	No	-	-	No
Fluorescence Microscopy	Image	High/Very High	Very low, bulky	Variable	No	No	-	-	No
Flow Cytofluorimetry	Ensemble measure, statistical information	-	Low	Very high	No	No	-	-	No
Iterative phase retrieval algorithms (GS-based)	Image	Moderate	Moderate	Low (convergence issues)	Yes	Yes	$\geqslant 2$	Very long	Yes
Deterministic TIE solvers	Image	Moderate	Moderate	Low, boundary conditions issue	Yes	Yes	$\geqslant 2$	Very long	Yes
DEM	Image	Moderate	Moderate	Low, fine calibration and cell alignment required	Yes	Yes	2	-	No
PSI	Image	High	Low	Low, multiple measures	Yes	Yes	3-4	Moderate	Yes
OFM	Image	Moderate	Very high	Theoretically high	Yes	No	1	-	No
HOM	Image	Low	Very high	High	Yes	Yes	1	Long	Yes
DH Microscopy	Image	High	Low	Potentially very High, simple recording	Yes	Yes	1	Short	Yes

Table 1: A comparison between the most effective imaging techniques for studying biological samples in a microfluidic environment.

2

DIGITAL HOLOGRAPHY

The word holography derives from the merge of two Greek words, namely *holos*, meaning whole, and *graphein*, meaning to write. As the name suggests, holography allows to record and reconstruct the whole complex information contained in an optical wavefront. Indeed, both the wavefront amplitude and its phase are accessible once these are coded as a pattern of interference fringes, called the hologram. In this sense, holography provides added value information with respect to standard photography, where just the intensity is recorded. Holography was introduced for the first time by Dennis Gabor in 1948, as a means for improving the resolution of electron microscopes by a lensless acquisition process [84]. However, holography did not receive much attention because of the poor quality of holographic images, due to the low power and coherence of the existing light sources. The invention and the development of the lasers in the 60s gave a sudden impulse to the spread of optical holography, in particular in the visible wavelength region, thanks to the availability of high coherence and very powerful light sources [102-106].

Holography is made of two separate steps: the recording of the hologram, and the object retrieval (also referred to as hologram reconstruction). In order to record the hologram of an object on a photographic plate, an interference has to be produced between two light waves derived from the same coherent source, as shown in Fig. 2.1(a). A first wave is scattered by the object, while a second wave goes directly toward the recording surface and acts as a reference. Since the two waves are allowed to interfere, they form a fringe pattern on the photographic plate, i.e. the hologram. Since the intensity at any point in this interference pattern also depends on the phase delay of the object wave, the resulting hologram contains information on the phase as well as the amplitude of the object wave. The second stage is the formation of the objects image. If the hologram is illuminated once again with the original reference wave, it reconstructs the object wavefront, as shown in Fig. 2.1(b). Indeed, while hologram recording is an interference process, hologram reconstruction is due to diffraction. Illuminating the hologram with the original collimated beam, two diffracted waves are produced, one reconstructing an image of the object in its original location, and the other, with the same amplitude but the opposite

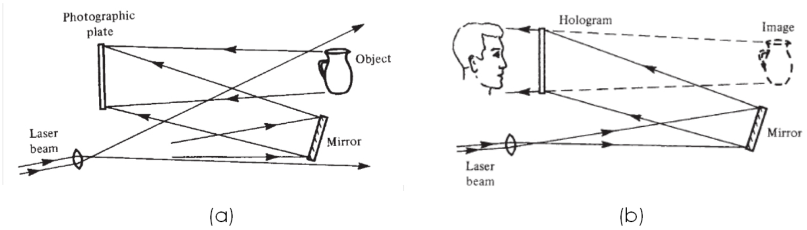

FIGURE 2.1: (a) Hologram recording: the interference pattern produced by the reference wave and the object wave is recorded; (b) Image reconstruction: light diffracted by the hologram reconstructs the object wave.

phase, forming a second, conjugate image. Thus, when the photographic plate is illuminated with the reference wave, an observer can look at the 3D shape of the object (as sketched in Fig. 2.1(b)). In Gabors configuration [84], the poor quality of the reconstructed image was also due to the spatial superposition of the two diffracted waves (i.e. the real and the twin image of the object), as well as the scattered light from the directly transmitted beam (i.e. the zeroth diffraction order). The twin-image problem was overcome by Leith and Upatnieks when they invented the off-axis holography [102,107].

In the in-line holography geometry, the interference was produced between the light scattered by the object and undisturbed light. Instead, in off-axis geometry a separate reference wave directly impinging on the photographic plate was used, incident on the plate at an appreciable angle, with respect to the object wave. As it will be discussed in the following, such strategy has the effect of introducing a carrier to the object signal, so that the diffraction orders are shifted to different spatial frequencies. As a result, when the hologram was illuminated with the original reference beam, the two images were separated by large enough angles from the directly transmitted beam, and from each other. Thus, they could not overlap. Thanks to the off-axis geometry and the use of lasers, holography became a useful technique to acquire new quantitative information from the illuminated objects, which led to the development of holographic metrology [103,108]. Indeed, measuring the wavefront phase changes allows to measure with high sensitivity any physical quantity affecting the phase, e.g. surface roughness or deformations in the order of the wavelength. The use of a photographic plate as a recording support made the recording process slow, and the need for a separate illumination step to reconstruct the recorded image were limiting factors to the spread of holography.

Thus, the introduction of a digital support to record the hologram was a groundbreaking novelty, first proposed by Goodman and Laurence in 1967 and then by *Kronrod et al.* [104,109]. The development of computer technology and solid state image sensors made it possible to record hologram directly on Charge Coupled Device (CCD) cameras. This important technological advance allowed full digital recording and reconstruction of holograms without the use of photographic media, commonly referred to as Digital Holography (DH) [106].

In DH, the reconstruction process is performed numerically with short computational time. As it will be shown in the following, numerical propagation of the recorded wavefront allows to scan all the planes along the optical axis, so that multiple objects placed at different z can be sequentially refocused. Numerical processing of the complex wavefront makes possible to use image processing techniques to add new capabilities for the recovery of the object information (as it will be shown in Chapter 3 and Chapter 4). Above all, the phase-contrast information can be directly extracted, which constitutes one of the major strengths of DH microscopy [110,111].

The holographic principle and its digital development led to many remarkable applications such as optical metrology in experimental mechanics, biology and fluid dynamics [112-115], 3D object recognition [116] and 3D dynamic display [117]. Moreover, DH at mid and far Infrared wavelengths has recently seen important developments in the fields of homeland-security [118-119] and non destructive testing of aerospace composites [120]. A breakthrough achievement in DH was presented in 2013 by M. K. Kim, showing the fascinating possibility to record holograms under incoherent illumination, obtaining for the first time full-color, three-dimensional images of daylight-illuminated outdoor scenes [121]. Holographic 3D imaging was proved to be a promising tool for biomedical applications in microfluidic platforms, recently showing exciting improvements [114-115]. In fact, merging holography with LoC devices, quantitative, high resolution, and marker-free studies of biological unstained samples was made possible. Combining the Optical Tweezers (OT) capabilities with DH, quantitative 3D reconstructions was achieved, thus solving the problem of biovolume estimation and 3D rendering of motile cells [122]. Actually, the most common and well-established methods to calculate biovolume are based on more or less complicated geometrical models. Experiments for measuring biovolumes need isolation and sorting of the cells. Cumbersome observation procedures at microscope are also requested [123]. DH microscopy allows quantitative phase-contrast and label-free imaging that can be of great help in visualizing low-amplitude contrast objects [124-126]. Simultaneous trapping and holographic imaging of the sample was also realized. Under particular conditions of optical trapping power and distance from the chamber walls, the specimen is put in rotation [127] and images of different parts of the cell can be recorded without mechanical contact. During the rotation a holographic sequence is recorded and for each hologram of the sequence the Quantitative Phase Maps (QPMs) are calculated. An emerging concept of great interest is to estimate the biovolume of the cell by exploiting many QPMs, and applying the Shape-From-Silhouettes (SFS) algorithm. SFS is a very powerful method for estimating the 3D shape of an object from its silhouette images [128]. This procedure is attractive because the silhouettes can be computed quickly and with great accuracy. Optical trapping based on DH microscopy was also used to investigate cell mechanics by cell stretching [27]. Furthermore, impressive advances have been shown in 3D tracking of micro-objects [129] based on DH microscopy, where the capability to perform a scanning along the optical axis is an essential feature in estimating the 3D position of the sample. Several efforts were spent in resolution and depth-of-field enhancement in terms of experimental arrangements, as well as numerical processing [130-132]. In particular, in ref. [98] a super-resolution method was presented, that allows lateral phase resolution below the $100\ nm$ barrier exploiting the well-known concept of synthetic aperture in microscopy. Ongoing research efforts are currently carried out with the aim to improve resolution, SNR, and FoV of DH microscopy.

Other specific issues have to be tackled when the sample needs to be studied in a microfluidic environment under unideal imaging conditions, due to the turbidity of the medium flowing inside the channel, presence of occluding objects, or scattering channel walls due to fabrication processes (e.g. laser ablation). In all these cases, environmental factors impair clear imaging, as well as quantitative mapping, due to light scattering processes or unpredictable phase delays. Thus, specific countermeasures need to be adopted for restoring clear imaging. Chapter 3 will be devoted to afford these issues. This chapter describes in detail the whole process of image formation in DH (we paid particular attention to Digital Fresnel Holography [133]), from the creation of the hologram coding the object wavefront information, to the extraction of the object signal. In the last section, we will spotlight DH microscopy, underlying its useful capabilities in microfluidics LoC imaging of biological samples.

HOLOGRAM FORMATION

In this section we will describe in detail the whole process of hologram formation and reconstruction in order to derive the relation between the real object field and the reconstructed field. Since the physical processes determining the hologram formation and the DH image reconstruction are linear, the sought relation has to assume the form of a convolution product.

Considering a reference system of coordinates {x, y}, attached to the principal surface of a real object, and a z-axis, perpendicular to this surface, that corresponds to the propagation direction of the diffracted light beam, we can model the holographic process as a Linear Space Invariant system (LSI) with an impulse response $T(x, y)$, transforming the real object signal $U(x, y)$ in the reconstructed field

$$U_R(x, y) = U(x, y) \otimes T(x, y), \tag{2.1}$$

where $\otimes$ is the spatial convolution operator. Processes of interference, diffraction, spatial integration, sampling and digital reconstruction determine the shape of the impulse response $T(x, y)$. Let

$$U(x, y) = |U(x, y)| \exp(j\varphi_U(x, y)) \tag{2.2}$$

be the complex wavefront produced in the plane (x, y) when the object is illuminated by a coherent beam. According to the diffraction theory [134], the diffracted field in a generic plane (x', y') orthogonal to the optical axis is expressed by the Rayleigh-Sommerfelds integral as [135]:

$$O(x', y', d_0) = \frac{1}{j\lambda} \iint\limits_{\mathbb{R}^2} U(x, y) \frac{\exp(jk\rho)}{\rho} \cos\Omega dx dy, \tag{2.3}$$

where λ is the source wavelength, d_0 is the distance between the planes (x, y) and (x', y'), i.e. the propagation distance of the diffracted wavefront, $k = 2\pi/\lambda$ is the wavenumber, $\cos\Omega$ is the obliquity factor, usually set to unity due to the small angles assumption [134], and

$$\rho = \sqrt{d_0^2 + (x' - x)^2 + (y' - y)^2} \tag{2.4}$$

is the distance between a generic point in the plane (x', y') and a given point belonging to (x, y). If the Taylor series expansion of the square root formula in Eq. (2.4) is performed, excluding the terms of higher order than the first two, the distance ρ takes the form

$$\rho \approx d_0 \left(1 + \frac{1}{2}\frac{(x' - x)^2}{d_0^2} + \frac{1}{2}\frac{(y' - y)^2}{d_0^2}\right), \tag{2.5}$$

which is valid under the assumption of large propagation distances, precisely when d_0 satisfies the Fresnel zone sufficient condition [134]:

$$d_0^3 \gg \frac{\pi}{4\lambda}\left[\left(x'-x\right)^2+\left(y'-y\right)^2\right]^2_{max}. \tag{2.6}$$

Applying this approximation to the exponent of the spherical factor in Eq.(2.3) (which is the most critical factor due to the presence of the wavenumber amplifying approximation errors), while dropping all terms but the first in the denominator, the diffraction integral reduces to:

$$O\left(x',y',d_0\right)=\frac{je^{j\frac{2\pi}{\lambda}d_0}}{\lambda d_0}\iint\limits_{\mathbb{R}^2}U\left(x,y\right)\exp\left\{j\frac{\pi}{\lambda d_0}\left[\left(x'-x\right)^2+\left(y'-y\right)^2\right)\right]\right\}dxdy. \tag{2.7}$$

After some trivial manipulations, Eq. (2.7) can be written in terms of Fourier transform:

$$\begin{aligned}O\left(x',y',d_0\right)&=\left|O\left(x',y',d_0\right)\right|\exp\left[j\varphi\left(x',y',d_0\right)\right]=\\&=Z\left(x',y',d_0\right)\mathcal{F}\{U\left(x,y\right)W\left(x,y,d_0\right)\},\end{aligned} \tag{2.8}$$

where $\varphi\left(x',y',d_0\right)$ is the object phase signal, and we defined

$$\begin{cases}Z\left(x',y',d_0\right)=\frac{j}{\lambda d_0}\exp\left\{\frac{2\pi}{\lambda}\left[d_0+\frac{x'^2+y'^2}{2d_0}\right]\right\}\\ W\left(x,y,d_0\right)=\exp\left\{\frac{j\pi}{\lambda d_0}\left(x^2+y^2\right)\right\}\end{cases} \tag{2.9}$$

Equation (2.8) well describes the relation between the wavefront in the object plane and the diffracted wavefront in whatever plane along the optical axis satisfying the sufficient condition in Eq. (2.6). This is a distribution of complex values, and both the amplitude and phase contain useful object information, depending on the acquisition configuration. However, any employable sensor can only register intensity distributions, so that a recording device placed in the plane (x',y') would only capture the 2D signal $|O\left(x',y',d_0\right)|^2$, thus losing the phase information. In order to recover the phase, this should affect in some way the recorded intensity distribution. Holography exploits the phenomenon of interference between two waves to code the phase information in an intensity signal, specifically as a modulated fringe pattern. Thus, a reference wave has to be introduced to allow interference with the object wave. Let

$$R\left(x',y',d_0\right)=a_R\exp\left\{j2\pi(u_Rx'+\nu_Ry')+j\Gamma\left(x',y'\right)\right\} \tag{2.10}$$

be the reference wave in the acquisition plane (x',y'), modeled as a plane wave oscillating with spatial frequencies u_R and ν_R. In Eq. (2.10), $\Gamma\left(x',y'\right)$

represents the wavefront aberration factors in the acquisition plane (x', y'). The object wave interferes with the reference in the recording plane to produce the hologram

$$\begin{aligned} H\left(x', y', d_0\right) &= \left|O\left(x', y', d_0\right) + R\left(x', y'\right)\right|^2 = \\ &= \left|O\left(x', y', d_0\right)\right|^2 + \left|R\left(x', y'\right)\right|^2 + \\ &+ R^*\left(x', y'\right) O\left(x', y', d_0\right) + R\left(x', y'\right) O^*\left(x', y', d_0\right), \end{aligned} \tag{2.11}$$

where * denotes the conjugate operator. In the right hand side of Eq. (2.11), four terms are present, that are usually called the diffraction orders. The first two terms are only intensity signals, of little interest because the phase information is lost due to the square module operation. These can be grouped in a signal

$$D_0(x', y', d_0) = \left|O(x', y', d_0)\right|^2 + \left|R(x', y')\right|^2 \tag{2.12}$$

referred to as the zero-th diffraction order. The third and the fourth term are the +1 and -1 orders of diffraction, hereafter denoted with $H^{+1}\left(x', y', d_0\right)$ and $H^{-1}\left(x', y', d_0\right)$ and representing the real image and the virtual image of the object respectively. Applying Eq. (2.10), the +1 order takes the form:

$$\begin{aligned} &H^{+1}\left(x', y', d_0\right) = R^*\left(x', y'\right) O\left(x', y', d_0\right) = \\ &= a_R \left|O\left(x', y', d_0\right)\right| \exp\left[j\varphi\left(x', y', d_0\right)\right] \exp\left[-j2\pi\left(u_R x' + \nu_R y'\right) - j\Gamma\left(x', y'\right)\right] \end{aligned} \tag{2.13}$$

Since it results $H^{+1}(x', y', d_0) = \left\{H^{-1}(x', y', d_0)\right\}^*$, we can rewrite Eq. (2.11) in a different form

$$\begin{aligned} &H(x', y', d_0) = \\ &= D_0(x', y', d_0) + H^{+1}(x', y', d_0) + H^{-1}(x', y', d_0) = D_0(x', y', d_0) + \\ &+ 2a_R \left|O\left(x', y', d_0\right)\right| \cos\left\{2\pi\left(u_R x' + \nu_R y'\right) + \Gamma\left(x', y'\right) - \varphi\left(x', y', d_0\right)\right\}, \end{aligned} \tag{2.14}$$

where it is apparent that the amplitude and phase of the object wave are encoded as amplitude and phase modulation, respectively, of a set of interference fringes equivalent to a carrier with spatial frequencies u_R and ν_R. This gives us a good chance to recover the phase. The spatial frequencies are proportional to the angles between the reference and the object beam, $(\theta_x,\ \theta_y)$, according to the relation

$$u_R = \frac{\sin\theta_x}{\lambda} \ ; \ \nu_R = \frac{\sin\theta_y}{\lambda} \tag{2.15}$$

which makes clear the advantage of using an off-axis configuration [102]. Indeed, the real image, the twin image (i.e the -1 order), and the zero-th order are not spatially overlapped if the angles $(\theta_x,\ \theta_y)$ are large enough. Thus, when the hologram is illuminated again with the reference beam, the three contributions get clearly visible.

Noise components

So far, the case of ideal recording has been considered, leading to the formulation of the hologram in Eq. (2.14). In practice, a mixture of two kinds of noise components corrupts the recorded hologram. The first is a multiplicative noise, n_S, referred to as speckle, inherently due to the coherence of the source employed in holography and correlated to the useful signal [136]. Besides, an additive Gaussian noise component, n_G, degrades the hologram. Hence, in the case of real recordings this takes the form:

$$\begin{aligned} H_N(x',y',d_0) &= D_0(x',y',d_0) + 2a_R \left|O\left(x',y',d_0\right)\right| \cdot \\ &\cdot \cos\left\{2\pi\left(u_R x' + v_R y'\right) + \Gamma\left(x',y'\right) - \varphi\left(x',y',d_0\right) + n_S(x',y')\right\} + n_G(x',y'). \end{aligned} \tag{2.16}$$

Many approaches are commonly adopted to suppress the noise components in Holography and ongoing research efforts are made to decrease the corresponding artifacts, in both the recording and the reconstruction step [114,137-140]. These will be briefly discussed in Chapter 3. For the sake of simplicity, in the following sections of this chapter we will keep on using the ideal hologram, H, to describe the image formation process. All the results we will obtain trivially extend to the real case of noisy hologram by replacing H with H_N.

Recording on digital supports

In DH, the hologram is acquired by a digital sensor (e.g. a CCD or a CMOS camera) and stored in a computer. The recording process is the sampling of an interference pattern consisting of spatial frequencies, the highest of which is given by the largest angle between object and reference wave. The limited resolution of the CCD chip and similar digital devices decides the maximum frequency allowed for sampling and severely restricts the experimental set-up configuration. According to the Nyquist/Shannon sampling theorem [141,142,134], each period must be recorded by at least two detector elements. For the sake of simplicity, and without loss of generality, we will herein refer to a one dimensional

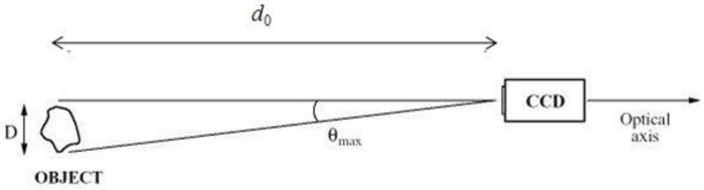

FIGURE 2.2: Schematic view of the angular extent of the object: θ_{max} is the angular extent of the object and the maximum angle between object and reference wave; d_0 is the distance along the optical axis between the CCD chip and the object; D is the transversal size of the object, normal to the optical axis.

case to discuss the problem of proper fringe sampling. If Λ is the fringe spacing and p_x is the detector pitch (centre-to-centre spacing between neighboring detector elements) in the x direction (which is orthogonal to the optical axis), the relation for proper sampling must be fulfilled.

$$2p_x \leqslant \Lambda \tag{2.17}$$

A geometrical evaluation of the angle θ_x between the object and the reference wave gives

$$\Lambda = \frac{\lambda}{2\sin\left(\frac{\theta_x}{2}\right)} . \tag{2.18}$$

Combining Eq. (2.17) and Eq. (2.18) we obtain

$$\theta_x \leqslant \sin^{-1}\left(\frac{\lambda}{2p_x}\right), \tag{2.19}$$

where $(1/2p_x)$ is the sampling frequency. This means that the angular extent $\theta_{x,max}$ in Fig. 2.2 must not exceed this limit. In order to use the entire available bandwidth of the recording device, the equal sign in Eq. (2.19) should be used. Another geometrical evaluation shows that if the distance d_0 between the CCD and the object is

$$d_0 \approx \frac{2p_x}{\lambda} D \tag{2.20}$$

then the maximum bandwidth is obtained without violating the sampling theorem. D is the transversal size of the object, and small angular values are assumed according to Eq. (2.19). Returning to a general 2D formulation of the

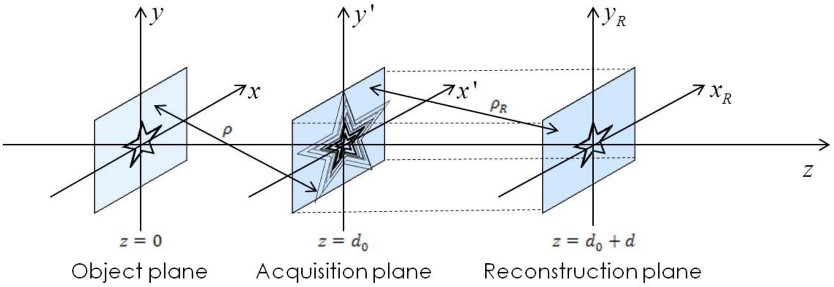

Figure 2.3: Geometry for recording and numerical reconstruction of digital holograms. The object (a star in this sketch) is in the plane $(x, y, z = 0)$. The hologram is recorded in the acquisition plane $(x', y', z = d_0)$, capturing an out-of-focus object information. Numerical propagation of the hologram from the acquisition plane to the reconstruction plane, $(x_R, y_R, z = d_0 + d)$, allows to scan all the planes along the optical axis, z, till providing the refocused image of the object.

problem, in the recording process the hologram is sampled by a matrix of pixels, each of them performing a spatial integration due to its extended surface. Let us consider a sensor having N_x x N_y pixel, each one with area $A_P = \Delta_x$ x Δ_y, and pixel pitches (p_x, p_y). The action operated on the hologram by the sensor can be modeled as a convolution process with a sequence of rectangular pulses. This returns a numerical version of the hologram, i.e.

$$H_s(kp_x, lp_y, d_0) = \left[H(x', y', d_0) \otimes \prod_{\Delta_x, \Delta_y} (x', y') \right]_{(kp_x, lp_y)}, \tag{2.21}$$

where $k = 1, \dots, N_x$, $l = 1, \dots, N_y$, and

$$\prod_{\Delta_x, \Delta_y} (x', y') = \begin{cases} \frac{1}{\Delta_x \Delta_y}, & \|x'\| < \frac{\Delta_x}{2}, \|y'\| < \frac{\Delta_y}{2} \\ 0 & \text{otherwise} \end{cases} \tag{2.22}$$

is the pixel function. We can then rewrite Eq. (2.14) in its numerical version to take into account the recording process:

$$H_s\left(kp_x, lp_y, d_0\right) = D_{0s}\left(kp_x, lp_y, d_0\right) + H_s^{+1}\left(kp_x, lp_y, d_0\right) + H_s^{-1}\left(kp_x, lp_y, d_0\right). \tag{2.23}$$

where the subscript s denotes the sampled version of the signals in Eq. (2.14), obtained after convolution with the pixel function.

NUMERICAL RECONSTRUCTION

Hologram reconstruction was classically performed illuminating the recording support again with the reference beam. Hence, the image formation is a process of diffraction from the hologram aperture, as schematically depicted in Fig. 2.3. Under Fresnel approximation, the complex wavefront reconstructed in a plane (x_R, y_R), at a generic distance d from the hologram plane, (x', y'), can be written as:

$$C(x_R, y_R, d) = \frac{j e^{j\frac{2\pi}{\lambda}d}}{\lambda d} \iint_{\Sigma_0} R(x', y')\, H(x', y')\, e^{\left\{j\frac{\pi}{\lambda d}\left[(x_R - x')^2 + (y_R - y')^2\right]\right\}} dx' dy', \tag{2.24}$$

that can be rearranged, similarly to Eq. (2.8), in terms of a Fourier transform:

$$\begin{aligned} C(x_R, y_R, d) = {} & Z(x_R, y_R, d)\, \mathcal{F}\left\{R(x', y')\, H(x', y')\, W(x', y', d)\right\} = \\ & = \mathcal{F}r\{H; d\}. \end{aligned} \tag{2.25}$$

The operation described in the right hand side of Eq. (2.25) is generally referred to as the Fresnel transform, $\mathcal{F}r\{H; d\}$, or the hologram propagation. Similarly, the reconstruction method that adopts the formulation written above is called the Fresnel method. The reconstructed wavefront $C(x_R, y_R, d)$ is a complex field containing the three diffraction orders, propagated at distance d, from which the intensity and the phase signals can be extracted:

$$\begin{aligned} I(x_R, y_R, d) &= C(x_R, y_R, d)\; C^*(x_R, y_R, d) \\ \Psi(x_R, y_R, d) &= \tan^{-1} \frac{\mathrm{Im}\{C(x_R, y_R, d)\}}{\mathrm{Re}\{C(x_R, y_R, d)\}}, \end{aligned} \tag{2.26}$$

where $\mathrm{Im}\{\ldots\}$ and $\mathrm{Re}\{\ldots\}$ respectively take the imaginary part and the real part of a complex signal. If d is the object best-focus distance for the given optical system used to capture the hologram, then the signal $C(x_R, y_R, d)$ is the object image reconstruction.

The formulation in Eq. (2.24) gives the possibility to emulate the propagation process by numerical techniques. The simplest method is to directly implement Eq. (2.25) in a computer, i.e. numerical propagation is applied to the digital hologram, $H_s(kp_x, lp_y)$, exploiting the Fresnel approximation. Since the Fresnel transform is proportional to a Fourier transform, as shown in Eq. (2.25), the numerical Fresnel transform will be proportional to the Discrete Fourier

Transform (DFT). This can be efficiently implemented in a computer by using the Fast Fourier Transform (FFT) algorithm. Hence, we can write the DH reconstruction as:

$$\begin{aligned} & C\left(n\rho_x, m\rho_y, d\right) = \\ & = Z_S\left(n\rho_x, m\rho_y, d\right) \mathcal{FFT}\left\{R_s\left(kp_x, lp_y\right) H_s\left(kp_x, lp_y\right) W_s\left(kp_x, lp_y, d\right)\right\} = \\ & = \mathcal{F}r\left\{H_S; d\right\} = \mathcal{F}r\left\{D_{0S}\left(kp_x, lp_y\right); d\right\} + \\ & + \mathcal{F}r\left\{H_S^{+1}\left(kp_x, lp_y\right); d\right\} + \mathcal{F}r\left\{H_S^{-1}\left(kp_x, lp_y\right); d\right\}, \end{aligned} \tag{2.27}$$

where the last equality is valid due to the linearity of the Fresnel transform and

$$\begin{cases} \rho_x = \frac{\lambda d}{N_x p_x} \\ \rho_y = \frac{\lambda d}{N_y p_y} \end{cases} \tag{2.28}$$

are the pixel pitches in the reconstruction plane. For the sake of clarity, we will make an abuse of notation, referring in the following to the dimensionless set of coordinates in the reconstruction plane, i.e.

$$\begin{cases} n\rho_x = n \\ m\rho_y = m \end{cases} \tag{2.29}$$

The object distribution has to be recovered from Eq. (2.27) by filtering out the orders out of interest. Since it results:

$$\mathcal{F}r\left\{H_S^{-1}; -d\right\}_{(n,m)} = \mathcal{F}r\left\{H_S^{+1}; +d\right\}^*_{(-n,-m)} \tag{2.30}$$

the twin image is a useless signal. Moreover, the zeroth order term carries a redundant information about the object intensity, and the phase map cannot be recovered from this distribution. Thus, this is usually suppressed. When the hologram is recorded in off-axis configuration, the presence of a spatial carrier has the effect of separating the orders in the reconstruction plane. For large enough angles, these can be filtered out by spatially masking the DH reconstructions to extract the +1 order from Eq. (2.27). In general, a high-pass filtering of the hologram is sufficient to suppress D_{0S}. In the case of in-line DH geometries, the orders overlap and iterative algorithms have to be adopted to reduce the zero order and to solve the twin image problem, as discussed in Chapter 1 [70-72,90,91,143]. We will hereafter assume to filter out the orders out of interest and we will focus on the first order of diffraction, $\mathcal{F}r\left\{H_S^{+1};d\right\}$. It is possible to prove that [144]

$$\begin{aligned} U_R\left(n,m;d\right)=\mathcal{F}r\left\{H_S^{+1};d\right\}_{(n,m)}=KU\big(-\frac{d_0}{d}n,-\frac{d_0}{d}n\big)\otimes \\ \otimes\prod_{\Delta x,\Delta y}(n,m)\otimes\tilde{W}_{a,b}(n,m)\otimes\tilde{W}_d(n,m)\otimes\delta(n+\lambda u_R d,m+\lambda v_R d). \end{aligned} \tag{2.31}$$

In Eq. (2.31) the reconstructed wavefront, U_R, is related to the object distribution, U, by convolution operations with a number of functions. In other words, the object distribution is subject to the cascade of four LSI systems, whose impulse responses affect the output signal resulting from the holographic process. The first term is the pixel function described above, the second is due to aberrations of the reference wavefront, i.e. if $\Gamma\left(x',y'\right)=0$ then $\tilde{W}_{ab}\left(n,m\right)=\delta\left(n,m\right)$, the third is due to the focusing error, i.e. if d is the object best-focus distance, $\tilde{W}_d\left(n,m\right)=\delta\left(n,m\right)$, and the last convolution term is a localization function in the reconstructed field [145]. Finally, K includes irrelevant constants and phase terms. Combining Eq. (2.1) and Eq. (2.31) we end up with the impulse response of the whole DH process under Fresnel approximation:

$$T(n,m)=K\prod_{\Delta x,\Delta y}(n,m)\otimes\tilde{W}_{a,b}(n,m)\otimes\tilde{W}_d(n,m)\otimes\delta(n+\lambda u_R d,m+\lambda v_R d), \tag{2.32}$$

also called the resolution function of the Digital Fresnel Holography.

CONVOLUTION METHOD

A different way to demodulate the object distribution is to think to the Rayleigh-Sommerfeld diffraction formula as a convolution integral, i.e.

$$\begin{aligned} C\left(x_R,y_R,d\right)=\frac{1}{j\lambda}\iint_{\Sigma_0}R\left(x',y'\right)H\left(x',y'\right)\frac{\exp\left(jk\rho_R\right)}{\rho_R}\cos\Omega dx'dy'= \\ =\iint_{\Sigma_0}R\left(x',y'\right)H\left(x',y'\right)g\left(x_R-x',y_R-y';d\right)dx'dy'= \\ =[R(x',y')H(x',y')]\otimes g(x',y';d) \end{aligned} \tag{2.33}$$

where

$$g(x',y';d)=\frac{1}{j\lambda}\frac{\exp\left(jk\rho_R\right)}{\rho_R}\cos\Omega\approx\frac{1}{j\lambda}\frac{\exp jk\sqrt{d^2+x'^2+y'^2}}{\sqrt{d^2+x'^2+y'^2}} \tag{2.34}$$

is the Point Spread Function (PSF) of the diffraction process from the hologram plane to the reconstruction plane under Fresnel approximation, and ρ_R is the distance between a generic point in the plane (x', y') and a given point belonging to (x_R, y_R). Standing the convolution property of the $\mathcal{F}\{\ldots\}$ operator, the diffracted wavefront is given by:

$$C_{conv}(x_R, y_R, d) = \mathcal{F}^{-1}\left\{\mathcal{F}\left\{R(x', y')H(x', y')\right\}\mathcal{F}\left\{g(x', y'; d)\right\}\right\}_{(x_R, y_R)}, \tag{2.35}$$

which can be numerically calculated by three FFTs. Hence, the digital wavefront reconstructed at distance d using the convolution method takes the form

$$\begin{aligned} &C_{conv}\left(n\rho_{Cx}, m\rho_{Cy}, d\right) = \\ &= \mathcal{FFT}^{-1}\left\{\mathcal{FFT}\left\{R_s\left(kp_x, lp_y\right)H_S^{+1}\left(kp_x, lp_y\right)\right\}\mathcal{FFT}\{g\left(kp_x, lp_y; d\right)\}\right\}, \end{aligned} \tag{2.36}$$

where $G = \mathcal{FFT}\{g; d\}$ has a known distribution independent on the input hologram, and can be calculated just once for a more rapid computing:

$$G = \mathcal{FFT}\{g; d\} = \exp\left\{\frac{j2\pi d}{\lambda}\sqrt{1 - \frac{\lambda^2\left(n + \frac{N_x^2 p_x^2}{2\lambda d}\right)^2}{N_x^2 p_x^2} - \frac{\lambda^2\left(m + \frac{N_y^2 p_y^2}{2\lambda d}\right)^2}{N_y^2 p_y^2}}\right\}. \tag{2.37}$$

Noteworthy, differently from the Fresnel method, the convolution method yields a wavefront reconstruction with pixel pitches independent on the propagation distance, i.e.

$$\begin{cases} \rho_{Cx} = p_x \\ \rho_{Cy} = p_y \end{cases}. \tag{2.38}$$

This is an advantage of the convolution method with respect to the Fresnel strategy, as no resolution loss occurs when the reconstruction distance increases. On the other hand, the price to pay is an increase of the computational time required for calculating three FFTs.

ANGULAR SPECTRUM METHOD

Both the Fresnel and the convolution method discussed above are valid under Fresnel approximation, which stands for propagation distances higher than the threshold value reported in Eq. (2.6). In practice, this limits the minimum reconstruction distance. A way to avoid the limitations deriving from the Fresnel approximation is to adopt the Angular Spectrum (AS) method. Considering the hologram plane located in the origin of the optical axis, $z = 0$, the AS of the hologram $H(x', y', z = 0)$ in this plane is given by

$$G_A(k_x, k_y, 0) = \iint_{\Sigma_0} H(x', y', 0)\, e^{[-j(k_x x' + k_y y')]} dx' dy' = \mathcal{F}\{H(x', y', 0)\}_{(k_x, k_y)}, \tag{2.39}$$

where we indicated with k_x and k_y the spatial frequencies corresponding to x' and y', respectively. As discussed above, if the spatial carrier is properly adjusted, the three diffraction orders are spatially separated in the AS domain and the +1 order can be extracted by band-pass filtering the signal G_A. We will indicate with G_A^{+1} the version of the AS obtained after filtering out the diffraction orders out of interest, and we will refer to $H^{+1}(x', y', 0)$ as the object signal in the plane $z = 0$. This can be rewritten as the inverse Fourier transform of its filtered AS, i.e.

$$H^{+1}(x', y', 0) = \iint_{\Sigma_0} G_A^{+1}(k_x, k_y, 0) \exp\left[+j\left(k_x x' + k_y y'\right)\right] dk_x dk_y. \tag{2.40}$$

The exponential function $\exp\{j(k_x x' + k_y y')\}$ can be thought as the projection onto the plane $z = 0$ of a plane wave propagating along the optical axis with a wave vector

$$k = \left(k_x, k_y, k_z = \sqrt{k^2 - k_x^2 - k_y^2}\right) \tag{2.41}$$

Thus, the wavefront propagated from the hologram plane to the reconstruction plane can be written as

$$\begin{aligned} C_{AS}(x_R, y_R, z) &= \iint_{\Sigma_0} G_A^{+1}(k_x, k_y, 0) \exp\left[+j\left(k_x x' + k_y y' + k_z z\right)\right] dk_x dk_y = \\ &= \iint_{\Sigma_0} \left[\mathcal{F}\left\{H^{+1}\left(x', y', 0\right)\right\}_{(k_x, k_y)} \exp(jk_z z)\right] \exp\left[+j\left(k_x x' + k_y y'\right)\right] dk_x dk_y = \\ &= \mathcal{F}^{-1}\left\{\mathcal{F}\left\{H^{+1}\left(x', y', 0\right)\right\}_{(k_x, k_y)} \exp(jk_z z)\right\}_{(x_R, y_R)}. \end{aligned} \tag{2.42}$$

If z=d is the object best-focus distance, then C_{AS} is the DH reconstruction of the object. This can be numerically obtained by calculating two FFTs, so that the numerical image reconstruction at distance d using the AS method is given by:

$$C_{AS}\left(n\rho_{ASx}, m\rho_{ASy}, d\right) = \mathcal{FFT}^{-1}\left\{\mathcal{FFT}\left\{H_S^{+1}\left(kp_x, lp_y, 0\right)\right\}\exp\left(jk_z d\right)\right\}, \tag{2.43}$$

where

$$\begin{cases} \rho_{ASx} = p_x \\ \rho_{ASy} = p_y \end{cases} \tag{2.44}$$

are the pixel pitches in the reconstruction plane, which are independent on the propagation distance, similarly to the convolution method. Noteworthy, the AS method allows to save one FFT with respect to the convolution method and, above all, this works for short propagation distances too (i.e. when the condition in Eq. (2.6) does not stand).

DIGITAL HOLOGRAPHY MICROSCOPY

In this section we will describe the set-up adopted to obtain, by DH microscopy, both amplitude imaging and quantitative phase-contrast mapping of transparent biological samples. Besides, a description of the whole hologram reconstruction process will be provided, showing examples of DH reconstructions corresponding to recordings in microscope transmission configuration. At this scope, we reconstruct the holograms of adherent fibroblasts and Red Blood Cells sharing the same microfluidic environment. Then, we moved to more complex specimens, namely C-elegans samples in embryo stage and first L1 stage. These two DH acquisitions are good examples of non-invasive quantitative imaging of live samples.

A typical DH setup, adopted at this scope, is sketched in Fig. 2.4. This is a classical Mach-Zehnder interferometer in transmission configuration. The coherent light beam emitted from a laser source is first divided in two parts by an Optical Fiber Splitter (FS). In alternative, a Beam Splitter (BS) cube can be adopted. The resulting wavefronts, propagating through the fiber, constitute the reference and the object beam of the interferometer. The object beam reaches the sample plane, (x, y), where the specimen is positioned (in the case of LoC imaging this is the plane where placing the microfluidic device, as sketched in the inset on the right side of Fig. 2.4). After passing through the object, the beam acquires information about its optical density and absorbance properties. In the case of transparent biological samples and symmetric interferometer configurations, the phase delay the specimen introduces on the object beam can be used to measure the sample optical thickness, i.e. the product be-

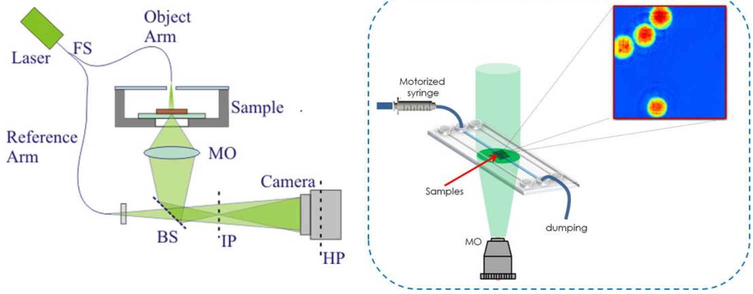

FIGURE 2.4: DH microscopy setup in transmission configuration. FS: Fiber Splitter. MO: Microscope Objective. BS: Beam Splitter/Combiner. IP: Image Plane. HP: Hologram Plane. The inset on the right shows a sketch of the sample plane, where the LoC is positioned, and a phase-contrast map of fibroblast cells in suspension.

tween the sample refractive index and its physical thickness. Hence, the phase signal of the object beam is particularly relevant and has to be extracted, as discussed above. After exiting the fiber, the reference beam is directed toward a BS cube, here employed as a Beam Combiner (BC), where it recombines with the object beam. Thus, the object beam and the reference interfere in the acquisition plane (x',y'), i.e. the hologram $H(x',y')$ is formed. A typical DH microscopy setup is also equipped with microscope objectives providing image magnification, polarizers, optical filters and attenuators to adjust the intensity of the reference wave, the object wave, or both in order to optimize the fringe visibility. Note that the hologram plane (HP) can be, in general, different from the sample best-focus plane, allowing out-of-focus acquisitions of multiple samples displaced in a liquid volume, followed by numerical refocusing. The hologram of the samples inside the FoV is recorded by a CCD camera and stored in a computer as the matrix of real values H_s, as shown in Figures 2.5(a-d), where the holograms corresponding to four different portions of the chip are recorded with a 60x Microscope Objective (MO). In off-axis DH geometries, the BC is slightly tilted in order to provide an angle between the object beam and the reference beam. This tilt introduces a spatial carrier, required to easily separate the diffraction orders in the Fourier plane. Indeed, if Eq. (2.14) is Fourier transformed it results that the +1 and -1 diffraction orders are shifted to the frequencies (u_R, v_R) and $(-u_R, -v_R)$, while the signal corresponding to $\mathcal{F}\{D_{0S}\}$ is in the center of the object spectrum, as shown in Figs. 2.6(a-d). These report the distribution of the matrices $|\mathcal{FFT}\{H_S\}|$ corresponding to the holograms shown in Fig. 2.5.

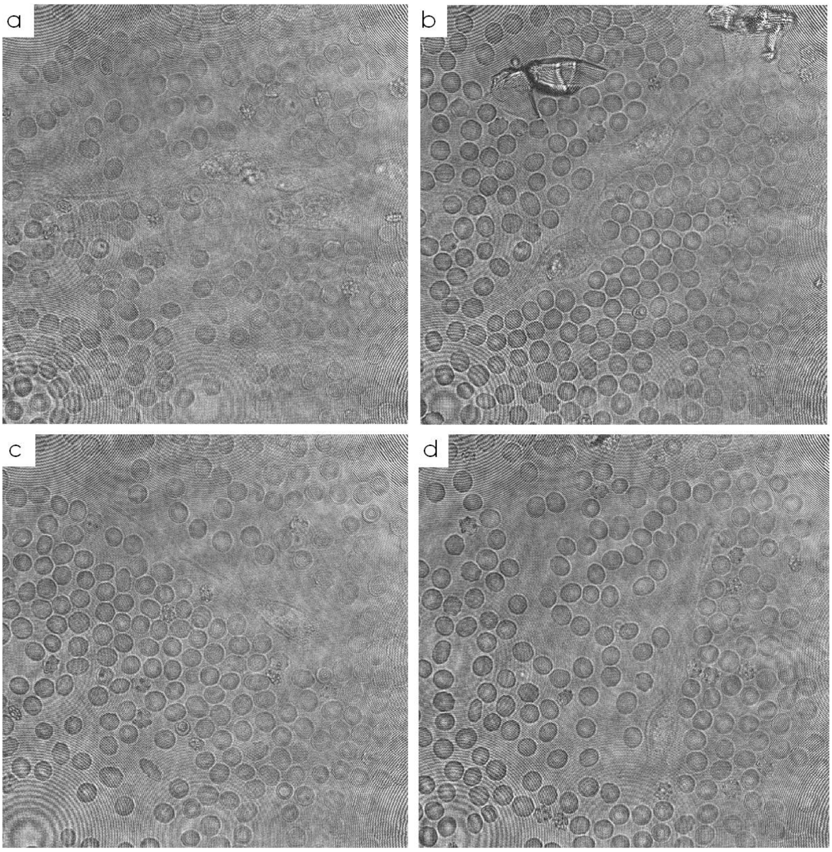

FIGURE 2.5: Fibroblast cells are let adhere on the inner substrate of a microfluidic channel, where RBCs are then inserted. Figures (a-d) shows the holograms, H_S, of the samples corresponding to four different portions of the channel, recorded using the setup sketched in Fig. 2.4.

The +1 order can be extracted in the Fourier plane, re-shifted to the center of the Fourier spectrum and back Fourier transformed. Then, numerical propagation of the filtered hologram to the image plane can be performed, using one of the reconstruction methods described above, to obtain the object complex signal in focus. In alternative, the hologram containing all the diffraction orders can be propagated, returning the complex wavefront reconstruction in the image plane. Figs. 2.7(a-d) show an example of amplitude reconstructions, $|C\left(x_R, y_R, d\right)|$, of the three diffraction orders obtained after propagation, using the Fresnel method, of the four holograms of Fig. 2.5 at a generic coordinate $z = +20cm$ from the recording plane. The three main orders of diffraction are clearly recognizable from Figs. 2.7(a-d). In this case, despite the introduction of a spatial carrier due to the off-axis geometry, its frequency is not enough large to avoid overlapping between the orders, so that a non optimal extraction of the +1 order can be obtained. It is clear from this example the usefulness of approach based on the extraction of the +1 term directly from the Fourier spectrum of Fig. 2.6, as discussed above. For each hologram, the amplitude distributions of the extracted +1 diffraction orders after propagation at the best focus distance, namely $\left|C^{+1}\left(x_R, y_R, d\right)\right|$, are shown in Figs. 2.8(a-d).

It is worth to notice that the propagation of the hologram of a pure-phase, transparent object to its own best-focus plane provides an amplitude reconstruction where the contrast of the object is minimum. Hence, in the images of Fig. 2.8 the best refocusing condition is reached for the adherent fibroblasts and some of the RBCs adhering on the channel substrate, while a number of non adhering RBCs are reconstructed slightly out-of-focus, (a different propagation distance, d, should be chosen to image them in focus). On the contrary, the phase contrast-map maximizes the contrast of the in-focus objects. These two properties can be exploited to look for the best-focus distance automatically by means of algorithms that optimize a proper contrast metric, thought as a function of d, as it will be discussed in section 3.3.3.

As regards the phase signal, some considerations are due. Indeed, the extraction of the phase from the complex reconstruction, C, does not directly yield the optical thickness of the object, but the matrix (shown in Figs 2.9(a-d)):

$$\Psi\left(x_R, y_R, d\right) = \{\varphi(x_R, y_R, d) - \Gamma(x_R, y_R, d)\}|_{2\pi} - \pi \tag{2.45}$$

also referred to as the wrapped phase, where the symbolism $\{\ldots\}|_{2\pi}$ indicates the 2π modulus of a signal. In other words, the extracted phase assumes values in the range $(-\pi, \pi)$. Since the real phase distribution can span, in general, over a wider range, the retrieved phase shows sudden unwanted jumps which needs to be compensated to restore the correct phase dynamic. This issue is known

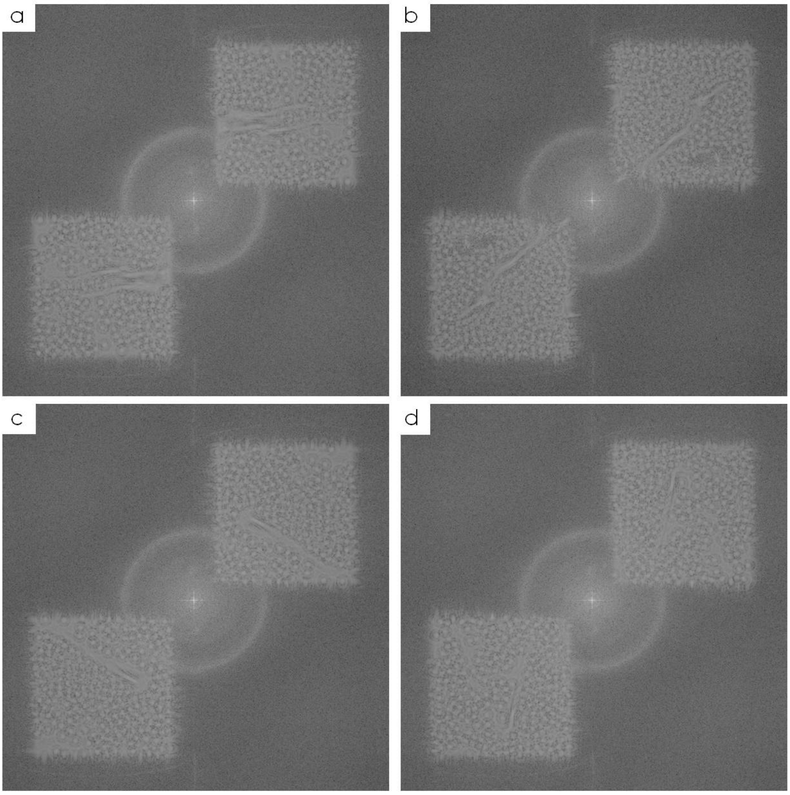

Figure 2.6: Amplitude Fourier spectra, $|\mathcal{FFT}\{H_S\}|$, of the holograms shown in Fig. 2.5. The three main orders of diffraction are clearly recognizable and, due to the off-axis geometry introducing a spatial carrier, these are just slightly overlapped and can be spatially filtered out to extract the +1 term.

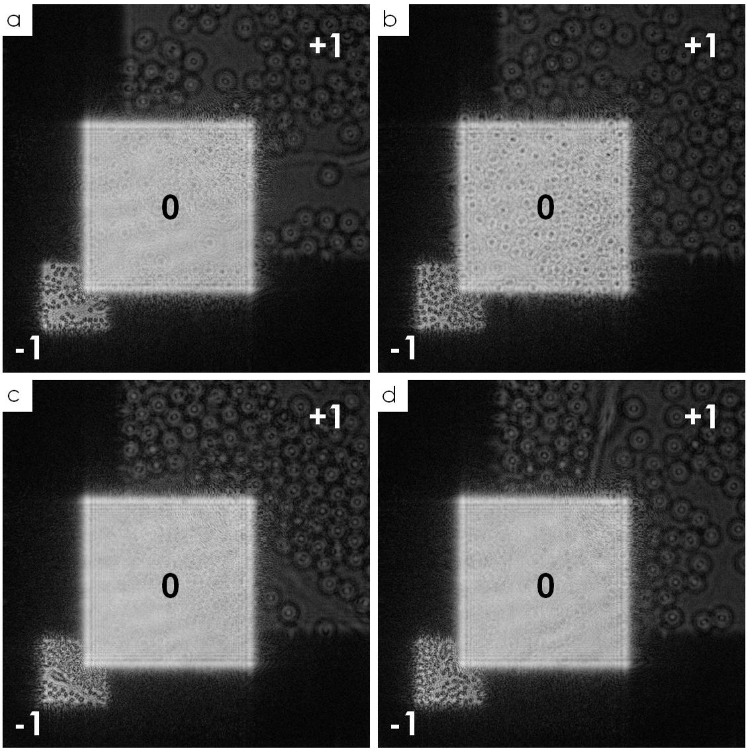

FIGURE 2.7: An example of amplitude reconstructions, at distance z=+20 cm from the recording plane, of the holograms shown in Fig. 2.5. The reconstruction is performed by means of the Fresnel method, i.e. the signals, $|C(x_R, y_R, d)| = |\mathcal{F}r\{H_S\}|$, are shown. The three main orders of diffraction are clearly recognizable. In this case, despite the introduction of a spatial carrier due to the off-axis geometry, its frequency is not enough large to avoid overlapping between the diffraction orders, so that a non optimal extraction of the +1 order can be obtained.

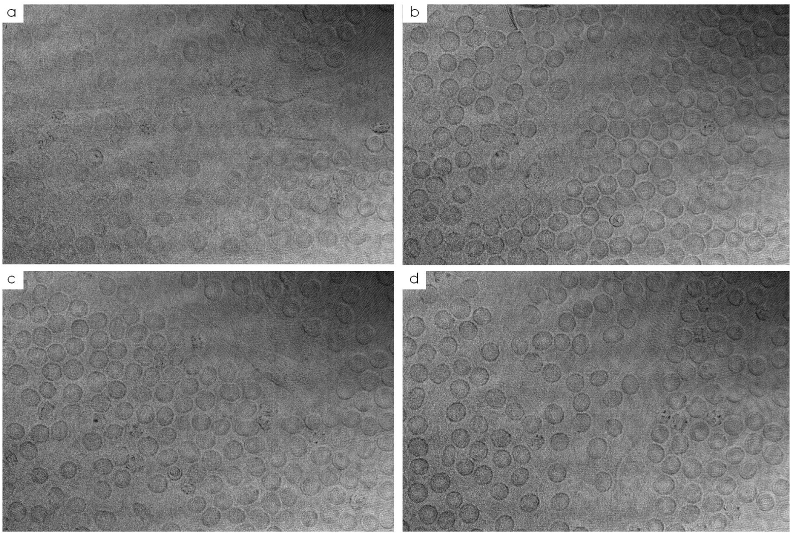

FIGURE 2.8: Amplitude DH reconstructions, $\left|C^{+1}\left(x_R, y_R, d\right)\right|$, of the holograms shown in Fig. 2.5.

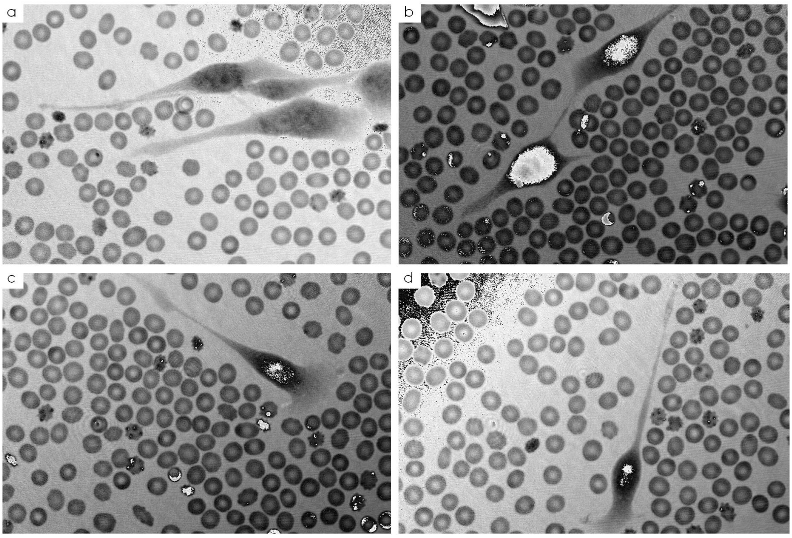

FIGURE 2.9: Wrapped phase reconstructions, $\Psi(x_R, y_R, d)$, of the holograms shown in Fig. 2.5.

as the phase unwrapping problem [146], and many algorithms exist, which are not discussed here, to extract the phase distribution. Once the signal Ψ is unwrapped, the aberration terms have to be estimated by polynomial fitting procedures and compensated to yield an estimate of the sample phase-contrast map, $\hat{\varphi}\left(x_R, y_R, d\right)$. In alternative, a reference hologram can be acquired in absence of the sample, and reconstructed to get the complex matrix $C_{Ref}\left(x_R, y_R, d\right)$, carrying information about the aberrations of the optical system. Hence, the phase reconstruction formula can be written as:

$$\hat{\varphi}\left(x_R, y_R, d\right) = Unwrap\left\{Angle\left[\frac{C^{+1}\left(x_R, y_R, d\right)}{C^{+1}_{Ref}\left(x_R, y_R, d\right)}\right]\right\}, \tag{2.46}$$

where $Angle\{\ldots\}$ and $Unwrap\{\ldots\}$ respectively extract and unwrap the phase distribution. Figures 2.10(a-d) show the unwrapped phase signals of the holograms shown in Fig. 2.5 after unwrapping and aberration compensation. Pseudo-3D views of the unwrapped phase-contrast maps of Fig. 2.10 are shown in Fig. 2.11. Finally, the spatial distribution of the sample optical thickness is given by

$$O_T\left(x_R, y_R\right) = \Delta n\left(x_R, y_R\right) P_T\left(x_R, y_R\right) = \frac{\lambda}{2\pi}\hat{\varphi}\left(x_R, y_R\right), \tag{2.47}$$

where P_T is the physical thickness of the object, while Δn indicates the refractive index difference between the sample and the surrounding medium.

As further examples of the DH reconstruction steps described in this Chapter, holograms of C-elegans samples, i.e. complex objects with an inner structure more stratified and complex than the RBCs and fibroblasts, have been acquired and reconstructed. Figure 2.12 resumes the main processing steps required to reconstruct the DH of a C-elegans embryo. In particular, Figs 2.12(a,b) respectively report the recorded hologram of the sample, H_S, and its amplitude Fourier spectrum, $|\mathcal{FFT}\{H_S\}|$, while Figs. 2.12(c-e) respectively show the reconstructed amplitude, $\left|C^{+1}\left(x_R, y_R, d\right)\right|$, wrapped phase, $\Psi\left(x_R, y_R, d\right)$, and unwrapped phase-contrast map, -$\hat{\varphi}\left(x_R, y_R, d\right)$.

Similarly, Fig. 2.13 shows the DH reconstruction of two embryos, where only the external shell of one of them (the sample on the left of the image) is imaged in focus. In order to show the possibility to analyze live samples, we recorded holograms of a C-elegans in L1 stage. Due to the typical size of this sample, it is often very difficult to image this entirely with high magnification, even though the L1 is the first stage after the embryo has disclosed, corresponding to the minimum size for this specimen. In Chapter 4, a method to overcome this limitation will be introduced. The reconstructions of the L1 DHs, corresponding to three different time instants of the recorded hologram

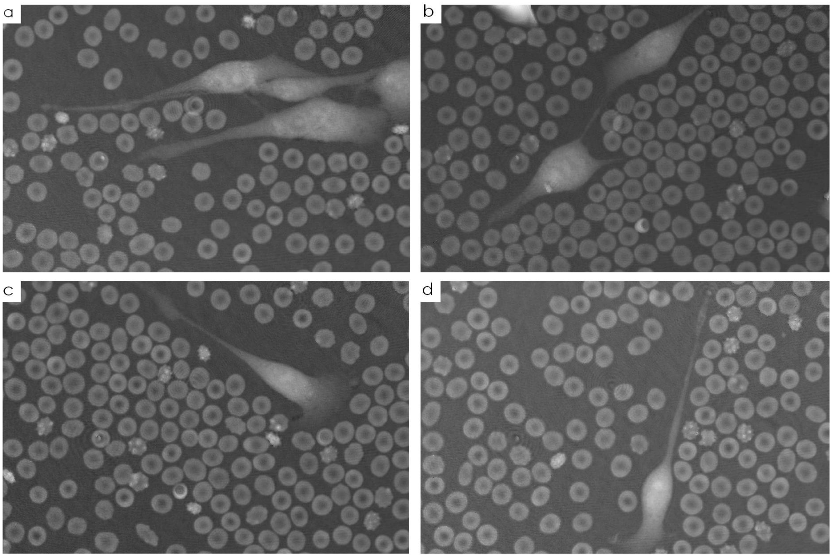

FIGURE 2.10: Unwrapped phase-contrast maps, $\hat{\varphi}(x_R, y_R, d)$, of the holograms shown in Fig. 2.5.

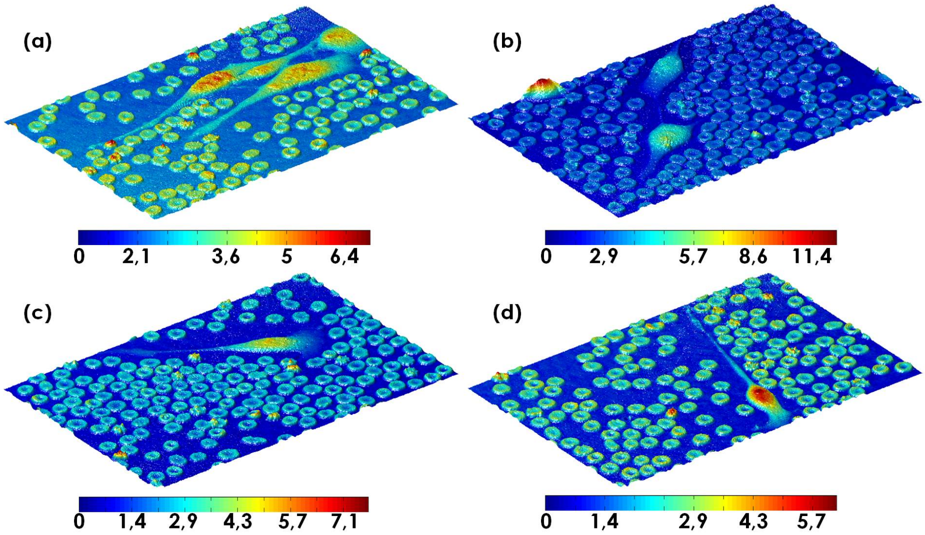

FIGURE 2.11: Pseudo-3D views of the unwrapped phase-contrast maps, $\hat{\varphi}(x_R, y_R, d)$, shown in Fig. 2.10. The phase values are expressed in radians.

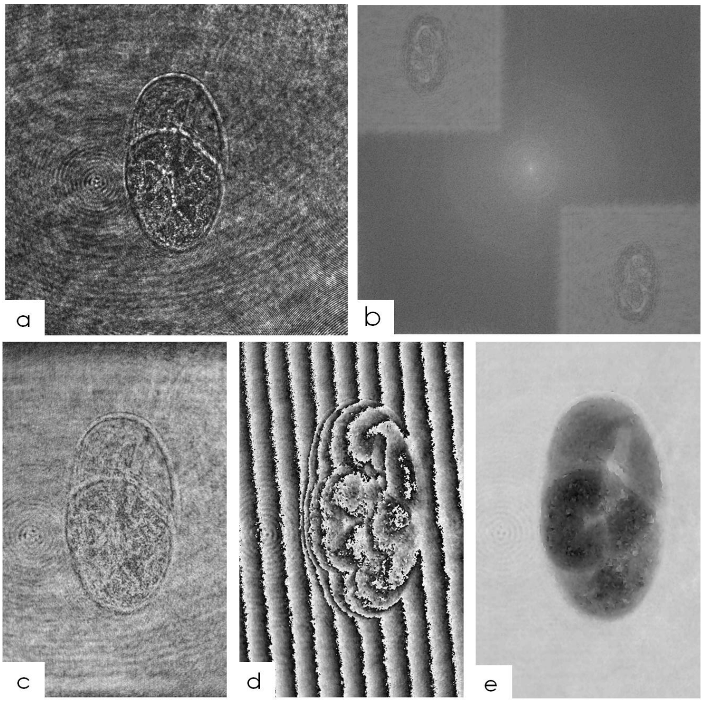

FIGURE 2.12: An overview of all the DH reconstruction steps in the case of a C-elegans embryo. (a) Hologram, H_S. (b) Amplitude Fourier spectrum, $|\mathcal{FFT}\{H_S\}|$. (c) Amplitude reconstruction, $\left|C^{+1}\left(x_R, y_R, d\right)\right|$. (d) Wrapped phase reconstruction, $\Psi\left(x_R, y_R, d\right)$. (e) Unwrapped phase-contrast map (inverted colors), $-\hat{\varphi}\left(x_R, y_R, d\right)$.

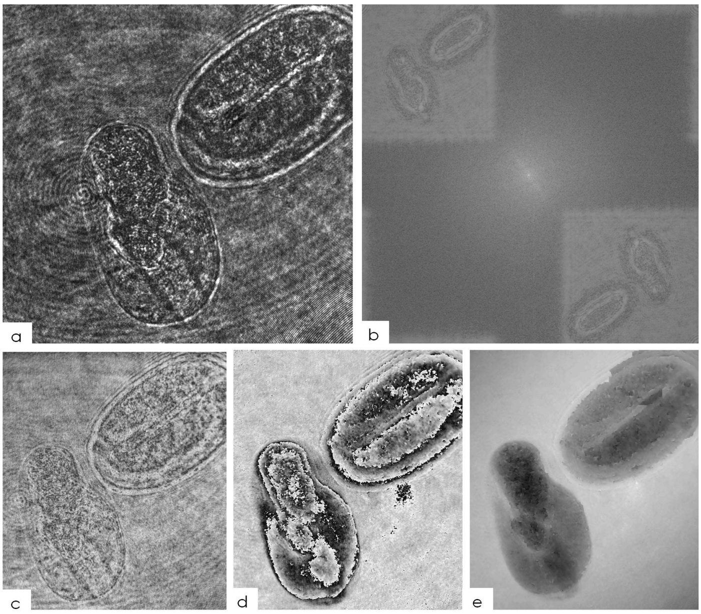

FIGURE 2.13: An overview of all the DH reconstruction steps in the case of two C-elegans embryos. (a) Hologram, H_S. (b) Amplitude Fourier spectrum, $|\mathcal{FFT}\{H_S\}|$. (c) Amplitude reconstruction, $\left|C^{+1}\left(x_R, y_R, d\right)\right|$. (d) Wrapped phase reconstruction, $\Psi\left(x_R, y_R, d\right)$. (e) Unwrapped phase-contrast map (inverted colors), $-\hat{\varphi}\left(x_R, y_R, d\right)$.

time sequence, are reported in Fig. 2.14. The holograms, H_S , are shown in Fig. 2.14(a), while Figs. 2.14(b-d) respectively report the signals $\left|C^{+1}\left(x_R, y_R, d\right)\right|$, $\Psi\left(x_R, y_R, d\right)$, and $\hat{\varphi}\left(x_R, y_R, d\right)$. Once the phase-contrast maps are extracted, further post-processing techniques can be applied to reduce the residual noise or to enhance the contrast. A final example is shown in Figs. 2.15(a-h), where enhanced quality (post-processed) phase-contrast maps of live C-elegans embryos and adult samples are reported.

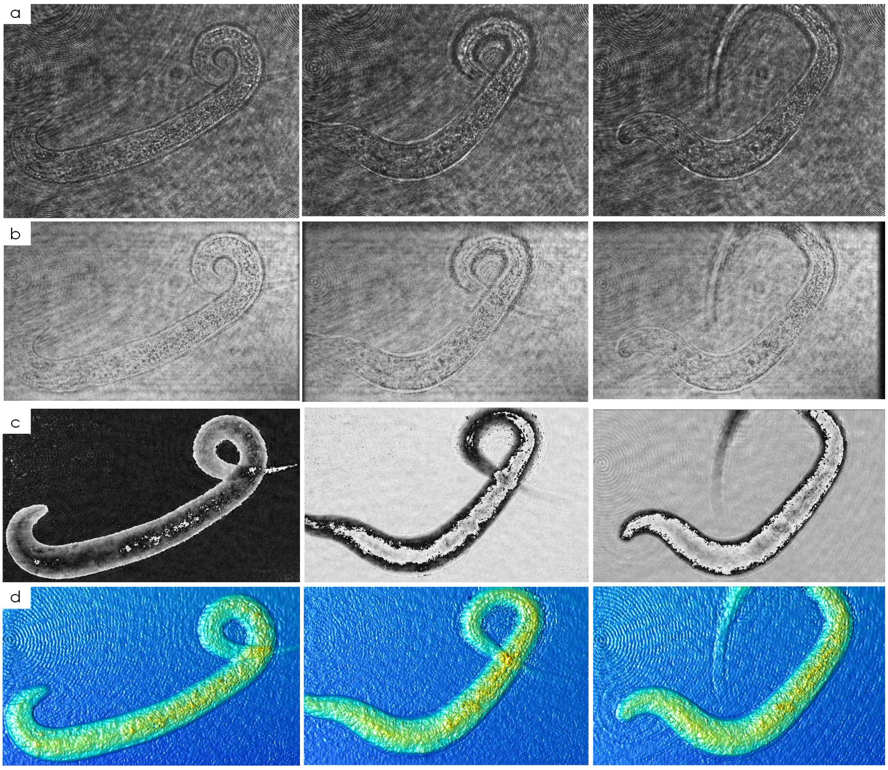

FIGURE 2.14: An overview of all the DH reconstruction steps in the case of a live C-elegans specimen (L1 adult stage), recorded at three different time instants. (a) Holograms, H_S. (b) Amplitude reconstructions, $\left|C^{+1}\left(x_R, y_R, d\right)\right|$. (c) Wrapped phase reconstructions, $\Psi\left(x_R, y_R, d\right)$. (d) Unwrapped phase-contrast map, $\hat{\varphi}\left(x_R, y_R, d\right)$.

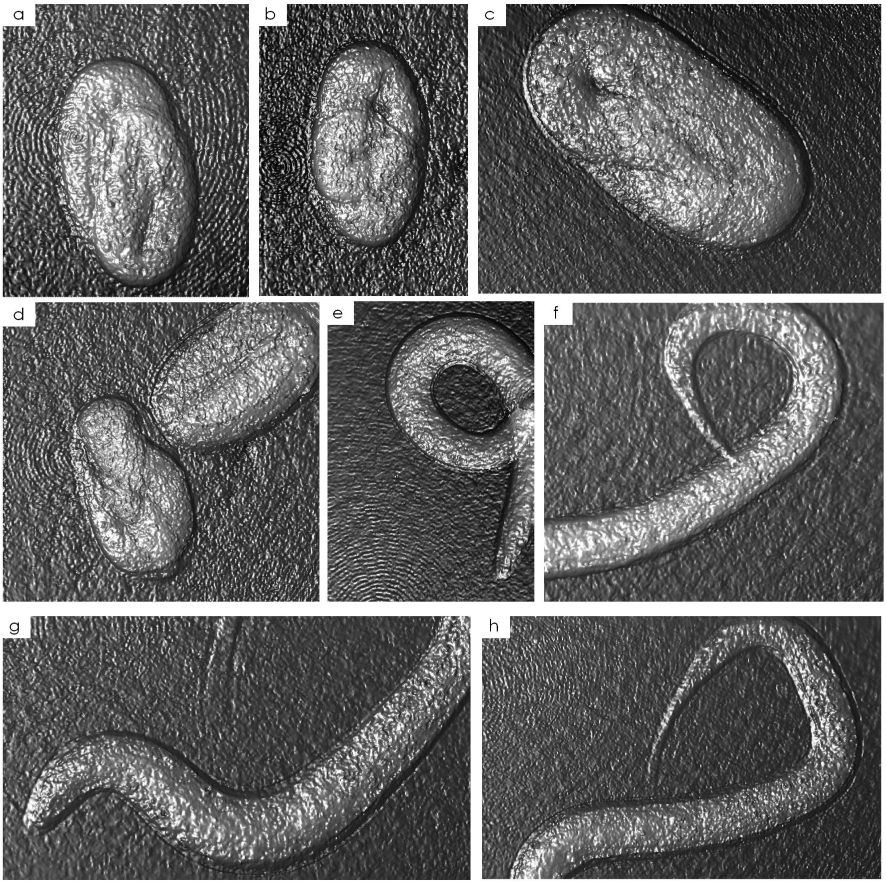

Figure 2.15: Post-processed phase-contrast maps of live C-elegans embryos (a-d) and L1 stage adult samples (e-h).

3

DH MICROSCOPY THROUGH COMPLEX MEDIA

IMAGING through complex media is a challenging and fascinating topic. At first sight, wavefront control and image formation would seem to be practicable only when the beam path is simple and easily predictable by deterministic models. Strongly scattering environments pose a binding constraint to the capability of exploiting beam propagation in our daily life applications. In the framework of wireless communications, there is a major need to cover wide areas with enough powerful signal, and to realize controlled multiple access to the network by several users located at different access points. Hence, the presence of a complex urban environment, or multiple walls in the case of indoor communications, severely affects the quality of the received signal, and the multipath fading issue has to be coped with [147]. In these cases, the free-space propagation model does not stand, and the received signal is the coherent superposition of multiple contributions, namely multiple replicas, of the useful undistorted signal. Each replica experiences a different attenuation due to the surfaces met in its own path, and undergoes a different phase delay. Therefore, the channel where the signal propagates cannot be treated anymore as a Linear Time Invariant (LTI) system and more complex stochastic models have to be considered. Similarly, spaceborne remote sensing, and radiofrequency communications can be adversely affected by atmosphere conditions or obstacles to the wavefront path [148]. In underwater environment, acoustic communications and imaging are severely impaired by turbidity [147]. In Optics, imaging through scattering layers is severely degraded due to diffusion processes and in many cases this is completely hindered [149,150]. In microfluidics, the presence of a turbid liquid volume can completely undermine optical imaging.

However, in recent years it has become more and more apparent that the information transmitted through complex media is not necessary lost but, rather, this is scrambled. In some cases, there is a hope to recover this information by reversing the effects of scattering [147,149,150]. Many efforts have been spent to find reliable methods offering a clear vision through complex media. The range of application of such novel capability is enormously wide, going from homeland security to biological tissue analysis. Imaging through fog or smoke is crucial in all fields of safe transportation as well as in the detection and continuous monitoring of people involved in dangerous situations like, e.g., in the case of fires, where a clear vision by conventional optics is hindered [118,119]. Imaging through tissues is an ongoing research field in biology and medicine, being essential for a deeper understanding of complex biological systems and for diagnostic purposes. Many research groups have been recently very active in the field of information recovery through scattering layers [149,150,151-158]. Two of the most important novelties in this field will be resumed in Section 3.1.1 and Section 3.1.2.

Moving the focus on microfluidics, current imaging methods work only if the liquid filling the chip is transparent, greatly limiting its use. When a turbid liquid flows inside the channel, clear imaging of the processes occurring inside the chip is impaired and the corresponding information gets lost. A liquid is considered turbid when dispersed particles provoke strong light scattering, thus destroying the image formation by any standard optical system. Generally, colloidal solutions belong to the class of turbid media since dispersed particles have dimensions ranging between 200nm to a few microns and interact with light as scatterers, impairing any image formation. Furthermore, media that start off clear, often get turbid because of the chemical reactions that occur during the process. Since in most cases turbidity in LoC environment is due to dynamic or quasi-static media, this provokes time variable scattering events, wavefront distortions, and unpredicible, random, phase delays. Moreover, in microfluidic experiments another annoying problem can occur whenever a transparent medium flows inside a channel. In some cases, the flowing liquid can deteriorate the channel walls making them rough or scattering [159,160]. Sometimes, the inherent fabrication process of the chip produces a scattering surface at one of the channel walls, thus preventing imaging in through transmission. It is also usual that residuals of chemical reactions occurring inside the chip settle down the inner channel faces. At the same time, the particle uptake by the channel cladding or its damaging due to corrosive substances could unavoidably degrade the LoC. More frequently, a simple deposit due to sedimentation of colloids dispersed in the liquid could make the channel internal walls acting as scattering surfaces. Even a vapor condensation can occur on the external channel faces as a function of humidity and temperatures. An impairing factor for the imaging capabilities in microfluidic devices is the presence of bio-films, typically made of bacteria, in which groups of microorganisms stick to each other creating a scattering surface [160-164]. Such degradations can occur while the channel is under observation, so that the microfluidic chip cannot be simply replaced. In all these cases, such observations cannot be performed at all, impairing the monitoring of phenomena developing over long time periods. This strongly limits the variety of tests which can be performed in microfluidic platforms.

As it will be discussed in the following, in the case of stationary layers, the scattering problem can be tackled whenever the transmission matrix of the layer can be characterized [150,154]. This approach could be applied to tackle the problem of imaging through scattering channel walls whenever direct access to the layer in absence of the object is allowed. In Section 3.1.3 a simpler approach to afford some practical situations in LoC imaging will be described [158]. However, in the case of turbid liquids, even if quasi-static, the transmission matrix is not available at all, because the way the medium acts on light propagation rapidly varies in time. Therefore, all these strategies cannot be applied to restore clear imaging in turbid LoCs.

Nevertheless, in this Chapter we will show that LoC imaging of biological samples through turbid microfluidics can be made possible in a number of practical cases adopting a modified DH microscopy strategy. We believe that the number of different uses of LoC platforms for cell studies will be greatly increased adding the new capability of microfluidic microscopy through turbid media [115,158,165-169]. In particular, we will afford some practical cases in LoC microscopy where clear imaging is impaired by conventional optics and different solutions based on variations of the DH technique can be provided. First, we will focus on DH microscopy through scattering microfluidic channels for the recovery of information from suspended samples [158]. Then, the problem of imaging through different kinds of turbid colloidal solutions will be investigated [115,165-169]. In particular, label-free quantitative imaging of adherent cells through blood, a particularly interesting type of colloid, will be proved [168]. Noteworthy, it will be demonstrated that the presence of a turbid medium, generally considered as an impairment, can also have a positive effect, improving the performance of a coherent imaging system. In other words, DH can benefit from the presence of a liquid volume filled with RBCs, providing enhancement in terms of numerical resolution and noise suppression, thus obtaining images whose quality is higher than the quality achievable in the case of a liquid without occlusive objects [168].

IMAGING THROUGH STATIC SCATTERING LAYERS

In this Section, we resume two of the most effective approaches, recently introduced in literature, to cope with the problem of imaging objects hidden behind strongly scattering layers. In particular, in Section 3.1.1 we will describe the

Turbid Lens Imaging (TLI) method [150,154,170,171], while Section 3.1.2 will be devoted to describe a novel strategy based on the speckle autocorrelation properties [149,151]. Both these approaches have been shown to be very effective and promising for applications in biology and medicine as new diagnostic tools for tissue and through-tissue analysis. In the following, their strengths and weaknesses will be underlined, with reference to the issues tackles in this work. Finally, the proposed approach to allow information recovery through scattering microfluidic channels will be presented in Section 3.1.3 [158].

Turbid Lens Imaging (TLI)

One of the smartest approaches to cope with the scattering issue is the TLI [150,154,170,171]. In TLI, the presence of a scattering layer in between the object and the recording device is not treated as an obstacle, but the complex medium is exploited as an useful optical element enhancing the performance of the imaging system. Indeed, multiple scattering processes inside the complex medium can redirect the highest object frequencies inside the numerical aperture of the recording system. In absence of turbidity, such spatial frequency components would be unavoidably lost. Hence, in principle a scattering layer can be used to improve the image resolution as well as the FoV [150,171]. In order to achieve a gain from turbidity, the object image has to be recovered from the scrambled information. TLI starts from the principle that the wavefront distortion due to scattering from a static layer is a deterministic process that can be inverted once the Transmission Matrix (TM) of the medium is known [170]. In particular, when a plane wave impinges on an object, the complex object image at the object plane can be written in terms of the coherent superposition of multiple plane waves with different propagation angles, modulated by the angular spectrum of the object image, i.e. by a distribution of complex coefficients multiplying each plane wave [150]. When this wavefront enters the complex medium, every plane waves, independently of each other, experience multiple scattering events depending on their path inside it. However, at the exit the complex coefficient distribution between these waves (i.e. the angular spectrum) remains unaltered, due to the linear response of the medium. In other words, it is possible to write the distorted image as a coherent superposition of distorted plane waves governed by the angular spectrum distribution. The set of distorted plane waves at the image plane is the TM stack [170], describing the input-output relationship typical of the complex, scattering medium. Thus, in order to obtain the original object in the image plane, the angular spectrum has to be estimated from the received signal. This can be done by projecting, for each angular frequency of the spectrum, the corresponding matrix of the TM stack onto the received distorted image. If the elements of the TM stack are orthogonal [170,171], each projection provides the measured angular spectrum at the corresponding couple of angular frequencies. Once the angular spectrum is completely measured, the object wavefront is trivially obtained [150]. Therefore, it becomes clear that the TLI approach is based on the possibility to measure the TM stack. This can be performed by sending plane waves with different propagation angles toward the scattering medium in absence of the object. Each plane wave is transformed by the medium TM and the resulting received signal constitutes one element of the measured TM stack. After covering all the angular range, the TM stack is fully characterized and can be used to invert the turbid medium effect. Although very effective, the TLI approach requires the access to the medium in absence of the object, multiple measures need to be carried out to fully characterize the TM stack. This can be often a complex procedure, unfeasible in many practical cases. Moreover, it is required that the medium keeps stationary during the whole recording process, preventing the use of TLI in the case of imaging through turbid liquids, i.e. when the TM cannot be characterized. Nevertheless, TLI has recently found remarkable applications in endoscopic imaging, where the TLI procedure is applied to optical fibers used in a DH reflection configuration [150]. In other words, the fiber is used both to illuminate the sample area and to receive the reflected signal. The fiber is well-known to be a complex, dispersive medium, scrambling the signal reflected from the object. However, once this is fully characterized, the scrambled information can be recovered, thus showing interesting perspectives in DH endoscopic inspection of blood vessels and tissue analysis for biomedical studies.

An approach based on the speckle memory effect

A different approach to see through a severely scattering layer was proposed by A. Mosk's research group [149,151]. Instead of trying to suppress speckle artifacts in coherent imaging systems, the features of the speckles can be fruitfully exploited to recover clear imaging through an obstacle. In a recently published work, fluorescence imaging through an opaque layer was achieved exploiting the so called memory effect of the speckle [136,172]. In particular, this approach is aimed at using the speckle correlation to transmit information through the layer. The object is placed behind the opaque medium, which is illuminated by a coherent laser beam. Due to the diffusion process operated by the layer, the object is reached by a diffused speckle pattern and fluorescence excitation is promoted. However, the fluorescence signal emitted by the object, after passing through the opaque medium is severely scrambled and reaches the detector in the form of a speckle pattern where the object spatial distribution is not recognizable at all. Although the distribution of speckle spots could appear to be random, this contains enough correlation that can be usefully exploited. In particular, a small change in the illumination angle only results in a shift of the resulting speckle pattern of a known extent. In other words, the speckle pattern remains unchanged (i.e. it keeps memory) for small angular steps. Hence, multiple measure are carried out slightly changing the illumination angle, and the total received fluorescence intensity, thought as a function of the angle, is integrated [151]. This turns out to be a convolution product between the object fluorescence signal and the speckle intensity. In order to separate the object from the speckle, the autocorrelation product of the measured intensity is calculated, which can be written as the convolution product between the object autocorrelation and the autocorrelation of the speckle pattern. Since, the latter is known to be an impulsive function, the measured autocorrelation signal provides the object autocorrelation with a resolution imposed by the average speckle size [136,151]. The last step is aimed to estimate the object starting from its autocorrelation function. This can be done using iterative approaches, e.g. based on the Gerchberg-Saxton algorithm [70-72]. Referring to the iterative approaches discussed in Section 1.3.3, an object retrieval algorithm based on one intensity measure and proper constraint can be adopted. In the case of fluorescence imaging through an opaque layer, the fact that the object image has to be real and positive can be used as a constraint. In this way the hidden object can be recovered despite scattering. This work was a groundbreaking novelty in this field, as it potentially allows to get information of biological samples seen through tissues, thus paving the way to important innovations in biology and medicine. Differently from TLI, direct access to the medium in absence of the sample is not required, as the layer does not need to be fully characterized. However, multiple measures have to be performed, preventing to adopt the method for imaging moving samples through the opaque layer, or imaging stationary objects through a moving complex medium.

Coherent imaging through scattering microfluidic channels

In this section we investigate the issue of recovering by DH qualitative and quantitative information about specimens flowing inside severe scattering microfluidic channels. The diffusion process can be due to residual deposits resulting from chemical reactions inside the chip and settling down the inner

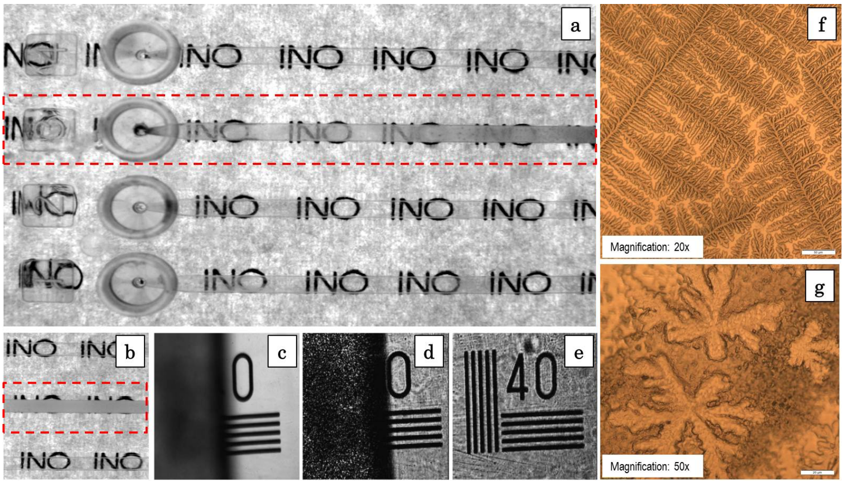

FIGURE 3.1: Imaging through scattering microfluidics [158]. (a) White-light image of a microfluidic chip with four channels. A salt deposit is settled only in the second channel (red dashed box), with opacity increasing from left to right. (b) White-light view of a different portion of the chip, with the maximum layer thickness. (c-d) Only the left part of a test target is placed behind a scattering channel imaged respectively by (c) white-light microscopy and (d) coherent laser microscopy at $\lambda = 632,8\,\mu m$. (e) Coherent laser microscopy of the target in absence of the scattering layer. (f-g) White-light images of the salt deposit inside the chip obtained with (f) 20x and (g) 50x magnification.

channel faces during the observation period, salt depositions or bio-film formation. As a consequence, a severe scattering layer will appear onto the internal or external channels walls, thus impairing the vision by any white-light or coherent laser source based microscope. An example is reported in Fig. 3.1, where white-light and optical images of a microfluidic chip with four channels is shown. In particular, in Fig. 3.1(a) the channel in the red dashed box, after usage experienced residual deposit of salts thus creating diffusing elements [158]. As it can be clearly observed, the scattering density of the inner channel walls increases from left to right, starting from the inlet port. Therefore, the visibility through the channel decreases accordingly and any object behind the channel or flowing along it cannot be clearly imaged, or it is completely occluded. A challenging situation is shown in Fig. 3.1(b), where we reported the white-light view of a different portion of the chip (red dashed box in Fig. 3.1(b)). Indeed, in figure the scattering is so severe that visibility is completely lost thus making impossible to retrieve any information of what occurs inside the microfluidic channel. For instance, PIV analysis and cell counting [173,174], as well as the recovery of morphologically relevant parameters of the flowing particles cannot be achieved. With the aim to illustrate better the reduced visibility effect, we placed a test resolution chart target behind and across the channel of Fig. 3.1(b). Figures 3.1(c,d) show that only the left part of the target is visible, that is outside the scattering area when imaged respectively with white-light and coherent laser light at $\lambda = 632,8\mu m$. Again, the image degradation introduced due to the scattering layer is apparent and no information can be drawn about the test target, whose microscopy image obtained by a coherent laser source is shown in Fig. 3.1(e). In Fig. 3.1(f) and Fig. 3.1(g) we show two images of the deposit layer acquired by an optical microscope with two different magnifications. Typically, such degradations could occur after the first usages of the chip, or even during a single process, and often force to use the same chip just once and for a limited amount of time, impairing a clear monitoring of slow processes.

In this section we investigate the problem of information recovery from microscopic cells flowing inside a rough scattering channel where a clear vision is impaired if the mere conventional optics are employed. More specifically, we show here that by DH microscopy it is possible to detect, count and measure the speed of flowing cells and at same time to recover their intensity and phase-contrast maps, despite the harsh scattering effect in the inner channel walls. In Section 3.1.3 we propose a model to account for the presence of the scattering layer at the channel wall and its effect in holographic reconstructions. Then, we show how the intrinsic features of the holographic method can be exploited to obtain good visualization, detection and the velocity measurement of target cells which would be, otherwise, not recognizable at all by white-light microscopy. Imaging experiments have been carried out in both clear and scattering channels and the results of the proposed processing are shown in Section 3.1.3.

Working principle

The proposed model mainly treats the effect of the undesired scattered radiation as a speckle noise [166]. Many approaches were suggested in literature to reduce the speckle in coherent imaging systems, mostly relying on spatial filtering of a single image [137,138,175], or averaging multiple DH reconstructions acquired in time-diversity. Here we exploit the diversity provided by the cell movement with respect to the scattering surface, with the aim to select a set of holograms in which the speckle patterns are uncorrelated. During the sample motion, different portions of scattering channel contributes to the random interference process on the detector and, after a proper matching of the holographic reconstructions, the proposed processing is nothing else than a temporal integration providing a significant improvement in the final recovered image. Differently from the work by *Bertolotti et al.* no ad hoc set-up is required to obtain the temporal diversity [151] but the time sequence is recorded while the cell flows inside the field of view of the recording device and the scattering process itself offers the solution. If samples flowing inside scattering LoCs are imaged by means of DH microscopy, the hologram recorded at time t can be expressed as

$$\begin{aligned}
&\tilde{H}_N(x',y',t) = \left|D_0(x',y',t)\right|\left|Ch(x',y',t)\right| + 2a_R\left|O(x',y',t)\right|\left|Ch(x',y',t)\right| \cdot \\
&\cdot \cos\left\{2\pi(u_R x' + v_R y') + \Gamma(x',y') - \varphi(x',y',t) + n_S(x',y',t) + n_{Ch}(x',y',t)\right\} + \\
&+ n_G(x',y',t) + n_{A,Ch}(x',y') = \tilde{D}_0(x',y',t) + \tilde{H}_N^{+1,-1}(x',y',t) + \\
&+ n_G(x',y',t) + n_{A,Ch}(x',y'),
\end{aligned} \tag{3.1}$$

where we denoted with $\tilde{H}_N^{+1,-1}$ the noisy and distorted component of the hologram including both the +1 and the -1 order of diffraction. In Eq. (3.1), the channel scattering is modeled introducing the presence of a complex noise term, $Ch\,(x',y',t)$, which is correlated to the useful signal and varies during the recording period due to the cell motion. Moreover, we indicated with $n_{A,Ch}\,(x',y')$ the incoherent additive scattering contribution due to the turbid channel. Noteworthy, this is static during the acquisition period as it only extends over the background area of the field of view. In case of continuous particles sedimentation (or bio-film growth), we can also foresee the presence of a time-dependent scattering contribution, i.e. we can divide $n_{A,Ch}\,(x',y')$ into two portions, one of them being time-variable. However, in the most of the cases of interest the deposition process is greatly slower than the cell movement so that we can assume this contribution as static during the cell passage inside the field of view. After hologram refocusing at distance d and extraction of the order of interest, due to the linearity of the Fresnel transform we obtain the Single-Look (SL) image [158]:

$$\begin{aligned}
C_{SL}(x_R, y_R, t; d) &= \mathfrak{F}r\Big\{\tilde{H}_N\,(x',y',t)\,;d\Big\} \approx \\
&\approx \mathfrak{F}r\left\{\tilde{H}_N^{+1}\,(x',y',t)\,;d\right\} + \mathfrak{F}r\Big\{n_{A,Ch}\,(x',y')\Big\},
\end{aligned} \tag{3.2}$$

where we neglected the additive Gaussian noise for the sake of clarity. In fact, in our case the degradation introduced by n_G is much weaker than the degradation due to the channel scattering, $n_{A,Ch}$. However, some algorithms exist, specifically designed for digital holography, which suppress efficiently the

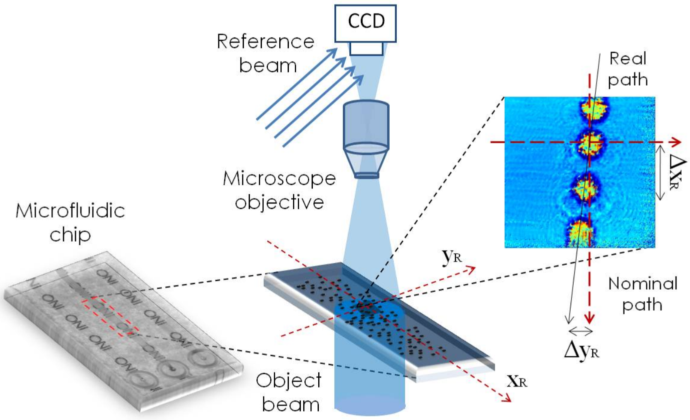

FIGURE 3.2: Sketch of the experimental set-up [158]. On the right side of the image a phase contrast map is shown of the cell flowing through the scattering channel along the x nominal direction.

Gaussian noise, so that a further improvement can be provided if it is necessary [138,139]. In such a case, after suppressing the Gaussian noise, the Eq. (3.2) would not be an approximation anymore. Thanks to the coherence of the laser source employed in DH it is trivial to compensate $\mathcal{F}r\{n_{A,Ch}(x',y')\}$ in Eq. (3.2) by recording and reconstructing a reference hologram. In fact, this problem can be handled as the typical compensation of the lens aberrations in holographic interferometry [176]. This constitute the first intrinsic advantage of DH with respect to the mere white-light microscopy. Hence, the detection of the specimens behind the scattering layer is achievable, e.g. for cell counting purposes, and measurements of the cell velocity can be performed as well. Unfortunately, in the target area the point-to-point relationship between the hologram of interest and the reference one is lost due to the presence of the cell (whose extent depends on the cell refractive index), acting as a sort of lens, so that the correlated channel noise results to be time variant and cannot be extracted from the former term of Eq. (3.2). As Eq. (3.1) suggests, this can be handled as a speckle multiplicative noise combined to the useful signal, and a numerical processing is required to improve the image quality. Hence, in order to reduce the speckle, a time sequence of N holograms can be reconstructed, which are acquired while the sample cell flows through the turbid channel, as sketched in Fig. 3.2. While the cell moves inside the camera field of view, different portions of the turbid channel are responsible for the disturbing scattering and each hologram records a different speckle pattern in the target area.

Thus, if properly co-registered, the incoherent combination of their reconstructions returns a Multi-Look (ML) image with improved quality. In particular, the first image of the time sequence can be selected as a master (herein denoted with the subscript $\mathcal{M}$), acquired at time $t = T_0$, and $N - 1$ slave images can be shifted along the two spatial coordinates in order to match the master image. For each slave image (herein denoted with the subscript $\mathcal{S}$) the shifts $[\Delta\hat{x}_R, \Delta\hat{y}_R]$ are estimated in order to maximize a correlation coefficient $\rho(\Delta x_R, \Delta y_R)$, i.e.

$$\begin{aligned}
\hat{\boldsymbol{\Delta}} &= [\Delta\hat{x}_R, \Delta\hat{y}_R] = \underset{\Delta x_R, \Delta y_R}{\mathrm{argmax}}\{\rho(\Delta x_R, \Delta y_R)\} = \\
&= \underset{\Delta x_R, \Delta y_R}{\mathrm{argmax}}\left\{\frac{E\langle \bar{C}_{SL,\mathcal{M}}(x_R, y_R, t{=}T_0) \odot [\bar{C}_{SL,\mathcal{S}}(x_R, y_R, t) \otimes \delta(x_R{+}\Delta x_R, y_R{-}\Delta y_R)]\rangle}{\sqrt{E\langle|\bar{C}_{SL,\mathcal{M}}(x_R, y_R, t{=}T_0)|^2\rangle E\langle|\bar{C}_{SL,\mathcal{S}}(x_R, y_R, t) \otimes \delta(x_R{+}\Delta x_R, y_R{-}\Delta y_R)|^2\rangle}}\right\}
\end{aligned} \tag{3.3}$$

where $\odot$ denotes the Hadamard product, $E\langle\ldots\rangle$ indicates the expectation operator, and

$$\bar{C} = |C_{SL}| - |\mathcal{F}r\{n_{A,Ch}\}| \approx \left|\mathcal{F}r\left\{\tilde{H}_N^{+1}\right\}\right| \tag{3.4}$$

constitutes (due to the triangular inequality) an underestimated measure of $\left|\mathcal{F}r\left\{\tilde{H}_N^{+1}\right\}\right|$. Once the vector $\boldsymbol{\Delta}$ is estimated, the SL amplitude images and the SL phase-contrast maps can be shifted and separately (i.e. incoherently) averaged to get the matrices I_{ML} and Ψ_{ML}, respectively being the ML amplitude and phase-contrast maps:

$$\begin{aligned}
I_{ML}(x_R, y_R; d) &= \frac{1}{N}\sum_{n=1}^{N}[\hat{C}_R(x_R, y_R) \otimes \delta(x_R - \Delta x_{R,n}, y_R - \Delta y_{R,n})] \\
\Psi_{ML}(x_R, y_R; d) &= \frac{1}{N}\sum_{n=1}^{N}[\hat{\Psi}_R(x_R, y_R) \otimes \delta(x_R - \Delta x_{R,n}, y_R - \Delta y_{R,n})]
\end{aligned} \tag{3.5}$$

where we denoted with $\bar{\Psi}_n$ the n-th SL phase image obtained after subtracting the reference hologram and, if necessary, after applying the phase unwrapping algorithm.

Experiments

In our experiments, we let fibroblast cells (line NIH-3T3) in DMEM (Dulbecco's modified eagle medium) cell cultivation medium flow along straight microfluidic channels 200 µm thick. This is a case in which white-light microscopy performs well as no scattering layers obstacle the wavefront propagation. Then, the same experiment was repeated after drying the cell cultivation medium inside the channel, whose effect is the presence of a rough layer, similarly to what is shown in Fig.3.1. In order to test the DH capability of extracting information related to the specimen we employed in our experiments a classical Mach-Zehnder interferometer and we acquired a time sequence of the sample cell flowing through the channel along a straight trajectory inside the camera field of view (nominal path in the sketch of Fig. 3.2), so that we can assume that the main flow direction is parallel to the x_R axis. Here the nominal path coincides with the longer channel dimension (i.e. the x_R axis). However, the following analysis can be extended to the case of particles flowing along a nominal trajectory rotated of a certain angle with respect to the x_R axis. Possible displacements in the y_R direction can be recovered as in Eq. (3.3) and rotations of the cells can be compensated as well. Again, possible displacements along the optical axis direction can be compensated taking advantage of DH autofocusing and 3D tracking techniques [179]. In the case of clear channel, the sole noise contributions inherently due to the acquisition system can be contemplated. Figure 3.3 shows a typical phase-contrast map of the suspended fibroblast achievable in this situation. The circular cell shape is clearly imaged and it is possible to measure a maximum phase dynamic approaching 4.4rad.

In case of scattering channel, DH allows the rapid detection of the flowing cells simply defining inside the field of view of the optical system a detection gate, i.e. an ensemble of neighboring rows where to perform a spatial average, and a threshold for counting purposes. Moreover, a first-cut measure of the cell average velocity is obtainable by selecting a set of average windows displaced at uniform distance along the nominal cell path (the average is performed in order to make the measure less sensitive to the channel noise). While the cell flows along the channel, the derivative of the average phase-contrast, Ψ_{ML}, exhibits a spiky behavior with time, as plotted in Fig. 3.4, where an example of velocity measure employing four gates is shown.

We selected N_G gates where we measured the average phase derivative, from which we estimated the average cell velocity as

$$\hat{v}_x = \frac{1}{N_G - 1} \sum_{i \neq j} \frac{D_{i,j}}{\Delta T_{i,j}} \tag{3.6}$$

where $D_{i,j}$ represents the distance between the gate i and the gate j, which is a function of the pixel size, $\Delta T_{i,j}$ are the time intervals in which the cell moves between the gates i and j, measured on the leading edge of the phase derivative signals (see Fig. 3.4), and the average is performed over a number of gate combinations given by $N_G - 1$. Indeed, after the cell detection the po-

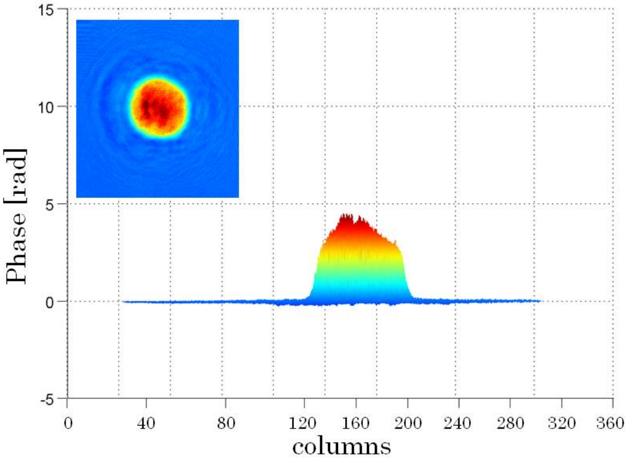

Figure 3.3: Phase-contrast mapping of a sample cell flowing into a clear microfluidic channel. In the inset the top view is shown [158].

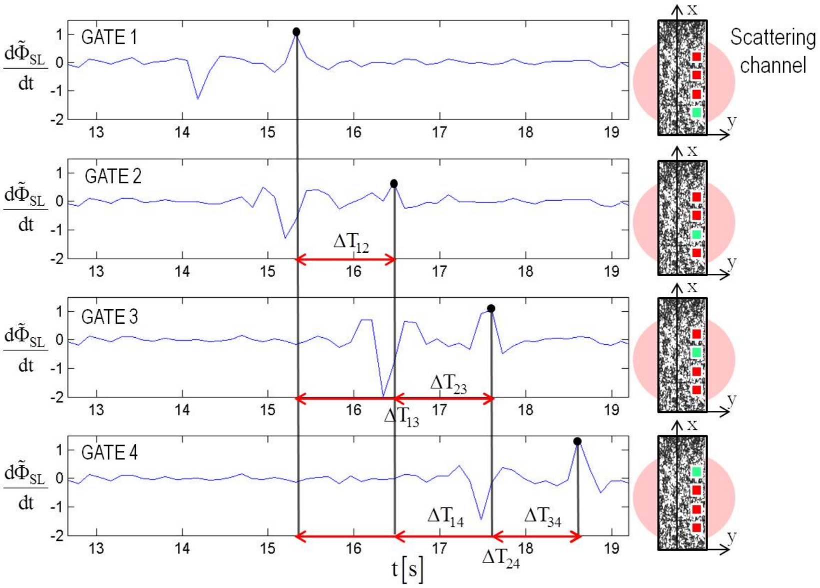

Figure 3.4: Derivative of the average phase-contrast vs. time. An example of mean velocity estimation employing four gates is shown. On the right the scattering channel is sketched showing in green, for each plot, the window where the average is performed [158].

sitions where to place the detection windows are determined, and their size affects the accuracy of the measure. We found that a window size of 5 pixels is a good compromise between noise mitigation and accuracy of the measure. Thus, we performed $N_G - 1$ velocity measures, and we found an average value $\bar{v}_x = 611.4 \pm 2.6\,[\mu m/s]$, in good agreement with the nominal velocity of the flow injected into the channel. Noteworthy, in order to calculate the speed it would be in principle possible to adopt the ML method described above to estimate the displacement vector, $\hat{\boldsymbol{\Delta}}$. However, relying on the SL phase derivative, the co-registration process can be avoided if velocity measures and cell counting are the sole scope of the experiment. Conversely, if measures of cell morphology and thickness are of interest, a ML reconstruction is required to recover the missing phase information. Figure 3.5(a) shows the SL phase-contrast DH reconstruction of the fibroblast cell. The degrading effect due to the rough layer is apparent, even if the diffraction pattern due to the cell shape is of help to recognize the cell location. Indeed, thanks to the DH double exposure approach, only dynamic scattering corrupts the useful signal in the phase-contrast map. In order to test the proposed ML method, we acquired a time sequence of $T = 3.6s$, resulting in $N = 30$ frames carrying uncorrelated speckle patterns. We decimated the sequence at rate $R_D = 1/3$, corresponding to $N = 10$ holograms being processed as previously discussed [166]. Figure 3.5(b) shows the obtained ML phase-contrast map. For a further image enhancement, we applied a Lee spatial smoothing filter to both the SL and the ML phase images [178]. The channel scattering is much mitigated both in the background and in the sample area as an effect of the ML gain, and the typical circular shape of the cell is recovered. It is worth to consider the typical diffraction pattern surrounding the cell, which does not change during its movement along the x_R direction, i.e. while the channel noise decorrelates. As a consequence, after speckle averaging, its contribution becomes more powerful with respect to the channel noise and, in turn, the diffraction pattern becomes more regular and visible. The quality improvement resulting from the speckle reduction is more apparent in the side-views of Fig. 3.6, where the phase maps are represented at different processing stages. In the SL map (Fig. 3.6(a)) the sudden spikes are an apparent effect of the turbid channel scattering. Conversely, this looks reduced in the ML representation of Fig. 3.6(b). Since the SL map is rapidly oscillating in space, the spatial smoothing results in a dynamic shortening and the quantitative information gets corrupted. For this reason, this kind of spatial averaging is not effective for quantitative phase retrieval if applied to SL images. On the contrary, the spikes are almost totally compensated in the ML case and the spatial filtering returns a phase map in which the maximum phase

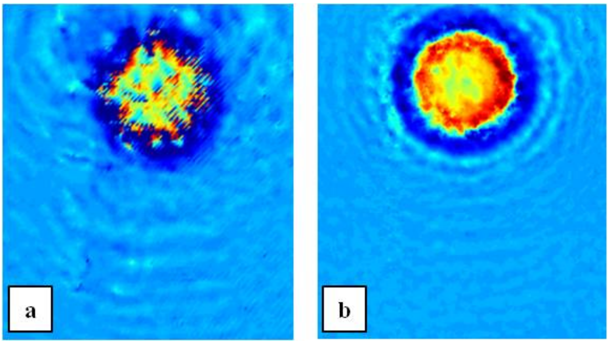

FIGURE 3.5: Holographic reconstructions of a sample cell flowing into a scattering channel [158]. (a) SL phase-contrast map. (b) ML phase-contrast map.

dynamic is preserved. We measured 3.5rad in the processed image, in good agreement with the one obtained in case of clear channel, while in the SL image this value lowers up to 2.2rad. As a consequence of the noise reduction, the image sharpness is expected to improve. As a sharpness metric, we measured the image gradient of the SL and ML phase images. The higher gradient, the higher sharpness enhancement. It is remarkable that a gradient improvement of 33.8% can be reached with only $N = 10$ images, so that the overall processing requires a computational time lower than 5.5min (0.2s for each SL phase reconstruction and 35s for each co-registration of 1024x1024 double precision images, depending on the hardware/software features of the machine employed for the scope). In case multiple particles are present in the field of view, the cell counting can be easily performed by means of the SL phase derivatives, so that the computational burden keeps unaltered. On the contrary, to obtain ML phase maps of a cell group inside the field of view a Region Of Interest (ROI) has to be selected for each cell and the co-registration has to be performed for each ROI. The smaller the ROI, the faster the search for the maximum of the correlation coefficient. In this sense, the main limitation of this approach is the necessity to find non overlapping ROI, in order to avoid possible co-registration errors.

DH MICROSCOPY THROUGH TURBID FLOWING FLUIDS

The idea to use holography for seeing through scattering media is not new and was intuited at the early stage of holography in the late 60ties. In the paper by K. A. Stetson, one of the pioneer of holography and inventor of holographic interferometry, imaging through the fog was presented [179]. Successively a

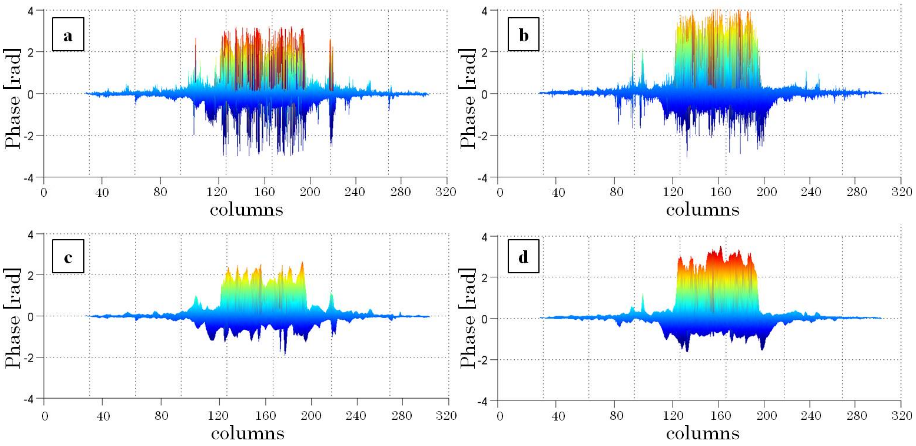

Figure 3.6: Phase-contrast mapping of a sample cell flowing into a scattering microfluidic channel [158]. A side-view is shown along the columns of the image at fixed row. (a) SL. (b) ML. (c) SL post-filtered. (d) ML post-filtered.

theoretical analysis by Lohmann and co-workers was accomplished and further investigations were performed with the aim of demonstrating that holography had interesting prospective for solving vision through fog thanks to the filtering action due to the Doppler frequency shift of the scattered radiation [180]. All these works mainly dealt with naked-eye vision of large scenes and the potentialities in quantitative microscopy were not investigated yet. Moreover, in classical holography, direct access to the phase information was not obtainable. Recently, the progresses in microfluidics, with channels and chemical/physical transducers embedded in the same structure at lab-on-chip scale, have motivated new research efforts. The introduction of DH recording and reconstruction has led to novel possibilities, as the recorded data can be now numerically processed to improve the performance and to synthesize novel functionalities, leading to the development of new branches of DH microscopy, suitable to tackle a specific group of problems.

Theoretical background

In 1967 Spitz and Stetson [179,181] proved that the hologram of an object recorded on a photographic plate through simulated moving fog provides better vision than a photograph through the same fog. In 1973, Lohmann and Shuman [180] presented a theoretical validation of holographic imaging through fog, i.e. a colloid with a suspended liquid in a dispersed medium of air. Interestingly, their formulation can be applied to any colloidal solution like, e.g. turbid liquids flowing inside microfluidic channels. In the following we will describe a simplified model useful to understand the working principle of the holographic approach for imaging through flowing colloidal fluids.

Let consider, for the sake of simplicity, a 4f system with focal distance f. This system can be thought as a black box receiving as an input the object distribution $U(x, y)$, and returning as an output the object wavefront in the hologram plane, $O(x', y')$. Let the hologram plane be the image plane of the object U through the 4f system and let (x_F, y_F) be its intermediate plane, where the colloids flow at constant velocity ν along a direction orthogonal to the optical axis. For the sake of clarity, we will herein discuss a one dimensional case, considering a flow along the sole direction x_F. All results trivially extend to the 2D case. Due to the properties of 4f systems, the intermediate plane is Fourier transform related to the object plane. Analogously, the image plane is Fourier transform related to the intermediate plane. In absence of a turbid medium, the wavefront U_F in the intermediate plane would result:

$$U_F(x_F) = \mathcal{F}\{U(x)\}_{\left(\frac{x_F}{\lambda f}\right)} \tag{3.7}$$

and the object wavefront in the hologram plane would exactly reproduce the object distribution:

$$O\left(x'\right) = \mathcal{F}^{-1}\{U_F\} = \mathcal{F}^{-1}\{\mathcal{F}\{U\}\} = U\left(x'\right). \tag{3.8}$$

We can account for the presence of the turbid medium introducing a filtering amplitude transmittance $\tau(x_F)$, so that in the intermediate plane it results

$$U_F(x_F) = \mathcal{F}\{U(x)\}_{\left(\frac{x_F}{\lambda f}\right)} \tau(x_F), \tag{3.9}$$

and, applying the product property of the Fourier transform, the object image can be written as:

$$O\left(x'\right) = \mathcal{F}^{-1}\{U_F(x_F)\} = \mathcal{F}^{-1}\left\{\mathcal{F}\{U(x)\}_{\left(\frac{x_F}{\lambda f}\right)}\right\} \otimes \mathcal{F}^{-1}\{\tau(x_F)\}. \tag{3.10}$$

Each moving particle can be modeled as a prism inclined at a certain angle with respect to the optical axis, producing a shift of the image, ξ. Considering just one static colloidal particle (i.e. one prism and $\nu = 0$), the medium transmittance takes the form [180]

$$\tau(x_F) = \exp\left(-j2\pi x_F \xi / \lambda f\right) \tag{3.11}$$

so that, substituting Eq. (3.11) in the right hand side of Eq. (3.10), the object image becomes

$$O\left(x'\right) = U\left(x'\right) \otimes \delta\left(x' - \xi\right) = U\left(x' - \xi\right). \tag{3.12}$$

If the particle motion is considered, the medium transmittance has to be modified as:

$$\tau\left(x_F\right) = \exp\left[-j2\pi(x_F - \nu t)\,\xi/\lambda f\right] \tag{3.13}$$

and the object image, apart from being shifted, will have a different temporal frequency:

$$O\left(x'\right) = U\left(x' - \xi\right)\exp\left(j2\pi\nu_D t\right), \tag{3.14}$$

where we denoted the frequency shift with

$$\nu_D = \frac{\xi v}{\lambda f} = \left(\frac{\xi}{f}\right)\left(\frac{c}{\lambda}\right)\left(\frac{v}{c}\right) = \nu_D\left(\xi\right). \tag{3.15}$$

This is proportional to an angular deflection factor, to the light frequency and to the relative velocity of the scattering particle. Hence, it is trivial to recognize ν_D as a Doppler frequency shift.

Finally, in a more general case, the amplitude transmittance of the medium has to be modeled as the weighted superposition of many prisms (i.e. many colloidal particles) of different deflection angles, all moving with velocity v:

$$\tau\left(x_F\right) = \int w\left(\xi\right)\exp\left[-j2\pi(x_F - \nu t)\,\xi/\lambda f\right]d\xi. \tag{3.16}$$

Hence, the object image will be the superposition of a number of object replicas, each one spatially shifted by a different extent ξ and frequency shifted by different amounts $\nu_D\left(\xi\right)$ [180]:

$$\begin{aligned}
O\left(x'\right) &= U\left(x'\right) \otimes \mathcal{F}^{-1}\left\{\int w\left(\xi\right)\exp\left(-\frac{j2\pi x_F\xi}{\lambda f}\right)\exp\left(j2\pi\nu_D\left(\xi\right)t\right)d\xi.\right\} = \\
&= U\left(x'\right) \otimes \int w\left(\xi\right)\mathcal{F}^{-1}\left\{\exp\left(-\frac{j2\pi x_F\xi}{\lambda f}\right)\right\}\exp\left(j2\pi\nu_D\left(\xi\right)t\right)d\xi = \\
&= \int w\left(\xi\right)\left[U\left(x'\right) \otimes \delta\left(x' - \xi\right)\right]\exp\left(j2\pi\nu_D\left(\xi\right)t\right)d\xi = \\
&= \int w\left(\xi\right)U\left(x' - \xi\right)\exp\left(j2\pi\nu_D\left(\xi\right)t\right)d\xi,
\end{aligned} \tag{3.17}$$

where the physical meaning of the weighting function $w(\xi)$ is the image amplitude of a point source observed through a stationary colloidal solution. If $w(\xi)$ is very broad the image will result severely blurred.

However, the Doppler shift gives a chance to get clear imaging through the turbid medium. In holographic configuration, a detector in the image plane records, during an exposure time τ, the intensity of the superposition of the wavefront $O(x')$ and the reference wave $R(x')$. If the +1 order of diffraction is considered (the diffraction terms out of interest can be easily filtered out) the recorded exposure takes the form [180]:

$$\begin{aligned} E_\tau(x') &= \int_{-\tau}^{\tau} H^{+1}(x')\,d\tau = \int_{-\tau}^{\tau} R^*(x')\,O(x')\,d\tau = \\ &= R^*(x') \int w(\xi)\,U(x'-\xi) \left[\int_{-\tau}^{\tau} exp\,(j2\pi\nu_D(\xi)\,t) \right] d\xi = \\ &= R^*(x') \int w(\xi)\,U(x'-\xi)\,sinc\,(\tau\nu_D(\xi))\,d\xi. \end{aligned} \tag{3.18}$$

Eq. (3.18) shows that the recorded signal is a weighted sum of many replicas of the object distribution, laterally shifted of various ξ and producing image blurring. The most degrading contributions comes from the replicas with higher angular deflection. However, the exposure is mainly amplitude modulated by a low pass filter $sinc\,(\tau\nu_D(\xi))$, i.e. by a function of the angular deflection being essentially different from zero for $|\nu_D(\xi)| \leqslant 1/\tau$. Thus, hologram recording acts as a temporal heterodyne receiver with bandwidth $1/\tau$. Only light components frequency shifted of an extent ν_D lower than the system bandwidth are allowed to participate to the process of fringe formation, i.e. the hologram acts as a selective temporal frequency filter.

In other words, the image blurring is bounded by the condition on the Doppler shift, as only spatial image shifts up to $\xi_B = \lambda f / v\tau$ will occur. According to the Rayleigh resolution criterion, the image blur is tolerable if ξ_B does not exceed the Rayleigh resolution, i.e. if it results:

$$\xi_B \leqslant \frac{\lambda f}{A_W} \implies v \geqslant v_T = \frac{A_W}{\tau} \tag{3.19}$$

where A_W is the aperture width of the system [180]. Eqs. (3.18) and (3.19) state that scattering colloidal particles moving at speed higher than the threshold velocity, v_T cannot affect the holographic imaging system, so that clear reconstruction of the samples through moving colloidal solutions is in principle obtainable.

Microfluidic application of the Doppler theory

Recently, amplitude and quantitative phase-contrast imaging in microscopy configuration has been achieved through milk, i.e. a colloidal solution with suspended particles of about $500\mathrm{nm}$ size [115,165]. The working principle is sketched in Fig. 3.7. In general, whenever turbid colloidal solutions flow at sufficient speed, a single hologram capture is required to get clear coherent imaging of the specimen through the turbid medium. In fact, the detector receives the coherent superposition of two kinds of contributions, corresponding to the wavefront directly passing through the sample and the photons scattered by the moving colloidal particles of the fluid where the sample is immersed. The scattered light experiences a frequency shift proportional to the fluid velocity, according to the formulation in Section 3.2.1. Since an hologram only records the interference pattern between waves in the same frequency band, if the fluid speed overcomes the threshold velocity, the scattered light cannot interfere with the reference. It follows that the hologram acts as a filter, discarding the contribution of the medium and enhancing only the useful signal.

The set-up adopted is a Mach-Zehnder interferometer in transmission configuration, as described in Section 2.3. The laser wavelength is $0.532\ \mu\mathrm{m}$, while the CCD pixel size is $6.7\ \mu\mathrm{m}$. The *Polymethylmethacrylate* (PMMA) channel dimensions are $1000\ \mu\mathrm{m}$ [width], $200\ \mu\mathrm{m}$ [depth], $58.5\ \mathrm{mm}$ [length]. Milk is injected inside the channel at a fixed velocity, ν, by means of a motorized syringe while biological samples are fixed on the inner channel wall [165]. In particular, bovine spermatozoa, i.e. pure phase objects were pumped into the channel in order to prove the effectiveness of DH in recovery both amplitude and phase imaging in such condition. After they dried, a hologram was acquired. Then the turbid medium was inserted and some holograms were recorded, both when the medium was motionless and when it flew at different velocities. The camera integration time was $\tau = 40\mathrm{ms}$, while the liquid-milk velocity increased from $30\mu\mathrm{m}/s$ up to $330\mu\mathrm{m}/s$ with steps of $10\mu\mathrm{m}/s$. Out of focus DH recordings were performed, and then the holograms were propagated till the object best-focus plane. Fig. 3.8 shows amplitude reconstructions and phase-contrast maps of the samples in different acquisition conditions [115,165]. In particular, Fig. 3.8(a) and Fig. 3.8(b) respectively show clear amplitude and phase-contrast maps obtained letting water flow inside the channel. On the contrary, the introduction of quasi-static milk provokes a severe image degradation which impairs a clear sample mapping (see Figs. 3.8(c,d)). However, when the milk velocity is augmented till reaching $\nu = 330\mu\mathrm{m}/s$, very clear imaging as well as phase-contrast mapping is achievable thanks to the selec-

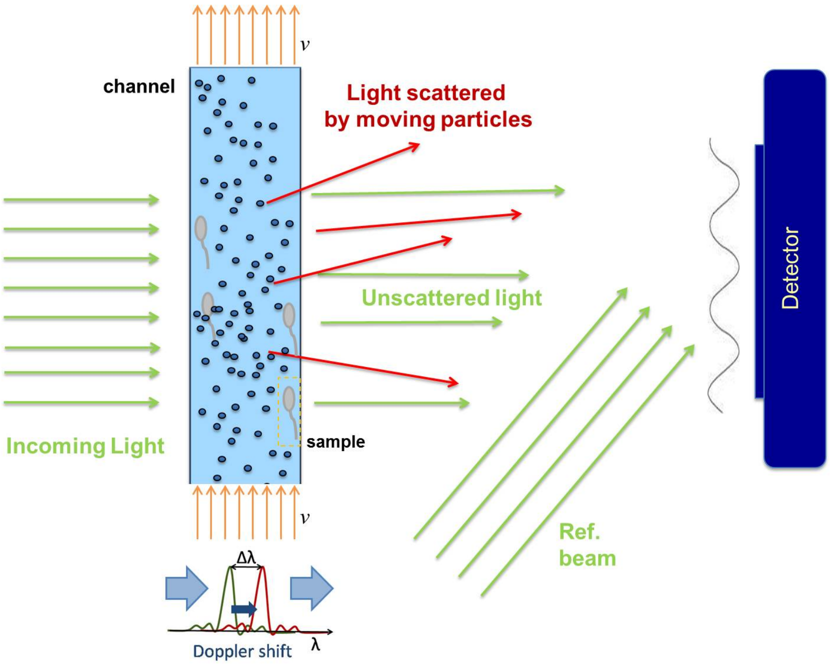

FIGURE 3.7: DH microscopy through flowing colloidal solutions [115]. The Doppler frequency shift experienced by scattered photons is used to discard the contribution of the turbid medium.

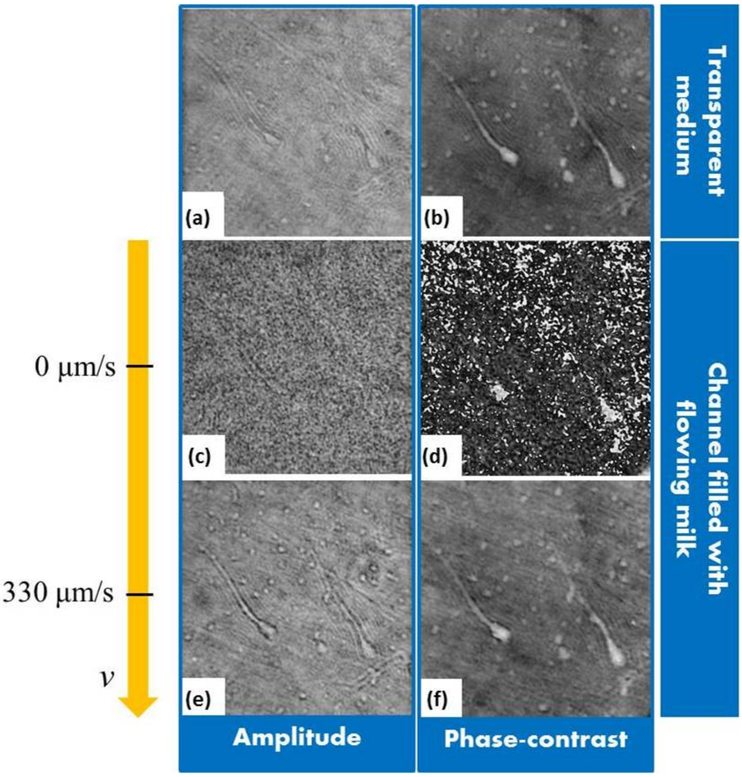

FIGURE 3.8: Imaging bovine spermatozoa layered on a microfluidic channel respectively filled with (a,b) water and (c-f) milk. (a,c,e) Amplitude reconstructions. (b,d,f) Phase-contrast mapping. (c,d) Severe image degradation in the case of quasi-static liquid. (e,f) Clear imaging and phase mapping in the case of liquid flowing at $\nu = 330 \mu m/s$ [115].

tive frequency process intrinsic of DH, as shown in Figs. 3.8(e,f). For higher velocities there is no further image improvement. Comparing the amplitude and phase reconstructions of the spermatozoa in water (Figs. 3.8(a,b)) with the reconstructions obtained through milk flowing at $330\mu m/s$ (Figs. 3.8(e,f)), there are no significant differences.

CLEAR COHERENT IMAGING THROUGH QUASI-STATIC TURBID MEDIA

In this Section we afford the case of quasi-static turbid fluids, where no relative velocity can be contemplated between the samples and the colloids, so that the Doppler effect is not of help. In quasi-static turbid microfluidics, the radiation scattered by the colloids superimpose coherently to the recording device (e.g., a CCD camera), thus provoking severe image degradation, as shown in Figs. 3.8(c,d). In particular, the complex field in the hologram plane results from the superposition of K contributions so that each resolution element of the CCD camera records an intensity pattern resulting from the coherent addition of a number of complex components, i.e. the random walk [182]:

$$R_W = \left| \sum_{k=1}^{K} \alpha_k \exp\left(j\beta_k\right) \right|^2, \tag{3.20}$$

where α_k and β_k are the random amplitude and phase of the $k-th$ interfering contribution at time Our approach to tackle the quasi-static case is to treat the ensemble effect of scattering due to the colloidal particles of the medium as a speckle noise [166]. Hence, speckle reduction methods have to be applied to the observed data in order to restore clear imaging. Speckle is a multiplicative noise that can be traced back to the well-known phenomenon of the random walk in the complex plane [182]. This produces on the reconstructed holograms a typical pattern with a closely spaced succession of dark and bright spots depending on the constructive or destructive interference.

Many approaches were adopted in the framework of DH to reduce the speckle contrast. In [175] a spatial multi-look (ML) was performed where close-by pixels were seen as independent realizations of the same random process. Because of the spatial average, the speckle contrast improved at the cost of a resolution worsening. In [183] a homomorphic approach was followed, involving a logarithmic transform of the image intensity to force the speckle to get additive. Then, classical processing techniques are applied that are commonly used to filter additive noise (e.g., Wiener, Lee filters). Again, this implies a resolution loss. A different class of methods exploits some kind of diversity to record a set of holograms with statistically independent speckle patterns and to combine them incoherently to reduce the speckle contrast. In [184], multiple holograms are recorded in polarization diversity, while in [185,186] rotating glass diffusers or rotational mirrors are employed. A shift of the CCD camera is introduced to obtain a stack of uncorrelated holograms, which can be seen as an aperture synthesis along the shift direction [187]. In [138,139] speckle diversity is numerically simulated by random resampling binary masks applied to one single DH capture. We will hereafter refer to these techniques as Multi-Look Digital Holography (MLDH) [118,138,139,158,166-169]. In the experiments shown in the following we will prove that, in the case that the object of interest is dipped into a quasi-stationary turbid medium or hidden by quasi-static colloidal particles distributed in a liquid volume, no ad hoc setup is required to recover clear imaging, but the medium itself contributes to the decorrelation process at the receiver. Hence, a time sequence of recorded DHs with nearly uncorrelated speckle can be digitally reconstructed and incoherently processed to improve the speckle contrast, in turn restoring clear imaging without losing pixel resolution.

Working principle of Multi-Look Digital Holography

In the case of imaging through quasi-static turbid fluids, a statistical approach has to be followed to study the process of scattering that degrades the recorded hologram. If one single hologram is captured, the reconstructed wavefront at time t_i in the plane (x_R, y_R) turns out to be a complex random variable. We will herein refer to this distribution as the Single-Look (SL) reconstruction:

$$\begin{aligned} C_{SL-i}\left(x_R, y_R, d; t=t_i\right) &= P\left\{H\left(x', y', t=t_i\right)\right\} = \\ &= \sqrt{I_{SL}\left(x_R, y_R, d; t=t_i\right)} \exp\left[j\hat{\varphi}_{SL}\left(x_R, y_R, d; t=t_i\right)\right], \end{aligned} \tag{3.21}$$

where $\sqrt{I}$ and Ψ are real random variables with variance $\sigma^2_{\sqrt{I},SL}$ and $\sigma^2_{\hat{\varphi},SL}$ respectively, and we denoted with $P\{\ldots\}$ the propagation operator. A complete statistical modeling of the distribution of these two random processes is out of the scope of this work. Here we just point out that they have the useful amplitude and phase distribution of the object as their average values, i.e.

$$\begin{aligned} &E\langle\sqrt{I\left(x_R, y_R, d\right)}\,\rangle = |O(x_R, y_R, d)| \\ &E\langle\hat{\varphi}_{SL}(x_R, y_R, d)\rangle = \varphi(x_R, y_R, d) + \Gamma(x_R, y_R, d). \end{aligned} \tag{3.22}$$

Since the ensemble effect of turbidity is the introduction of random fluctuations of both the amplitude and phase of the decoded object signal around their respective mean values, we treat this as a speckle noise contribution. Hence, our strategy is to reduce the noise variance, both in amplitude and phase, to obtain a better estimate of the object. The simplest way to reduce the noise in the image processing framework is to operate directly on the image in the spatial domain. In particular, assuming spatial ergodicity, it is possible to think to the signal spatial fluctuations as different realizations of the same random variable. Hence, a spatial average has the effect of reducing the noise variance at the cost of a deterministic resolution loss (a spatial average over a square window with size l worsens the resolution of a factor l^2, since the equivalent pixel size enlarges). However, in the case we are tackling such strategy would not provide an estimate of the object in absence of turbidity, as the spatial ergodicity assumption does not stand. What would be required are independent realizations of the received signal, over which performing an average. MLDH [118,138,139,158,166-169] is a simple approach aimed at exploiting some kind of noise diversity between multiple recordings, which is introduced in the experimental setup, to achieve noise reduction. Such strategy is successful whenever the useful signal is almost stationary while the unwanted noise contribution decorrelates fast over time. For example, a moving diffuser can be introduced to provide noise diversity while the object is kept fixed. The basis of the MLDH approach is a temporal ergodicity assumption, i.e. the temporal variations of the received signal can be treated as independent realizations of the same random variable.

Let $\{H_1, ..., H_N\}$ be a sequence of N holograms of the object, recorded while producing some kind of diversity in the setup, and let r be the frame rate of acquisition. Each hologram of the sequence can be separately reconstructed and the ML amplitude and phase distributions can be synthesized as:

$$\begin{aligned} A_{ML}(x_R, y_R, d) &= \frac{1}{N}\sum_{i=1}^{N} \left|P\left\{H_i\left(x', y', t = t_i\right)\right\}\right| \\ \hat{\varphi}_{ML}(x_R, y_R, d) &= \frac{1}{N}\sum_{i=1}^{N} Unwrap\left\{Angle\left[\frac{P\{H_i\left(x', y', t = t_i\right)\}}{P\{H_{Ref}\left(x', y'\right)\}}\right]\right\}. \end{aligned} \tag{3.23}$$

A common way to evaluate the ML improvement in terms of noise reduction is to measure the noise contrast of the reconstruction as

$$N_C = \frac{\sigma}{\mu}, \tag{3.24}$$

where σ and μ respectively denote the standard deviation and the mean value of the gray level distribution of the image. This is measured over an homogeneous segment of the amplitude reconstruction, where a flat gray level distribution is expected and any fluctuation has to be attributed to noise. Hence, the lower the noise contrast, the higher image quality in terms of SNR. In other words, a spatial ergodicity assumption is exploited to get the estimate, so that the standard deviation and the mean value are measured over the spatial coordinates of the image instead of evaluating different realizations of the noise process. The noise contrast is expected to improve as a result of the ML processing. Indeed, it can be shown that the superposition of N statistically independent random variables returns a random variable whose variance is reduced by a factor $1/N$ [118]. Let X_1 and X_2 be two uncorrelated random variables and let

$$Y = aX_1 + bX_2 \tag{3.25}$$

be a linear combination of them through the coefficients a and b. After trivial manipulations, it is possible to find that

$$\sigma_Y^2 = a^2\sigma_{X_1}^2 + b^2\sigma_{X_2}^2 \tag{3.26}$$

Hence, if we denote with

$$\bar{X} = \frac{1}{N}\sum_{i=1}^{N} X_i \tag{3.27}$$

the mean of N uncorrelated random variables X_i, each with the same mean $\mu_{X_i} = \mu_X$ and variances $\sigma_{X_i}^2 = \sigma_X^2 \; \forall \; i = 1, \ldots, N$, the variance of $\bar{X}$ is given by

$$\sigma_{\bar{X}}^2 = \frac{1}{N^2}\sum_{i=1}^{N} \sigma_{X_i}^2 = \frac{\sigma_X^2}{N}. \tag{3.28}$$

Since it results $\mu_{\bar{X}} = \mu_X$, the noise contrast reduces to

$$N_{C,\bar{X}} = \frac{1}{\sqrt{N}}\frac{\sigma_X^2}{\mu_X} = \frac{1}{\sqrt{N}} N_{C,X_i}\,, \tag{3.29}$$

Hence, in the case of N holograms with statistically uncorrelated noise patterns, the noise contrast of the ML reconstruction improves by a factor of $1/\sqrt{N}$ [118,182].

Exploiting the Brownian motion of small colloidal particles

In the case of quasi-static colloidal fluids with small particle size (e.g. colloids with typical diameter $D < 1\,\mu m$) the Brownian motion of the colloidal particles can be exploited to get holograms with nearly uncorrelated speckle. Due to the small size of the colloids, the effect of the Brownian motion is enough to provide the required diversity in speckle pattern [166]. Hence, a MLDH strategy can be adopted to achieve microscopy imaging through the turbid medium. The proposed processing was applied to both amplitude targets and pure phase samples. As a test colloid for the experiments we employed milk, since the typical size of the milk colloids is $D \sim 500nm$, so that their Brownian motion is expected to be significant. A performance analysis was carried out at different flow velocities, and the results are compared with the ones obtained in the case of milk in dynamic regime. Similarly to what is described in Section 3.2.2, in a first set of experiments we put some bovine spermatozoa in a straight channel filled with the colloidal solution. In this case the medium was first kept static and we recorded $N = 250$ holograms. For each of them, we performed the numerical propagation by means of the Fresnel method after dropping the zeroth diffraction order. Then we synthesized the MLDH amplitude reconstruction as in Eq. (3.23), i.e. the holograms are incoherently combined. Figure 3.9 shows the SL and the ML amplitudes. As a performance measure, we calculated the noise contrast of the ML image defined by Eq. (3.24), normalized with respect to the contrast of the SL image. This can be expressed as a function of the number of looks adopted to synthesize the ML reconstruction, i.e the following dispersion index is evaluated:

$$DI_{C,ML}(n) = 100 \frac{\sigma_{n-looks}}{\mu_{n-looks}} \frac{\mu_{SL}}{\sigma_{SL}} = 100 \frac{N_{C,ML}(n)}{N_{C,SL}} [\%] \qquad n = 1, \ldots, N. \tag{3.30}$$

The degrading effect of the speckle noise is apparent in the SL image (Fig. 3.9(a)), which inhibits a clear vision of the objects. After superimposing $N = 250$ consecutive frames, the improvement in image quality is clearly appreciable (Fig. 3.9(b)), the spermatozoa can be clearly imaged, and the speckle contrast decreases. Then we performed some uniform decimations of the full image stack to extract frame subsets with variable lengths. Indeed, a significant role in determining the ML improvement is played by both the number and the temporal distribution of the extracted frames. In Figure 3.10 we reported the values of dispersion index versus the number of superimposed holograms, n. In particular, the blue dotted line refers to a set of consecutive frames, while the black dashed one refers to the full stack decimation at variable rates. In Figure 3.10, we also plotted the trend of the function $100/\sqrt{N}$, which in principle should be obtained when statistically uncorrelated reconstructions are superimposed. Hence, it can be regarded as a boundary line for the ML gain. The noise contrast gets lower when N increases, as expected. However, a gap with respect

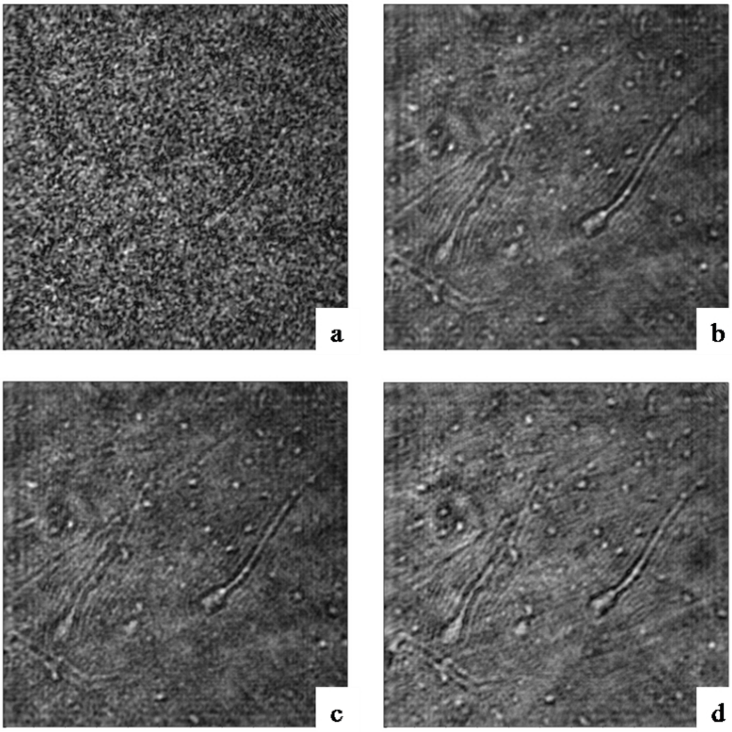

FIGURE 3.9: Amplitude images of spermatozoa in turbid medium [166]. (a) N=1, $v = 0$ μm/s; (b) N=250, $v = 0$ μm/s; (c) N=25 (decimated), $v = 0$ μm/s; (d) N=1, $v = 330$ μm/s.

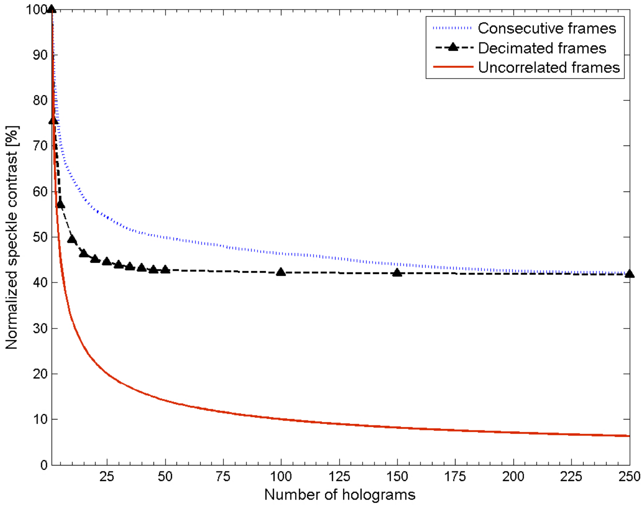

Figure 3.10: Normalized speckle contrast versus N [166].

to the ideal behavior is still present, and the improvement saturation suggests a residual correlation between the recorded frames. That a value of dispersion index close to the saturation can be obtained with a few samples, if they are properly selected, is noteworthy. In particular, $N = 25$ decimated frames assure the same contrast of $N = 250$ consecutive ones, allowing us to gain a factor of 10 in terms of computational time. In Fig. 3.9(d) we also reported the SL amplitude image obtained with the turbid medium flowing at $v = 330\ \mu m/s$. The gain due to the Doppler is apparent in this case, and the samples are well visible. Nevertheless, similar performance can be obtained after processing the decimated sequence, as shown in Fig. 3.9(c) ($N = 25$ decimated). This result is of great importance whenever the flowing velocity is not enough to benefit of the Doppler effect. As a further test, a different target was placed behind a channel where milk was injected at tunable velocity by means of a motorized pump [166]. For each v, $N = 100$ holograms were recorded at sampling distance $T_C = 0.1s$ and processed as previously described. Figure 3.11 reports the ML improvement versus v. As expected, the gain due to the ML decreases when v gets higher, i.e. when the number of particles contributing to the fringe formation is not enough to assure a proper decorrelation between the combined frames. Figure 3.12 shows the obtained SL and ML amplitude images. When

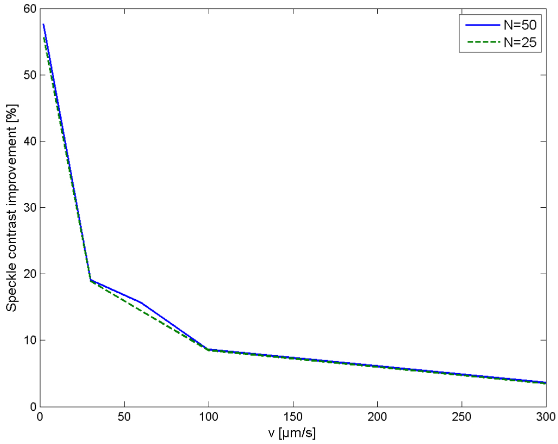

FIGURE 3.11: ML improvement versus v [166].

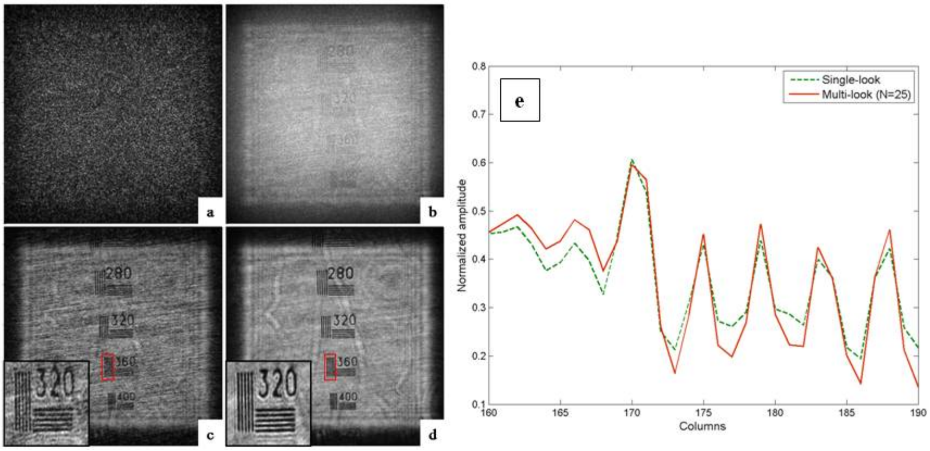

FIGURE 3.12: Amplitude images ofa test target seen through a colloidal solution [166]. (a) $\nu = 0\ \mu m/s$, N=1; (b) $\nu = 0\ \mu m/s$, N=25; (c) $\nu = 30\ \mu m/s$, N=1; and (d) $\nu = 30\ \mu m/s$, N=25. (e) Image amplitude signals in the box under test.

$\nu = 0 \mu m/s$, the Doppler effect does not play any significant role, and the target is hidden by particle scattering. After the processing, it becomes visible as a result of the ML. At $\nu = 30\ \mu m/s$, the quality of the SL image improves; again the processing benefit is apparent. Moreover, noise reduction does not imply a resolution loss. As a clear evidence, in Fig. 3.12(e) we show the image contrast along the columns of the red boxes of Figs. 3.12(c,d) (amplitudes are averaged along the rows). In this case, a wider dynamics corresponds to a better resolution capability, and no significant differences have been recognized between the SL and the ML trends. The incoherent combination of multiple frames improves the quality of both the amplitude and the phase-contrast images. Indeed, as a final test, the reconstructed phase maps of the targets under analysis were processed as described in Eq. (3.23) [166]. Figure 3.13 clearly shows the ML gain in both the cases of static and moving turbid media. In particular, the case of quasi-static milk ($\nu = 0 \mu m/s$, Figs. 3.13(a,b)) is very challenging since no Doppler gain is achieved and the phase object is not clearly resolved in the SL image, while it becomes visible after the MLDH phase processing. In the case of a slow turbid flow ($\nu = 30\ \mu m/s$, Figs. 3.13(c,d)) a better quality of the phase image is obtained as a result of the noise reduction. A further processing of the ML phase-contrast map yields the enhanced MLDH pseudo-3D view of the bovine sperm seen through a stationary turbid fluid, shown in Fig. 3.13(e). Again, this is achieved without loss of resolution.

Imaging through a live bacteria suspension

In the previous section we have shown that in the case of small size colloids, even if quasi-static, MLDH offers a solution to the imaging problem, as the turbid medium itself provides the required uncorrelation between multiple holograms. Unfortunately, for big size scattering objects, the Brownian motion does not provide enough time-diversity and such strategy fails [167]. However, sometimes the turbid volume can be constituted of living material, such as bacteria colonies, which could grow in favorable environmental conditions, e.g. during the monitoring of slow biological processes [188]. A different possibility is offered by MLDH whenever the living objects exhibit a self-propelling feature. In particular, here we study the interesting situation in which a live bacteria suspension is responsible for light scattering and the self-propelling feature of its individual elements causes a whole time diversity in speckle patterns [169]. Indeed, their dynamic behavior obeys different displacement laws if compared to the inanimate micro-particles and thus a different speckles diversity effect is expected. Investigation on the interaction of light with bacteria was carried out

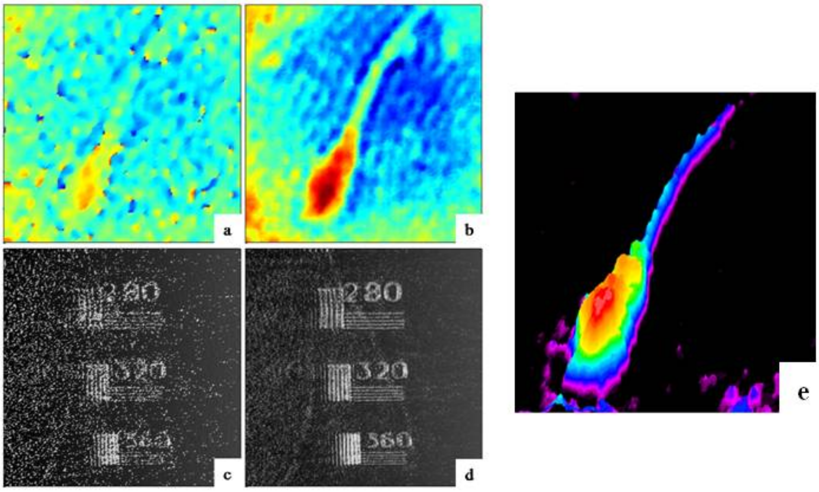

FIGURE 3.13: Phase contrast mapping through quasi-static milk [166]. (a) $v = 0\ \mu m/s$, N=1; (b) $v = 0\ \mu m/s$, N=50; (c) $v = 30\ \mu m/s$, N=1; and (d) $v = 30\ \mu m/s$, N=25. (e) Enhanced pseudo-3D view of the map in (b).

by means of scattering and diffraction characterizations [189-193]. Scattering properties of bacteria are of great importance and were intensively studied in the field of environmental monitoring for early detection of biological contamination with the aim to prevent the spread of diseases, or even in cutting-edge applications as photobioreactors to constitute elements of photosynthetic plasmonic voltaic cells [189,190]. Great effort was spent to find reliable ways to distinguish between different bacteria species. In [191] estimates of diameter and length of single E-coli were performed by Inverse Light Scattering (ILS), relying on prior assumptions about the characteristic shape of the investigated bacteria culture. Elastic Light Scattering (ELS) was proved to accurately estimate bacteria size by multiple measures at different angles [189]. Noteworthy, a reliable classification of different species was achieved by statistical analysis of the diffraction pattern produced by bacteria biofilms [192,193]. However, the research about thick and severely scattering live bacteria volumes in terms of their scattering properties and how these affect the imaging, i.e. by means of an ensemble characterization of the speckle pattern, was never considered before. Bacterial contamination of a liquid volume results in severe scattering and strongly hinders the capabilities of any imaging system. Actually, the characteristic size of the scattering objects considered in our case ranges from 1 μm to 3 μm (thickness), depending on the considered species. Moreover, bacteria

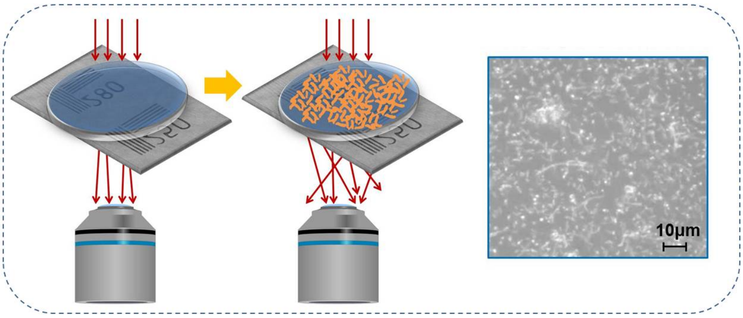

FIGURE 3.14: A sketch of the experiment aimed at imaging a test target through a severely scattering bacteria volume [169]. On the right a 20x microscope image of the bacteria suspension is shown.

typically organize in longer aggregates (from 10 μm to 100 μm), as shown in the microscope image of Fig. 3.14, so that the uncorrelation due to the Brownian motion cannot be exploited. Nevertheless, bacteria have the unique feature to be self-propelling microorganisms. When observed at the microscope, they show frenetic and random movements that are expected to be uncorrelated at long time scales. In other words, live bacteria accomplish the optical task of decorrelating the scattering disturbance they produce, acting just as a moving diffuser [169]. This effect can be exploited by MLDH to achieve imaging and flexible refocusing capabilities through the scattering suspension.

The next subsections are organized as follows. At first, we analyze the time correlation properties of the bacteria culture, showing different statistics with respect to occluding objects with comparable characteristic length and we will define a criterion for automatic blind refocusing through the scattering volume [169]. Starting from this characterization, we demonstrate that the speckle decorrelation effect, due to the self-propelling feature of the elements in the suspension, is sufficient to restore clear imaging, allowing us to take advantage of a multi- look strategy without the need for prior information or scattering measures [150,158]. In this way, we can afford a challenging quasi-static case, where the typical dimensions of the occluding objects would impair any clear imaging, since the Brownian motion is not of help.

Automatic focusing through a live scatterings ensemble

In our experiments, an USAF test resolution target was placed behind a Petri dish filled with a bacteria culture, as shown in Fig. 3.14. The ensemble effect of the introduction of the bacteria volume is a degradation of the hologram as a

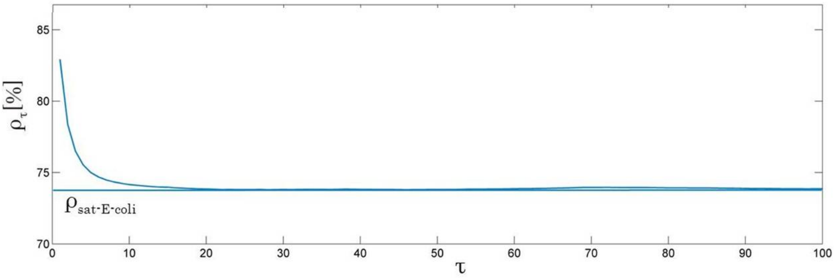

FIGURE 3.15: Average correlation coefficient [%] between holograms couples acquired at time lags τ [169].

time variable noise pattern superposing to the useful object information. Hence, a characterization is required to study the time correlation of the noise patterns. In particular, we measured the average correlation coefficient ρ_τ, which is defined as:

$$\rho_\tau = \frac{1}{N-\tau}\sum_{i=1}^{N-\tau}\frac{|H_i|\,|H_{i+\tau}|}{\sqrt{|H_i|^2|H_{i+\tau}|^2}}, \tag{3.31}$$

i.e. the average of the correlation coefficients measured between all the holograms couples acquired at time lags τ. In Fig. 3.15 the trend of ρ_τ vs. τ is shown. A saturation value $\rho_{sat} < 75\%$ is reached, suggesting to exploit the self-propelling property of bacteria to acquire and incoherently combine a stack of uncorrelated hologram reconstructions, according to the MLDH principle. Thanks to the possibility to obtain a ML image which is less affected by noise due to the bacteria scattering, and taking advantage of the DH flexible focusing capability, the proposed approach also allows an automatic numerical focusing to look for the proper object best-focus plane. In fact, an autofocusing algorithm [194] can be simply applied to ML images obtained by the incoherent combination of holograms propagated at different distances. In particular, the best-focus plane can be obtained optimizing the Tamura coefficient, $T_C(z)$ [194]. This is known to be a proper contrast estimator for the scope as $T_C(z)$ is a function of z exhibiting a maximum at the object best-focus plane. Hence, the focus distance can be estimated as [169]

$$\hat{z}_{focus} = \underset{z}{\operatorname{argmax}}\left\{T_C\left[\tilde{A}_{ML}(z)\right]\right\}, \tag{3.32}$$

where $\tilde{A}_{ML}(z)$ is the stack of ML amplitude reconstructions propagated at various distances after selecting the diffraction order of interest. In the next

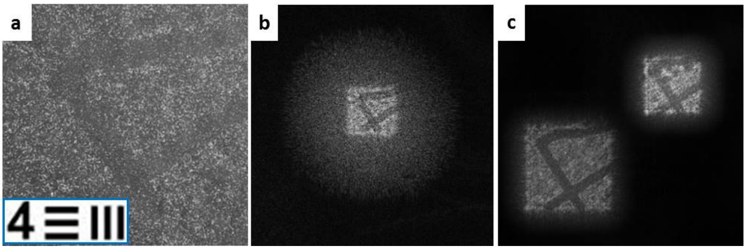

FIGURE 3.16: Imaging a test target through a thin scattering bacteria layer [169]. (a) Hologram of the target shown in the inset. (b) Hologram spectrum (+ 1 order). (c) ML reconstruction.

Section we will show and discuss the results of experiments carried out with the aim to demonstrate the possibility to achieve clear imaging with flexible autofocusing capabilities, starting from blind out-of focus recordings of targets hidden by a severely scattering bacteria suspension.

Experimental results

E. coli DH5-alpha were plated and incubated on agar plates. The day before the beginning of experiment, a single bacterial colony was picked and cultured in LB broth medium at 37°C in a shaker incubator for 16-18 hours to achieve saturation conditions. A 1:5 volumetric dilution of cell culture was then grown in LB until reaching the log phase. Then the growth was stopped and bacteria were harvested by centrifugation at 5000 rpm for 10 min in order to separate the cells from the medium. Cells were then resuspended in fresh LB in order to obtain a final concentration of 6×10^6 $\mathrm{cells/mL}$. Bacteria concentration was calculated by spectrophotometric measurement of suspension absorbance at $600\mathrm{nm}$ (Optical Density at $600\mathrm{nm}$, i.e. OD600), considering that 8×10^8 $\mathrm{cell/mL}$ have an OD600 = 1. In our tests, $N = 500$ holograms were registered with frame rate $r = 12s^{-1}$ and the experiment was repeated progressively decreasing the dilution percentage, i.e. the density of bacteria present inside the analyzed suspension. In the beginning, the ensemble effect of a thin bacteria layer ($200\mu\mathrm{m}$ thickness) was investigated studying the time variation of the hologram spectra [169]. The test object and the corresponding hologram are shown in Fig. 3.16(a). From the digital hologram, the speckle-like pattern superposing to the useful signal is apparent. Noteworthy, the analysis of the hologram spectra clearly shows the ensemble effect of the scattering suspension, as higher spatial frequencies are visible constituting a cloud superposing to the useful signal. Unfortunately, the scattering noise overlaps to the higher object frequencies in the hologram spectrum, as shown in Fig. 3.16(b), so that this cannot be simply discarded by band -pass filtering in the Fourier domain. However, the time-analysis of the spectra confirms the indications of the correlation coefficient trend, revealing the variability of the spurious contributions and suggesting that a ML gain can effectively enhance the useful signal. Figure 3.16(c) shows the ML amplitude reconstruction in the object focus plane, where, as expected, the hidden target is well visible. In a second experiment we imaged a target ($200\ lines/mm$) through volumes of liquid filled with bacteria (a $500\ \mu m$ thick container was used for the scope) at different concentrations, ranging from $1.4 \times 10^5\ cell/mL$ to $2.0 \times 10^5\ cell/mL$. Figure 3.17 shows the corresponding SL and ML amplitude reconstructions. In particular, the SL images look severely degraded even in case of low bacteria concentration (dilution higher than 80% in Fig. 3.17(a) and Fig. 3.17(d), corresponding to $1.4 \times 10^5\ cell/mL$ and $1.5 \times 10^5\ cell/mL$ respectively) while a high density bacteria suspension ($2.0 \times 10^5\ cell/mL$) completely hides the target, as shown in Fig. 3.17(g). On the contrary, the ML strategy is successful in restoring the useful object signal, providing enhanced quality images (in terms of noise rejection) in case of $1.4 \times 10^5\ cell/mL$. (see Fig. 3.17(b)) and $1.5 \times 10^5\ cell/mL$ (Fig. 3.17(e)), and clearly revealing the hidden target in case of volumes with high bacteria density (i.e. $2.0 \times 10^5\ cell/mL$), as shown in Fig. 3.17(h). This is also apparent from the plots reported in Figs. 3.17(c,f,i), showing the image amplitude signals, measured over the horizontal bars indicated in the corresponding SL and ML images. The blue lines refer to the SL, while the red lines correspond to the ML images. In particular, in Fig. 3.17(c) and Fig. 3.17(f) the ML gain results in a contrast enhancement on the vertical lines and, hence, an improved resolution. Moreover, the structure of the lines becomes resolvable in the ML plot of Fig. 3.17(i), while these are not appreciable at all in the SL plot, as the useful signal is entirely covered by noise. Obviously, the boundary dilution is set by the power of the beam reaching the biological samples and the target. If the laser power is increased, clear imaging is expected although the boundary condition is overcome, as the detector collects unscattered photons with higher probability. As a performance measure, we calculated the $DI_{C,ML}(n)$ [166,168], over an homogeneous segment of the image (red box in Fig. 3.17(g)), so that a dispersion decrease is expected as a result of noise mitigation. We found a remarkable ML improvement with respect to the SL amplitude (up to 75% decrease of $DI_{C,ML}(n)$, as shown in the plot in Fig. 3.18(a)). Some of the most significant ML reconstructions, corresponding to the acquisitions of Figs. 3.17(g,h), are reported in Fig. 3.18(a). Noteworthy, the dispersion index saturation shows that a lower number of acquisitions is sufficient to provide the

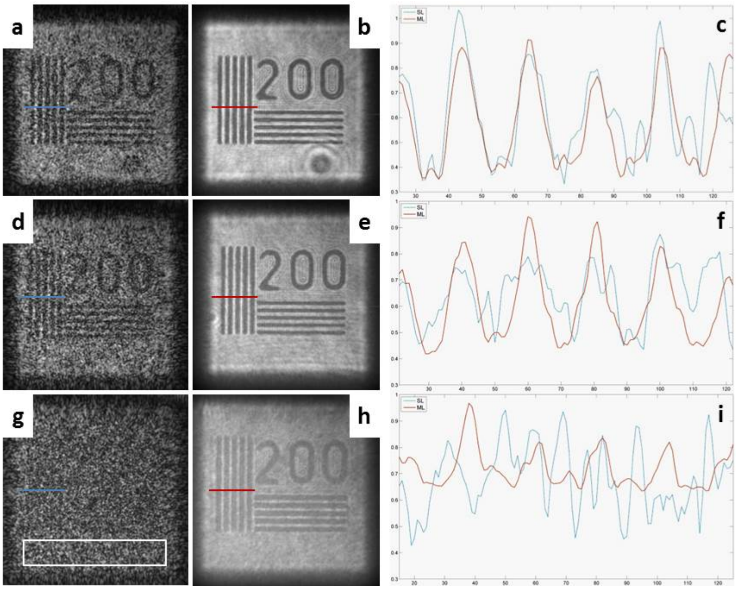

FIGURE 3.17: Amplitude reconstructions of a test target (200 lines/mm) through bacteria volumes at different concentrations [169]. (a,d,g) SL images. (b,e,h) ML images. (c,f,i) Image contrast over the lines indicated with the horizontal bars. Blue: SL image. Red: ML image.

desired image enhancement, thus allowing us to save computational time. If a proper decimation of the hologram stack is performed, this time can be further reduced without losing ML gain.

In order to show the flexible focusing capability of MLDH, two further experiments were carried out. In particular, we inserted a hair along the object beam path at very long distance from the target. Starting from the same stack of holograms, propagations at different distances provide ML reconstructions where the target (Fig. 3.18(c)) or the hair (Fig. 3.18(d)) are clearly imaged in their own best focus planes, while these objects are not visible in the SL reconstructions of Fig. 3.18(b). Such capability allows one to acquire holograms of objects placed in different positions along the optical axis, and to reconstruct them in a condition where it is impossible to determine each object focus plane by mechanical scanning. With the aim to demonstrate the full automatic refocusing of the object, we applied the contrast optimization expressed in Eq. (3.32) to the acquisitions corresponding to Fig. 3.17(d) (concentration of 1.5×10^5 $\mathrm{cell/mL}$). In Fig. 3.19 the plot of $T_C(z)$ vs. $z\,[\mathrm{cm}]$ is reported, along with some ML reconstructions after propagation at various distances (see the insets in Fig.

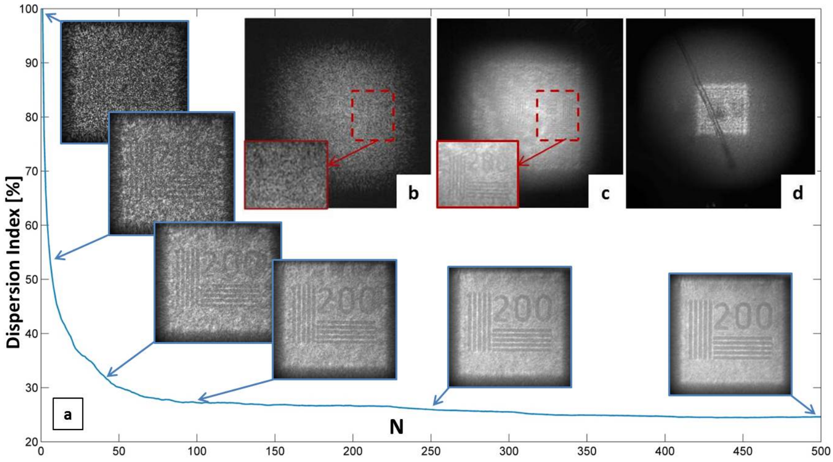

FIGURE 3.18: (a) Dispersion index [%] vs. the number of looks, N. In the insets some of the corresponding n-looks amplitude reconstructions are shown. (b-d) To show MLDH flexible focusing a hair is inserted along the object beam path. (b) SL, target on focus. (c) ML, target on focus. (d) ML, hair on focus [169].

3.19), showing that the z maximizing the contrast actually corresponds to a ML reconstruction where the test object is in focus. On the contrary, in the SL reconstruction shown in the bottom left corner of Fig. 3.19 the object signature is just slightly recognizable, impairing the convergence of any autofocusing algorithm. Hence, it becomes possible to fully exploit the flexible holographic refocusing to obtain images of hidden objects in focus, in a condition where it would not be possible by conventional microscopy [169]. Indeed, this would require a mechanical scanning along the optical axis to look for $\hat{z}_{\mathrm{focus}}$, but the presence of the scattering volume would impair the formation of a recognizable image of the object in all the inspected planes.

CLEAR COHERENT MICROSCOPY THROUGH BLOOD

Among the huge variety of turbid fluids, blood has always conveyed broad interest in all fields of bio-medical research. In [195] DILH microscopy was performed to achieve imaging and quantitative phase-contrast mapping of human blood samples with a lensless set-up. In [195-198] a real-time blood testing system was developed to obtain interferograms and phase-maps of RBCs with nanoscale sensitivity, in order to measure their volume distribution and other clinically relevant parameters. Several works were carried out using confo-

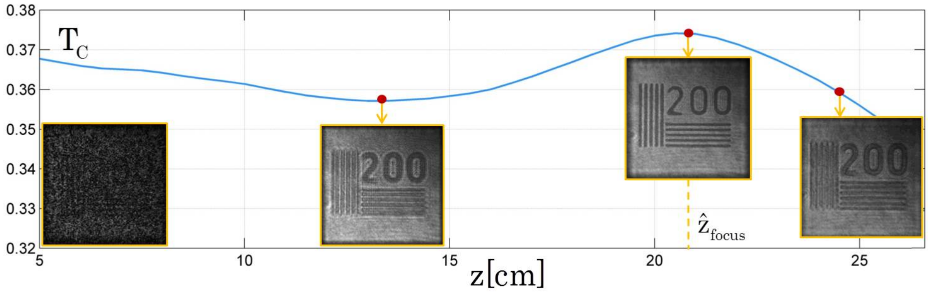

FIGURE 3.19: Tamura coefficient vs. z[cm]. The inset on the bottom-left corner shows the SL reconstruction. The insets indicated by the vertical arrows show ML reconstruction after propagation at various distances [169].

cal particle image velocimetry (PIV) systems to study the in-vitro blood flow behavior in PDMS microfluidic channels with straight or complex geometries simulating the micro-vessel features [199,200]. Laser speckle contrast imaging and laser doppler blood flowmetry were adopted in [201] to perform in-vivo noninvasive blood flow measurements. In [202] DH microscopy was employed to measure the motion of RBCs in a microscale volume. Noteworthy, in [203] DH microscopy was firstly combined with Endoscopy to perform PIV and to measure the deformation of the vessel wall for different vein models. Recently, the optical features of RBCs have been investigated, showing that these behave as adaptive microlenses when immersed into a buffer with proper osmolarity features [47]. Thinking to a RBC as a lens can be exploited for imaging purposes, especially when combined with holographic optical tweezers modules [115] adding the possibility to move the lens in the whole 3D space. On these basis, the study of the focus spots can be used to discriminate between healthy and sick RBCs, i.e. a DH pre-screening tool can be used for diagnostic purposes [47]. Flow engineering can be also used to induce controlled rotations in the RBCs for tomography purposes [204]. However, the problem of seeing amplitude targets or pure phase samples through a turbid flow of RBCs, thought as occluding objects, has never been considered before.

The destroying effect of scattering caused by colloidal particles in the medium is shown in Fig. 3.20, for images obtained in case of stationary blood [167]. In particular, in Fig. 3.20(a) only the left side of a test target was placed behind a microfluidic channel filled with blood and imaged by means of a white-light microscope, as sketched in Fig. 3.20(e) (see the blue dashed box labeled with **a** in Fig. 3.20(e)), showing that the fluid behaves in this case as an opaque cover completely impairing the visualization of the target. In Fig. 3.20(b), the white-light microscope image of the channel filled with blood is reported (image corresponding to the channel portion labeled with **b** in Fig. 3.20(e)), showing the strong scattering due to the RBCs. As the amount of blood in the solution increases, the target becomes less and less detectable. Eventually, obtaining white-light images at the target location is completely impaired due to the turbid fluid. In the following sections we will show the results of experiments carried out with the aim to demonstrate the DH microscopy capabilities of providing clear coherent imaging through blood. In particular, microscopy in through transmission will be shown, both in the case of amplitude imaging of a test target [167], and the more challenging situation in which a pure phase biological sample adheres on the inner wall of a microfluidic channel where a turbid volume of RBCs is injected, thus opening new perspectives for lab-on-chip investigations of cell adhesion processes and cell-substrate interactions [168]. We believe this study traces the route for real time noninvasive vessel inspection of microscopic particles dipped inside blood. As a fascinating perspective, in this way heart diseases could be prevented by detection and thickness measure of cholesterol plaques as well as blood clots settling down the internal vessel faces.

Blood flow producing a speckle-like pattern

In the previous sections, imaging through a turbid colloidal solution was demonstrated both in the dynamic and the quasi-static case. In the dynamic case, the Doppler frequency shift experienced by light that is scattered due to the moving colloids can be exploited to discard the unwanted radiation [115,165]. In the case of quasi-static liquid, the ensemble effect of scattering can be treated as a noise disturbance and a MLDH strategy can be implemented, taking advantage of the noise diversity introduced by the turbid medium [166]. The same method is demonstrated to be successful when live self-propelling objects are responsible for light scattering [169]. However, in these initial experiments the test turbid medium was a solution made of milk, whose colloidal particles have a typical diameter of about $500\ \mathrm{nm}$, so that the sole action of the Brownian motion was sufficient to provide enough temporal diversity between the holograms in case of quasi-static fluid. In the case of blood, which is a biological fluid of higher interest for biomedical applications, the typical diameter size of the colloids (i.e. the RBCs) is about $7-8\ \mu\mathrm{m}$. Hence, a characterization is required to assess whether the typical dimensions of the RBCs enables us to take advantage of their Brownian motion in order to see what lies beyond them. Moreover, an analysis aimed to study the interaction of the Doppler shift and

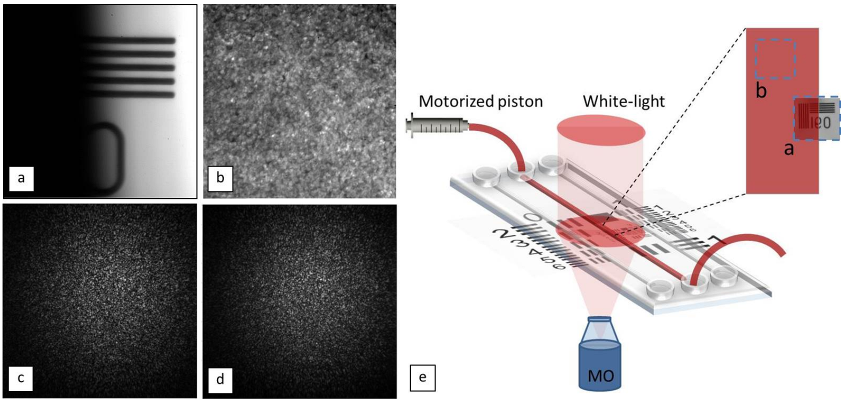

FIGURE 3.20: Imaging a test target through stationary blood [167]. (a) White-light image. Only the left side of the target is placed behind a microfluidic channel filled with blood. (b) White-light image of the channel filled with blood. (c) SLDH amplitude reconstruction. (d) MLDH amplitude reconstruction. (e) Sketch of the set-up used to obtain the images in (a) and (b). MO: Microscope Objective.

ML gain at different fluid velocities is of great interest to understand which conditions provide clear imaging through blood. In the following subsections we will first describe the analysis method we adopted to assess the feasibility and the limits of imaging through blood. This is based on properly defined correlation coefficients. Then, the experimental results will be reported and discussed.

Analysis method

In a first experiment we recorded and processed multiple holograms of a test target placed behind a microfluidic chip where blood was injected at a tunable velocity, as sketched in Fig. 3.20(e). Our aim was to prove the capability of Single-Look Digital Holography (SLDH) of seeing through blood flowing at a velocity overcoming a proper threshold (hereafter we will refer to this condition as the dynamic case) [167]. We gradually decreased the fluid speed to study the behavior of the imaging system in a velocity range herein referred to as low-speed region. In particular, it is interesting to estimate the boundaries of the low-speed and the dynamic regions, i.e. respectively the velocity for which the DH recording system starts to be sensitive to the Doppler shift (equivalently to the threshold in Lohmann's work [180]) and the fluid speed in correspondence of which the contribution of the RBCs is completely discarded.

In the case of quasi-static blood the object beam brings both the contributions of the ballistic photons scattered by the RBCs and the useful information diffused by the target, i.e. the signal corresponding to the photons passing through the turbid layer without experiencing collisions with the colloids. The probability to receive unscattered photons is proportional to the laser power (i.e. to the photon density) and decreases when the dimensions of the colloids augment. If the blood velocity overcomes a certain threshold, these contributions cannot participate in the process of fringe formation on the recording plane, thus getting discarded. In these conditions, no further processing is necessary. Conversely, if the medium speed is not enough to take advantage of the Doppler, the recording device receives the coherent superposition of multiple interfering contributions due to the useful signal diffused by the target and the scattering of the photons impinging on the RBCs. In the low speed region we can model the behavior of the imaging system by foreseeing the presence of two velocity thresholds, namely ν_{T1} and ν_{T2} . If $\nu < \nu_{T1}$all the photons scattered by the RBCs contribute to the interference process on the hologram plane. When $\nu_{T1} < \nu < \nu_{T2}$ more and more scattering contributions start to be shifted due to the Doppler effect, so that they are discarded. Finally, if $\nu < \nu_{T2}$ most of the photons hitting the RBCs are rejected from the formation of the fringe pattern (beginning of the dynamic region). In other words, since the dynamic region is reached, the turbid medium starts to behave, from the imaging system point of view, as a transparent fluid [167]. As a result of the ML processing, the useful signal is expected to get enhanced with respect to the unwanted scattering radiation, resulting in a smoother trend of the gray level distribution in the homogeneous areas of the image and a sharpness improvement on the edges. Again, the Dispersion index can be used to quantify the ML improvement. In this analysis we consider the Dispersion index $DI_{C,ML}(\nu)$ [%] as a function of the fluid speed. To measure the boundaries of the aforementioned velocity regions, we calculated the correlation coefficient $\rho_{SL-n} = \rho(n, \nu)$ of each image with respect to the first frame of the stack (i.e. the SL image). Furthermore, we defined and measured a global correlation coefficient as follows:

$$\rho_G = \frac{1}{\binom{N}{2}} \sum_{\substack{i,j=1 \\ i \neq j}}^{N} \frac{\langle |C_{SL-i}| \left|C_{SL-j}\right| \rangle}{\sqrt{\langle |C_{SL-i}|^2 \rangle \langle \left|C_{SL-j}\right|^2 \rangle}} = \rho_G(\nu), \tag{3.33}$$

where the sum is performed over the number of possible combinations of the observables, i.e. it accounts for the correlation between each couple of images of the stack.

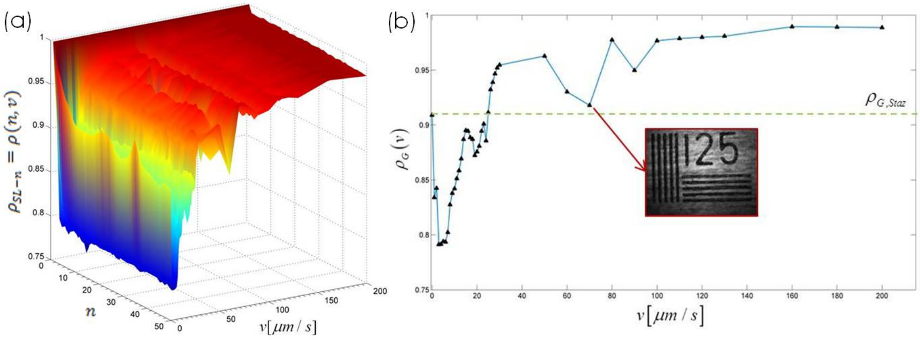

FIGURE 3.21: (a) Correlation coefficient with respect to the first acquisition, as a function of v and the frame index, n. (b) Global correlation coefficient as a function of the fluid speed, v [167].

Results and discussion

The employed DH set-up is the MachZehnder interferometer in transmission configuration described in Section 2.3. The laser source emits a beam at $\lambda = 669\ \mathrm{nm}$ wavelength and the detector is a CCD camera with $p_x = p_y = 6.7\ \mu\mathrm{m}$ pixel pitch. In our experiments, a USAF test resolution chart ($125\ \mathrm{lines/mm}$) was placed behind a microfluidic channel, whose depth was $200\ \mu\mathrm{m}$ in the optical axis direction, where blood was injected at tunable velocity varying in the range $\{1-200\}\,[\mu\mathrm{m/s}]$. The CCD integration period was $\tau = 40\ \mathrm{ms}$. . For each velocity, $N = 50$ holograms were captured and processed as previously described. In Fig. 3.20(c), the SL amplitude, $|C_{SL-1}(x_R, y_R, d; v = 0)|$ is reported, showing the severe scattering of the colloidal particles, i.e. the RBCs. In these conditions, the test target cannot be imaged or even detected through the turbid fluid.

Noteworthy, in this case the Brownian motion of the colloids is not sufficient to guarantee enough uncorrelation between the acquired holograms of the stack, as confirmed by the MLDH amplitude reconstruction $A_{ML}(x_R, y_R, d; v = 0)$ of Fig. 3.20(d). This result can be due to the diameter of the RBCs, which is about 15 times larger than the maximum size of the milk colloids [165,166], so that a movement of the fluid is needed to further decorrelate the holograms. In Fig. 3.21(a) and Fig. 3.21(b) we respectively report the 3D plot of the correlation coefficient $\rho_{SL-n} = \rho(n, v)$ and the global correlation coefficient $\rho_G(v)$, from which it is worth to notice that [167]:

1. As expected, for each fixed v the correlation decreases with time, as an effect of the fluid movement, till reaching a saturation value.

II. $\rho\left(n, \nu=0\right)=\rho_{Staz}\left(n\right)<1$, i.e. also in the stationary case a de-correlation is observed which is mainly due to the effect of the Brownian motion of the RBCs. Similarly, $\rho_G\left(\nu=0\right)<1$.

III. When ν increases from the null value, $\rho\left(\nu\right)$ and $\rho_G\left(\nu\right)$ decrease till reaching a minimum when $\nu=\nu_{T1}=5\mu m/s$. In this velocity region the imaging system is sensitive to the presence of the turbid fluid. After overcoming ν_{T1} more and more contributions reach the sensor after being frequency shifted out of the frequency band where the interference is allowed, so that the imaging system is expected to observe the target like it was seen through a fluid with a lower and lower colloid density.

IV. When $\nu=\nu_{T2}>30\mu m/s$ the correlation coefficients keep almost constant around a saturation value higher than 0.95 for each frame. Moreover, starting from $\nu=25\ \mu m/s$, the uncorrelation introduced by the colloids is lower than the uncorrelation corresponding to the stationary case, namely $\rho_{G,\,Staz}$. After exceeding ν_{T2}, any further velocity increase does not significantly affect the correlation functions, suggesting that the imaging system becomes insensitive to the presence of the RBCs. In Figure 3.21(b), the decrease of the correlation curve for some the velocity values higher than ν_{T2} is probably due to a temporary malfunctioning of the fluid injection system. Nevertheless, whenever the global correlation function is higher than $\rho_{G,\ Staz}$ in the dynamic region, the imaging system is found to provide a clear image of the target through the moving blood (see the inset in Fig. 3.21(b)). In other words, due to the Doppler effect, the imaging system starts to see less contributions due to the RBCs than in the stationary case.

Figure 3.22 shows the SL amplitude reconstructions of the holograms acquired at different fluid velocities. As expected, the target is not detectable until the first threshold is reached as a result of the strong medium scattering, while it becomes more and more visible when ν increases. In particular, it starts to be detectable, though barely visible, at $\nu=10\mu m/s$, and clearly observable for $\nu>\nu_{T2}$, i.e. when the decorrelating colloids are not perceptible anymore. The spatial resolution of the restored images is 845 nm in both the x_R and the y_R directions. Noteworthy, the oscillation of $\rho_G\left(\nu\right)$ in the region $\nu\in\left[\nu_{T1}, \nu_{T2}\right]$ reflects in the amplitude reconstruction of Fig. 3.22(e), appearing slightly worse (i.e. more degraded) than the image shown in Fig. 3.22(d), despite this was obtained at higher velocity. The oscillating behavior of the improvement in this region can be modeled as a cardinal sinusoid function of the Doppler shift for each fixed integration time of the sensor [180]. Moreover, the uncorrelation

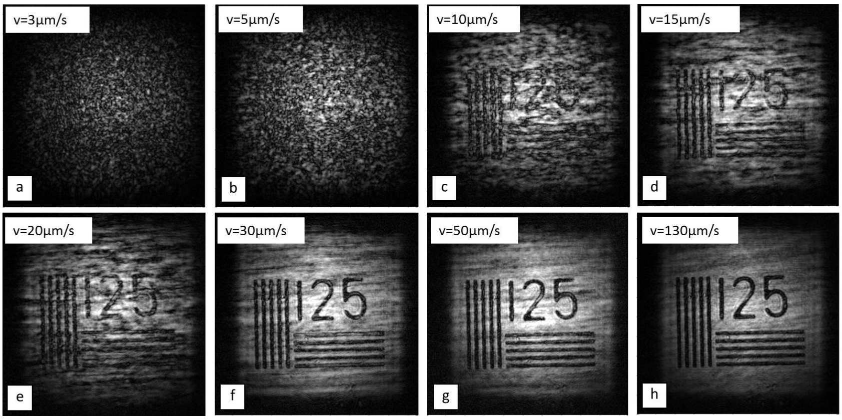

FIGURE 3.22: Amplitude SL reconstructions of the test chart through blood flowing at different velocities [167].

provided by the movement of the RBCs in the velocity region $\nu < \nu_{T1}$ suggests that a significant improvement can be achieved thanks to the ML processing. The pseudo 3-D views of Fig. 3.23 show a comparison between $|C_{SL}|$ and A_{ML} at the same velocity. It is apparent the action of the ML which reinforces the useful signal and improves the image sharpness, lowering the contribution of the undesired scattering. As a result, the target gets detectable at a lower velocity at the price of multiple recordings (see Figs. 3.23(a,b)). For instance, at $\nu = 10\mu m/s$ (Fig. 3.23(c)) the target is clearly visible in the ML reconstruction. At higher velocities ($\nu > \nu_{T2}$) the Doppler shift plays the major role (with respect to the ML gain) in determining the overall improvement and both the SL and the ML images provide a clear vision of the target through blood (see Fig. 3.23(d)). The ML improvement at different velocities has been quantified measuring the dispersion index $DI_{C,ML}(\nu, N = 50)$, whose trend is shown in Fig. 3.24. The lower $DI_{C,ML}$ is, the higher ML improvement is achievable. Again, we observe the maximum gain when $\nu = \nu_{T1}$ and a gain saturation when $\nu > \nu_{T2}$. Remarkably, these results are in good agreement with the analysis carried out in [180], which suggests that H^{+}, after accounting for the time integration of the recording system, is mainly modulated by the function:

$$\operatorname{sinc}(\tau\nu_D) = \frac{\sin(\pi\tau\nu_D)}{(\pi\tau\nu_D)}, \tag{3.34}$$

i.e., the photons shifted more than $1/\tau$ do not contribute significantly to the integral of Eq. (3.18). In this sense, we can interpret the correlation functions of Fig.

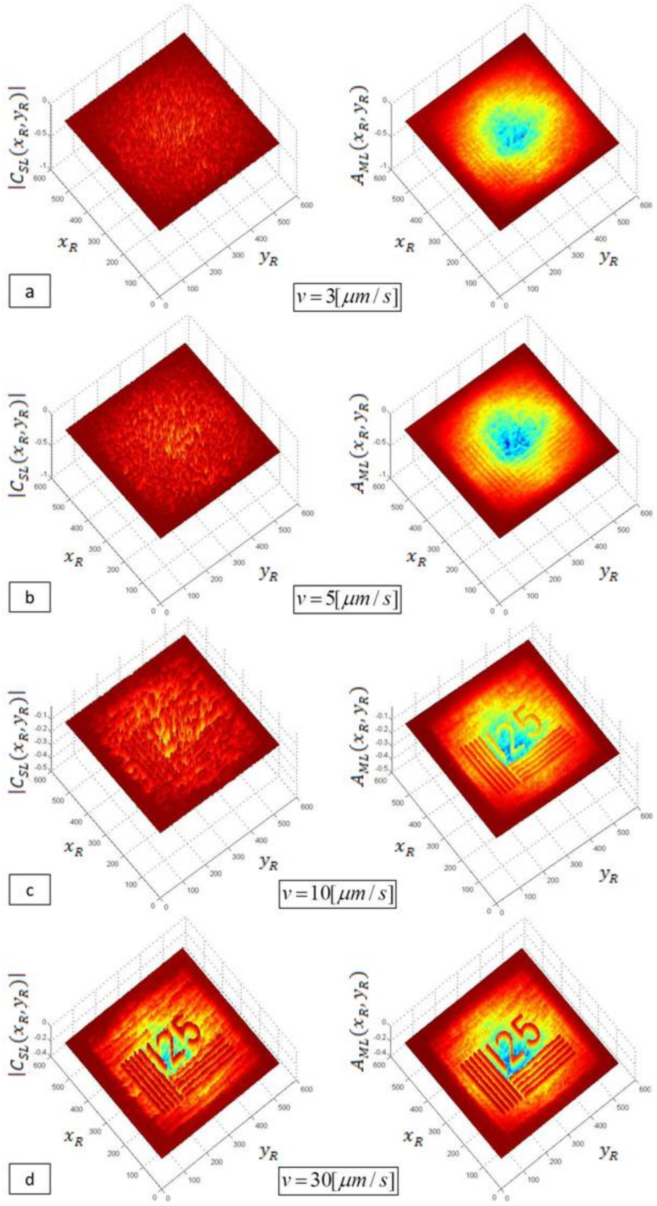

Figure 3.23: Comparison between SL (left) and ML (right) amplitude reconstructions of the test chart seen through blood moving at different velocities. Thanks to the ML gain the target gets visible at lower speed [167].

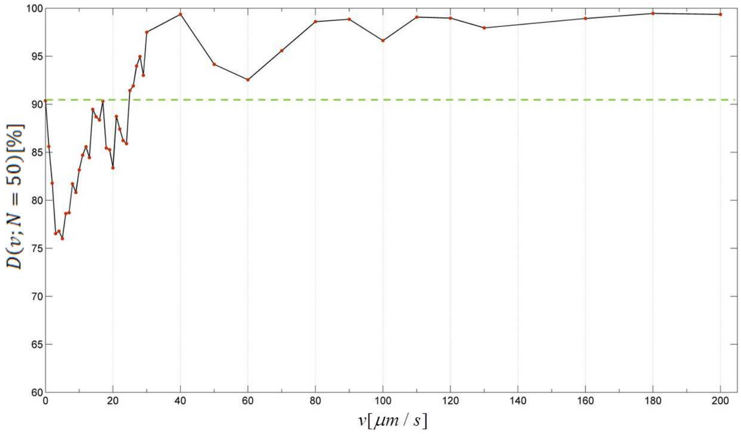

FIGURE 3.24: Normalized dispersion index, D [%] versus v. The plot is obtained for N=50 holograms being processed [167].

3.21 as indicators of the visibility of the fringes due to the sole ballistic photons scattered by the RBCs. The range of speed analyzed in this study corresponds to the velocities usually employed in microfluidic systems [167]. In case of human veins examinations, the typically wide velocity distribution of the RBCs in human vessels could be taken into account simply foreseeing an enlarging of the region between the two thresholds, as not the whole population of RBCs would move at enough speed to be discarded. Nevertheless, the blood flow speed in capillaries and arteries varies from 300 $\mu m/s$ to 300 mm/s, depending on the vessel diameter. Therefore, we believe that the proposed technique could be suitable for in-vivo vein investigations, as the velocities of the RBCs are in the saturation region of the correlation coefficient. This study traces the route for the real-time noninvasive inspection of human blood vessels, in order to achieve quantitative information about the thickness of cholesterol plaques or even blood clots settling down on the vessel walls. In the next Section, the problem of phase contrast imaging through blood will be addressed, studying the adhesion of a fibroblast cell immersed in a liquid volume filled with RBCs at high concentration [115,168].

IMAGING ADHERENT CELLS THROUGH A TURBID FLOW OF RBCS

For the sake of clarity, in Fig. 3.25 we resume different cases we have investigated so far, compared in terms of the ratio $R = D_O/D_T$ between the size

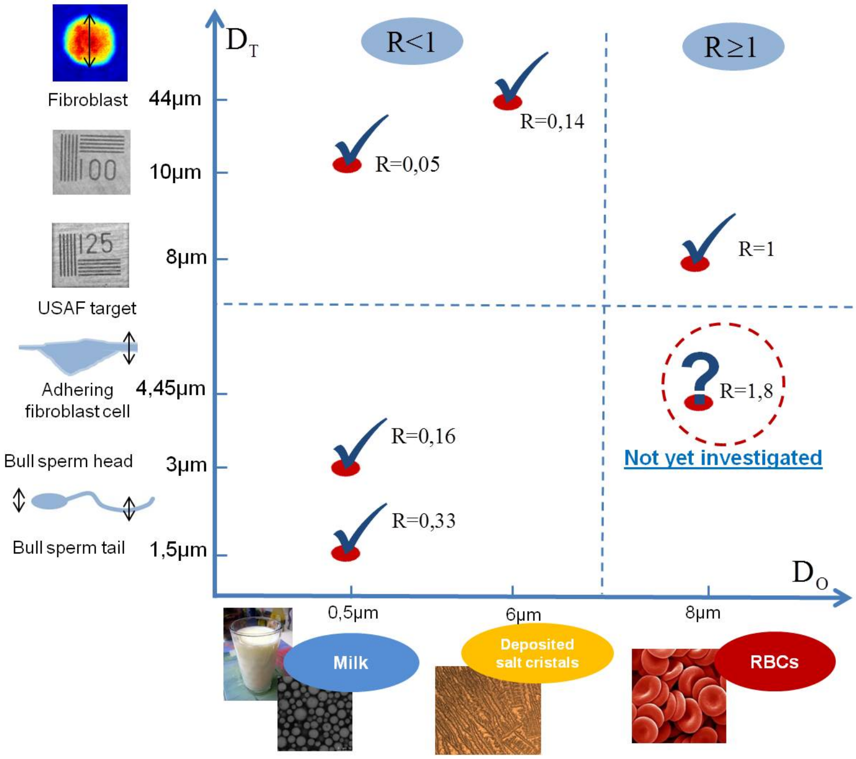

FIGURE 3.25: An overview of the experiments so far carried out to investigate the problem of revealing targets hidden behind turbid/scattering layers. For each case, the ratio R between the characteristic length of the occluding objects and target size is reported. Depending on R, different strategies have to be adopted to solve the imaging problem [168].

of the occluding objects, D_O, i.e. the dimension of the smaller element of the scattering/turbid medium, and the dimensions of the target to be imaged and/or detected D_T. As it can be seen in Fig. 3.25, one quadrant has not been explored yet. Indeed, a different approach has to be adopted when the size of the specimen is comparable to the dimen-sions of the flowing objects, and also when the size of the specimen is big enough to prevent one from considering them as scattering particles, and instead they need to be considered as elements that introduce distortions in the optical wavefront passing through the sample [168]. In particular, a volume filled with RBCs is a challenging case as the typical diameter of the colloids is in the range of $5 - 10\ \mu m$ and their Brownian motion does not provide enough diversity to allow MLDH to look beyond quasi-static blood. In Section 3.4.1, amplitude images of a test resolution target ($125 lines/mm$) have been obtained through a low-speed blood flow. As shown in Fig. 3.25, all the cases faced so far correspond to values $R \leqslant 1$. It is worth analysing the situation in which $D_T < D_O$, i.e. the dimensions of the target are smaller than the size of the occluding objects, corresponding to the region $R > 1$. In fact, in this case the obstacles cannot be assumed as scattering sources. The distance between the acquisition plane and the objective lens is so small that each single occluding object introduces an unknown time variable phase delay, and the ensemble effect cannot be regarded as a speckle pattern, but a wavefront distortion due to multiple refractions by thin pure phase objects. In the following sub-sections we will show a challenging result, i.e. that both amplitude imaging and phase-contrast mapping of cells hidden behind a flow of RBCs can be obtained in harsh noise and blurring situation. Moreover, we will show that the decorrelation introduced by the movement of the occluding objects inside the FoV allows for the enhancement of the useful signal, thus providing very clear images [168]. This permits the non-invasive visualization of cell adhesion processes in LoC platforms and many other study cases where conventional microscopy is not of help.

Synthesis of the ML phase-contrast map

The imaging problem we afforded is sketched in Fig. 3.26. A DH recording setup in transmission configuration was adopted for the scope. The object beam impinges on the channel where a turbid RBC solution flows at speed v and a cell (i.e. a pure phase object) adheres on its inner wall. The velocity of each RBC inside the medium is considered here unknown and not adjustable. Moreover, this is neither constant in time nor in space, depending on the position inside the channel of each occluding object. These assumptions stand in all the cases in which a control of the medium is not achievable. While flow-

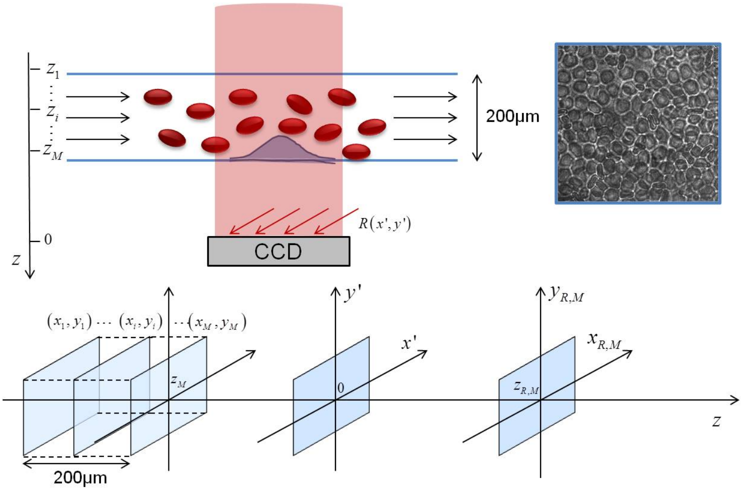

FIGURE 3.26: The experimental conditions: a cell adheres on the inner wall of a microfluidic channel with the RBC flow occupying different positions on the optical axis [168]. An out-of-focus recording in the plane (x', y') collects information from the whole volume and numerical reconstruction is performed in the cell best-focus plane, $(x_{R,M}, y_{R,M}; z = z_{R,M})$.

ing along the channel, the RBCs occupy different positions $(z_1, \ldots, z_i, \ldots, z_M)$ along the z axis, so that we can study the blood volume as composed of M planes $\{(x_1, y_1), \ldots, (x_M, y_M)\}$, and we can assume the cell located in the plane $(x_M, y_M, z = z_M)$. The object beam passes through the considered volume bringing the whole complex information of both the RBCs and the cell adhering on the inner channel face. After the object wave and the reference wave interferes in the acquisition plane (x', y'), the recorded hologram contains the 3D information of the objects present inside the whole analyzed volume. Unfortunately, the object beam brings the integral information of all the objects on its path, so that it is not possible to resolve them. As a consequence, the SL complex reconstruction in the cell focus plane, $C_{SL}(x_{R,M}, y_{R,M}; z = z_{R,M})$ is unavoidably corrupted due to the signal diffused by the RBCs. However, the movement of the occluding objects provides a time uncorrelation between multiple acquisitions, while the cell remains static during the acquisition time, so that a stack of holograms can be exploited to enhance the useful signal. Hence, a ML amplitude reconstruction can be trivially synthesized as in Eq. (3.23). If the cell best-focus plane is unknown, this can be estimated using Eq. (3.32). In order to obtain an ML phase map, an incoherent average of the unwrapped SL phase signals would be required, i.e. the synthesis formula given in the second row of Eq. (3.23) should be implemented. Unfortunately, in such a challenging case, due to the severe distortion introduced by the occluding objects, any unwrapping algorithm fails to recover reliable phase maps, introducing errors and unexpected phase jumps which are strongly dependent on the phase error of each SL wrapped phase signal. Such error variability prevents us from combining the phase reconstructions using Eq. (3.23). However, a good quality ML wrapped phase reconstruction can be obtained if the sine and cosine components of the SL phase signals are separately averaged as follows [168,187,205]:

$$\begin{aligned}&\hat{\varphi}_{ML}\left(x_R, y_R, z=\hat{z}_{R,M}\right) = \\ &= \mathrm{Unwrap}\left[\tan^{-1}\left\{\frac{\sum_{n=1}^{N}\sin\left[\mathrm{Angle}\left(C_{SL-i}\left(x_{R,M}, y_{R,M}; z=\hat{z}_{R,M}\right)\right)\right]}{\sum_{n=1}^{N}\cos\left[\mathrm{Angle}\left(C_{SL-i}\left(x_{R,M}, y_{R,M}; z=\hat{z}_{R,M}\right)\right)\right]}\right\}\right],\end{aligned} \tag{3.35}$$

where each component of the sum is obtained after compensating the same reference hologram. In this way the unwrapping algorithm has to be applied just once to the ML wrapped phase signal, thus avoiding the above mentioned processing errors.

Experimental results

In our experiments we placed a fibroblast cell in a Polymethylmethacrylate (PMMA) microfluidic channel coated with polylysine in order to favorite the mechanism of cell adhesion. The channel was 1000 μm wide, 58.5 mm long and 200 μm deep. We inserted the chip on the object beam path of an interferometer in transmission configuration, as sketched in Section 2.3. A 400 mW at 532 nm, fiber-coupled laser light acts as source for the Mach-Zehnder interferometer, whose main beam is directed into a customized inverted microscope equipped with an oil-immersion 100x objective, allowing bright-field imaging of the sample. The reference beam is recombined with the object beam, generating digital holograms of the samples that are recorded by a 1024×1024 CCD camera, 6.45 μm pixel size (AVT Technologies). All experiments were done with heparinized blood drawn within the hour before use. The sample was prepared as follows: approximately 3 mL of heparinized whole blood were withdrawn into a hematocrit tube. Blood was centrifuged at room temperature, for 15 minutes at 2500 rpm in order to separate it into its component parts (plasma, buffy coat and red blood cells at the bottom of the centrifuge tube). The pellet ($\approx$ 1.5 mL) was collected and 100 μL of erythrocytes were diluted

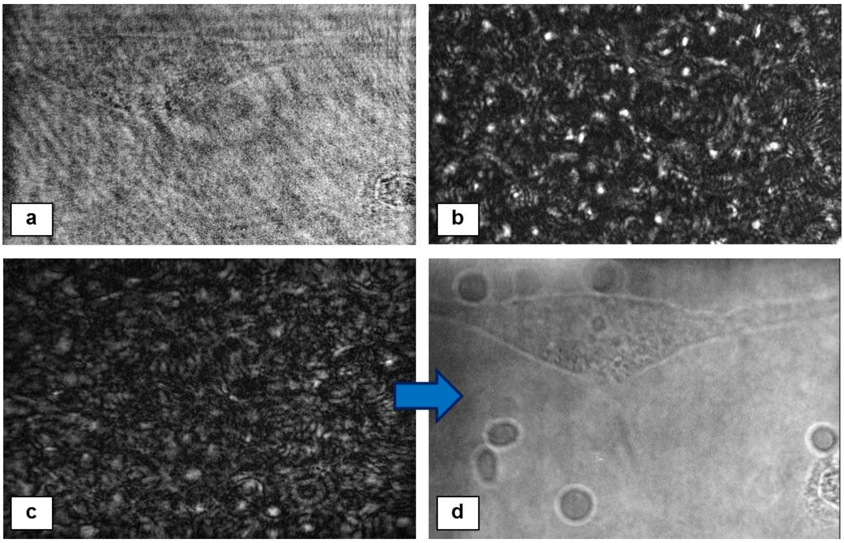

FIGURE 3.27: Imaging a fibroblast cell adhering on the channel wall [168]. (a) Amplitude reconstruction in the case of transparent medium. (b) Hologram acquired after injecting RBCs inside the channel. (c) SL amplitude reconstruction of the hologram in (b). (d) ML amplitude reconstruction, where the image of the adhering cell is recovered from turbidity.

with a saline solution of 0.90% w/v of Sodium chloride (NaCl) in sterile water up to a final volume of 2 mL. The osmolarity of the medium was about 308 $mOsm/L$ and it was isotonic with the membrane of red blood cells. No visible hemolysis occurred. RBCs thus obtained are injected into the microfluidic channel using a syringe pump controlled by a micrometric translator.

At first we acquired a hologram of the cell dipped inside a cell cultivation medium (Dulbecco's modified eagle medium, DMEM) after waiting for its adhesion on the inner channel wall [168]. The medium was transparent to the visible wavelength, so that from the amplitude reconstruction image of the cell in the plane $(x_{R,M}, y_{R,M}; z = \hat{z}_{R,M})$, shown in Fig. 3.27(a), it is possible to study the morphological change due to the cell spreading on the PMMA substrate. Since this is a pure phase object, a low-contrast image of the cell is provided by the amplitude image in its own best-focus plane, and the reconstruction is also corrupted by coherent speckle and additive incoherent noise components. Furthermore, a noise source is constituted by the presence of the PMMA channel walls introducing double reflections and, hence, an unwanted additional fringe pattern on the acquired hologram.

Then, we let RBCs flow inside the channel and we acquired a sequence of $N = 150$ holograms with frame rate $r = 11\ s^{-1}$, so that the overall acquisition time was $T = 13.6$ s (during the time T the cell keeps static on the substrate). Fig. 3.27(b) shows one of the acquired holograms extracted from the whole time sequence. In Fig. 3.27(b) neither the cell or the RBCs are in focus and the degradation due to the occluding objects inside the analyzed volume hinders the visualization of the sample. Similarly, if one single hologram is reconstructed at distance $z = \hat{z}_{R,M}$. the presence of the RBCs in different positions z_i, which are thus reconstructed out of their respective best-focus planes, hides the useful signal and definitely impairs the cell visualization, as shown in the SL image of Fig. 3.27(c). On the contrary, a very sharp amplitude map of the cell is provided by the ML reconstruction, A_{ML}, of Fig. 3.27(d), where the contribution of the RBCs is completely discarded and the cell can be imaged with enhanced contrast. Noteworthy, the decorrelation provided by the occluding objects has an advantageous effect on the ML reconstruction, as this results in a remarkable noise suppression in both the object area and the background. Hence, the numerical resolution of the image improves as well. It is worth noticing that the ML processing does not provide super resolution capabilities, i.e. it does not overcome the resolution limit allowed by the optical system. However, the noise mitigation in the ML image enables the enhancement of the useful signal so that the finer details of the object can be appreciated. In principle, these details could be also appreciated in the image of Fig. 3.27(a), because they correspond to spatial frequencies that are collected by the imaging system, but these are not visible because of the noise corrupting the image. On the contrary, from the map in Fig. 3.27(d) it is possible to distinguish clearly the cell points of adhesion and to locate the position of the cell nucleus, which are not visible in the reconstruction of Fig. 3.27(a) due to the noise sources mentioned above. In the map of Fig. 3.27(d) we visualize the signal of all the objects that keep static or move slowly during the acquisition time, T, so that some RBCs adhering on the inner channel wall or arrested in their movement by the cell itself are clearly recognizable (e.g. see the top of Fig. 3.27(d)) [168]. As a performance measure, we calculated the noise contrast $N_{C,ML}$, over the same homogeneous segment of the amplitude reconstructions obtained increasing the number of looks. The plot in Fig. 3.28 shows the behavior of $N_{C,ML}$ vs. N. In Fig. 3.28 we also reported the value $N_{C,ML}$ measured over the map obtained in the case of the channel free from RBCs (green dotted line), and the trend of the ideal curve obtainable in the case of the uncorrelated holograms (red solid line). As expected, the noise mitigation results in a reduction of the noise contrast (see the blue crosses in Fig. 3.28) and we found a good agreement between the

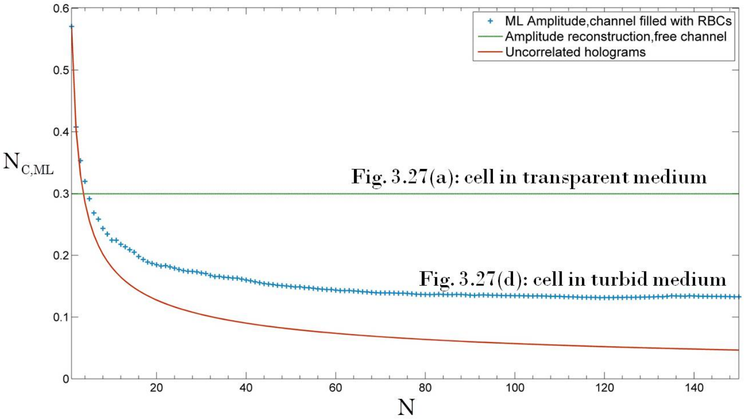

FIGURE 3.28: Noise contrast vs. the number of looks [168].

measured and the ideal trend. The degradation source constituted by the injection of RBCs inside the channel is at the same time the key to provide the time diversity highly required for the hologram denoising purposes. Noteworthy, $N = 5$ acquisitions are sufficient to improve the SNR with respect to the case of Fig. 3.27(a). Moreover, the saturation value is reached after combining $N = 50$ reconstructions, so that similar results could be obtained reducing the overall acquisition time significantly ($T_{n=50} = 4.5$ s). Indeed, we measured $N_{C,SL} = 0.57$, and $N_{C,ML}$ $(n = 50) = 0.15$ in the SL and ML image respectively, i.e. in correspondence of the saturation value we measured a ML gain of 74% with respect to the SL reconstruction, while we found $N_C = 0.30$ in case of the clear channel. In other words, the SNR of the image recovered through the turbid medium is twice the SNR value of the image acquired through a transparent channel, as the time diversity introduced by such random phase shifters (i.e. the RBCs) helps to significantly reduce the coherent artifacts affecting DH recordings. This is an intriguing result showing that the RBCs can accomplish an optical task, acting on the imaging system as a decorrelation device (just like a moving diffuser does) and providing an image quality comparable with any other incoherent diagnostic system [168].

The ML processing is also effective in retrieving the phase-contrast map of the cell. Figure 3.29(a) and Fig. 3.29(d) respectively show the phase map and the corresponding pseudo-3D view of the fibroblast dipped inside the transparent medium, resulting in high contrast images as a consequence of the local optical path variation of the object beam when passing through the cell. The severe degradation due to the injection of the RBCs is apparent in the map of Fig. 3.29(b), where the wrapped phase signal is represented. Apparently, in such conditions no information can be retrieved at all about the cell shape or its optical thickness, as the RBCs act as phase objects adding unpredictable contributions to the phase delay of the object beam. These also provoke phase jumps whose positions are strongly variable from one image to the other, thus impairing a classical ML of the unwrapped phase signals, as discussed above. On the contrary, if the ML is performed adopting the synthesis formula of Eq. (3.35), it is possible to combine wrapped phase signals where only the noise decorrelates over time while the useful contributions reinforce. The unwrapped ML phase map, $\hat{\varphi}_{ML}\left(x_R, y_R, z = \hat{z}_{R,M}\right)$, is reported in Fig. 3.29(c) and Fig. 3.29(e), where the cell shape is recuperated and its phase dynamic is almost totally recovered [168]. A noise degradation is still present in the signal $\hat{\varphi}_{ML}$, that can be minimized by increasing N or maintaining the same number of looks but increasing the time-decorrelation between them (e.g. decimating a longer sequence, as discussed in Section 3.3.2 [166]). However, despite the challenging noise conditions we found good agreement between the phase maps of Fig. 3.29(d) and Fig. 3.29(e). We quantified the phase accuracy by calculating the average phase dynamic between the object and the background area of the phase maps of Fig. 3.29(d) and Fig. 3.29(e). In terms of optical thickness, we found an error percentage lower than 0.1%, corresponding to an error percentage in terms of cell thickness lower than 1%.

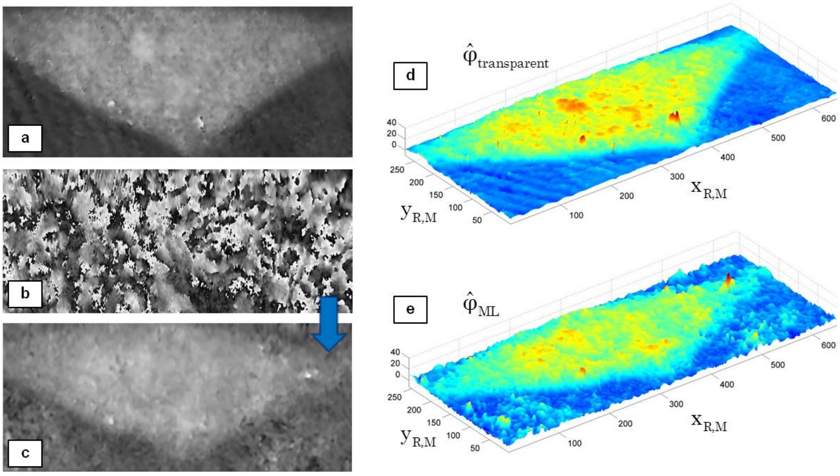

FIGURE 3.29: Phase-contrast mapping [115,168]. (a) Phase reconstruction in the case of the channel filled with transparent medium. (b) The SL phase reconstruction in the case of the channel filled with RBCs. (c) The ML phase reconstruction. (d) The pseudo-3D view of the phase map in (a). (e) The pseudo-3D view of the phase map in (c).

4

EMBEDDING DH IMAGING FUNCTIONS ONBOARD CHIP

In Chapter 1 the need for compact LoC systems with imaging functionalities embedded onboard has been highlighted, which is of great importance for the purposes of diagnostics at the point-of-care. However, at the current stage, the LoC is still far from being a widely used device in developing Countries and low-resource settings. As already discussed in Chapter 1, one of the major obstacles that prevent LoC from becoming a widely spread technology is the low compactness of the imaging system, so that a small chip is usually placed in a laboratory with bulky instruments, required for providing both imaging and fluidic control capabilities. From the imaging point of view, what is highly demanded is a recording modality that, using a compact setup and optical components, can yield high-throughput, quantitative, full-field imaging capabilities. Moreover, sample pre-treatment should be avoided, because diagnostics needs to be performed in absence of additional facilities and markers required to provide sample labeling. Furthermore, marking the sample is an invasive procedure which can alter its own behavior and, in turn, limits the variety of the experiment that can be performed onboard chip. By rapid inspection of Table 1, that compares the most used diagnostic methods exploitable for LoC microscopy, the most suitable ones are the HOM method [93] and the DH microscopy. The former is very compact but, as any lensless method, it suffers from poor magnification and, in turn, limited resolution. On the other hand, the main limitation of DH microscopy is the low compactness of the interferometric setup it requires. Moreover, at this stage, it does not fully exploit the one-shot volumetric imaging capabilities, which could augment the throughput dramatically. From our analysis, we recognize DH as the best candidate for LoC imaging, due to its potentially groundbreaking capabilities, and because it shows the most interesting development perspectives. Hence, our approach is to improve lens-based DH microscopy, introducing novel recording and reconstruction strategies, specifically suited to promote the compactness of the imaging system and augment the throughput, as it will be shown in the following of the current Chapter.

PHASE SHIFTING SPACE-TIME SCANNING INTERFEROMETRY (PS-STSI)

A common challenge to both DH and PSI is related to the quality enhancement of the interferograms/holograms in terms of FoV, resolution, and SNR. In this framework, many methods rely on scanning modalities to acquire multiple interference patterns. If properly combined, these provide images with improved resolution and extended FoV, as in the case of the synthesis of hologram aperture by femtosecond-pulsed DH [206], Optical Scanning Holography (OSH), where a point-detector collects light diffused by the object and a heterodyne demodulation decodes the useful object information [207,208], or Lensless Object Scanning Holography (LOSH) [209]. In LOSH, a scanning of the CCD camera or an illumination angle diversity has to be provided for the scope and the recorded fringe patterns have to be properly combined in a suitable domain to generate a synthetic hologram or interferogram entirely containing the required information. This operation can be complex and the method performance turns out to be object spectrum dependent. Besides, object scanning and illumination angle diversity are exploited in techniques such as Ptychography and the recently developed Fourier Ptychographic Microscopy (FPM) for retrieving, by an iterative algorithm, the full complex object field from a number of intensity measures obtained with coherent and LED sources respectively [210,211]. On the other hand, MLDH [138,139,158,166-169] incoherently combines multiple holograms acquired in time [212,213], wavelength [214], or polarization diversity [184] to achieve remarkable noise reduction in the numerical reconstruction.

Here we introduce and discuss a different imaging modality, named Space-Time Scanning Interferometry (STSI), which exploits the object movement to synthesize space-time interferograms with extended FoV and improved noise contrast, starting from interferograms acquired with a linear array of sensing elements instead of a 2D array detector [215]. CCD linear arrays are obviously less expensive and more compact than the standard 2D CCD sensor. Moreover, they can achieve higher frame rate of acquisition. They already find different successful applications such as in ref. [216], where a bacteria colony image scanner based on linear array CCD is patented or, for example, in Linear Array Panoramic Aerial Camera [217]. The modality presented here can be valuable and exploitable in many fields of application but especially where a relative lateral displacement between the imaging system and the object is intrinsic in the process under investigation. In particular, the new method we propose looks particularly advantageous whenever the object movement is an intrinsic feature of the investigated system, as e.g. in the case of microfluidics, thus

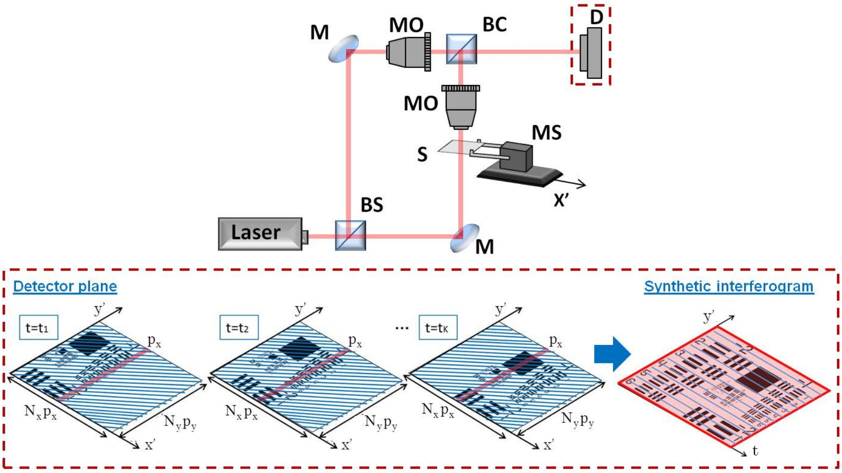

Figure 4.1: Set-up employed to build-up synthetic interferograms [215]. BS: Beam Splitter. M: Mirror. MO: Microscope Objective. BC: Beam Combiner. MS: Moving Stage. S: Sample. D: Detector. On the bottom the process of synthesis of an extended FoV space-time interferogram is sketched. The red line indicates the active sensor elements at each acquisition in case a linear detector is employed. The interferometric fringes are reported with the blue solid lines.

allowing to make a step toward the integration of the imaging functionalities onboard LoC platforms. On the other hand, if linear arrays made of more than a single pixel row (it is important to note that the most of commercially available liner arrays usually have a number of rows ranging from $N_x = 1$ to $N_x = 128$), or a common CCD camera are available, the proposed technique can be exploited to carry out PSI with enhanced FoV, SNR and, above all, with a small subset of detector elements. We named this approach PS-STSI [215].

Usually, in the standard PSI technique, the phase steps between three or more phase-shifted interferograms, acquired successively, are induced using piezoelectric devices in the reference arm. On the contrary, in PS-STSI the set-up does not rely on moving parts in order to induce the required phase-shift, but we exploit the object movement to create synthetic interferograms mapped in the hybrid space-time domain, shifted each other of the desired phase step. As described in the following subsection, starting from an interferogram with tilted fringes, each synthetic interferogram is built from the time sequence of a single row of the CCD sensor, recorded during the object movement. The number of rows needed to obtain all the phase-shifted interferograms, and, therefore, the dimension of the necessary CCD sensor, depends on the accepted phase-shifting error. Indeed, the minimum phase-shift obtainable with the proposed method is inversely proportional to the period of the spatial carrier. In principle, the whole complex object field could be retrieved from just only one synthetic interferogram if the spatial carrier frequency is such that in the Fourier transform the conjugated orders can be separated. This means that a single pixel row suffices as detector.

In the next subsection, the PS-STSI working principle will be described in detail, referring to the general case where multiple phase-shifted STSIs can be obtained, from which the whole complex information of the object can be retrieved [215]. Then, we will show some experimental results obtained testing the technique with different objects, a test target and some intricate shaped polymeric drops, respectively, while these are shifted by means of a linear translation stage. It is clear that such approach paves the way to new solutions in the field of bio-imaging and microfluidics, where the sample inherently moves along the channel, so that the proposed imaging modality offers the above mentioned advantages but having no cost associated with. The application of STSI to microfluidics will be discussed in Section 4.2.

THEORETICAL FORMULATION OF PS-STSI

Let

$$\begin{aligned}&\left[S_1\left(x',y',t=t_1\right),\ldots,S_Q\left(x',y',t=t_Q\right)\right],\\ &\qquad\qquad\qquad\qquad x'=p_x,\ldots,N_xp_x\\ &\qquad\qquad\qquad\qquad y'=p_y,\ldots,N_yp_y\end{aligned}\tag{4.1}$$

be the stack of $Q = Tr$ interferograms acquired in the recording plane $(x^{'},y')$ at the instants $\{t_1,\ldots,t_Q\}$ while moving the object along the direction. If the same selected line $x' = x_0^{'}$ is extracted from the acquired stack, we can obtain the set of vectors:

$$\begin{aligned}\mathbf{c}_{01} &= S_1\left(x'=x_0^{'},y',t=t_1\right)\\ \mathbf{c}_{02} &= S_2\left(x'=x_0^{'},y',t=t_2\right)\\ &\vdots\\ \mathbf{c}_{0Q} &= S_Q\left(x'=x_0^{'},y',t=t_Q\right).\end{aligned}\tag{4.2}$$

Sorting these vectors in a matrix, we can build a synthetic, space-time interferogram $I_0\left(y',t\right)$. The possibility to build an extended FoV synthetic interferogram from one single line can be exploited to replace the 2D $N_x \times N_y$ sensor with a linear detector consisting of N_y elements, more compact and achieving higher frame rate. The process of synthesis of a space-time interferogram is sketched on the bottom of Fig. 4.1, where the sensing elements of the detector are highlighted with a red line as well as the extended FoV obtainable after the interferogram synthesis [215]. Noteworthy, the spatial distribution of the noise, which is always present due to the acquisition system, changes when passing from a $x' - y'$ interferogram to a $y' - t$ synthetic one. Indeed, in the space-time interferogram this turns out to be variable only along the y' direction whenever the acquisition system keeps stable during the time T. As a consequence, this is easier to be estimated and filtered out in the Fourier domain. Moreover, if a 2D sensor is employed, N_x different synthetic interferograms are obtainable by sweeping all the lines $x' = x_i^{'}$, $i = 1, \dots, N_x$, so that we can build the following stack:

$$S = \begin{bmatrix} \mathbf{c}_{01} & \mathbf{c}_{02} & \cdots & \mathbf{c}_{0Q} \\ \mathbf{c}_{11} & \mathbf{c}_{12} & \cdots & \mathbf{c}_{1Q} \\ \vdots & \vdots & \ddots & \vdots \\ \mathbf{c}_{N_x 1} & \mathbf{c}_{N_x 2} & & \mathbf{c}_{N_x Q} \end{bmatrix} = \begin{bmatrix} I_0\,(y', t) \\ I_0\,(y', t) \\ \vdots \\ I_{N_x}\,(y', t) \end{bmatrix}, \tag{4.3}$$

corresponding to $N_x - 1$ different phase shifts. The minimum phase shift obtainable with the proposed method depends on the acquisition parameters as follows:

$$\Delta\varphi_{min} = \frac{2\pi p_x \sin\theta_x}{p} \tag{4.4}$$

where p is the pitch of the spatial carrier, and θ_x is the fringe inclination on the acquisition plane (x', y') with respect to the x' axis. The fringe inclination θ_x also establishes the relationship between p and the pitch of the spatial carrier in the plane (y', t), namely $p' = p/\cos\theta_x$. Hence, it results that a fringe system orthogonal to the movement direction ($\theta_x = \pi/2$) does not provide an interferogram in the plane (y', t), while fringes parallel to the x' axis ($\theta_x = 0$) allow the synthesis of space-time interferograms but cannot provide any phase-shift between them. In particular, the range of admissible angles depends on the sensor parameters as follows:

$$\tan^{-1}\left(\frac{p_y}{N_x p_x}\right) \leqslant \theta_x \leqslant \tan^{-1}\left(\frac{N_y p_y}{p_x}\right). \tag{4.5}$$

The complex object wavefront can be obtained applying a phase shifting algorithm to a subset of properly selected elements of S. These elements have to be

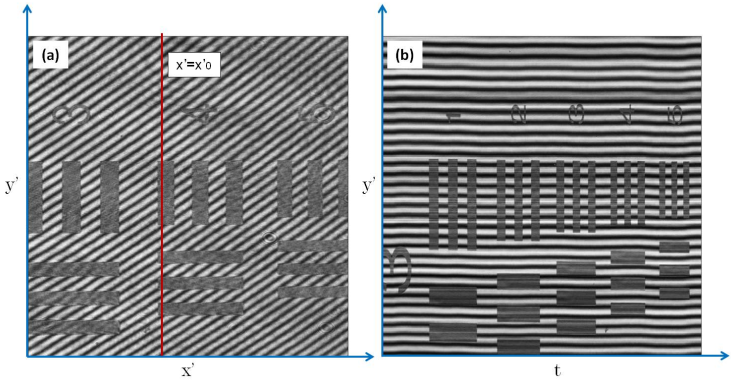

FIGURE 4.2: Interferometric imaging of a test resolution target [215]. (a) Acquired limited FoV interferogram. (b) Extended FoV synthetic interferogram built from the red column in Fig. 4.2(a) while scanning the target along the x' direction.

chosen in order to provide the required phase shift between them. Then, one of the formulas introduced in Section 1.3.4 (see Eqs. (1.10-1.12)) can be applied to estimate the object, both in amplitude and phase. Once the whole complex field is retrieved, this can be numerically propagated back or forth as occurs in DH modality. In PSI the phase variation is obtained introducing a delay line in the path of the reference beam, e.g. using piezoelectric mirror devices. On the contrary, we exploit the object movement as shown in the following section.

PHASE RETRIEVAL ADOPTING PS-STSI

The experimental set-up is the Mach-Zehnder interferometer shown in Fig. 4.1. The laser wavelength was $\lambda = 632$ nm, and a CCD camera with pixel pitches $p_x = p_y = 4.4$ µm was used to collect the pattern of interference between the object beam and the reference. A remote controlled linear stage was used to move the object along the x' direction at a proper speed, such that the object was well sampled. In order to obtain straight and parallel fringes, a Fourier configuration for the interferometer was adopted, i.e. the object beam and the reference beam were arranged in order to have the same curvature. As a first experiment, we acquired an interferogram of a test resolution chart, while moving the object along the x' direction. Figure 4.2(a) shows the interferogram corresponding to a fixed position x_0' of the target, where the fringe orientation is oblique with respect to the x' axis. In Figure 4.2(b) the synthetic interferogram is shown, which is obtained from the signal corresponding to one single

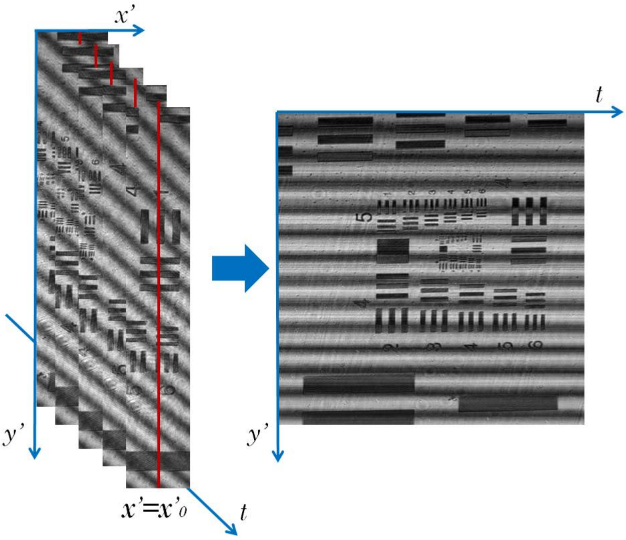

FIGURE 4.3: Interferogram synthesis from one single detector row (red line)[215]. Extended FoV is achievable exploiting the object shift. Improved visualization is also obtained, as the noise is constant along the t axis.

column of the acquired 2D matrix (see the red line in Fig. 4.2(a)) at different times. Indeed, if the time diversity is exploited, this is sufficient to synthesize the image of the whole object, also enlarging the system FoV. As expected, in the synthetic interferogram the fringe orientation is perpendicular to the y' axis. Figure 4.3 shows the creation of a synthetic interferogram from a time sequence of recordings. In this experiment, a small subset of pixel of the employed CCD camera was used. This would also allow to maximize the sensor frame-rate, r, so that geometrical super-resolution in the x' direction could be achieved as a result of a better sampling [218]. However, this was not the purpose of our study, so that a frame rate $r = 47,3\ s^{-1}$ was selected while the target velocity was set to $v = 208,3 \mu m/s$. Here we just want to show that a large FoV can be obtained from one single sensor line if the target movement is exploited. Again, it is worth to notice the expected change in the fringe orientation when passing from the acquired interferograms (oblique fringes) to the synthetic one. The spatial distribution of the noise corrupting the image changes as well, becoming constant along the time axis in the hybrid synthetic reconstruction. This results in improved image contrast and, hence, a better visualization of the target. In our second experiment, a pure phase object was analyzed, namely a

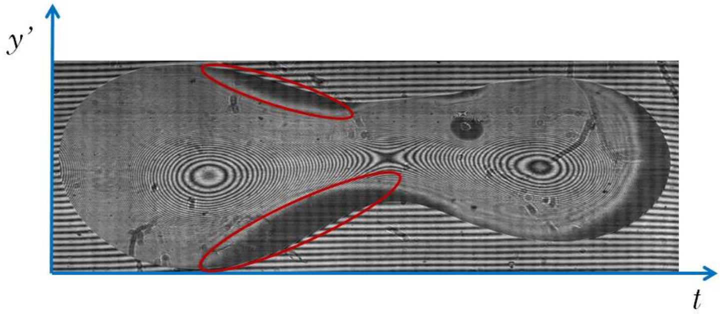

Figure 4.4: Synthetic interferogram of a PDMS drop. The red circled zones show the areas where the fringe spacing is too small to properly sample the high slope object parts [215].

PDMS drop having an intricate geometry. Figure 4.6(a) shows a microscope image of the drop, where it is apparent its very complex shape, with two thickness maxima on the left and the right side of the drop and a saddle point in the middle. The synthetic interferogram is shown in Fig. 4.4, where circular fringes, corresponding to the two thickness maxima, are well visible. Noteworthy, due to the complex morphology of the test object the fringe spacing is too small in those areas characterized by high slope, and undersampled areas are apparent where the useful signal gets lost (see the red circled zones in Fig. 4.4). Synthetic interferograms are extracted by tuning the selected column x'. A change in the column selected to build the synthetic interferogram has three main consequences [215]:

- A shift along the x' direction of the position of the object.
- A shift of the horizontal fringes in the y' direction.
- A phase shift in the object area, provided without the need of delay lines in the setup.

In particular, three synthetic interferograms, if properly selected, are sufficient to implement a three step PS algorithm, in order to retrieve the quantitative information about the object optical thickness. Figure 4.5 shows a flow chart sketching the main processing steps of the proposed PS-STSI technique. Starting from the acquired interferogram stack, $[S_1, \ldots, S_Q]$, we extract three ensembles of vectors, namely $[\mathbf{c}_{01}, \ldots, \mathbf{c}_{0Q}]$, $[\mathbf{c}_{11}, \ldots, \mathbf{c}_{1Q}]$, $[\mathbf{c}_{21}, \ldots, \mathbf{c}_{2Q}]$, respectively obtained selecting three different columns $x' = x'_i$, $i = 0, 1, 2$. In our experiments, the spacing between the most distant pixel rows employed as

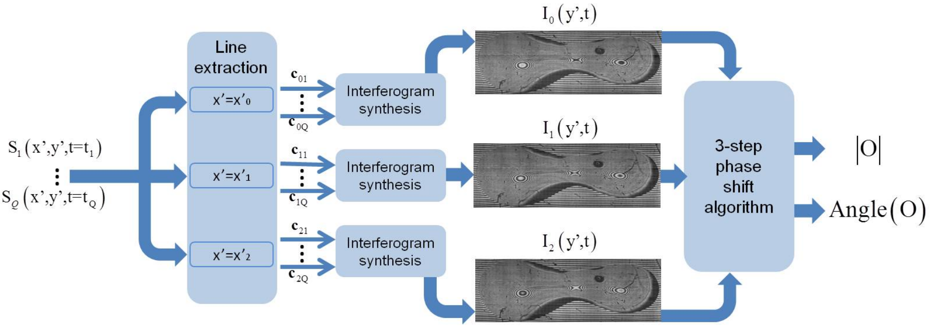

FIGURE 4.5: Flow chart illustrating the processing blocks of the PS-STSI technique [215].

detectors for PS purposes is $36p_x$, a number compatible with the dimensions of commercially available linear CCD arrays. Each ensemble leads to the synthesis of a space-time interferogram, namely:

$$\begin{aligned} I_0(y',t) &= I_{\Delta\varphi=0} \\ I_1(y',t) &= I_{\Delta\varphi=\pi/2} \\ I_2(y',t) &= I_{\Delta\varphi=\pi} \end{aligned} \tag{4.6}$$

corresponding to three different phase shifts $\Delta\varphi = [0, \pi/2, \pi]$. These synthetic interferograms are re-aligned along the x' direction so that they constitute the input of the processing block implementing Eq. (1.11), i.e. the three-step PS algorithm. This returns both the amplitude and the wrapped phase of the reconstructed complex wavefield, respectively shown in Fig. 4.6(b) and Fig. 4.6(c). We applied a phase unwrapping algorithm [146] to the map shown in Fig. 4.6(c), in order to obtain the unwrapped phase-contrast image of the object, shown in Fig. 4.6(d). A pseudo-3D map of the unwrapped phase signal, $\hat{\varphi}(y',t)$, is reported in Fig. 4.7, where it is apparent the capability of the proposed method to recover the 3D shape of the object. As a further validation, we chose a phase object of particular interest, namely a PDMS micro-axicon. This is widely studied due to its characteristic optical properties [219,220]. Indeed, axicon lenses can change Gaussian wavefronts into Bessel beams. The extended depth of focus of a Bessel beam can be exploited in various fields, e.g. optical tweezing [221,222], optical microscopy of biological samples and cell manipulation [221-226]. Besides, a small PDMS drop was layered on the moving stage near the axicon. Figure 4.8(a) shows the amplitude of the complex wavefield obtained after applying the proposed PS-STSI technique, while the wrapped phase of both the objects present inside the FoV is shown in Fig. 4.8(b). A mi-

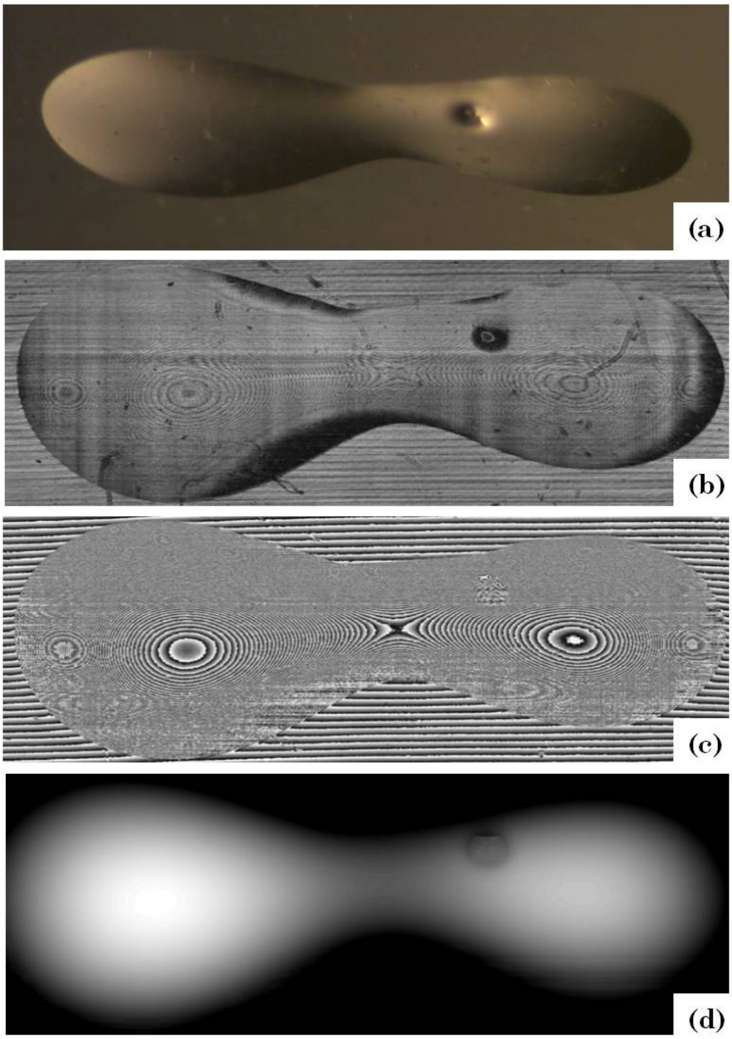

Figure 4.6: PS technique applied to a synthetic interferogram [215]. (a) Microscope image of a complex shape PDMS drop deposited on a plane substrate. (b-c) Synthetic amplitude (b) and wrapped phase (c) of the drop, obtained applying the three step PS algorithm. (d) Unwrapped phase-contrast map of the drop.

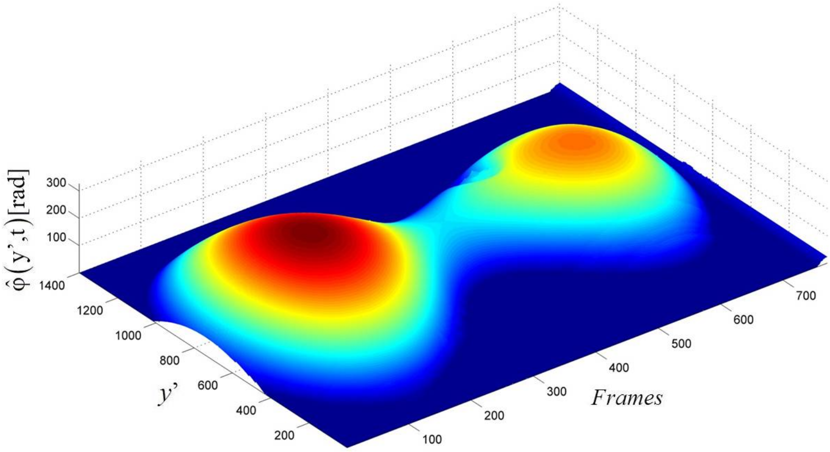

FIGURE 4.7: Pseudo 3D phase-contrast map of the PDMS drop obtained after unwrapping the signal reported in Fig. 4.6(c) [215].

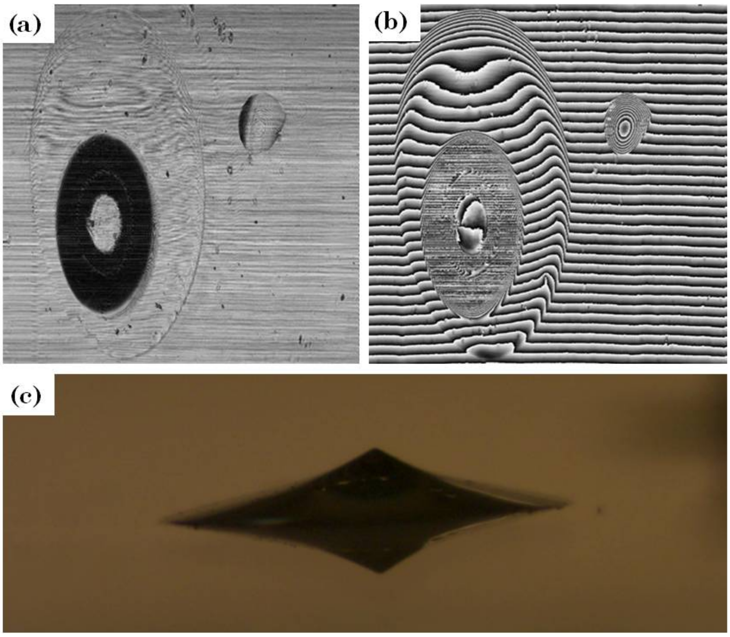

FIGURE 4.8: A PDMS micro-axicon and a PDMS drop are deposited on a plane substrate [215]. (a-b) Space-time amplitude (a) and wrapped phase (b) of the objects obtained applying the 3-step PS algorithm. (c) Microscope image of the micro-axicon.

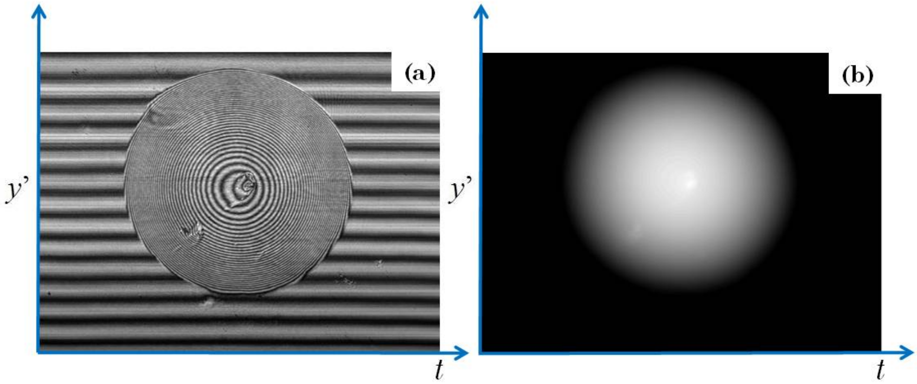

FIGURE 4.9: (a) Syntetic interferogram of a PDMS circular drop. (b) Unwrapped phase-contrast map of the object obtained after applying the 4-step PS formula of Eq. (1.10) [215].

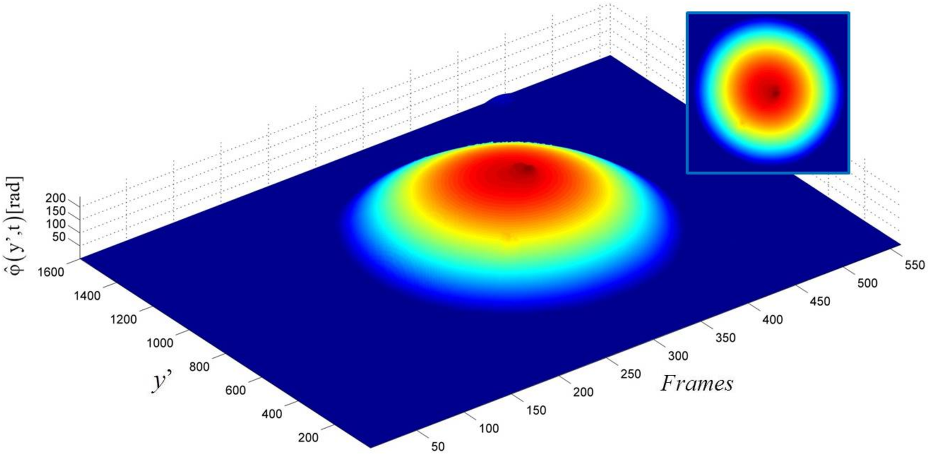

FIGURE 4.10: Pseudo 3D unwrapped phase-contrast map of the PDMS circular drop of Fig. 4.9 [215].

croscope image of the axicon (acquired at different orientation with respect to Figs. 4.8(a,b)) is shown in Fig. 4.8(c). Here we chose to implement the 3-step PS algorithm (Eq. (1.11)) to retrieve the phase from the synthetic interferograms. It is worth to notice that, once the interferogram stack is acquired, synthetic interferograms can be obtained corresponding to whatever phase shift required, e.g. a 4-step PS algorithm (Eq. (1.10)) or the L-measures method (Eq.1.12) could be applied without further acquisitions or changes to the optical set-up. In our last experiment, we put on the moving stage a PDMS drop which took a circular shape after being cured. The corresponding STSI is presented in Fig. 4.9(a). Circular fringes are well visible in the object area, whereas horizontal fringes are present in the background. The choice of any different column $x' = x_i'$, $i = 1, \dots, N_x$, provides a phase shift between the corresponding space-time interferograms. As explained above, we can select a-posteriori which PS algorithm to implement in order to obtain the best quality phase map. In this case we applied the 4-step PS algorithm of Eq. (1.10) to retrieve the phase map of the drop. Figure 4.9(b) and Fig. 4.10 respectively show the grayscale image and the pseudo-3D view of the unwrapped phase $\hat{\varphi}\,(y', t)$ [146], from which the optical thickness of the object can be measured [215].

OPTOFLUIDIC DH MICROSCOPY WITH CUSTOM FOV USING A LSA

The design of simple imaging schemes yielding high throughput is highly pursued with the final goal of fabricating a compact device with a set of imaging functionalities embedded in a single small chip. In this framework, great effort was spent to exploit the object motion along the chip for imaging purposes. A groundbreaking novelty in this direction is represented by the OFM, discussed in Section 1.3.2, which detects signals transmitted through skewed apertures realized in one of the microfluidic channel walls [51]. Thus, by adjusting the aperture spacing, it is possible to tune the achievable spatial resolution. However, in OFM the sample is bounded to stay in close contact with the apertures, which impairs imaging of flowing objects in a relatively deep channel and high liquid volume. Furthermore, phase information, as well as flexible refocusing, is not achievable by OFM.

A lensless microfluidic imaging system was designed recently, in which the samples were imaged simultaneously by three diode laser sources with different wavelengths, to record the resulting near-field diffraction patterns as inputs of a phase-retrieval algorithm [227,228]. Although phase-contrast mapping and flexible refocusing were demonstrated, such a system does not fully exploit the intrinsic sample motion in a microfluidic environment. An interesting lens-based approach which moves a step toward the integration of imaging functionalities inside the chip was reported in refs. [100,229], where diffraction from a slit was exploited to build a stack of images with angular diversity for tomography purposes, yielding re-focusable amplitudes and differential phase-contrast images of flowing samples. A remarkable way to exploit the object motion along the channel is to apply pixel super-resolution algorithms to subpixel shifted HOM images [93,95,101], as discussed in Section 1.3.4. Thus, a four-fold resolution gain can be obtained with respect to single-shot HOM recordings. Unfortunately, as it occurs with any 2D sensor-based approach, a trade-off exists between the chosen magnification and the obtainable FoV.

On the other hand, STSI exploits the object motion to generate synthetic interferograms with the desired phase shift between them, and PSI can be realized, adopting well-known algorithms [79,215,230,231]. Noteworthy, a small subset of detecting elements is proven to be sufficient to accomplish the PSI task. As discussed above, STSI seems to be particularly suited for all cases where the object shift is an intrinsic feature of the system, such as in microfluidics.

In Section 4.2.1 we will show the application of STSI to bio-microfluidic imaging (herein referred to as μSTSI), with the aim to demonstrate that phase-contrast mapping with unlimited FoV along the flow direction is obtainable with a compact Linear Sensor Array (LSA), that can be easily embedded onboard a LoC platform [232]. Besides, in Section 4.2.2 we demonstrate the 3D imaging capability of this novel hybrid information mapping, through the direct synthesis of what we named as Space-Time Digital Hologram (STDH), which still maintains all the advantageous capabilities of Digital Holography (DH), e.g. refocusing biological samples flowing inside the chip at different image planes along the optical axis. We prove that the trade-off between the desired magnification and the FoV can be overcome by STDH while providing fast unlimited FoV phase-contrast mapping without the need for hologram stitching. The synthesis and numerical propagation of a STDH are proven, which can be accomplished with just one line of the LSA, moving an important step toward the integration of quantitative and label-free 3D imaging functions onboard the chip for high throughput microfluidic applications.

Phase Shifting Microfluidics STSI (PS-μSTSI)

The experimental set-up is sketched in Fig. 4.11. The object beam passes through a portion of the microfluidic channel, where the samples flow at velocity v along the x' direction, and recombines with the reference to produce a fringe system in the acquisition plane, (x', y'). The produced interference pat-

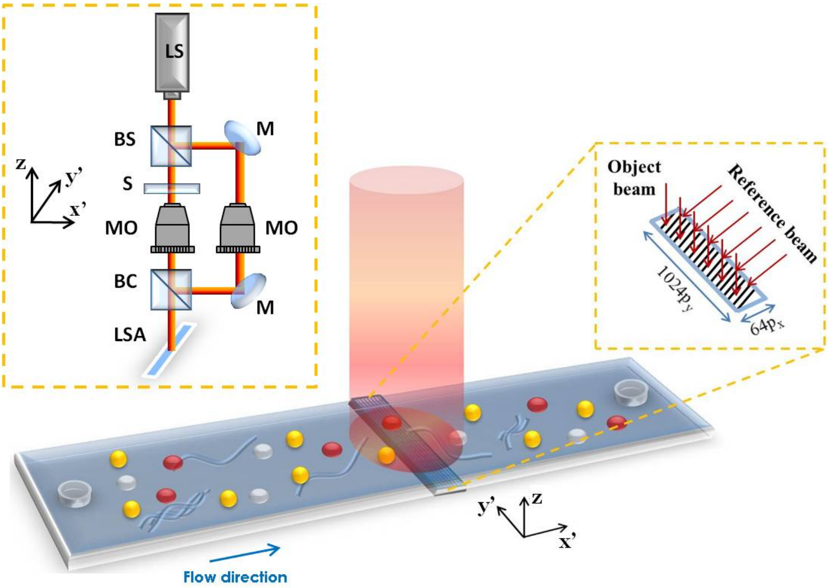

FIGURE 4.11: Experimental set-up for microfluidic SpaceTime Scanning Interferometry (μSTSI) [232]. Because of intrinsic scanning due to the sample flow, it is possible to build, with a compact Linear Sensor Array (LSA), a SpaceTime Digital Hologram (STDH) providing phase-contrast mapping with unlimited FoV in the flow direction. LS: laser source. BS: beam splitter. BC: beam combiner. S: sample. MO: microscope objective. M: mirror.

tern was recorded by using a compact LSA with $(N_x, N_y) = (64, 1024)$ square pixels whose pitch was $p_x = p_y = 5.5$ µm. A Fourier configuration for the interferometer was adopted, ensuring straight and parallel fringes on the recording plane, inclined at an angle θ_x with respect to the x' axis. We acquired time sequences of interferograms using the LSA, resulting in a very narrow FoV along the x' axis because of the LSA dimensions (352µm) in this direction. In a first experiment, we injected fibroblast cells and we let them flow along the channel using a remote-controlled pump. Figure 4.12 shows the generation process of a space-time interferogram obtained with a single pixel row of the detector (whose position is marked with a red solid line in Fig. 4.12(a)). In this experiment, the limited ROI selected in the LSA allowed us to achieve a higher frame rate, thus enabling to capture fast dynamics. It is worth noting that, in order to obtain an undistorted image, proper matching between the fluid speed and the acquisition frame rate has to be fulfilled, so that for an established acquisition frame rate, r, only the objects flowing with a velocity $v = rp_x$ will be correctly sampled in the synthetic interferogram. Faster objects will be undersampled and appear to be squeezed in the synthetic interferogram, while slower objects will be oversampled and seem to be stretched. In the reported sequence, the cells were pushed by an air bubble formed inside the channel. The ensemble effect is not appreciable in the limited FoV (x', y') interferograms (see the sequence in Fig. 4.12(a)), while it is clearly shown in the corresponding (y', t) interferogram in Fig. 4.12(b) (in Fig. 4.12, we denoted as t_i, $i = 1, \dots, Q$, the dimensionless temporal coordinate after accounting for the frame rate of acquisition).

As expected, the whole complex object information modulates horizontal fringes in the synthetic interferogram, from which a number of cells are visible inside the extended FoV as a result of their passage through the detection gate. It is noteworthy that, as an effect of the bubble pushing the fibroblasts, an acceleration in the x' direction is experienced by these cells, thus the requirement for a constant velocity and matching between v and r is not fulfilled. This is apparent in Fig. 4.12(b), where a deformation of circular cells occurs and the most accelerated cells get severely undersampled. Although this is a drawback of the µSTSI method, it also allows the recovery of information about the object dynamics (e.g. for speed-based sorting purposes) by looking at a single synthetic image [232]. In other words, relying on prior assumptions about the object shape, a synthetic reconstruction could automatically discard all the stretched objects, i.e. those flowing with a velocity lower than the selected speed, as well as the squeezed samples, i.e. those moving with a velocity higher than the threshold speed. In this way, from one recorded sequence, multiple maps

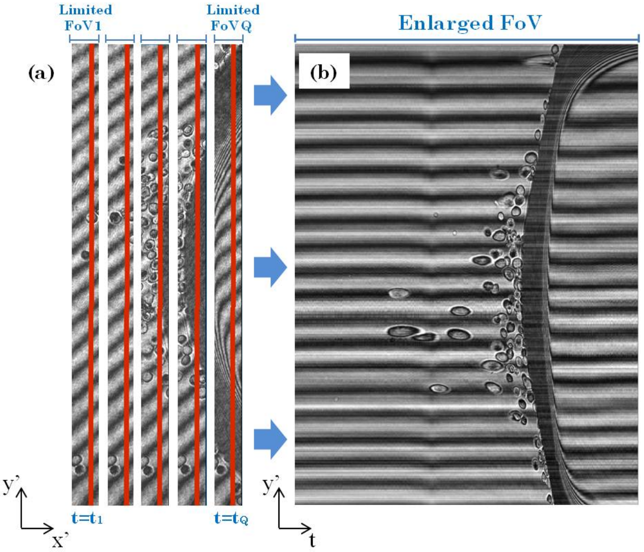

FIGURE 4.12: µSTSI synthesis [232]. Fibroblasts placed inside the channel are accelerated by an air bubble. The figure shows the process of generating a space-time interferogram with enlarged FoV (b), starting from limited FoV recordings (a). The red solid lines in (a) show the detection gate, i.e. the line used to build up the interferogram in Fig. 4.12(b).

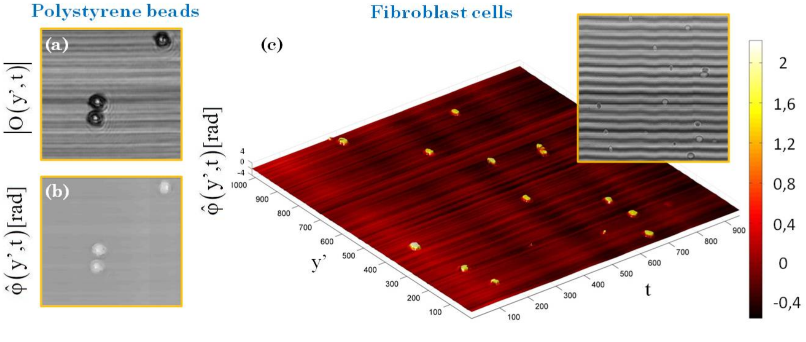

FIGURE 4.13: Full-field recovery by PS-µSTSI. Experiments carried out using different test samples show the retrieval of the whole complex object field after applying a PS-µSTSI technique [232]. (a) Amplitude reconstruction and (b) phase-contrast map of polystyrene beads. (c) High throughput phase contrast imaging of fibroblast cells flowing at constant velocity is shown, along with the corresponding extended FoV synthetic interferogram (in the inset).

could be provided as outputs, augmenting the information throughput of the optofluidic system. Besides, the FoV is only limited in the y' direction, while the acquisition of a longer time sequence ensures theoretically unlimited FoV along the x' coordinate, allowing to capture information from more and more objects flowing inside the chip. If the diversity between three appropriately selected space-time interferograms is exploited, the presence of interference fringes enables the direct estimation of the object field, $O(y', t)$, by using a PS algorithm, as discussed in Section 4.1. As test samples, polystyrene beads were let flow along the microfluidic channel at constant velocity and captured by the LSA. Synthetic interferograms are built up according to Eq. (4.6) and realigned along the t axis in order to be appropriately combined by means of a 3-step PS algorithm (Eq. (1.11)). The final object amplitude reconstruction and the phase-contrast map, extracted from the estimated field $O(y', t)$, are respectively shown in Fig. 4.13(a) and Fig. 4.13(b). Hence, PS-μSTSI yields quantitative and extended FoV phase-contrast maps which are useful in all cases where multiple objects flow inside the chip. As a further example, Fig. 4.13(c) shows a phase-contrast image of multiple fibroblast cells captured by the LSA while flowing at constant velocity along the channel (the corresponding synthetic interferogram is shown in the inset of Fig. 4.13(c)). In a second set of experiments, we studied biological samples of higher interest for biomedical investigations, namely C-elegans worms. C-elegans is an important model organism used to understand biological diseases. There are several features that make C. elegans an attractive model system for diverse biological approaches and applications. In particular, these features include (1) its fully sequenced genome [233], simplified nervous system and body transparency, which offers the advantage of visualizing individual neurons in living worms while the processes take place, (2) complete characterization of cell lineage, which is largely invariant between individual worms, (3) a small number of cells (959 in the adult hermaphrodite) and neurons (302 in the adult) and (4) the possibility to easily genetically manipulate it without many ethical concerns. All these features have paved the way for C. elegans to be the organism of choice for neurobiology, toxicology, ecology, developmental biology and molecular biology studies [234,235]. The similarity in the conservation of proteins and biological pathways between nematodes and humans, with more than 70% of disease genes present in a nematode orthologue, lead to the successful reproduction of a wide number of human diseases such as metabolic and neurological disorders (e.g. Parkinsons and Huntingtons disease) in C. elegans [236].

As pointed out before, in standard imaging, a trade-off exists between the obtainable FoV and the magnification, $\mathcal{M}$; thus, poor magnification and, in turn, spatial resolution are achievable when the whole sample interferogram has to be captured in a single shot. This is very important for multicellular organisms such as C. elegans that, measuring $1\ \mathrm{mm}$ in length as an adult, is compatible with microfluidics but can hardly be imaged as a whole organism. Our purpose is to demonstrate that such constraints can be overcome, as the μSTSI method provides interferograms with unlimited FoV in the flow direction, so that the desired magnification can be set and the spatial resolution is only bounded by the diffraction limit. We let C. elegans flow along the channel and we performed in-focus recordings using the LSA, as sketched in Fig. 4.14(a). In this experiment, a low magnification ($\mathcal{M} = 10$) was set, so that a limited FoV was sufficient to show the whole object. In Fig. 4.14(b), we reported one of the space-time interferograms obtainable with the LSA, showing the flowing specimen while being sampled by horizontal interference fringes. The corresponding hybrid phase-contrast maps, obtained by using a 3-step PS algorithm, are shown in Fig. 4.14(c) and Fig. 4.14(d), respectively reporting the unwrapped phase signal before and after compensating the curvature due to the channel shape.

Microfluidics Space-Time Digital Holography (μSTDH)

After the μSTSI concept has been introduced, it is trivial to extend it to out-of focus DH recordings. Let

$$\left[H_1\left(x',y',t_1\right),\ldots,H_Q\left(x',y',t_Q\right)\right] \tag{4.7}$$

be the time sequence of recorded holograms in the acquisition plane (x',y'). If a single line ($x' = x_0'$) is selected from the stack in Eq. (4.7), it is possible to extract the set of vectors:

$$\begin{aligned}
\mathbf{h}_{01} &= H_1\left(x_0',y',t_1\right)\\
\mathbf{h}_{02} &= H_2\left(x_0',y',t_2\right)\\
&\vdots\\
\mathbf{h}_{0Q} &= H_Q\left(x_0',y',t_Q\right)
\end{aligned} \tag{4.8}$$

that can be rearranged in a matrix $H_{ST,0}\left(y',t\right)$, constituting a synthetic Space-Time Digital Hologram (STDH), containing the whole complex information about the whole acquired time sequence, i.e. object signals coding both in amplitude and phase straight and parallel horizontal fringes. If a linear array is employed, unlimited FoV DH microscopy can be achieved by numerical

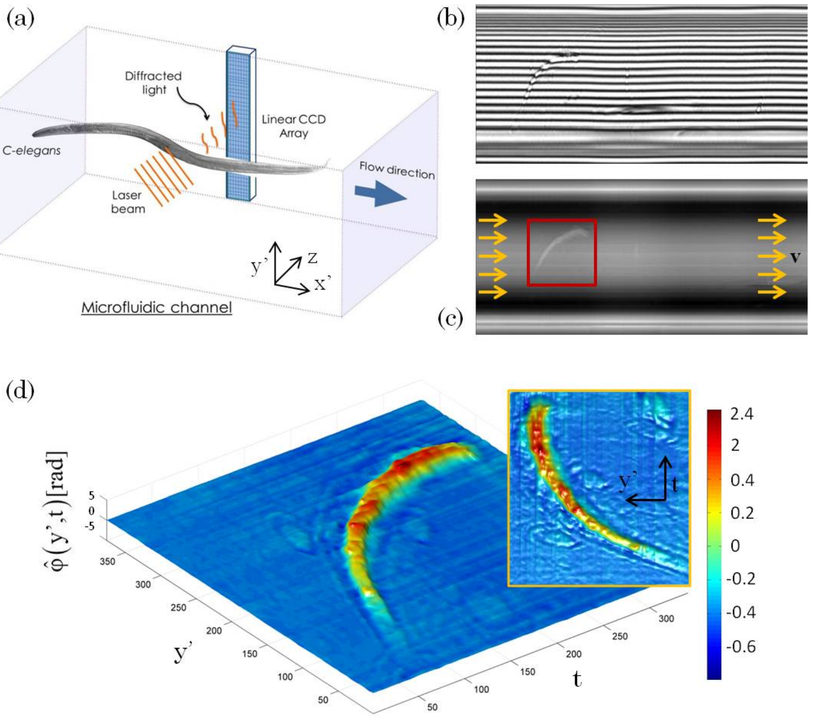

FIGURE 4.14: The phase-contrast map of C. elegans is estimated by PS-μSTSI [232]. (a) A sketch of the experiment. (b) Synthetic interferogram. (cd) Phase maps obtained before (c) and after (d) compensating the curvature due to the channel shape.

propagation of the matrix $H_{ST,0}(y',t)$, e.g. using the Fresnel transform or the angular spectrum method. In this case, it is convenient to select the angle θ_x in order to minimize p', thus providing proper sampling of the objects through the horizontal fringes. In a microfluidic experiment, starting from out-of-focus recordings, just one single detector array is sufficient to provide all the information necessary to build up the STDH. Its features can be so resumed [232]:

- Independent of the fringe orientation on the acquisition plane, this STDH shows horizontal fringes, i.e. parallel to the flow direction.
- Independent of the magnification, $\mathcal{M}$, and the FoV of the acquired (x', y') hologram, the STDH has unlimited FoV along the flow direction, depending only on the overall acquisition time T and obtainable without any complex hologram stitching procedure.
- This so-built STDH still maintains all the advantageous capabilities of spatial domain DH, i.e. the possibility to achieve quantitative phase-contrast mapping in the plane (y', t) and, above all, flexible refocusing by numerical propagation along the optical axis. In other words, once the set of vectors $\left[h_{01}, h_{02}, \dots, h_{0Q}\right]$ is acquired with a single line detector, it is possible to fill the whole stack couple:

$$\begin{aligned} A(y_R, t, z) &= |C_{ST}(y_R, t, z)| = \left|P\left\{H_{ST}, 0\left(y', t\right)\right\}\right| \\ \hat{\varphi}(y_R, t, z) &= \mathrm{Unwrap}\left\{\mathrm{Angle}\left[\frac{C_{ST}(y_R, t, z)}{C_{ST-Ref}(y_R, t, z)}\right]\right\}, \end{aligned} \tag{4.9}$$

- Different from the case of PS-μSTSI, the whole complex object field is achievable without the need for image co-registration.
- Due to the movement of the objects along the microfluidic channel, it is easy to build up a reference synthetic hologram, $H_{ST-Ref}(y', t)$ by selecting a temporal range in which no objects overcome the detection gate. In Eq. (4.9) we denoted with $C_{ST-Ref}(y_R, t, z)$ the numerical propagation of $H_{ST-Ref}(y', t)$. This allows direct estimation of the object optical thickness, inherently compensating the phase contributions due to the optical elements along the object beam path (e.g. lens aberrations) and/or the curvature due to the channel shape.

In a STDH system, the imaging time is the time it takes for the whole object to flow along the LSA. Hence, it depends on the object dimension in the x' direction and its speed. The achievable resolution is mainly limited, as in common

DH acquisition systems, by the sensor pixel pitches (p_x, p_y) unless sub-pixel shifting of the object is exploited to apply a pixel super-resolution algorithm [93,95,101]. As previously mentioned, the FoV is different along the two axis orthogonal to the optical one. Indeed, in the flow direction, this is proportional to the overall acquisition time, thus being theoretically unlimited. As in classical DH, the FoV along the y' axis depends on the system parameters and will be herein denoted as $\mathrm{FoV}_{y'} = N_y p_y / \mathcal{M}_y$ where $\mathcal{M}_y$ is the magnification in the y' direction. If we consider the throughput of this imaging system as the time required to acquire an image representing the whole object, we found that this proportionally depends, for a fixed object size, on the object velocity and the frame rate. Since these are matched in our system ($v = rp_x$), the one which has a lower value determines the maximum throughput. In other words, the throughput is not theoretically limited, but this only depends on the adopted hardware, still taking advantage of the fact that a LSA can achieve a higher frame rate with respect to a 2D sensor with comparable features [232]. In order to compare the results of the STDH generation and propagation process with the expected ones, we performed capture of the specimen while it flew along the channel, illuminated with one optical beam, and recorded in its own best-focus plane by using a common 2048 × 2048 CCD camera with $p_x = p_y = 5.5\mu m$ pixel pitches. We selected images corresponding to a limited ROI (930 × 1260 pixels), each one showing a small portion of the whole specimen (see Fig. 4.15(a)). Due to the sample length and the higher magnification that we set ($\mathcal{M} = 50$), one single hologram would not be sufficient to capture the whole object, and a hologram stitching process should be carried out to provide synthetic FoV enlargement. Indeed, it results:

$$\mathrm{FoV}_{CCD\_y} = \mathrm{FoV}_{CCD\_x} = 225.3\ \mu m. \tag{4.10}$$

Instead, here we performed out-of-focus recordings, setting closely spaced straight and parallel fringes, to appropriately code the specimen information [232]. Figure 4.15(b) illustrates the generated STDH obtained by one single raw detector. For the sake of clarity, a zoomed image of the background area in the red dashed box of Fig. 4.15(b) is reported in Fig. 4.15(c) along with the interference fringes obtained by selecting a line orthogonal to the flow direction. Given the system and the LSA parameters, it results $\mathrm{FoV}_{LSA\_y} = \mathrm{FoV}_{CCD\_x} = 225.3\ \mu m$, while FoV_{LSA_x} is infinite. In this experiment, the FoV exploited along the x' axis in order to capture the whole out-of-focus hologram of the sample was $\mathrm{FoV}_{LSA\_x} = 440\mu m$ (in STDH, this parameter can be chosen as large as desired depending on the object size and $\mathcal{M}_x$). We performed acquisitions with $r = 50s^{-1}$ ($v = 5.5\ \mu m/s$), so that the imaging time for this experi-

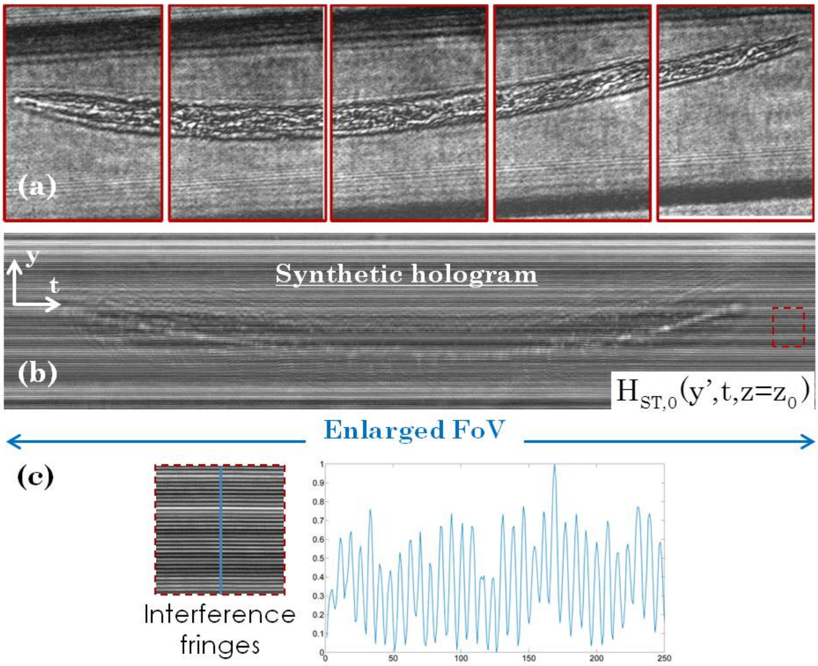

Figure 4.15: Synthesis of STDH. C. elegans is imaged with high magnification (M = 50) while flowing along the channel [232]. (a) Time sequence of limited FoV optical images showing small portions of the sample, recorded in-focus with a 2048x2048 CCD sensor for comparison. (b) STDH: a large FoV synthetic hologram is built up from out-of-focus recordings by using a single line detector, carrying 3D information from the whole sample at a glance. (c) The inset shows the interference fringes along a line orthogonal to the flow direction.

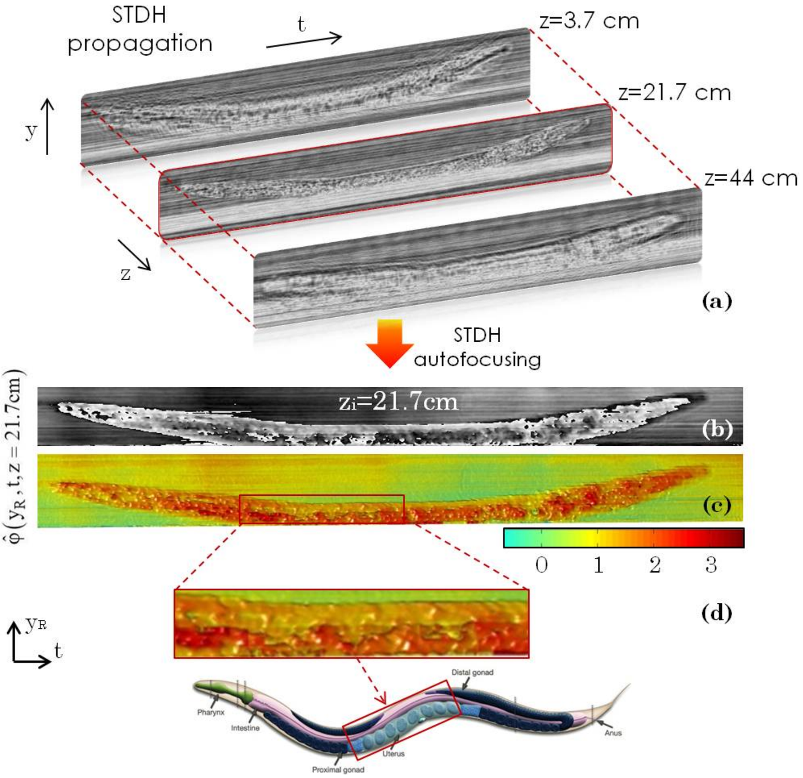

Figure 4.16: STDH z-scanning and phase-contrast mapping after propagation at the best-focus distance of the sample, z=21.7 cm. (a) Amplitude images extracted from the z-scanning stack are reported, showing the STDH automatic refocusing to estimate the best-focus distance of the sample. (b) Wrapped phase corresponding to the amplitude map in the red box in Fig. 4.16(a). (c) Unwrapped phase [rad]. (d) The inset shows details of the object, where the areas with different optical thicknesses are recognizable and reveal the inner structure of the worm [232]. The bottom part of Fig. 4.16(d) is reproduced from ref. [237].

ment was $T = 80$ s. For the sake of comparison, the previously reported HOM method [93] yields a shorter imaging time (about $2 - 3$ s) for a CMOS full-field of 24 mm^2, while the proposed STDH achieves synthetic sensor dimensions of 248 mm^2 at the cost of a longer imaging time. However, the time required to obtain a hologram of the object is not lower-bounded, and it could be drastically lowered by adopting a higher value of r and, in turn, a higher sample velocity inside the channel. Figure 4.15(b) corresponds to a blind recording where no prior information about the sample position inside the chip is exploited. However, according to Eq. (4.9), STDH propagation allows z-scanning until the sample best-focus plane is reached. In Figure 4.16(a), some significant amplitude reconstructions extracted from the stack $A\left(y_R, t, z\right)$ are reported, showing progressive image formation until the sample is focused at a distance of $z = 21.7$ cm and subsequent image defocusing obtained at $z = 44$ cm. An automatic focusing algorithm based on an appropriate contrast estimator can be applied to the elements of $A\left(y_R, t, z\right)$ to inspect all the planes in order to determine the sample best-focus distance, as discussed in Section 3.3.3. In Figure 4.16(b) and Fig. 4.16(c), we show the element $\hat{\varphi}\left(y_R, t, z = 21.7 \text{ cm}\right)$, respectively before and after applying the phase unwrapping algorithm [194]. The inset of Fig. 4.16(d) shows the areas with different optical thicknesses due to the inner structure of the specimen. The STDH propagation process is sketched in Fig. 4.16(a).

DH MICROSCOPY USING POLYMER LENSES PRINTED ON-CHIP

In order to move a further step toward the integration of the imaging functionalities onboard LoCs, we investigated the possibility to place lenses with a few mm diameter directly onto the top of the chip, in order to obtain the desired magnification of the objects flowing along microfluidic paths. Due to the small size of the channels and miniaturization specs, the capability of dispensing lenses of desired focal length is required. Besides, the accurate positioning of these lenses in correspondence of the proper channel area is an essential requisite. Nano-dispensing of liquids and direct printing methods are becoming the prominent nano-fabrication tools in multiple fields of application [238-241]. Among the various ink-jet printing approaches, the most promising techniques appear to be the electrohydrodynamic (EHD) based techniques, which are proved to print with challenging spatial resolution down to nanoscale [238]. During the years, various techniques were developed for manipulating polymers and dispensing droplets, such as ink-jet printing, piezoelectric print heads, EHD jetting [242-245]. A pyro-EHD approach was then developed, start-

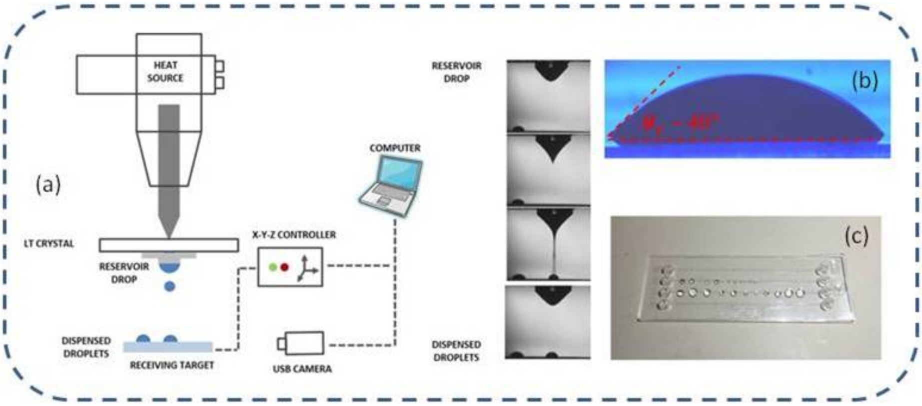

Figure 4.17: (a) Schematic view of the experimental set-up of the pyro-EHD printing system and side view images of a typical sequence of dispensed droplets. (b) Cross section view of a polymer lens on a surface treated using Fluorolink S10 providing a hydrophobic condition. (c) The representative image of the thin fluorinated layer onto microfluidic chip with printed and cured lenses formed with different diameters of 150-1500µm [249].

ing directly from a liquid drop reservoir lying in front of a pyroelectric crystal, extending the range of viscosity of the polymer processed [246-248]. Nevertheless, classic EHD and pyro-EHD suffer from the same limitation, since the receiving substrate has to be inserted in-between the two electrodes at a well-defined distance [249]. In classical EHD the target is inserted between the nozzle and the counter-electrode plate while, in case of the pyro set-up the target is placed between the liquid drop reservoir and the pyroelectric crystal. Limitations on thickness, material type (conductive, liquid, etc..) and geometric constraint reduce significantly the flexibility of EHD printing. In particular, limitations usually occur in all of the EHD based ink-jet printing systems, as the substrate where to print must be sandwiched between the electrodes. Such geometrical constraint represents a severe limitation in case is requested a dispensing/printing directly on devices ready for use, e.g. to functionalize them, and the thickness of such device makes it impossible to apply the EHD methods. Recently, forward electrohydrodynamic (EHD) ink-jet printing has been introduced, which is able to deliver, at nanoscale volume, drops forward the substrate without electrodes and nozzle, maintaining very high-resolution and uniformity in the printing action. Based on the scheme sketched in Fig. 4.17(a), this overcomes the limits of EHD, as the thickness's constraint of the receiving substrate is removed completely. Thus, printability directly on several devices is allowed, in turn resulting in the possibility to optically functionalize LoC devices [249]. In our experiments, polymer optical lenses made of PDMS were printed directly onto the top of a microfluidic chip, as shown in Figs. 4.17(b-c), where we respectively reported the cross section view of a polymer microlens (printed on a surface treated using Fluorolink S10 providing a hydrophobic condition), and a photograph of the LoC with embedded lenses. Details on the experimental set-up adopted for printing the lenses using the forward pyro-EHD method can be found in [249]. An optical characterization of these lenses was carried out, in order to study the optical features, aberrations and focusing properties of these components. An example result is reported in Section 4.3.1. Besides, the imaging capabilities of the PDMS lenses were directly tested in Section 4.3.2, performing microscopy imaging of biological samples flowing inside the LoC platform.

Interferometric characterization

In order to assess the lens behavior of the printed polymer, we performed an interferometric characterization based on DH microscopy. In particular, one of the lenses shown in Fig. 4.17(c) was tested to evaluate its optical aberrations and focusing properties [249]. The optical set-up is the Mach-Zehnder interferometer sketched in Fig. 4.18(a). The laser wavelength was $\lambda = 632.8nm$. The object beam is directed toward the object, namely the microfluidic chip where the sample micro-lens is deposited, and then recombines to the reference in the acquisition plane in order to produce the digital hologram shown in Fig. 4.18(b). The hologram is recorded by a CCD camera with $N_x \times N_y = 1024^2$ pixel with pitches $p_x = p_y = 4.4\ \mu m$. Once the hologram is recorded, numerical propagation provides the object complex field in whatever plane along the optical axis, from which the intensity and the phase distributions of the optical wavefield transmitted by the sample (i.e. the lens under test) can be extracted. A double exposure method was adopted to compensate for the aberrations of the optics in the set-up, as well as the phase delay introduced due to the passage of the object beam through the chip. Hence, the recovered phase-contrast map directly yields information about the lens optical behavior.

A 2D fitting was applied to the recovered phase map, using a Zernike polynomial expansion [250] to model and study the optical aberrations produced by the lens [250,251]. To assure the best fitting results, the hologram plane was chosen in order to obtain a proper sampling of the object information on the whole lens area. Thus, the optical aberrations were estimated in the hologram plane (x', y'), far $d_0 = 17,3\ cm$ from the lens exit pupil. As a fitting quality index, we computed the Mean Square Error (MSE) between the measured and

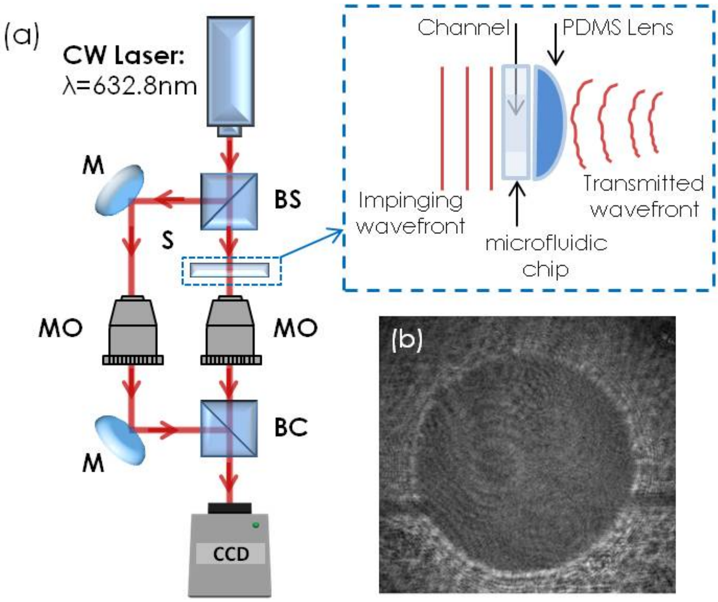

Figure 4.18: Interferometric set-up adopted to characterize the lens optical properties [249]. (a) Mach-Zehnder interferometer. M: Mirror. BS: Beam Splitter. BC: Beam Combiner. MO: Microscope Objective. S: Sample plane. (b) Recorded Digital Hologram.

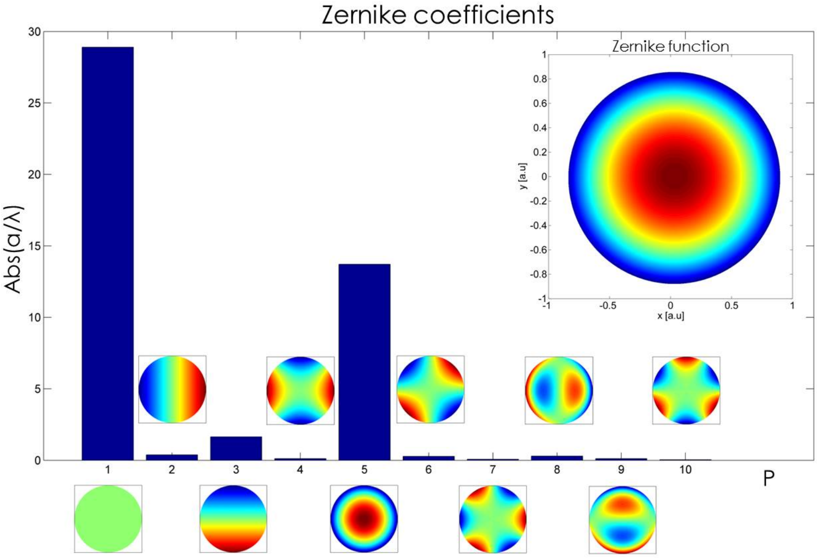

Figure 4.19: Normalized Zernike coefficients derived from the lens phase-contrast map. For each order P, the corresponding Zernike polynomial is shown [249,250].

the calculated phase distribution, normalized with respect to the maximum value of the measured phase map. When $P_{max} = 10$ terms were adopted to synthesize the Zernike function, a $MSE = 0.07\%$ was found, assuring a very accurate reconstruction quality. The first 10 orders of the linear combination of Zernike polynomials (i.e. the Zernike function) are shown in Fig. 4.19, along with the corresponding coefficients, a_P, representing the weight of each aberration term. From the bar diagram of Fig. 4.19 it is apparent that, except for the constant offset ($P = 1$), the main contribution to the development of the Zernike function is a defocus term ($P = 5$). This is an expected result due to the spherical shape of the lens. Moreover, a tilt along the y' axis ($P = 3$) is present, as well as a coma aberration along the x' axis ($P = 8$). The other terms give a negligible contribution. The distributions of the main aberration orders are reported in Fig. 4.20, while the coefficient values for each aberration term are listed in Table 2. If compared to the expected spherical contribution ($P = 5$), the aberration spatial distributions depicted in Fig. 4.20 show shorter dynamics. Hence, they play a minor role in determining the optical behavior of the PDMS lens. In order to estimate the lens focal length, we adopted two different strategies, whose results are in good agreement. As previously discussed, DH

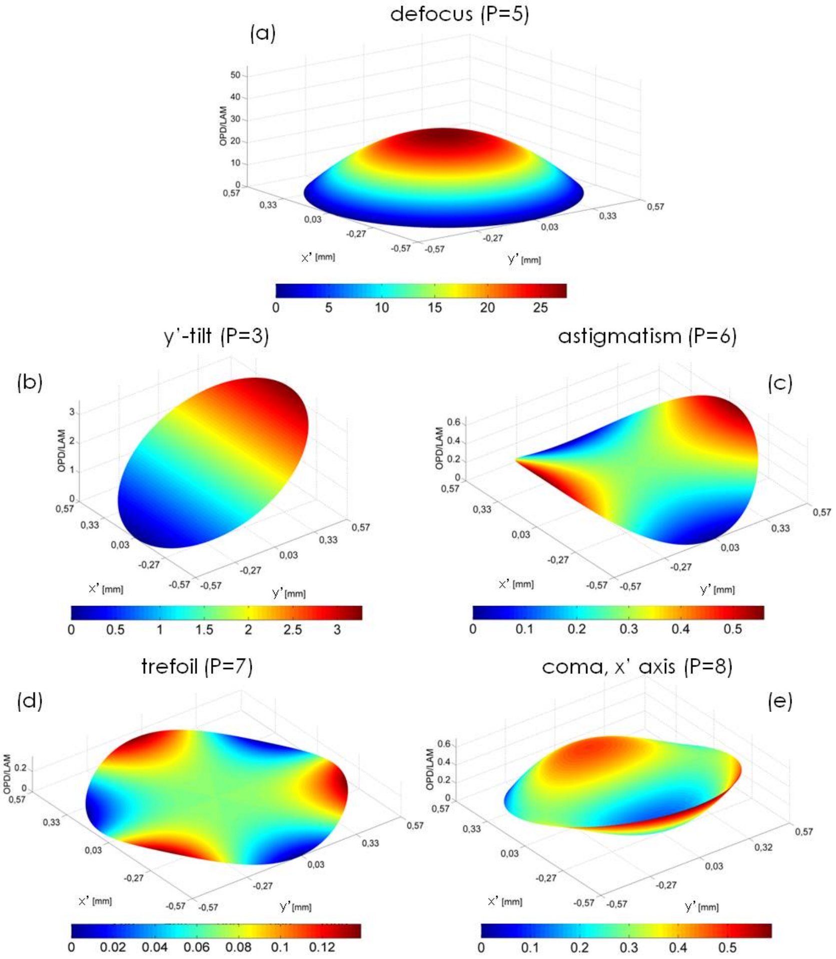

FIGURE 4.20: Spatial distribution of the main Zernike polynomials [249]. (a) Spherical factor. (b) Tilt along the y' axis. (c) Astigmatism. (d) Trefoil aberration. (e) Coma aberration, x' axis.

Polynomial order	Name	Shape	a/λ	$\mathrm{abs}(a_p/a_5)$ [%]
P=1	constant term	1	28.9	/
P=2	x'-tilt	$\rho\cos\theta$	-0.38	2.75
P=3	y'-tilt	$\rho\sin\theta$	1.64	12.0
P=4	astigmatism	$\rho^2\cos2\theta$	0.12	0.86
P=5	defocus	$2\rho^2$-1	-13.7	100
P=6	astigmatism	$\rho^2\sin2\theta$	0.28	2.04
P=7	trefoil	$\rho^3\cos3\theta$	-0.07	0.50
P=8	coma, x' axis	$(3\rho^3-2\rho)\cos\theta$	-0.29	2.15
P=9	coma, y' axis	$(3\rho^3-2\rho)\sin\theta$	-0.12	0.87
P=10	trefoil	$\rho^3\sin3\theta$	0.03	0.26

TABLE 2: The first ten Zernike radial functions, their common names and the corresponding coefficients [249].

allows to numerically perform a z-scanning in order to reconstruct the complex object wavefield in a convenient plane. Thus, it is simple to measure the focal length as the distance between the lens focus plane and its exit pupil. On the other hand, a geometrical approach can be followed. Indeed, the radius of curvature, R_C, can be measured from the phase-contrast map extracted in the plane corresponding to the lens exit pupil. Hence, we estimated the focal length as $\hat{f} = R_C/(n_l - 1) = 4,3$ mm, where $n_l = 1,46$ is the lens refractive index.

IMAGING TEST

Once the optical characterization of the polymeric lenses was carried out, their imaging capabilities were tested showing one of their possible applications onboard a LoC platform [249]. At this scope, fibroblast cells were let flow inside the microfluidic channel where the lenses were directly deposited and imaged through an optical microscope. Figures 4.21(a,b) show the images of the cells inside and outside the lens area. In particular, these are clearly imaged in focus only when they flow behind the lens, while these are out-of-focus in all the other portions of the channel. In Figure 4.21(a) it is also possible to notice the magnifying action operated by the lens, as the channel itself appears to be enlarged. In order to make this capability more apparent, the DH set-up described in Fig. 4.18 was employed to capture holograms of a test resolution target placed behind the chip in the sample plane. In particular, two out-of-

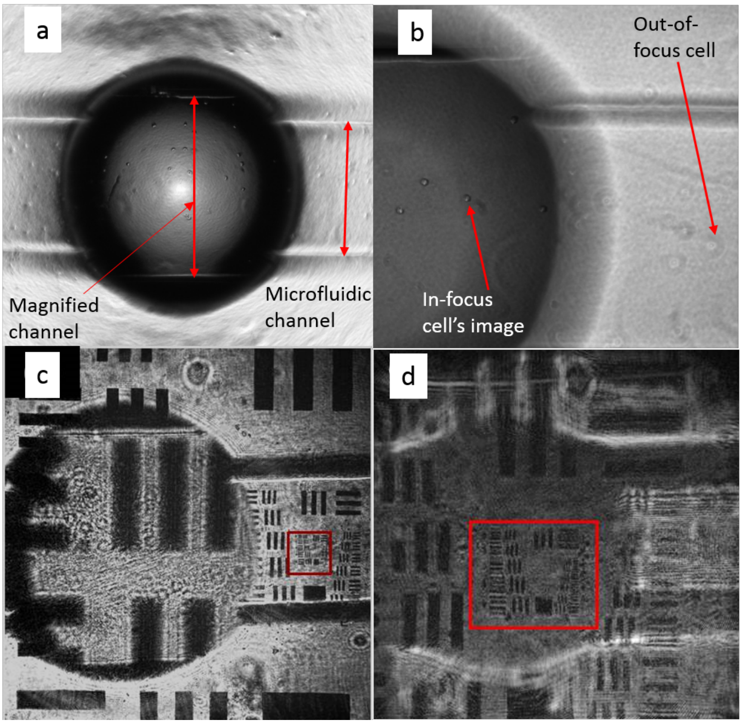

FIGURE 4.21: PDMS lenses were directly deposited onboard chip [249]. (a,b) Fibroblast cells flowing inside a microfluidic channel are imaged in focus through the lens, while out-of-focus images of the cells are obtainable outside the lens area. (c-d) A test resolution target was put behind the chip for test purposes. Two DH reconstructions show the magnification action operated by the lens. The microfluidic channel is clearly magnified as well as the target section indicated by the red box. The smallest target elements are not visible at all outside the lens (c), but these get resolved inside the lens area (d).

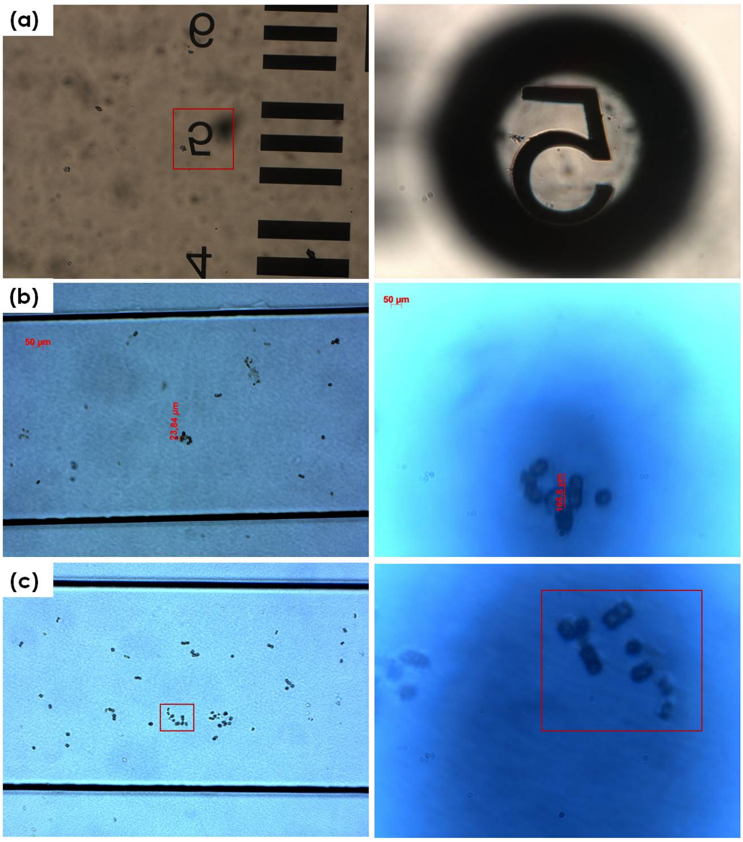

FIGURE 4.22: Imaging a test target and diatoms injected inside the channel. PDMS lenses are directly deposited onto the top of the chip, providing magnified imaging of the objects. (a) Optical microscope image of a test target, imaged (left) without and (right) through the lens. (b-c) Diatoms are let flow inside the channel. (Left) Imaging without the PDMS lenses. (Right) Magnified imaging of the diatoms through the lenses clearly show the formation of diatoms chains. In (b-c) the magnification operated by the PDMS lenses is $\mathcal{M}$=7.

focus holograms were recorded while shifting the target with respect to the lens, and numerical hologram propagation provided the refocused image of the object. In this way, it has been possible to proof the lens magnification. Indeed, the smallest target segments in the red box of Fig. 4.21(c) are not visible at all, while these get resolved when observed through the lens (see the area in the red box in Fig. 4.21(d)). Similarly, in Fig. 4.22 we show optical microscope images of different objects when these are seen (left) outside the lens area and (right) through the PDMS lenses. In particular, in Fig. 4.22(a) a test target is shown, which was placed behind a transparent substrate where the lenses were deposited. Then, we deposited the lenses onto the top of the chip and we let diatoms algae flow inside the channel. Optical microscope images of groups of diatoms are shown on the left side of Figs. 4.22(b,c), while magnified images of the diatoms corresponding to the red boxes in figure (seen through a PDMS lens) is reported on the right side and clearly reveal the formation of diatom chains. The measured magnification factor due to the action of the PDMS lens is M=7. Thanks to the possibility to directly write lenses onboard chip, it becomes possible to dramatically increase the information throughput from samples flowing along microfluidic paths. Different magnifications could be provided after a single passage of the specimens through a channel where a number of lenses with different focal lengths are deposited. If combined to the µSTDH paradigm, LSAs could be mounted in correspondence of each lens, dramatically augmenting the variety of information that could be acquired after a single sample travel along the microfluidic circuit. This perspective will be object of further engineering studies aimed at improving the platform miniaturization and functionalization.

COMMON PATH OFF-AXIS DH MICROSCOPY ON-CHIP

As previously discussed, in the fields of environmental monitoring and diagnostics there is an increasing request of testing equipment that are cost-effective, easy-to-use and rapid to furnish multiple data to collect statistics. This is particularly needed in developing countries that lack of adequate and costly facilities. The developing technologies pave the way to miniaturization of the imaging devices and integration with microfluidic platforms. An important goal in this framework is to develop optical imaging techniques that can be integrated in Lab-on-Chip (LoC) devices. In DH microscopy, this goal traduces in the need for simplifying the recording apparatus. In Section 4.3 we have shown the possibility to dispense polymer lenses onto a LoC device for imaging purposes, and in Section 4.2 the 2D CCD camera has been replaced with a LSA. Here we move a further step forward, showing the design and realization of a novel DH microscopy scheme, conceived as a common path interferometer allowing off-axis DH recordings. The single beam scheme, schematically depicted in Fig. 4.23 replaces the commonly adopted DH apparatus based on the interference between two beams following different paths and recombining in the acquisition plane. This has been realized by designing a grating of proper spacing to be written onto the chip top surface by lithography techniques, in order to directly extract, from the object beam, a reference wavefront enabling the formation of the hologram fringes. As sketched in Fig. 4.23(b), a single plane wavefront is directed toward the chip. The beam diameter has to be chosen large enough to impinge on both the channel area, i.e. where it encounters the flowing or static samples, and the grating zone. As apparent from the chip top-view of Fig. 4.23(a), the grating is written in order to be parallel to the channel. Thus, all the microfluidic channel portions can be in principle exploited for imaging. When a plane wave normally impinges onto a sinusoidal one-dimensional transmission grating with period g_P, diffracted plane waves are produced on the other side with propagation vector forming angles δ_i with the normal direction. The different exit angles correspond to the various diffraction orders emerging from the grating, related to the grating period and the beam wavelength as:

$$\delta_i = \sin^{-1}\left\{\frac{\lambda i}{g_P}\right\}. \tag{4.11}$$

As schematically depicted in Fig. 4.23(b), our strategy is to allow the interference between the wavefront that experienced the passage through the sample and the first order of diffraction from the grating, constituting a reference beam with off-axis angle $\delta_1 = \sin^{-1}\{\lambda/g_P\}$. Since the position of the diffraction orders depends on the wavelength, this approach would in principle allow multi-wavelength simultaneous recordings, where the contributions corresponding to each channel can be spatially filtered in the Fourier domain.

In order to assess the effectiveness of this common path, off-axis DH microscopy scheme, we realized the grating writing this directly onboard chip by means of photolithography methods. First tests were carried out letting diatoms (*Thalassiosira rotula* species) flow inside the channel and performing both in focus and out-of-focus recordings. Diatoms abundance and taxonomy are widely used as a criterion for the assessment of the status of freshwater ecosystems. Diatom potential as environmental indicators resides also in a species-specific sensitivity to particular heavy metal or pollutants. For example, species as *Achnanthidium minutissimum*, *Diatoma vulgaris*, *Fragilaria gracilis*, *F. rumpens*, *F. crotonensis*, and *F. tenera* are defined as good indicator species for

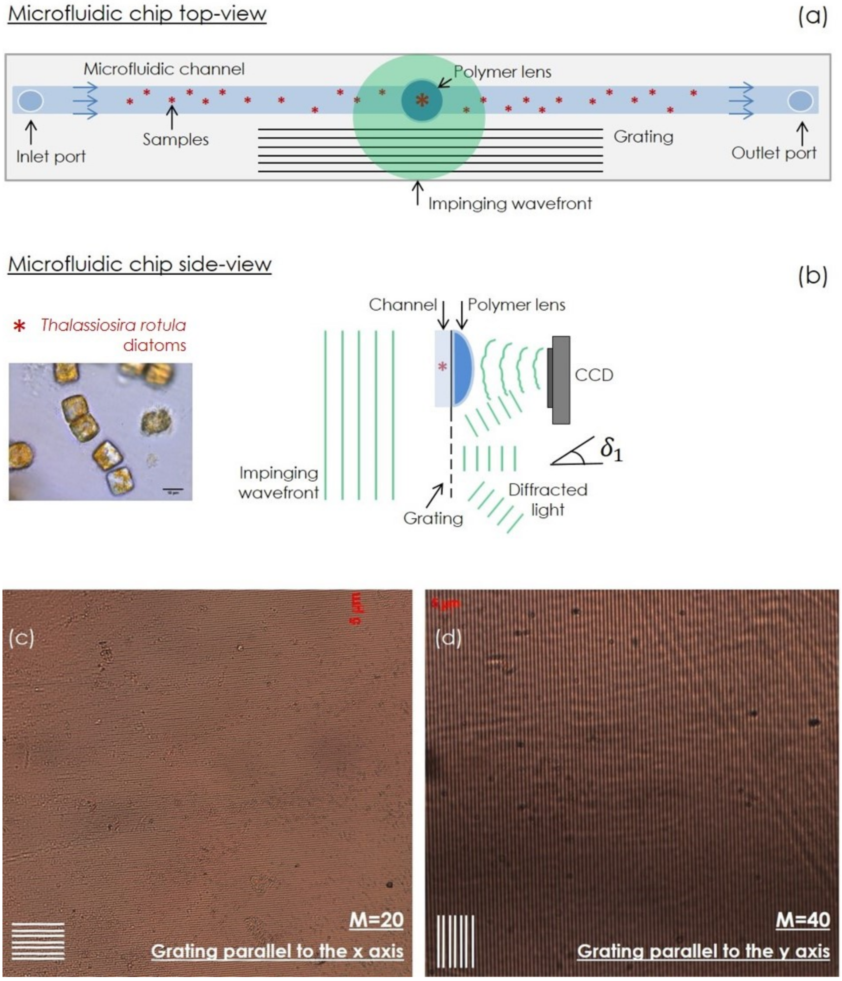

FIGURE 4.23: LoC platform with embedded DH microscopy functionalities. (a) Top-view scheme of the chip. (b) A side-view scheme of the chip shows the diffraction grating allowing to extract the reference beam from one single impinging wavefront. The inset shows an optical microscope image of the test samples used herein, namely *Thalassiosira rotula* diatoms. (c) Optical microscope image of the grating parallel to the x axis ($\mathcal{M} = 20$). (d) Optical microscope image of the grating parallel to the y axis ($\mathcal{M} = 40$).

heavy metal contamination (Cu, Zn, Hg, As and Pb), while *A. pyrenaicum* seems to highlight the presence of toxic compounds like, e.g. pesticides. If exposed to different kinds of stress during reproductive processes, in fact, diatom cell outline and striation pattern can change in different ways, producing teratological forms [252]. Teratological forms may be a valid indicator of ecosystem health and can be characterized by morphological features such as abnormal outline of the valves, atypical raphe system, and abnormal striaton. Unfortunately, due to the small diatom size (5-700μm) and their transparency, sometimes it is difficult to establish a threshold between normal and teratological forms. Usually, microscopy techniques are employed which overcome this limit by "fixation" and "staining", e.g. by fluorescence and electron microscopy. Indeed, autofluorescence signal of chloroplasts in diatoms is related to their photosynthesis activities and its change in presence of a contaminated environment is recognized as a reliable indicator of water quality. However, the need for sample pre-treatment severely reduces the throughput of these imaging systems and requires long analysis time. On the other hand, conventional microscopy methods can only detect 2D morphological diatom changes. In this framework, a quantitative imaging technique is highly demanded to detect 3D changes occurring in the whole diatom volume. Digital Holography microscopy represents a valid alternative to the methods so far adopted, allowing live transparent cell studies without needing of major sample alteration. Thus, the success of the compact configuration we proposed in imaging these samples could pave the way to the realization of a compact device to be used as a portable toolkit for environmental monitoring.

The grating was written with period $g_P = 1,67\mu m$. In particular, two different configurations were implemented and tested, respectively writing a grating parallel and orthogonal to the longer dimension of the microfluidic channel, as shown in the optical microscope images of Figs. 4.23(c,d). The parallel grating gives the possibility to move the beam along the entire length of the channel, while the orthogonal grating is designed in order to use a fixed portion of this, exploiting the sample motion to collect information from all the flowing objects. Although the first implementation is preferred, as it assures that the entire channel is exploitable (being this free from the grating), in these proofs we will show the results obtained with a grating written normally to the channel (i.e. a grating parallel to the y axis). Indeed, this implementation has shown the best results in terms of writing efficiency of the photolithography process. Nevertheless, no optical impairments obstacle the use of the design sketched in Fig. 4.23. Its use and optimization of the related optical setup parameters will be object of further studies. In our test, DH imaging was performed sending a laser beam with wavelength $\lambda = 632,8nm$ toward the chip (the beam is a normally impinging plane wave), which is both the environment containing the objects and the element providing the reference beam required to allow an off-axis DH capture. With these settings, the reference beam, corresponding to the +1 order of diffraction from the grating, forms an angle $\delta_1 = 22,3^o$ with the vector normal to the chip surface. In these first experiments, the pattern of interference between the object beam and the reference beam was collected by a microscope objective with $\mathcal{M}$=20 magnification factor in both the x and y direction, and numerical aperture NA=0,5. Further proofs will be devoted to test the proposed recording scheme in the case the microscope objective is replaced by a polymer lens, as sketched in Fig. 4.23. No other optical elements, such as beam splitters, beam combiners, mirrors, half-wave plates, pinholes, lenses, polarizers, power attenuators, are required. Moreover, the distance between the light source and the chip can be minimized, being no design constraints, which helps to reduce the size of the interferometer. A fiber-coupled laser diode could be also used for the scope, thus minimizing the encumbrance of the source. If the STDH method, introduced in Section 4.2, is adopted, the recording device can be a LSA embedded onboard the LoC platform, thus completing the embedded interferometer.

Using the configuration corresponding to the orthogonal grating, diatoms were let flow along the channel and recorded with frame rate $r = 11s^{-1}$. Diatoms were displaced inside the liquid volume at various arbitrary positions along the z axis, so that some of them were imaged in focus, while others are recorded out-of-focus. This helped us to test the refocusing capability of digital holograms recorded with the proposed setup. Although, rotula diatoms have a quite spherical shape, these are known to form chains, as shown in the inset in Fig. 4.23. Some of the recorded holograms are reported in Fig. 4.24(a), where the vertical fringes of interference are clearly appreciable (see also the insets marked with the green boxes in figure), having reasonably acceptable contrast. The off-axis spatial carrier has the effect of shifting the object distribution in the Fourier domain along the sole k_y coordinate, as shown in the amplitude Fourier spectra of Fig. 4.24(b). It is apparent that the chosen grating period is sufficient to separate the +1 order of interest, $\mathsf{FFT}\{H_S^{+1}\}$, marked with a red circle in Fig. 4.24(b), from the signal corresponding to the zero-th order term, $\mathsf{FFT}\{D_{0S}\}$, so that this can be extracted as reported in Chapter 2. The amplitude reconstructions, obtained after filtering out the orders out of interest in the Fourier domain, and corresponding to the holograms in Fig. 4.24(a), are reported in Fig. 4.24(c), showing single diatoms and diatoms chains slightly out-of-focus (the reconstruction parameter was set to z=0). A first experimental

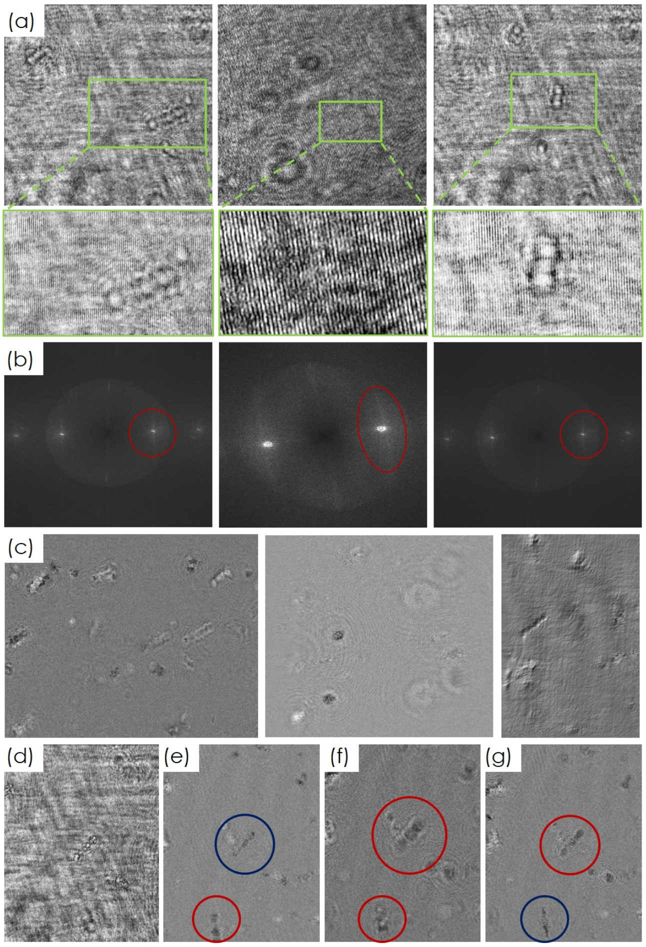

FIGURE 4.24: *Rotula* diatoms are let flow along the chip, and imaged as sketched in Fig. 4.23. The recordings correspond to the case of grating parallel to the y axis, shown in Fig. 4.23 (d). (a) Recorded holograms. The orthogonal interference fringes are apparent in the insets corresponding to the green boxes in figure, and these are modulated by the object distribution. (b) Amplitude Fourier spectra of the holograms in (a). (c) Amplitude reconstructions at z=0 (no propagation is performed), each one obtained after filtering out the order of interest and demodulating the hologram. (d) Recorded hologram showing a diatom chain in focus in the middle. (e) Amplitude reconstruction (at $z = 0$) of the hologram in (d) shows the objects in the blue circle in focus, while the objects in the red circle are out-of-focus. (f) Amplitude reconstruction at $z = -5\mathrm{cm}$ shows both the chains largely defocused. (g) Amplitude reconstruction at $z = 3,56\mathrm{cm}$ shows the refocusing of the objects marked with a blue circle.

proof of numerical refocusing is reported in Figs. 4.24 (d-g), where one of the holograms of the recorded time sequence, shown in Fig. 4.24(d), is numerically reconstructed at various propagation distances. In Fig. 4.24(e), the amplitude reconstruction in the acquisition plane (z=0) images in focus only the chain in the blue circle, while the chain in the red circle is clearly recorded out-of-focus. Propagation at distance z=-5cm from the acquisition plane provides both the chains largely defocused (see Fig. 4.24(f)), while the second chain is put in focus after propagation of the hologram at z=3,56cm, as marked with a blue circle in Fig. 4.24(g).

A second refocusing test is reported in the sequence of Fig. 4.25, where the hologram of a number of diatoms, recorded out-of-focus, is reconstructed at three different distances. In particular, on the left of Figs. 4.25(a-c) the amplitude reconstructions are reported, while the corresponding phase-contrast reconstructions of the diatoms are shown on the right side of the panel. Paying attention to the diatom chain in the middle of the FoV and the chain on the bottom-left corner, Fig. 4.25 is intended to show the flexible refocusing capability of the DH microscopy scheme introduced in this Section. The objects out-of-focus after the DH reconstruction process are indicated with a red circle, while the blue circle indicates the refocused objects. In particular, in Fig. 4.25(a) no propagation was performed (this corresponds to a numerical reconstruction at z=0), and both the chains are clearly out-of-focus. Figure 4.25(b) corresponds to propagation at z=-1,53 cm, sufficient to put in focus the chain in the middle of the FoV. Finally, propagation at z=-3,57 cm provides refocusing of the diatom chain on the bottom-left corner, as reported in Fig. 4.25(c). The phase unwrapped maps of Figs 4.25(d,e) show the two chains clearly refocused at different planes. As expected, the object best-focus plane corresponds to a contrast maximization for the unwrapped phase distribution. As a further example, in Fig. 4.26 we show refocused unwrapped phase-contrast maps of two diatoms agglomerates (indicated with **A** and **B** in figure). In particular, we report the most significant frames extracted from time sequences acquired while these flew along the channel occupying different positions inside the liquid volume. After refocusing, it is apparent the formation of chains both in **A** and **B**. However, after t=0,63s the agglomerate **B** started to experience a rotation after which the chain broke, while the chain in **A** keeps stable during the entire passage through the FoV. A pseudo-3D view of the agglomerate **B** before the chain break is reported on the bottom of Fig. 4.26.

The reported experiments clearly demonstrate the effectiveness of the proposed scheme in capturing refocusable off-axis digital holograms with one single light beam of coherent monochromatic light. If polymer lenses were writ-

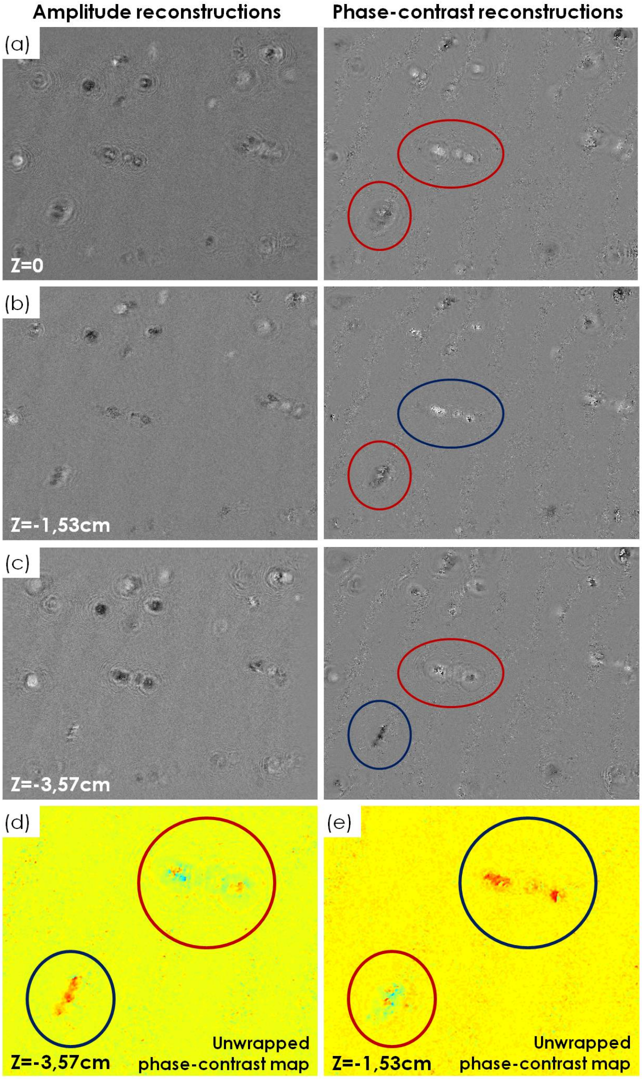

FIGURE 4.25: Refocusing the hologram of diatoms flowing inside a chip and recorded using the common path off-axis DH microscopy scheme of Fig. 4.23. In (a-c) DH propagation at different distances is reported. Left: amplitude reconstruction. Right: Wrapped phase-contrast reconstruction. Blue circles: objects in focus. Red circle: objects out-of-focus. (a) No propagation, $z = 0$. (b) Propagation at $z = -1,53cm$ provides refocusing of the diatom chain in the middle of the FoV. (c) Propagation at $z = -3,57cm$ provides refocusing of the diatom chain on the bottom-left corner. (d-e) Unwrapped phase contrast maps shows refocusing of the chain (d) on the bottom-left corner, and (e) the top-right corner.

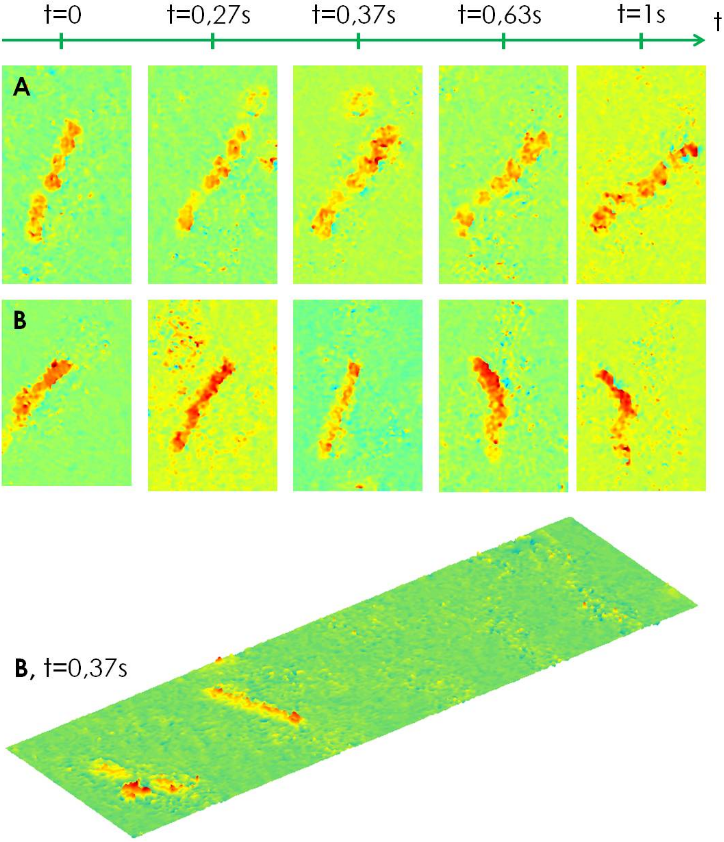

Figure 4.26: Time sequences acquired while letting diatoms flow along the channel. Diatoms form agglomerates, indicated with **A** and **B**. In particular, the unwrapped phase-contrast maps are reported, clearly showing the formation of diatom chains. Bottom: Pseudo-3D view of the unwrapped phase-contrast map corresponding to the agglomerate **B** at time $t = 0,37s$ from the reference time instant.

ten onto the chip top and the STDH technique was adopted, this configuration could definitely constitute an off-axis DH microscope embedded onboard chip, thus moving an important step toward the promotion of LoC portability for point-of care diagnostic purposes. This will be the next step of our work. As a final remark, in recent years DH microscopy adopting low-coherence sources has been demonstrated [121]. Future studies will be devoted to optimize the setup parameters in order to minimize the optical path difference between the object beam and the reference beam. A target of future works will be to investigate the possibility to replace coherent laser sources with small and cheap LEDs, in order to realize a compact on chip DH microscope where the light source is cheap and embedded too. The configurations introduced in this Chapter could be particularly advantageous for the scope.

CONCLUSIONS

Microfluidics is the ensemble of techniques and devices that allow to manipulate small amounts of fluids confined in small regions of space, providing capabilities to accurate control fluid streams [1]. Liquids confined in channels with micrometer size dimensions, obey different physical laws with respect to identical liquids confined in a bigger volume, i.e. the behavior of fluids changes when scaling down from macroscale to microscale [3-5]. For example, low Reynolds numbers typically characterize the microfluidic stream, so that only laminar flows are allowed to establish inside the channel [4]. The absence of turbulence assures a more accurate control and engineering of fluid flows to accomplish specific tasks [5,6]. The microfluidic paradigm has favored the rapid spread of LoC devices, i.e. pocket and cheap platforms consisting in microfluidic channels forming more or less complex circuits. Fluids can be delivered inside the LoC in controlled way and chemical/physical reactions can be induced and observed. Thanks to the realization and miniaturization of a variety of LoC components, like e.g. mixers, pumps, valves, and sorters, it is possible to emulate the functionalities of a modern analysis laboratory onboard chip. Besides, the optofluidic concept has been successfully introduced and developed during the last decade. The basic principle of Optofluidics is to combine Optics and microfluidic control to produce new tunable and reconfigurable optical elements, systems and functionalities. In particular, tunability can be obtained by filling the channels with liquids having different refractive indices, in order to change the features of the wavefront that propagates throughout the chip. Accurate fluid control results in accurate control of light. This led to the realization of liquid waveguides, adaptive lenses, optical switches, beam splitters, and tunable lasers [36].

Thus, optofluidic technology offers an extremely wide set of devices and experimental configurations that can be fruitfully exploited in various fields of biology and medicine. The LoC principle has shown a remarkable applicative potential for point-of-care diagnostics and global healthcare, taking advantage of the possibility to develop low-cost portable devices making possible the rapid analysis of biological samples for first screening purposes, with no need for big amounts of samples and in the lack of adequate facilities, e.g. in low resource settings of developing Countries [16-19,69,86,87]. Indeed, LoC devices can be realized in soft polymers like, e.g. PDMS, which is biocompatible and optically transparent to visible wavelengths. Hence, LoCs are suitable platforms to study biological samples, with the possibility to monitor the processes happening inside the channels. As regards the real need to study cells and biologically interesting samples onboard chip, some considerations are due.

A cell is a sensitive element basing its activities on external stimuli coming from mechanical interactions with other neighboring cells or the ECM, biochemical signals through soluble molecules produced from other neighboring or distant cells, soluble factors due to drug administration, or electrical cues. The typical behavior of a cell, e.g. the growth rate, duplication, migration, adhesion to substrates, mechanical interactions with the ECM and other cells, reaction to drugs, and death, is severely affected from the 3D shape and composition of its surrounding environment. Hence, any reliable study of cell samples requires the accurate emulation of their environmental conditions. It becomes more and more clear that a Petri dish is not the most suitable system to recreate the cellular environment and mimic all the external cues and forces affecting the cell behavior. On the contrary, a LoC looks appropriate for the scope [56]. Recently, the realization of organ models on chip platforms has been reported. These emulate the activities, mechanics and physiological response of entire organs and organ systems, thus opening fascinating perspectives for a deeper and more comprehensive study of human organ functionalities, as well as the elimination of animal testing [253].

In this framework, imaging play a fundamental role to observe and deeply understand the processes occurring inside the chip, and great effort has been spent to design new diagnostic tools, adding them to the existing chips for information recovery, and to find novel strategies to promote the integration of the imaging functionalities onboard. Label-free techniques have to be distinguished from marker-based methods, e.g. the ones based on fluorescence emissions. Diagnostic strategies can be also divided in two classes depending on the provided output, so that we distinguish between qualitative and quantitative techniques. A particularly relevant feature of any optofluidic microscopy technique is the compactness, as it results in field portability. On this basis we distinguish between lens-based and lensless approaches. Scanning based techniques are remarkable in this sense, as these fully exploit the sample motion along the microfluidic channel and allows lensless on chip imaging with reasonable resolution [51]. The OFM represented a groundbreaking novelty in this direction. Besides, the phase retrieval problem has to be accounted for, since added-value, quantitative information can be extracted from the phase distribution of a biological sample. In order to get the phase, different approaches can be followed, which have been resumed in Chapter 1. Iterative as well as deterministic algorithms aimed to estimate the phase from intensity measures can be used for the scope, having to face disadvantages related to convergence issues or boundary conditions [70-72,74-78]. In alternative, interferometric measures can be carried out, in order to estimate the phase from a recorded fringe pattern, where the object modulates the interference fringes in amplitude and phase. In particular, DILH has been demonstrated to be useful to get the phase from samples in a microfluidic environment, but the overlapping between the diffraction orders requires, in order to extract the useful signal, iterative algorithms whose convergence is not assured in all the cases [85,92]. PSI exploits a phase shift between multiple interferograms to retrieve the phase by means of deterministic formulas [79-83].

Following a similar principle, HOM places the chip containing the samples directly onto the top of the sensor (e.g. a CMOS camera), and makes use of a pinhole to augment the source coherence. Thus, HOM can replace the laser source with a LED, more compact and cost-effective, with the aim to promote the chip portability for telemedicine purposes and diagnostics at the point-of-care. However, HOM adopts a lensless recording geometry, resulting in low resolution imaging (iterative G-S based algorithms are required to enhance the resolution in HOM imaging) [93].

What is desirable, is a label-free, full-field method providing good image quality (in terms of resolution, FoV, and SNR) in both qualitative and quantitative fashion, and fully integrated onboard chip. Moreover, high-throughput imaging is required, in order to collect statistically relevant data from a sufficient number of samples. The capability to analyze cells displaced in a liquid volume in a fast manner is a fundamental feature to augment the throughput. The methods adopted in literature follow hybrid approaches trying to match all such requirements simultaneously, although these are conflictual. The most remarkable diagnostic strategies to study cells on chip, have been discussed in Chapter 1 and compared in Table 1.

The approach we followed in this work is to develop algorithms and novel recording strategies to improve the imaging performance in microfluidic environment, with the aim to overcome the shortages of the existing techniques. At this scope, we chose to rely on DH microscopy. Indeed, DH is intrinsically appropriate to yield label-free quantitative phase-contrast microscopy of suspended flowing cells, or samples adhering on channel substrates. Above all, DH is non invasive, so that the samples can be studied without altering their natural behavior.

As described in detail in Chapter 2, in DH the object wavefront can be recovered, both in amplitude and phase, without relying on iterative algorithms and with one single interferometric capture. Moreover, DH microscopy allows out-of-focus recordings of the object signal. The hologram contains the 3D information of objects displaced in different positions along the optical axis, i.e. the signal coming from the objects in focus and the diffraction from out-of-focus objects. Numerical algorithms allows to simulate the wavefront propagation, scanning all the planes along the optical axis until the sample image plane is reached. This permits to capture data coming from a whole liquid volume in a single-shot recording, followed by flexible reconstructions at different focus planes. If microfluidic control is exploited, these features provide high-throughput imaging.

In this work we designed and tested novel solutions, in terms of recording strategies and numerical algorithms, to afford some challenging problems arising in DH imaging onboard LoCs. First, the problem of imaging through turbidity has been tackled and described in detail in Chapter 3. Conventional microfluidic DH imaging is reliable and deeply exploited when the samples are immersed in a transparent fluid, and the polymer chip is transparent as well. However, when a turbid liquid flows inside the channel, clear imaging is impaired and the corresponding object information gets lost. A liquid is considered turbid when dispersed particles provoke strong light scattering, thus destroying the image formation by any standard optical system. The presence of a colloidal solution introduces diffusion of light, thus preventing clear imaging. On the other hand, media that start off clear, often get turbid because of the chemical reactions that occur during the observed processes, thus limiting the variety of experiments that can be performed and clearly observed inside the chip. Even when microfluidic experiments involve transparent liquids flowing inside a channel, scattering events can occur due to the roughness of the channel walls (inherently due to the fabrication process), residual deposits due to chemical reactions, particle uptake by the channel cladding, or formation of bio-films, typically made of bacteria, in which groups of microorganisms stick to each other creating a scattering surface [160-164]. In all these cases, observations cannot be performed at all, impairing the monitoring of phenomena developing over long time periods. However, in the case of imaging through complex media, the useful object distribution is not necessarily lost, but rather this is scrambled, and sometimes there is a chance to recover it. In the case of stationary scattering layers, the problem can be tackled whenever the transmission matrix of the layer can be characterized [150,154]. This approach can be applied to permit imaging through scattering channel walls whenever direct access to the layer in absence of the object is allowed [150,151]. Multiple measures are required to fully characterize the TM in absence of the object [151], or to apply methods based on the speckle correlation properties (the so called speckle memory effect) [151]. Here we presented a simple approach, based on double exposure DH, to recover information from cells flowing along a microfluidic channel with a severely scattering surface [158]. Velocity measure, amplitude imaging, and phase-contrast mapping have been successfully demonstrated in the case of a fibroblast cell flowing inside a chip where a residual deposit of salt crystals made the channel walls severely scattering.

However, in the case of dynamic or even quasi-static turbid liquids, the transmission matrix is not available at all, because the way the medium acts on light propagation rapidly varies in time. The presence of a turbid fluid in a LoC environment provokes time variable scattering events, wavefront distortions, and unpredicible, random, phase delays. Hence, all these strategies cannot be applied to restore clear imaging through turbid LoCs. Nevertheless, in this work we have shown that LoC imaging of biological samples through turbid microfluidics can be made possible in a number of practical situations, adopting a modified DH strategy that permits to increase the number of different uses of LoC platforms for cell studies. In particular, we focused our attention to the case of colloidal solutions, where dispersed colloids act on the object beam as scattering sources, thus provoking image blur and in most cases undermine any imaging option. In the case of adherent cells, if a relative velocity between the fluid and the samples can be contemplated, the interference process typical of DH allows to discard all the contributions coming from the scattered light, thus restoring clear imaging. This is due to the Doppler frequency shift experienced by the photons hitting the moving colloids, preventing them from interfering with the reference beam. In other words, if the turbid medium flows at a speed overcoming a fixed threshold, the hologram formation process acts as a selective filter, coding information from the sole unscattered photons. The threshold velocity depends on the recording configuration parameters, namely the sensor integration time, τ , and the aperture width of the optical system, A_w [180,165,115]. Imaging biological samples through milk, i.e. a test colloidal solution with small size particles (the typical diameter of the milk colloids is about $500nm$ has been achieved relying on this principle [115]. However, in the case of scattering from quasi-static turbid fluids, or dynamic solutions flowing at speed lower than the required threshold, the Doppler effect is not of help and imaging in through transmission gets blurred badly. In the case of small size colloidal solutions, the overall effect of scattering on the reconstruction can be treated as a noise disturbance, and speckle reduction techniques can be applied to restore clear imaging.

In particular, we presented the MLDH method, which is successful whenever multiple holograms can be acquired in a condition where the useful signal keeps stationary, while the scattering signal decorrelates fast over time. The holograms have to be separately reconstructed and incoherently combined to restore clear imaging in all the cases where the uncorrelation between the holograms is enough to benefit from a ML gain (see the ML reconstruction formula of Eq. (3.23)). In the case of quasi-static colloids of small size, the Brownian motion of the colloidal particles can be exploited to apply the MLDH strategy and to restore clear imaging, both in amplitude and phase, from turbidity. Remarkable examples of coherent imaging of sperm cells, seen through a severely scattering milk volume has been demonstrated [115,166]. In particular, a decimated sequence of holograms can provide similar results of a set of processed consecutive recordings, since what really matters is not the number of looks to be combined, but the temporal uncorrelation of the disturbance signal [166]. This result allows to achieve the same ML gain with a smaller number of reconstructions, thus saving computational time. MLDH has been also successfully applied to see through volumes of liquid filled with scattering live bacteria colonies (*E-coli*) at different concentrations. Since bacteria can form long aggregates, these can be regarded as large size objects. Hence, differently from the case of the milk colloids, the Brownian motion is not sufficient to provide the required uncorrelation. However, live bacteria are self-propelling biological elements and their movements establish a random temporal pattern. Studying the time uncorrelation between the reconstructions obtained through a volume filled with bacteria, it became apparent that a bacteria colony acts on the hologram just like a moving diffuser, i.e. a device typically inserted in the optical beam path to reduce the coherence of light and the resulting speckle artifacts. Thus, imaging through bacteria can benefit from a MLDH processing. DH microscopy through bacteria suspensions has been achieved, along with automatic refocusing through the turbid volume (this is obtained applying contrast optimization directly on the ML images propagated at different distances, as reported in Eq. (3.32)) [169].

Then, we focused on a colloid of higher interest for biomedical investigations, namely blood made of RBCs. Hologram sequences of a test target seen through blood have been captured progressively increasing the fluid velocity and correlation measures have been performed (see Fig. 3.21). From the analysis of a properly defined correlation coefficient between multiple DH reconstructions, thought as a function of the blood speed, v, and the number of looks, L, we estimated the threshold velocity required to fully benefit the Doppler, i.e. the speed in correspondence of which the medium acts, from the imaging system point of view, as a transparent fluid. As expected, clear imaging through blood has been achieved for velocity values higher than the threshold. The estimated threshold value is found to be in good agreement with the expected value derived from the theoretical formulation of holographic imaging through convective fog, reported in literature [180]. We then afforded the problem of seeing through blood flowing at a speed lower than the required threshold. We verified the uncorrelation of the reconstructions due to the Brownian motion of the RBCs. However, due to the size of the RBCs (whose typical diameter ranges from $7\mu m$ to $8\mu m$), the Brownian uncorrelation is not enough to take advantage from a MLDH strategy but a blood flow is required. Indeed, a velocity range exists where the imaging system is sensitive to the presence of the RBCs that move inside the FoV during the acquisition time and provide uncorrelation of the disturbance these provoke. Thus, by MLDH it is possible to get clear imaging through blood flowing at a speed lower than the required threshold [167].

We then performed a more interesting experiment, showing the possibility to carry out coherent microscopy of cells adhering on the functionalized substrate of a microfluidic channel where a multitude of RBCs, occupying various positions along the optical axis and sharing the same liquid volume of the sample, was let flow at uncontrolled velocity (however, the velocity was lower than the threshold speed). In this case, the effect of the RBCs was the introduction of random variable phase delays producing a wavefront distortion. In such a situation, the phase retrieval was particularly challenging, as the severe phase shift provided by the RBCs prevented us from using the ML formula of Eq. (3.23), as described in detail in Section 3.4.2. To solve the problem, we applied a different synthesis formula, reported in Eq. (3.35), which has been proved to be successful for recovering the phase distribution of the adherent sample from an apparently useless sequence of phase-contrast maps [168]. As regards the amplitude map, an unexpected and fascinating result has been obtained. The incoherent combination of hologram reconstructions by means of the formula in Eq. (3.23) allows to restore clear imaging from a time sequence of holograms where the sample was completely occluded in all the processed frames [115,168].

We believe this study can pave the way to the real time noninvasive vessel inspection of microscopic particles dipped inside blood. As a fascinating perspective, heart diseases could be quickly identified by detection and thickness measure of cholesterol plaques as well as blood clots settling down the internal vessel faces.

Moreover, by comparing the amplitude map restored from turbidity with the DH reconstruction obtained when the channel was filled with a transparent liquid, we found a surprising result. Indeed, qualitative and quantitative evaluations have shown a remarkable improvement, in terms of noise rejection and numerical resolution, of the ML amplitude map with respect to both the SL reconstruction of the cell hidden by RBCs and the case of the cell placed in transparent liquid (see Fig. 3.27 and Fig. 3.28). In other words, MLDH can benefit from turbidity, as the decorrelating action of the random phase shifters, instead of being an obstacle for imaging, helps to lower the coherence of the optical system. The reduction of speckle artifacts allows to obtain images whose quality is comparable, for the first time, to the quality achievable using non coherent techniques. Based on these results, further studies will be devoted to investigate the possibility to exploit RBCs as elements of microfluidic devices accomplishing useful optical tasks, e.g. to improve the performance of coherent imaging systems.

As discussed above, an important issue in LoC imaging is related to the possibility to augment the throughput of the system. When DH is used to study suspended biological samples, this is necessary to collect statistically relevant data. Besides, the system compactness is a key feature to promote the spread of LoC technology in the developing Countries, and many efforts have been spent to integrate imaging functions onboard chip. In this work we introduced two novel coherent imaging modalities, namely STSI and STDH, that allow to exploit a lateral displacement between the object and the detector to synthesize a new type of interferogram/hologram. This is mapped in a hybrid space-time domain, and possesses interesting features that can be exploited for the above mentioned purposes. Indeed, if the object motion can be exploited, a single linear sensor array is sufficient to build up a synthetic interferogram with unlimited FoV along the scanning direction and improved SNR. In a classical interferometric setup, object scanning is provided by a controlled stage, so that the FoV increase is obtained at the cost of complexity of the interferometer design. Besides, if a proper subset of lines of the detector are selected, synthetic interferograms can be obtained, shifted each other of the desired phase step for phase retrieval purposes. In other words, we found that STSI makes possible to implement a PS strategy simply tuning the detector, so that the use of piezoelectric actuators can be avoided (we referred to this technique as PS-STSI). In particular, three lines of the detector are sufficient for the scope.

In Chapter 4 we reported the theoretical formulation and experimental proofs of the STSI method [215]. PSI has been applied to properly shifted synthetic interferograms (PS-STSI) of polymeric drops of regular and arbitrary shape to demonstrate the capability of estimating the complex field transmitted by the objects and, in turn, their optical thickness distribution. Noteworthy, the PS-STSI principle is well suited to be adopted in all the cases where the object motion is an intrinsic feature of the system, such as in case of microfluidics, so that the advantages of STSI have no cost associated with. Starting from these considerations, we introduced and discussed the application of the STSI method to optofluidic microscopy (referred to as μSTSI). We proved that, by performing out-of-focus recordings using a single line detector, a Space-Time Digital Hologram (STDH) can be synthesized carrying full-field information of multiple samples in flow [232]. We demonstrated that so built STDHs still maintain all the advantageous capabilities of DH microscopy, i.e. quantitative phase-contrast mapping and tunable numerical focusing. A re-focusable STDH with unlimited FoV along the flow direction can be synthesized adopting a single, compact, linear detector and with no need for hologram stitching. Hence, the method performance are independent on the object shape or its Fourier spectrum. Thanks to the proper mapping of the holograms in the space-time domain, it is possible to overcome the trade-off existing between magnification and FoV, with the possibility to obtain unlimited FoV along the flow direction [232]. In other words, a so synthesized STDH possesses all the features of a common hologram built in a space-space domain, but the hybrid mapping assures high-throughput. It is sufficient to let the samples flow along the channel and to capture the time sequence of holograms, each one capturing (and mapping onto a 2D matrix) a sort of photograph of the entire liquid volume containing the samples at a certain time. The synthetic representation yields information of all the samples passing through the channel during the experiment, and its flexible refocusing allows to inspect the entire 3D space. Moreover, a STDH allows to perform microscopy imaging of long size specimens with high magnification, thanks to the custom FoV achievable. We demonstrated such capability by synthesizing the STDH of a $1\mathrm{mm}$ long *C-elegans* worm (adult L1 stage) with $\mathcal{M} = 50$ magnification factor. With this magnification set, a conventional hologram can provide the magnified image of only a small portion of the sample (e.g. the head, or part of the worm tail). On the contrary, the STDH provides information coming from the entire sample at a glance. Automatic focusing of the STDH has been demonstrated. Once we estimated the best-focus propagation distance, we extracted the phase-contrast map of the specimen. Hence, STDH shows promising perspectives as a powerful diagnostic method for optofluidic investigations of biological samples inside LoC platforms. The linear detector is easily embeddable onboard, which helps to move a step toward the integration of the imaging functionalities on-chip for high-throughput rapid diagnostics.

At this scope, we moved a further step toward the miniaturization of the imaging apparatus. In particular, we placed polymer lenses with a few mm diameter directly onto the top of the chip, in order to obtain the desired magnification of the objects flowing along microfluidic paths. Due to the small size of the channels and miniaturization specs, the capability of dispensing lenses of desired focal length is required for the scope. Besides, the accurate positioning of these lenses in correspondence of the proper channel area is a necessary requisite. In this framework, nano-dispensing of liquids and direct printing methods are becoming the preferred nano-fabrication tools [238-241]. Among the various ink-jet printing approaches, the most promising methods appear to be the electrohydrodynamic (EHD) based techniques and the more recently developed pyro-EHD, which are proved to print with challenging spatial resolution down to nanoscale [238,249]. However, in all the EHD based ink-jet printing systems, the substrate where to print must be sandwiched between the electrodes. Such geometrical constraint represents a severe limitation in case it is requested a dispensing/printing directly on devices ready for use, e.g. to functionalize them, and the thickness of such device makes it impossible to apply the EHD methods [249]. Recently, forward Pyro-EHD ink-jet printing has been introduced, which is able to deliver, at nanoscale volume, drops forward the substrate without electrodes and nozzle. Forward Pyro-EHD overcomes the limits of EHD, as the thicknesss constraint of the receiving substrate is removed. Hence, printability directly on several devices is allowed, in turn resulting in the possibility to optically functionalize LoC devices [249]. In this work, we applied the forward Pyro-EHD method by printing polymer optical lenses made of PDMS directly onto the top of a microfluidic chip. After printing the lenses, an optical characterization was carried out, by means of DH, in order to study the optical features, aberrations and focusing properties of these components. The study of the Zernike polynomial function has shown that lenses can be printed onto the chip with negligible aberrations. Besides, the imaging capabilities of the PDMS lenses were directly tested, performing microscopy imaging of biological samples flowing inside the LoC platform, and showing the formation of a magnified image of the samples through the lenses. Thanks to the possibility to directly deposit lenses onto the chip surface, it becomes possible to further increase the information throughput of the imaging system. Different magnifications could be provided after a single passage of the specimens through a channel where a number of lenses with different focal lengths are deposited. If combined to the STDH paradigm, LSAs could be mounted in correspondence of each lens, thus greatly augmenting the variety of information that could be acquired after a single sample travel along the microfluidic circuit. One of the major challenges of the LoC paradigm, and in particular of LoC diagnostics, is the miniaturization of all the devices and optical components external to the chip itself. Indeed, using a portable chip along with a bulky imaging apparatus would frustrate the efforts made to realize microfluidic efficient components of smaller and smaller size, and would disappoint the expectations of microfluidics to become a portable, widespread technology accessible by users in the lack of adequate facilities. In order to move a step toward the simplification of the imaging apparatus, we designed, implemented and tested a novel LoC-based interferometer that allows off-axis DH microscopy with single beam scheme. This is based on the extraction of the reference beam from the beam of light impinging onto the chip surface. A portion of this beam hits the channel and experiences an optical path delay due to the passage through the object, thus acquiring information on its optical thickness distribution. Noteworthy, a portion of the same beam hits a different part of the chip (close to the channel containing the sample), where a grating pattern is written by means of a photolithography process. Thus, the portion of light hitting this resist-coated channel section, diffracts from its surface with an angle, depending on the grating period, sufficient to provide an off-axis spatial carrier that can be exploited to reconstruct the formed hologram. Thus, off-axis DH microscopy is realized eliminating the need for the reference arm of the interferometer.

Hence, optical elements like e.g. beam splitters, beam combiners, mirrors, half-wave plates, variable power attenuators are not required anymore. The introduced setup has no particular design constraints, so that the distance between the light source and the chip can be minimized, which allows to reduce the size of the entire apparatus. If a small size laser diode was used as a light source, along with the printing of polymer lenses onto the chip surface, such recording scheme could constitute a compact, portable, off-axis DH microscope in transmission configuration. Further studies will be devoted to optimize the setup parameters for the scope. In particular, the minimization of the optical path difference between the object beam and the reference beam could allow the use of low-coherence sources, e.g. LEDs still permitting the formation of a hologram, but assuring enhanced quality in terms of SNR. With this idea in mind, STDH could be used to equip the LoC microscope with an embedded LSA as a recording device. This approach has been demonstrated to be a viable solution to definitely solve the problem of integrating the imaging functionalities onboard chip, and it could favorite the spread of LoC devices as useful tools for environmental monitoring and point-of-care diagnostics in the developing world.

REFERENCES

[1] G. M. Whitesides, *The origins and the future of microfluidics,* Nature **442**, 368-373, 2006.

[2] D. B. Weibel et al. *Torque-actuated valves for microfluidics,* Anal. Chem. **77**, 4726-4733, 2005.

[3] H. A. Stone et al. *Engineering flows in small devices: microfluidics toward a lab-on-a-chip,* Annu. Rev. Fluid. Mech. **36**, 381-411, 2004.

[4] T.M. Squires et al. *Microfluidics: fluid physics at the nanoliter scale,* Rev. Mod. Phys. **77**, 977-1026, 2005.

[5] D. J. Beebe, *Physics and applications of microfluidics in biology* Annu. Rev. Biomed. Eng. **4**, 261-286, 2002.

[6] J. Hsieh, *Tunable Microfluidic Optical-Fiber Devices Based on Electrowetting Pumps and Plastic Microchannels,* IEEE Phot. Tech. Lett., **15**(1), 81-83, 2003.

[7] E. M. Lucchetta, et al. *Dynamics of Drosophila embryonic patterning network perturbed in space and time using microfluidics,* Nature **434**, 1134-1138, 2005.

[8] Q. Zhang et al. *Applications of Microfluidics in Stem Cell Biology,* Bionanoscience **2**(4), 277286, 2012.

[9] P. J. Hung et al. *Continuous perfusion microfluidic cell culture array for high-throughput cell-based assays,* Biotechnol. Bioeng. **89**, 1-8, 2005.

[10] B. G. Chung, et al. *Human neural stem cell growth and differentiation in a gradient-generating microfluidic device,* Lab Chip **5**, 401-406, 2005.

[11] E. M. Walters et al. *Mammalian embryo culture in a microfluidic device,* Methods Mol. Biol. **254**, 375382, 2004.

[12] M. A. McClain, et al. *Microfluidic devices for the high-throughput chemical analysis of cells,* Anal. Chem. **75**, 5646-5655, 2003.

[13] B. S. Cho, et al. *Passively driven integrated microfluidic system for separation of motile sperm,* Anal. Chem. **75**, 16711675, 2003.